https://doi.org/10.15388/vu.thesis.1018
https://orcid.org/0009-0000-9456-9975

VILNIUS UNIVERSITY
CENTER FOR PHYSICAL SCIENCES AND TECHNOLOGY

Karolis Adomavičius

Development of Full-Field Optical Coherence Tomography Methods for High-Resolution and Extended-Depth Biomedical Imaging

DOCTORAL DISSERTATION

Natural Sciences,
Physics (N 002)

VILNIUS 2026

This dissertation was written between 2020 and 2025 at Center for Physical Sciences and Technology.

Academic Supervisor – Dr. Egidijus Auksorius (Center for Physical Sciences and Technology, Natural Sciences, Physics – N 002)

Dissertation Defense Panel:
Chairman – Assoc. Prof. Dr. Zigmas Balevičius (Center for Physical Sciences and Technology, Natural Sciences, Physics, N 002).
Members:
Dr. Marius Franckevičius (Center for Physical Sciences and Technology, Natural Sciences, Physics, N 002),
Assoc. Prof. Dr. Saulius Galgauskas (Vilnius university, Medical and Health Sciences, Medicine, M 001),
Dr. Lena Golubewa (Center for Physical Sciences and Technology, Natural Sciences, Physics, N 002),
Dr. Léo Puyo (Institut Langevin, Paris, Natural Sciences, Physics, N 002).

The dissertation shall be defended at a public meeting of the Dissertation Defense Panel at 15:00 on 27 November 2026 in Room D401 of the Center for Physical Sciences and Technology, Vilnius.

https://doi.org/10.15388/vu.thesis.1018
https://orcid.org/0009-0000-9456-9975

VILNIAUS UNIVERSITETAS
FIZINIŲ IR TECHNOLOGIJOS MOKSLŲ CENTRAS

Karolis Adomavičius

Viso lauko optinės koherentinės tomografijos metodų kūrimas didelės skiriamosios gebos ir padidinto vaizdinimo gylio biomedicininiams tyrimams

DAKTARO DISERTACIJA

Gamtos mokslai,
Fizika (N 002)

VILNIUS 2026

Disertacija rengta 2020–2025 metais Fizinių ir technologijos mokslų centre.

Mokslinis vadovas – dr. Egidijus Auksorius (Fizinių ir technologijos mokslų centras, gamtos mokslai, fizika, N 002)

Gynimo taryba:
Pirmininkas – doc. dr. Zigmas Balevičius (Fizinių ir technologijos mokslų centras, gamtos mokslai, fizika, N 002).
Nariai:
Dr. Marius Franckevičius (Fizinių ir technologijos mokslų centras, gamtos mokslai, fizika, N 002),
Doc. dr. Saulius Galgauskas (Vilniaus universitetas, medicinos ir sveikatos mokslai, medicina, M 001),
Dr. Lena Golubewa (Fizinių ir technologijos mokslų centras, gamtos mokslai, fizika, N 002),
Dr. Léo Puyo (Institut Langevin, Paryžius, Prancūzija, gamtos mokslai, fizika, N 002).

Disertacija ginama viešame Gynimo tarybos posėdyje 2026 m. lapkričio mėn. 27 d. 15:00 val. Fizinių ir technologijos mokslų centro D401 auditorijoje, Vilniuje.

CONTENTS

CONTENTS 5
LIST OF ABBREVIATIONS 6
ACKNOWLEDGEMENTS 9
1 INTRODUCTION 10
1.1 Major goal . . . 10
1.2 Tasks of this Work . . . 11
1.3 Scientific Novelty . . . 11
1.4 Statements for Defense . . . 11
1.5 Author Contribution . . . 12
1.6 List of publications . . . 12
2 LITERATURE OVERVIEW 16
2.1 Development of Optical Coherence Tomography . . . 16
2.2 Basic principles . . . 16
2.3 Full-Field OCT . . . 21
2.4 Noise . . . 27
2.5 Medical applications . . . 28
3 FOURIER-DOMAIN FULL-FIELD OCT 35
3.1 Multimode fiber as a tool to reduce cross talk in Fourier-domain full-field optical coherence tomography . . . 35
3.2 Spatio-temporal optical coherence tomography use for retinal imaging . . . 49
3.3 Deformable Membrane for modal noise reduction . . . 61
3.4 High-Throughput Spatio-Temporal Optical Coherence Tomography (STOC-T) . . . 75
4 TIME DOMAIN OCT 88
4.1 Time-domain full-field optical coherence tomography with a digital defocus correction . . . 88
4.2 Time-Domain Full-Field Confocal Optical Coherence Tomography with Digital Scanning . . . 101
CONCLUSIONS 113
5 SANTRAUKA LIETUVIŲ KALBA 114
BIBLIOGRAPHY 158
CURRICULUM VITAE 174

LIST OF ABBREVIATIONS

1D	One-Dimensional
2D	Two-Dimensional
2D-FFT	Two-Dimensional Fast Fourier Transform
3D	Three-Dimensional
A-line	Axial Depth Profile
AO	Adaptive Optics
AOTF	Acousto-Optic Tunable Filter
A-scan	One-Dimensional Axial-Amplitude Profile
BS	Beam Splitter
B-scan	Two-Dimensional Cross-Sectional Image
CC	Choriocapillaris
CCD	Charge-Coupled Device
CMOS	Complementary Metal-Oxide-Semiconductor
COST	Cone Outer Segment Tips
CT	Computed Tomography
DC	Direct Current (Zero-Frequency Component)
DCP	Deep Capillary Plexus
DDR	Double Data Rate
DDR RAM	Double Data Rate Random-Access Memory
DM	Deformable Membrane or Deformable Mirror, depending on context
DMD	Digital Micromirror Device
DOF	Depth of Focus
EDI	Enhanced Depth Imaging
FAZ	Foveal Avascular Zone
FD	Fourier Domain
FD-FF-OCT	Fourier-Domain Full-Field Optical Coherence Tomography
FD-OCT	Fourier-Domain Optical Coherence Tomography
FF	Full Field
FF-FD-OCT	Full-Field Fourier-Domain Optical Coherence Tomography
FF-OCT	Full-Field Optical Coherence Tomography
FFT	Fast Fourier Transform
FOV	Field of View
FWC	Full Well Capacity
FWHM	Full Width at Half Maximum
GCL	Ganglion Cell Layer
HL	Haller's Layer
HT	High Throughput
HTDF	High-Throughput Dark-Field
HT-STOC-T	High-Throughput Spatio-Temporal Optical Coherence Tomography
ICD	Intercapillary Distance
ICGA	Indocyanine Green Angiography
ICP	Intermediate Capillary Plexus
ILM	Inner Limiting Membrane
INL	Inner Nuclear Layer

IR	Infrared
IS/OS	Inner/Outer Segment Junction
IVUS	Intravascular Ultrasound
LDF	Laser Doppler Flowmetry
LDH	Laser Doppler Holography
LED	Light-Emitting Diode
LMH	Lamellar Macular Hole
MEMS	Microelectromechanical Systems
MLDH	Multiwavelength Laser Doppler Holography
MM	Multimode
MMF	Multimode Fiber
MMF+DM	Multimode Fiber and Deformable Membrane
MRI	Magnetic Resonance Imaging
NA	Numerical Aperture
ND	Neutral Density
NFL	Nerve Fiber Layer
OCT	Optical Coherence Tomography
OCTA	Optical Coherence Tomography Angiography
OD	Optical Density
OPL	Outer Plexiform Layer
PDMS	Polydimethylsiloxane
Postop.	Postoperative
Preop.	Preoperative
PSD	Power Spectral Density
PSF	Point Spread Function
RAM	Random-Access Memory
RIN	Relative Intensity Noise
RMS	Root Mean Square
ROI	Region of Interest
ROST	Rod Outer Segment Tips
RPE	Retinal Pigment Epithelium
SCP	Superficial Capillary Plexus
SD	Spectral Domain
SD-OCT	Spectral-Domain Optical Coherence Tomography
SLD	Superluminescent Diode
SLM	Spatial Light Modulator
SM	Single Mode
SNR	Signal-to-Noise Ratio
SOA	Semiconductor Optical Amplifier
SS	Swept Source
SS-FF-OCT	Swept-Source Full-Field Optical Coherence Tomography
SS-OCT	Swept-Source Optical Coherence Tomography
STOC	Spatio-Temporal Optical Coherence
STOC-T	Spatio-Temporal Optical Coherence Tomography
TD	Time Domain
TD-FF-OCT	Time-Domain Full-Field Optical Coherence Tomography
TD-OCT	Time-Domain Optical Coherence Tomography
TEM	Transverse Electromagnetic Mode

THz	Terahertz
TIR	Total Internal Reflection
USAF	United States Air Force
UV	Ultraviolet
VCSEL	Vertical-Cavity Surface-Emitting Laser
VIS	Visible
v/v	Volume-to-Volume Ratio
w/v	Weight-to-Volume Ratio

ACKNOWLEDGEMENTS

First of all, I want to thank my supervisor dr. Egidijus Auksorius for optimism and support during my career in science. And dealing with my random randomness. And never stoping kicking me up to fix mistakes and upgrade whatever I did not good enough. And very special Rūtčikui-Koldūnčikui (Rūtai Adomavičienei) (wife, Koldūn and moral support) for bearing with me writing this thesis, talking about OCT before sleep and listening to my rants about lasers. And keeping company at work when measurements needed an extra hand at night. And helping me learning LaTeX and fixing my errors. And Danielis Rutkauskas, for occasionally calling me pedantic (when no more nitpicking was possible). Took that as a compliment and motivation. And I thank Austėja Trečiokaitė for not stabbing me during all this time working together. And Erikas Tarvydas for technical support and questioning my precision. Special thanks to Domas Paipulas for fabricating experimental mirror-pin-holes. I thank My Family, my parents, my grandma for keeping interest in math since early school, my mum for baking amazing cakes which motivated me writing this thesis, my father for that childhood memory of walking under a starry night which inspired me to never stop asking and pursuing science in the future. And Sergėjus Orlovas for that online argument about probabilities when I said I'll study physics at VU. Thanks to all coauthors. And I thank my friends for understanding why I kept ignoring them all these years. If I missed a point or a punctuation mark, there are some bellow. Cheers to everyone reading!



1. INTRODUCTION

In 1960 the first laser was built by Theodore Maiman at Hughes Research Laboratories. This was the key moment in optics almost as important as first fire discovery in human history. Laser has enabled fast development in many fields one of which is medicine. Later on, not only laser, but commercially available LEDs (Light emission diodes) were further developed which led to wider access to light manipulating tools. Today's medicine could not be possible without diagnostic tools based on light emission and detection. One of those tools is optical coherence tomography (OCT) and stands together with X-rays, CT (computed tomography) scans, MRIs (magnetic resonance imaging), ultrasounds and THz (terahertz) imaging.

Optical coherence tomography is a noninvasive diagnostic technique that provides real time, high resolution, depth-resolved volumetric images. First time optical coherence tomography (OCT) was described in Science journal in 1991 [1]. By using superluminescent diode (SLD), single mode fiber and photodiode human retina was measured in-vitro. From that moment numerous optical coherence tomography techniques and variations have emerged: from conventional single-point scanning time domain optical coherence tomography to fast full-field Fourier domain imaging, flow detecting Doppler OCT, dual-axis OCT, polarization-sensitive OCT, etc. Today, optical coherence tomography is an example of the successful implementation of biophotonic science into clinical practice [2]. OCT spread to various medical fields providing delicate organ imaging for ophthalmology, cardiology, oncology, dermatology, etc. However, different OCT applications arise new challenges, e.g. in-vivo retinal imaging needs fast data acquisition to avoid blur from involuntary eye movements whereas fixed tissue samples prefer higher resolution and imaging depth in exchange of imaging time. While switching from Time Domain to Fourier Domain OCT can benefit one parameter at cost of another, gradual improvements are needed in both imaging configurations. Thus development of Full-Field OCT techniques provide not only high resolution and imaging depth but also maintain growth of imaging speed [3]. This results in comfortable measurement times in clinical applications and high quality images.

1.1. Major goal

The aim of this work is to develop and experimentally validate optical and computational methods for improving image quality and usable imaging depth in Fourier-domain and time-domain full-field OCT by reducing coherent and modal noise [4], increasing interferometric throughput, enabling digital refocusing, and implementing programmable confocal gating.

1.2. Tasks of this Work

1. Develop and evaluate FD-FF-OCT/STOC-T methods using a long MMF and rapid phase modulation to reduce coherent crosstalk and modal noise, and assess retinal and choroidal imaging.

2. Develop and characterize a high-throughput STOC-T interferometer and quantify its sensitivity and SNR.

3. Develop and evaluate TD-FF-OCT digital refocusing and programmable DMD confocal gating for extending the usable imaging range in scattering samples.

1.3. Scientific Novelty

1. Demonstration of a multimode fiber based crosstalk suppression for FD-FF-OCT, which enables combined both retinal and full-thickness choroidal imaging in a single in vivo volume.

2. Demonstration of multimode fiber and deformable membrane combination for STOC-T which enables cellular-scale visualization of the ganglion cell layer and photoreceptors.

3. A High-Throughput beamsplitter and pick-off-mirror design increased STOC-T sensitivity to 100 dB, which was the highest sensitivity documented for an FF-OCT system when publication was released.

4. Demonstration that digital defocus correction in a TD-FF-OCT system can refocus images from far outside the physical DOF of the objective, with the correction depending on coherence of the light source. This extends the usable imaging depth limited by defocus in scattering ex vivo tissue without re-scanning or mechanical adjustment.

5. Patented DMD double-pass design that uses one half of the mirror array for illumination spots and the other half as digital confocal pinholes, eliminating the DMD back-reflection problem that previously limited its use in FF-OCT, and giving software-adjustable spot size/pinhole size/spacing.

1.4. Statements for Defense

1. A long (300 m), small-core-diameter (50 µm) multimode fiber passively suppresses coherence-noise crosstalk in Fourier-Domain Full-Field OCT (FD-FF-OCT) by up to 11.8 dB, and this suppression is sufficient to resolve both the retina and the full-thickness choroid (choriocapillaris, Sattler's, and Haller's layers) within a single in vivo acquisition volume.

2. Combining the multimode fiber with a fast deformable membrane (MMF+DM) further reduces modal noise, increasing STOC-T system sensitivity to approximately 80 dB and increasing SNR by up to 13.6 dB over the passive-only configuration, enabling in vivo visualization of the retinal ganglion cell layer and photoreceptor inner/outer segments.

3. A High-Throughput (90/10 beamsplitter with pupil-plane pick-off mirror) interferometer redesign increases STOC-T sensitivity by 3.5× (5.4 dB) over the standard MMF+DM configuration, reaching close to 100 dB after averaging 30 volumes (0.3 s acquisition) which enables lower illumination power and reduced motion-averaging requirements for in vivo retinal imaging.

4. In Time-Domain Full-Field OCT (TD-FF-OCT), computational (digital) defocus correction restores in-focus images from data acquired 500–1000 µm out of focus (which is roughly 100 more than the physical depth of focus of the imaging objective). Such defocus correction can be applied for both scattering and reflective ex vivo samples, without mechanical refocusing.

5. A reworked double-pass digital micromirror device (DMD) geometry gives TD-FF-OCT software-reconfigurable confocal gating (multi-spot and multi-line scanning modes) which improves SNR by up to 29× (14.6 dB, from 67 a.u. to 1914 a.u.) under separately optimized acquisition conditions relative to standard full-field detection and extending usable imaging depth in scattering tissue from 400 µm to 800 µm.

1.5. Author Contribution

Author designed and built OCT systems, conducted experiments, analyzed data. Author also collaborated with other authors for publications. Author attended conferences where he presented new achievements and also contributed to raising public awareness of OCT through popular media.

1.6. List of publications

On the dissertation topic

1. Auksorius, Egidijus & Borycki, Dawid & Węgrzyn, Piotr & Sikorski, Bartosz & Lizewski, Kamil & Zickiene, Ieva & Rapolu, Mounika & **Adomavicius, Karolis** & Tomczewski, Slawomir & Wojtkowski, Maciej. **Spatio-temporal optical coherence tomography provides full thickness imaging of the chorioretinal complex.** iScience. (2022)

https://doi.org/10.1016/j.isci.2022.105513.

2. Auksorius, Egidijus & Borycki, Dawid & Węgrzyn, Piotr & Žičkienė, Ieva & **Adomavicius, Karolis** & Sikorski, Bartosz & Wojtkowski, Maciej. **Multimode fiber as a tool to reduce cross talk in Fourier-domain full-field optical coherence tomography.** Optics Letters (2022) https://doi.org/10.1364/OL.449498

3. Borycki, Dawid & Auksorius, Egidijus & Węgrzyn, Piotr & Liżewski, Kamil & Tomczewski, Slawomir & Žičkienė, Ieva & **Adomavicius, Karolis** & Karnowski, Karol & Wojtkowski, Maciej. **Multiwavelength laser doppler holography (MLDH) in spatiotemporal optical coherence tomography (STOC-T).** Biocybernetics and Biomedical Engineering. (2024). https://doi.org/10.1016/j.bbe.2024.03.002.

4. Treciokaite, Austeja & **Adomavicius, Karolis** & Auksorius, Egidijus. **Time-domain full-field optical coherence tomography with a digital defocus correction.** Optics Letters (2024) https://doi.org/10.1364/OL.520911

5. Rutkauskas, D., **Adomavičius, K.**, & Auksorius, E. **Time-Domain Full-Field Confocal Optical Coherence Tomography with Digital Scanning.** Photonics (2025). https://doi.org/10.3390/photonics12040304

6. Marta Mikuła-Zdańkowska, Dawid Borycki, Piotr Węgrzyn, **Karolis Adomavičius**, Egidijus Auksorius, Maciej Wojtkowski. **Imaging of retinal ganglion cells and photoreceptors using Spatio-Temporal Optical Coherence Tomography (STOC-T) without hardware-based adaptive optics.** Biocybernetics and Biomedical Engineering, 2025, https://doi.org/10.1016/j.bbe.2025.01.001.

7. **Adomavičius K.**, Treciokaite A., Tarvydas E., Auksorius E. **High-throughput spatio-temporal optical coherence tomography (STOC-T)** Optics Continuum 4(9), 2099-2106 (2025), DOI 10.1364/OPTCON.564109.

Patents

1. Auksorius E., Rutkauskas D., **Adomavičius K.**

Fast and programmable reflectance confocal microscopy with digital micromirror device European patent EP4550021B1, published 31 December 2025 (application EP23208082.0).

Conference proceedings

1.Adomavičius, K., Žickienė, I., Auksorius, E., & Wojtkowski, M. Ultraspartus tridimensinis (3D) žmogaus tinklainės vaizdinimas su optine koherentine tomografija. Conference: FizTech. Vilnius, Lietuva (2020).

2. Adomavičius, K., Jakštas, V., Žickienė, I., & Auksorius, E. Pilnojo lauko optinė koherentinė tomografija su skaitmenine aberacijos korekcija. Conference: FizTech. Vilnius, Lietuva (2021).

3. Adomavičius K., Žičkienė I., Auksorius E., Borycki D., Tomczewski S., Wojtkowski M. Ultrafast Volumetric (3D) Human Retina Imaging With Fourier-Domain Full-Field Optical Coherence Tomography. Conference: Open Readings. Vilnius, Lietuva (2021).

4. Adomavičius, K., Jakštas, V., Žičkienė, I., Trečiokaitė, A., Rutkauskas, D., & Auksorius, E. Applications of full field optical coherence tomography. Conference: FizTech. Vilnius, Lietuva (2022).

5. Adomavičius, K., Trečiokaitė, A., Borycki, D., Auksorius, E. et al. Crosstalk reduction with a multimode fiber in Fourier domain full-field optical coherence tomography. Conference: Open Readings. Vilnius, Lietuva (2022).

6. Adomavičius, K., Borycki, D., Wegrzyn, P., Žičkienė, I., Wojtkowski, M., & Auksorius, E. Retinal Imaging with Fourier-Domain Full-Field Optical Coherence Tomography and a Multimode Fiber for Coherence Noise Reduction. Conference: ECAMP14. Vilnius, Lietuva (2022).

7. Adomavičius, K., & Auksorius, E. High Throughput Optical Coherence Tomography. Biophotonics Summer School in Hven, Švedija (2023).

8. Adomavičius, K., Trečiokaitė, A., & Auksorius, E. High-Throughput Fourier-Domain Optical Coherence Tomography for Retinal imaging. Conference: FizTech. Vilnius, Lietuva (2023).

9. Adomavičius, K., Trečiokaitė, A., Tarvydas, E., Rutkauskas, D., & Auksorius, E. Application of the high throughput dark-field full-field optical coherence tomography system. Conference: Open Readings. Vilnius, Lietuva (2024).

10. Adomavičius, K., Trečiokaitė, A., Tarvydas, E., & Auksorius, E. Pilno lauko optinė koherentinė tomografija su mažais koherentiniais triukšmais. Conference: FizTech. Vilnius, Lietuva (2024).

11. Adomavičius, K., Trečiokaitė, A., Tarvydas, E., & Auksorius, E. Full Field Optical Coherence Tomography with Low Coherence Noise. Conference: The COINS. Vilnius, Lietuva (2025).

12. Adomavičius, K. Didelio pralaidumo erdivinė-laikinė optinė koherentinė tomografija. Conference: Lietuvos nacionalinė fizikos konferencija. Vilnius, Lietuva (2025).

13. Adomavičius, K.,Trečiokaitė, A., Auksorius, E. High-Throughput

Spatio-Temporal Optical Coherence Tomography. Conference: ICAPI. Tartu, Estija (2025).

2. LITERATURE OVERVIEW

2.1. Development of Optical Coherence Tomography

Optical coherence tomography (OCT) is a non-invasive and non-contact imaging technique based on backscattered light detection. It was first published in 1991 [1] and became one of the main tools for medical imaging. Optical coherence tomography can be compared to ultrasound imaging where ultrasound wave is sent into tissue and back-reflected signal delays are registered as depth. However, since OCT is based on light, there are no fast enough electronics to register such short times between light reflections. Thus OCT is based on interferometric (such as Michelson interferometer) imaging. When low coherence (broadband) light source is used, light interferes only when distances between sample arm and reference arm is matched. This condition allows to measure tissue in depth (depending on distance and signal strength). First uses of this technique relied on single point depth profiles (A-lines) which were obtained by scanning reference arm in axial direction to obtain changes in signal strength distance-wise. Such technique was called Time Domain OCT (TD-OCT). However, early TD-OCT systems were very slow at obtaining images (even more recent systems obtain only up to hundreds of A-lines per second) [5] which resulted in tremendous acquisition times for full images. Thus another type of OCT emerged. The first Fourier Domain (FD) OCT systems were demonstrated a few years later. Spectral Domain (SD) OCT system was demonstrated in 1995 [6] and Swept-source (SS) OCT was shown in 1997 [7].

2.2. Basic principles

The defining characteristic of optical coherence tomography is interferometric backscattered light detection. Depth is be resolved by measuring singly backscattered light from a sample interfering with light reflected by a reference arm. Axial resolution is determined by coherence length of the light source l_c :

$$l_c = \frac{2ln2(\lambda_0^2)}{\pi\Delta\lambda} \tag{2.1}$$

Where λ_0 is the center wavelength of the light source, $\Delta\lambda$– bandwidth (full-width at half maximum). Thus, to achieve high axial resolution a broadband light source (superluminiscent diode, broadband laser) is typically used. Lateral resolution is determined by the focused beam size and numerical aperture of imaging lens. Such condition enables high resolution imaging in situations where high-numerical-aperture optics are cannot be used such as retinal and catheter-based imaging. However lateral resolution is limited by imaging depth.

We can calculate depth of focus b:

$$b = \pi \frac{(\Delta x^2)}{2\lambda} \tag{2.2}$$

and spot size Δx:

$$\Delta x = \frac{4\lambda f}{\pi d} \tag{2.3}$$

Where f is the focal length, d is aperture diameter of the focusing optics. Overall, lateral and axial resolution separation allows many different task-specific OCT designs. The core element of any interferometer (and thus OCT setups) is the beamsplitter which splits source light into sample and reference arms. Reflected light is then combined via same beamsplitter into a detector. There are many OCT variations, but two main branches are: Time domain and Fourier domain OCT. In time domain OCT systems axial imaging is based on reference mirror being scanned via optical delay line [8,9]. When light returning from sample and reference arms is recombined via beamsplitter an interference can be registered via a point detector or a camera. As interference occurs only within coherence length of a light source, by scanning reference arm mirror the produced temporal interference signal on the detector corresponds to axial sample structure (Figure 2.1).

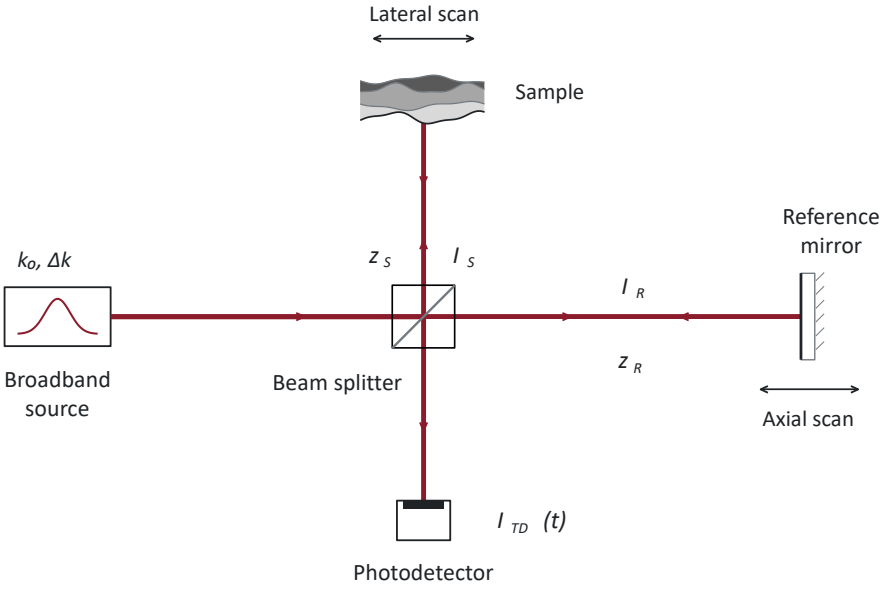


Figure 2.1: Schematics of the standard time-domain OCT setup based on interferometer with a photodetector. This configuration needs lateral scanning for the sample.

In Fourier domain OCT systems instead of temporal delay pattern a spectral interference pattern is registered [10, 11]. In this case the use slow delay line is avoided by replacing detector to spectrometer or replacing broadband light source into swept-source laser. With this configuration registered spectral interferogram is inverse-Fourier transformed into axial OCT scan (Figure 2.2).

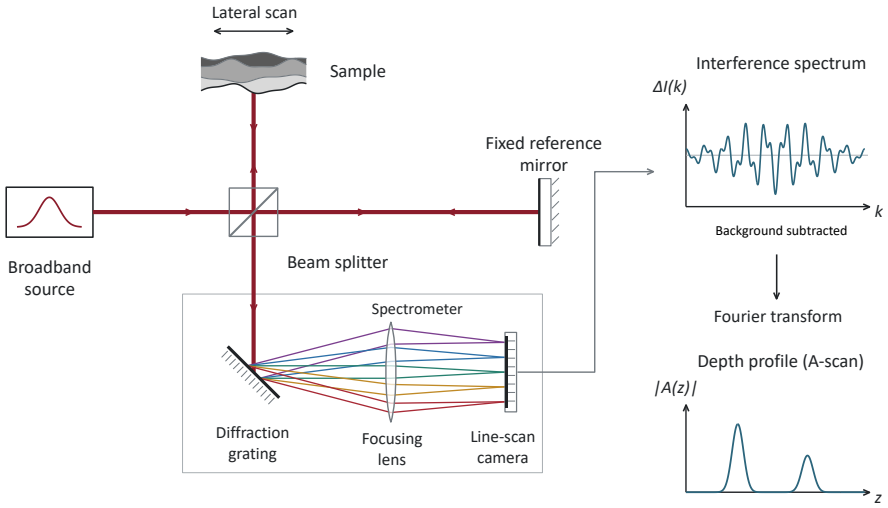


Figure 2.2: Schematic setup of a spectral domain OCT (SD-OCT). Optical grating is used to disperse spectrum on CCD, which is then Fourier transformed into depth profile. In such configuration is scanned laterally.

While time domain OCT provides simpler and cheaper approach, Fourier domain OCT benefits from faster acquisition rate and can be easily implemented into in-vivo experiments that require high capturing speed. Finally, discussing OCT images and system capabilities main describing terms (A-scan, B-scan, enface) should be explained (Figure 2.3):
A-scan: a one-dimensional axial-amplitude function (c);
B-scan: a two-dimensional cross-section (xz / yz) of the sample (a);
enface: a two-dimensional (xy) lateral image of a selected layer (b).

Fourier domain OCT can be split in terms of illumination detection: either when broadband light source and a spectrometer are used it is called Spectral Domain (SD) OCT or spectral OCT) and when rapidly tunable laser and point detector are used it is called Swept Source (SS) OCT or Optical Frequency Domain Imaging.

In both approaches, the reflected spectra are detected individually and used to reconstruct a depth-resolved reflectivity profile [13]. The detector records an interference signal as a function of wavenumber k; after resampling uniformly in k, a Fourier transform yields the depth-resolved reflectivity profile, the detected signal provides information about the amplitude of periodic refractive

index variations. The spatial periodicity of these variations is related to the wavevector $k = 2\pi/\lambda$.

When signals acquired over a range of wavelengths are combined, they form a reflectivity spectrum expressed as a function of the wavevector. Applying a Fourier transform to this spectral data produces the depth profile, as depth information is encoded in the frequency components of the interference signal in k-space.

These advancements in OCT technology provided not only increase in speed, but also in signal to noise ratio (SNR).

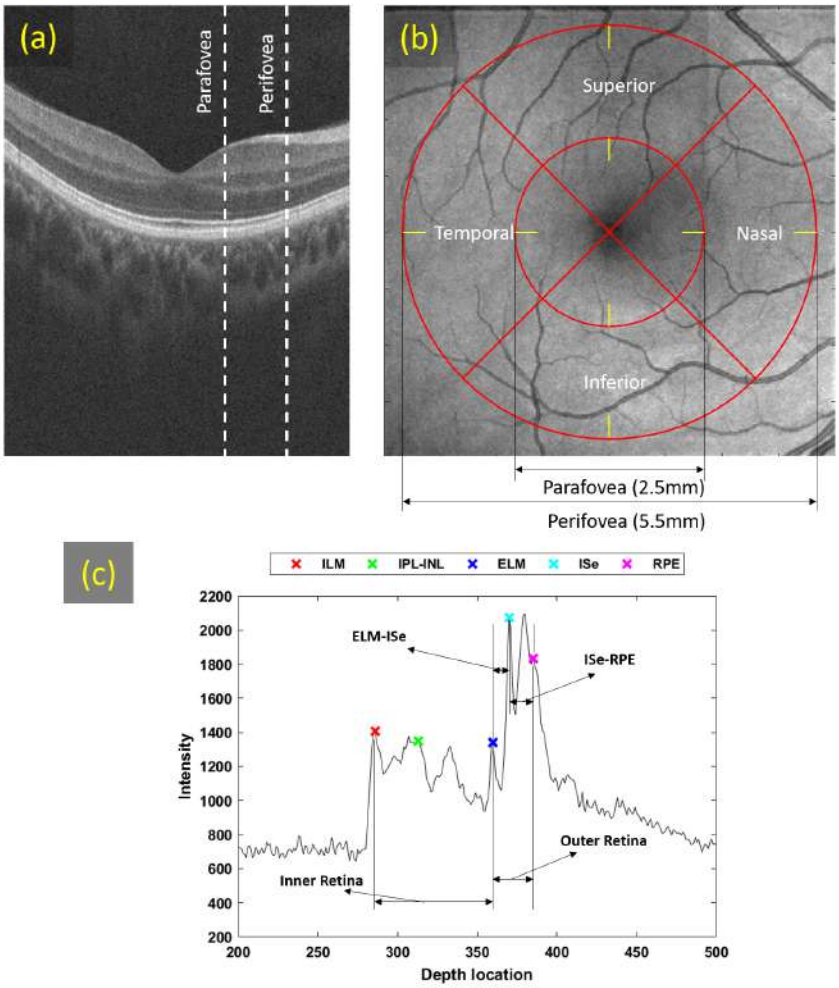


Figure 2.3: (a) Representative retinal B-scan OCT image. (b) Representative enface OCT image with illustration of retinal quadrants. (c) A-line profile shows reflectance intensities of individual retinal layers [12].

2.3. Full-Field OCT

Full-Field Optical Coherence Tomography (FF-OCT) is an interferometric technique that uses a camera for interferogram detecting, which enables acquisition of OCT signal in parallel [14–16]. FF-OCT is most known for high resolution OCT images that contain very few, if any, coherent artefacts [15,17]. Namely, the FF-OCT images are largely free of coherent speckle and crosstalk. due to the use of spatially and temporally incoherent light sources, such as arc lamps and LEDs.

Full-Field Optical Coherence Tomography was first introduced in 1998 [14]. The key distinction between conventional Optical Coherence Tomography systems and Full-Field Optical Coherence Tomography is that FF-OCT obtains images without the need of transverse (lateral) scanning. In traditional OCT , imaging is done by registering an axial line (A-line). A-line can be acquired by single point detector or a line detector. The beam is then moved laterally across the sample surface. Then B-scans and later C-scans are obtained by scanning whole sample point by point. The full-field configuration works differently. Instead of scanning point by point, it records a complete two-dimensional en-face image at a specific depth using a 2D camera. A volumetric image is then created by translating the imaging plane along the axial direction and capturing images at different depths within the sample. In both imaging techniques, the thickness of the optical section is mainly determined by the temporal coherence length of the illumination source, which is inversely proportional to its spectral bandwidth. By reducing 2 dimensional scanning to one dimensional scanning (z axis) introduces both benefits and challenges [18].

Since Full-Field Optical Coherence Tomography obtains whole 2D image layer at a time, it can operate with a shallow depth of field. This allows the use of objective lenses with a high numerical aperture (NA), which improves lateral resolution. With visible light sources, the transverse resolution can reach values below 1 µm. On the other hand, there is a trade-off between exposure time and the achievable field of view in scanning OCT systems. Each pixel is illuminated only for a very short time, typically a few microseconds. In contrast, in FF-OCT the entire field of view is illuminated uniformly for a longer period, usually several milliseconds. This difference can influence the total light dose delivered to the sample. In addition, rapid speckle fluctuations tend to be averaged during the longer exposure in FF-OCT measurements [19].

Recently, it has begun to be called time-domain (TD-) FF-OCT, to differentiate it from Fourier-domain (FD-) FF-OCT, described below, also called swept-source (SS-) FF-OCT. In Time Domain FF-OCT, acquisition speed is limited by the frame rate of the camera, which is typically longer than 1 ms per frame. By comparison, some scanning OCT systems can now record more than 100,000 A-lines per second [20]. In scanning OCT, each pixel of the image is

recorded sequentially at different times during the scan. In FF-OCT, however, all pixels are captured simultaneously when the camera operates in global shutter mode. This can lead to motion-related artifacts in OCT images of moving samples. As a result, phase differences can be calculated between corresponding depths in repeated complex OCT measurements [21] but in order to retrieve the optical phase in FF-OCT it is required to have several measurements acquired with different phase shifts.

In TD-FF-OCT, the coherence gate is scanned axially, so a shallow DOF does not limit the total scanned depth as it limits the simultaneously sharp depth range in FD-FF-OCT. For a long time NA of the objectives, and thus, the resolution was limited (to about 1 µm), which was because it can be challenging to match the dispersion between the sample and reference arms in the Linnik-type of interferometer, which is the most commonly used platform for implementing FF-OCT. High axial resolution (of 1 µm or less) is also easily achievable since white light sources, such as, for example, a Xenon arc lamp can be readily employed in FF-OCT. Recently, high-NA objectives were successfully used to generate FF-OCT images with static and dynamic contrast [22–24]. The record lateral resolution of 280 nm was recently demonstrated by using $NA = 1.25$ [25]. However, to generate 3D volumes, a sample (or, alternatively, the reference mirror) needs to be translated axially. This and the absence of confocal gate in FF-OCT, as well as lack of fast cameras with high full well capacity (FWC) of individual pixels, made FF-OCT too slow for a lot of in vivo imaging applications, despite of the parallel acquisition of OCT signal, limiting its use only for ex vivo eye imaging [26–29] or in vivo imaging of anesthetized rat's eye [30]. Specifically, the missing confocal gate in FF-OCT put higher demand on cameras because it detects all the out-of-focus light that is not coherent with the reference arm, which is reflected to the camera. The incoherent light does not contribute to the formation of useful OCT signal but rather increases the background taking up significant amount of its detection bandwidth that reduces the overall sensitivity. Some type of incoherent light (like specular reflections) could be suppressed with the dark-field detection [31, 32], or added confocality [33], however, most of multiply scattered light will be detected by the camera. However, in vivo volumetric imaging is still challenging with TD-FF-OCT. Nonetheless, off-axis TD-FF-OCT – that use single-shot instead of slower phase-shifting method – was shown capable of generating axial images (B-scans) of the retina in 1 s [34, 35], albeit with significant crosstalk noise due to the use of spatially coherent laser and camera detection that effectively limited the imaging depth in the retina.

Thus, another approach Fourier Domain Full Field OCT (FD-FF-OCT) is used to solve issues arising in TD-FF-OCT and enable fast FF-OCT imaging in vivo [3].

Fourier-Domain Full-Field Optical Coherence Tomography uses a rapidly

tunable laser source, commonly called a swept-source, instead of the spectrally broadband incoherent illumination used in Time-Domain Full-Field Optical Coherence Tomography [3]. In this approach, signal detection is performed in the Fourier domain. When this detection method is combined with parallel image acquisition using a camera, it can achieve voxel rates of approximately 10 GHz [36]. As a result, FD-FF-OCT is one of the fastest volumetric imaging method of Optical Coherence Tomography which also maintains relatively high sensitivity.

Another advantage is the stability of the optical phase extracted from the recorded data. In FD-FF-OCT, the phase remains consistent across the entire field of view (contrary to obtaining A-lines via scanning OCT). Stable phase information in OCT is particularly valuable because it enables computational aberration correction, which enables the final image improvement [36].

Fourier-domain full-field optical coherence tomography (FD-FF-OCT) has made its way into eye imaging as a viable and versatile tool because of its ability for fast imaging speed and acquisition of stable phase information across the whole field of view. However, visualization of choroid is usually prevented by cross-talk noise. Choroid imaging provides information about different ocular diseases pathogenesis of the posterior pole as its principal role is to supply oxygen to the outer retina. Wide field detection and spatially coherent laser induces cross-talk noise which compromises image quality by gradually reducing spacial resolution imaging deeper tissue layers. In order to remove crosstalk a spatially incoherent light source can be used in order to average laterally scattered photons. While the first spatially incoherent wavelength-tunable laser system for FD-FF-OCT was made in 2006 [37].

It was complicated, had limited axial imaging range and images had residual cross-talk noise. However it did not have to rely on photoelastic birefringence modulator [15] or piezo element [38] becoming FD-FF-OCT what we call today. When Sweep source lasers became more and more available, Fourier Domain OCT became more viable. Together with the growth high speed imaging technology, swept source lasers combined fast cameras enabled full-field imaging of en-face images. However, since swept source lasers sweep narrow spectral line over wide spectrum, strong coherence artifacts such as speckles are unavoidable. Speckles are unwanted interference patterns produced by the coherent superposition of fields returned by unresolved scatterers from a sample (Figure 2.4) which reduce image quality [39]. As more coherent light source is, the more impact of coherence noise is introduced onto OCT image. Thus, a lot of FF-FD-OCT development is aimed to coherence reduction.

Another big step in FF-FD-OCT was made imaging human retina in-vivo in 2010 [40] using swept source laser and fast CMOS (complementary metal-oxide-semiconductor) camera capable of registering 640×24 pixels area at 100 000 frames per second. The experiment was limited by light source power thus

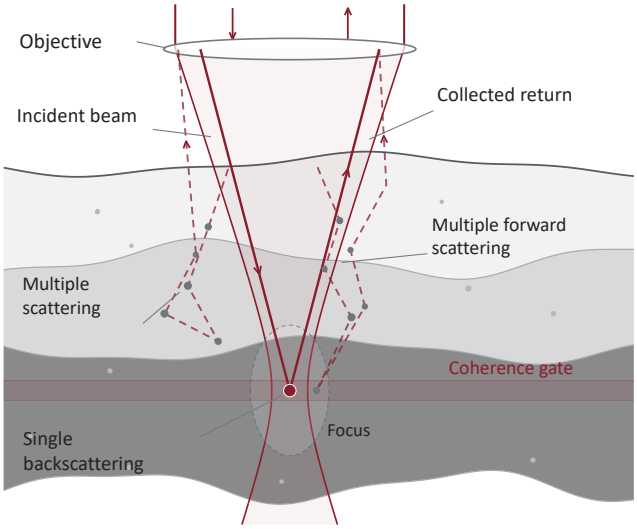


Figure 2.4: Propagation of a focused beam in tissue. The two main processes that distort the wave front of the returning wave—multiple forward scatter and multiple backscatter – are depicted here.

measured area had to be limited into a line (by using cylindrical lenses). Setup was based on Michelson interferometer and coherent illumination was injected via single-mode fiber. Obtained B-scan images had residual coherence and motion blur artifacts (Figure 2.5) but the principle was achieved and optimization was feasible.

To combat coherence noise a interferometric spatiotemporal optical coherence (STOC) manipulation was introduced in 2013 (and this term is often used for full field Fourier domain OCT systems which incorporate spatial coherence manipulation) [41]. A spatial light modulator (SLM) was used as a sample in Michelson interferometer to control fringe pattern by altering phase. This experiment lead in further possibilities to reduce coherence noise in biomedical OCT imaging by introducing phase manipulation.

Furthermore, a rotating diffuser [42] was used to reduce spatial coherence of a laser. Later on as a successor of a rotating diffuser, a narrow-band VCSEL (vertical-cavity surface-emitting laser) array [43] and an ultra-fast deformable membrane was used to account for high frame registration speeds as rotating diffusers are too slow to reduce spatial coherence in short period of time thus increase frame acquisition time.

Later, a larger field of view imaging was achieved by utilizing a much faster camera for imaging retinal vascular dynamics, after recognizing that the phase is stable across the whole field of view [44]. Not only it enabled in vivo volumetric retinal but it even surpassed the speed of any OCT technique by achieving 10 GHz voxel rate [36] with relatively high sensitivity. Even though the

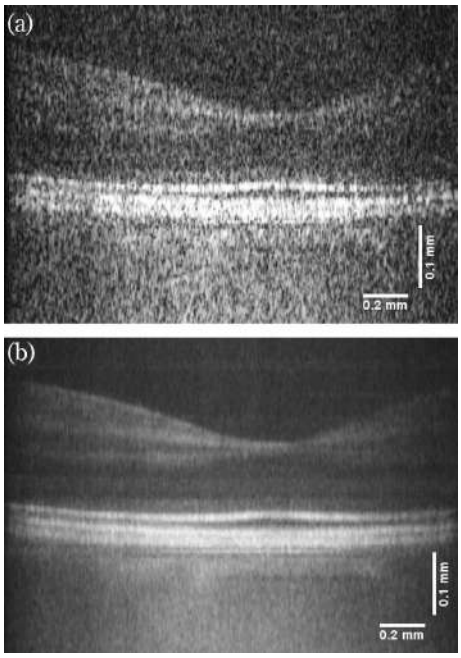


Figure 2.5: (a) Single B-scan of human retina recorded with 1,500,000 A-scans/s at 1:5 mW radiant flux. (b) Averaged image of 24 A-scans of the imaged volume [40].

same volumetric imaging speed is possible with TD-FF-OCT [45], the achieved sensitivity can be orders of magnitude lower. Just like in FD-OCT – in FD-FF-OCT too – the chromatic dispersion mismatch between the sample and reference arms and also the axial motion, which appears as a chirp in recorded interference spectrum and is inevitable in in vivo imaging, can be corrected computationally, which is not possible in TD-FF-OCT. The volumetric speed of FD-FF-OCT and its scanless nature comes at the price of achievable lateral resolution due to the necessity to have a substantial depth of focus in order to be able to acquire multiple axial planes semi-instantaneously. However, for a long time FD-FF-OCT suffered from cross talk issues due to use of spatially coherent laser and full-field detection [36, 40, 44], [46–48], which arise from multiply scattered photons that travel to neighboring region when imaged onto camera, while remaining coherent with the reference beam. Crosstalk noise limited imaging depth in the retina, preventing from resolving choroidal structure.

Another way to reduce spatial coherence is to use deformable membrane [49], [3]. It is done by directing laser light onto a deformable membrane that oscillates chaotically at frequencies up to 500,000 vibrations per second. These rapid fluctuations impose random, uncorrelated phase changes across the beam at a rate much higher than the inverse of the camera's exposure time. As a result, its effective, exposure-averaged spatial coherence is reduced. Typically

membrane is positioned before the interferometer so that identical phase patterns are projected onto both the sample and the reference arm. This configuration preserves interferometric fringes associated with single backscattering events (Figure 2.6).

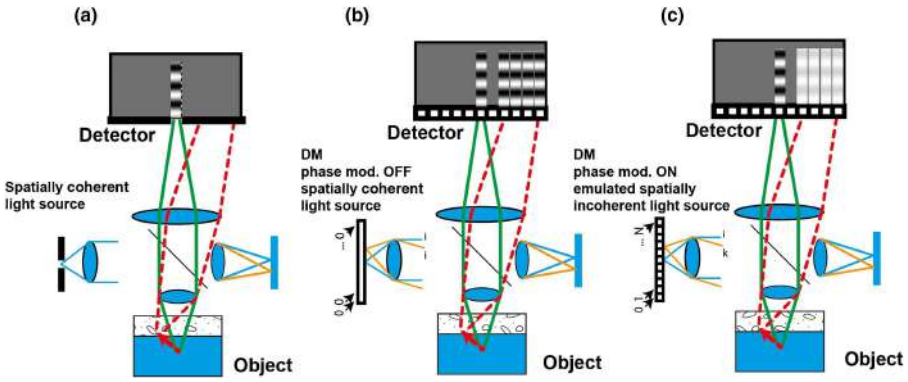


Figure 2.6: Principle of crosstalk-reduced FD-FF-OCT: (a) Multiply scattered light can be rejected by using a pinhole placed in the front of the photodetector—the solution used in scanning OCT devices; (b) Origin of the crosstalk: Full-field OCT with partially coherent illumination uses numerous detection channels, hence the multiply scattered light contributes to interference in pixels that are improperly mapped with respect to the real image of the measured object; (c) Crosstalk-reduced FF-OCT: The spatial phase modulation introduced by the deformable membrane (DM) placed in front of the interferometer washes out fringes originating from multiply scattered light, effectively reducing the crosstalk [49].

However, the deformable membrane is not an optimal tool as it works in limited imaging depth [3, 50] and produces hard-to-remove artifacts in the obtained images. Another way to reduce spatial coherence is to use multimode (MM) fiber as it breaks down spatially coherent light into a number of spatial modes and reduces coherent artifacts. This effect is typically used in laser projection displays [51]. Moreover, spectrally broadband laser light could be coupled into MM fiber to produce partially spatially coherent illumination for time-domain (TD) FF-OCT which has been used to image a fruit fly [38] and an aluminum plate [52]. Even though powerful LEDs and other alternative light sources could be used for TD-FF-OCT, there are no alternatives that emit partially spatially coherent, narrow instantaneous spectral bandwidth ($\sim$0.1 nm) and tunable across tens of nanometers. Closest commercially available source would be a swept source laser but narrow spectral bandwidth beam coupled into a short MM fiber produces a high-contrast speckle pattern at the second end of the fiber.

However, it was later found that a long multimode fiber with relatively small core can also be used to reduce the spatial coherence of the laser with

certain advantages over the membrane approach [53]. Namely, it resulted in fewer image artefacts and it acted as a passive device (no bending or twisting of the fiber was necessary). This was despite the difficulty of using the multimode fiber with narrow (instantaneous) bandwidth (0.1 nm) illumination, which was 2-3 orders of magnitude narrower compared to that used in TD-FF-OCT (10-100 nm). However, even though, this narrow bandwidth produces a speckle pattern at the distal end of the fiber and also in FF-OCT images, it can be easily computationally filtered out [53] without losing too much of the signal.

2.4. Noise

Experimental conditions are always non-ideal. Not only equipment may be flawed, whole system usually imperfect. One of the common problems in imaging is noise. There are 5 most common forms of noise: shot noise, modal noise, coherent cross-talk noise, detector noise and relative-intensity noise.

Shot noise is a fundamental limit to the observed optical intensity noise. While historically treated as an issue with photodetection (random event when photon is absorbed in a photodetector), shot noise is a property of light field [54]. Shot noise is typically described as quantum noise following Poisson statistics. While shot noise cannot be eliminated, increasing light source power, reducing optical losses in the system, using higher quantum efficiency detectors and increasing integration time increases signal-to-noise ration (SNR). Since shot noise increases as a square root of detected photons [55], SNR can be calculated as $SNR = N/\sqrt{N} = \sqrt{N}$ which suggests that increasing signal 100 times, shot noise increases 10 times.

Relative intensity noise (RIN) is the fluctuation of a laser's optical power output, which is normalized to its average power [56]. Typically RIN is described with a power spectral density (PSD), which specifies the strength of the noise per unit bandwidth at a certain noise frequency. The two sources of noise in semiconductor lasers arises from spontaneous emission and from electron-hole recombination shot noise [57].

Modal noise is related to Interference noise induced in multimode fibers when coherent or partially coherent sources excite multiple modes which have nonuniform distribution. This nonuniform distribution results in speckle pattern at the second end of the multimode fiber. The fluctuation in the received optical power induced by fluctuation of speckle pattern is modal noise. Modal noise inversely proportional to the laser linewidth [57]. In order to reduce modal noise, coherence of the light source should be reduced e.g. broadening linewidth or physically agitating fiber to scramble modes.

Detector noise consists mainly of thermal noise and dark current noise. Even when there is no light reaching detector, dark current flows through the reversed-biased photo diode and is caused by thermal effects induced electron-

hole pairs creation in the p-n junction. Moreover, due to thermal effects randomly moving electrons in load resistance induce an additional thermal noise component, also known as Johnson noise, to the photocurrent [57]. These effects can be mitigated by cooling the detector.

Coherent cross-talk noise typically arises in FF-OCT systems due to multiple scattered photons. In interferometer light interferes withing temporal coherence length. By adjusting reference mirror different depth of the sample can be obtained as interference pattern. When light source with high coherence is used, light reflected from multiple scatterers can interfere in the same manner as light coming from a deeper layer and such unwanted signal introduces cross-talk noise [4]. This effect can be typically mitigated by using lower coherence light sources.

2.5. Medical applications

Ophthalmology

The need for non-invasive medical imaging is critical to the rapid growth of medical treatment of diseases, especially sensitive organs. The evolution of OCT has brought about a significant revolution in eye care. Anterior and posterior segment tissues can now be examined non-invasively, helping the physician make faster and better treatment decisions based on objective structural imaging [58]. This technology can quantitatively assess various ocular structures including the cornea, retina, iris, iridocorneal angle, and optic nerve [59].

One of the OCT branches is optical coherence tomography angiography (OCTA) which utilizes motion contrast to detect blood flow [59]. Before the advent of OCTA, traditional structural OCT images mainly visualized low-contrast anatomical changes between small vessels and tissues within the retinal layers [59]. Such technique provides information before and after treatment of various retinal diseases. (Figure 2.8). Therefore, other imaging modalities such as fluorescein angiography or indocyanine green angiography were commonly used to evaluate retinal and choroidal vasculature (Figure 2.7) [62]. OCTA uses the principle of temporal decorrelation caused by moving erythrocytes between repeated OCT measurements to localize the blood vessel in different segments of the eye without using intravascular dyes. OCTA technology allows visualization of retinal blood flow, and the choroidal vasculature can be visualized using depth-encoded anterior panels. These panels are presented together with structural OCT B scans. Together they provide detailed images of the deep retinal choroid plexuses and choriocapillaris blood flow that were not well visualized by previous imaging techniques [63]. Today ophthalmologists have mastered optical coherence tomography to detect glaucoma, age-related macular degeneration, diabetes-related retinopathy, cystoid macular edema, cone and cone-rod dystrophies, tumors in choroid and retina [64], macular puckers

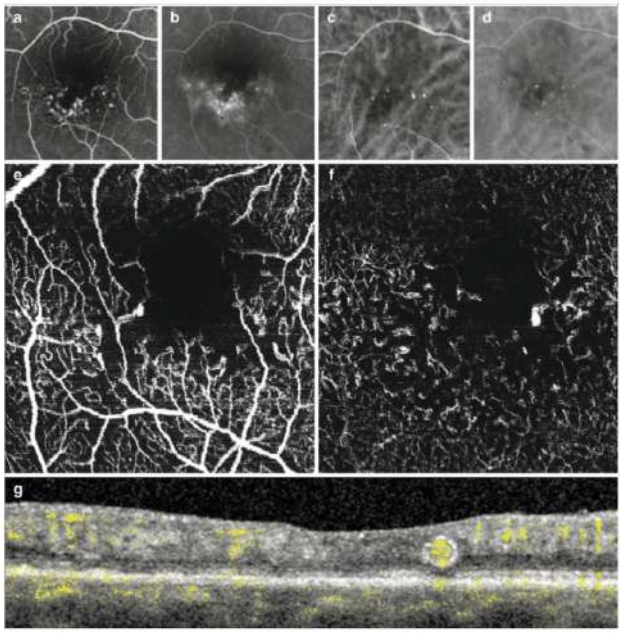


Figure 2.7: Multimodal imaging of Type I idiopathic macular telangiectasia. Fluorescein angiography (a, b) and indocyanine green angiography (ICGA) (c, d) showing the dilated telangiectatic perifoveal vessels with leakage in the late phase. OCTA at the superficial retinal capillary plexus (e) and deep (f) retinal capillary plexus revealing the dilated telangiectatic perifoveal vessels. The B-Scan (g) displaying the dilated telangiectatic vessel with flow sign inside [60].

and holes, etc.

Although OCT has many advantages over standard angiographic procedures, limitations of this technology must be considered. One of them is a small field of view. In addition, frequent artifacts prevent correct interpretation of the images. The most common artifacts [65] arise from eye movements, false-identification of retinal layers, projections, and coherence noise. Artifact identification and mitigation must be taken into account for adequate diagnosis and follow-up of patients.

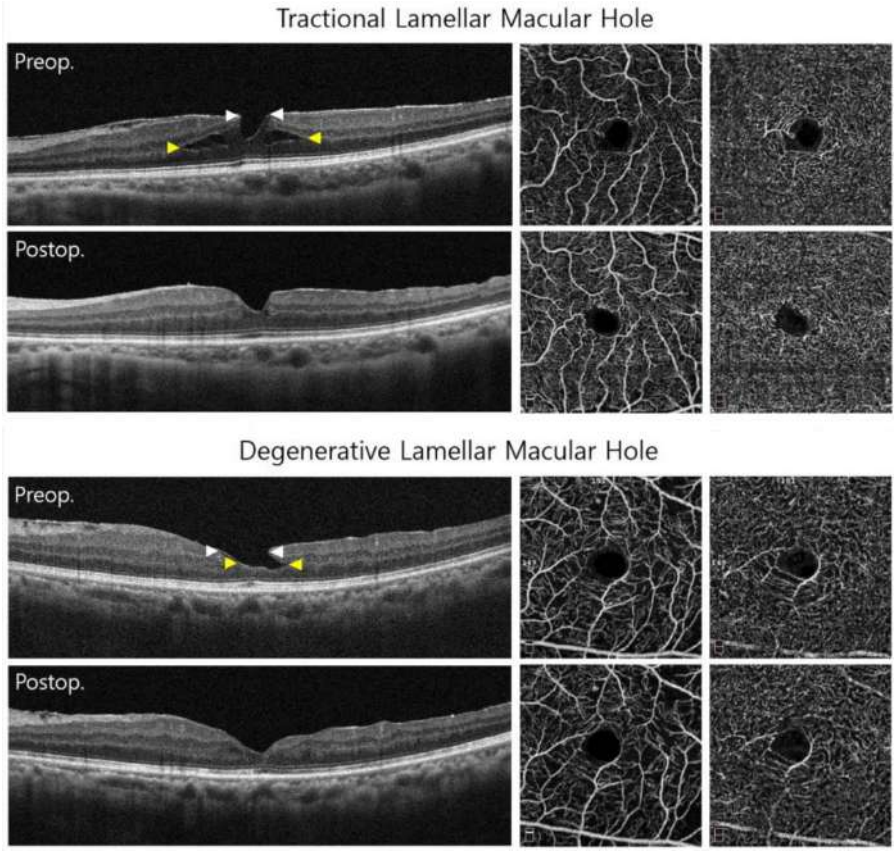


Figure 2.8: Preoperative and postoperative optical coherence tomography (OCT) and OCT angiography of the eyes with tractional and degenerative lamellar macular hole (LMH). (Top) Tractional LMH. The inner diameter (white arrowheads) measured at the level of the internal limiting membrane was 345 µm. The outer diameter (yellow arrowheads), the maximum diameter of the intraretinal schisis, was 1,670 µm. After the tractional epiretinal membrane was removed in surgery, the foveal and parafoveal vessel densities in the superficial capillary plexus increased. In addition, foveal avascular zone (FAZ) area increased from 0.191 to 0.214 mm^2. (Bottom) Degenerative LMH. Compared with tractional LMH, degenerative LMH had a larger inner diameter (400 µm, white arrowheads) and a smaller outer diameter (506 µm, yellow arrowheads). No significant microvascular changes were observed at 6 months after surgery. Postoperative FAZ area was 0.249 mm^2, with no significant difference from the preoperative FAZ area (0.250 mm^2). Preop. Preoperative, Postop. postoperative [61].

Cardiovascular disease remains the primary cause of morbid illnesses and death in the United States [66]. Medical imaging has an essential role in the early detection of cardiovascular conditions (Figure 2.9), as well as in procedural guidance, follow-up, and the evaluation of preclinical disease models. In the field of cardiology, optical coherence tomography (OCT) serves as an analogical optical approach to intravascular ultrasound (IVUS) and is widely applied for imaging the coronary arteries [67]. In OCT, the ultrasound acoustic waves used in IVUS are replaced by near-infrared light, typically around 1,300 nm in wavelength, which exhibits relatively low absorption by red blood cells, water, lipids, and proteins. During intravascular OCT, blood is transiently displaced with an iodinated-contrast or saline flush because it strongly attenuates the signal. By using a rotating glass fiber probe, coherent infrared light is delivered to and reflected from the tissue, enabling the acquisition of highly detailed, high-resolution cross-sectional tomographic images that are comparable to those produced by IVUS.

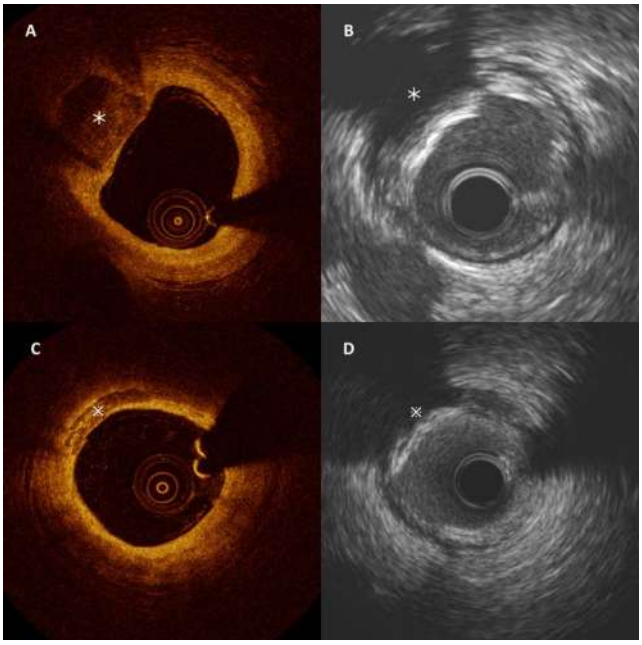


Figure 2.9: A shows thick calcium; C shows thin calcium. Calcium on IVUS is visualized as a bright superficial reflection followed by acoustic shadow that prevents thickness assessment (B and D) [68].

Due to its superior spatial resolution of approximately 10–15 µm, OCT enables clear differentiation of the internal and external elastic laminae as well as the intima, media, and adventitia, a level of detail that cannot be achieved with

lower-resolution IVUS (100–150 µm) [69]. Polarization-sensitive OCT can measure depth-resolved birefringence and retardation, providing additional contrast related to collagen organization and other tissue properties. Regions with high birefringence, caused by polarization changes, are associated with fibrous tissue, collagen, and lipid components, whereas areas of low birefringence are indicative of calcified tissue. By overlaying maps of low and high birefringence onto standard OCT images, tissue structures can be identified according to their composition which leads to better overall diagnostic accuracy.

Oncology

In oncology, medical imaging is essential because it provides detailed morphological, anatomical, metabolic, and molecular information that supports more advanced treatment strategies and, as a result, improved outcomes for patients with cancer [70]. The use of OCT is constantly expanding, encompassing clinical uses such as endoscopic imaging and tumor margin assessment, as well as small animal studies for monitoring tumor progression and evaluating responses to therapeutic drugs.

In contrast to healthy tissue, which typically exhibits an ordered structural organization, cancerous tissue is often disordered and marked by variations in cell size, irregular cell shapes, and enlarged nuclei (Figure 2.10). These features lead to altered optical scattering properties, which may help OCT distinguish between normal and cancerous tissue with high spatial resolution [71]. When compared with conventional cancer imaging techniques, OCT provides superior soft tissue contrast based on refractive index variations, allowing more precise visualization of soft tissue anatomy, which is particularly important for early cancer detection. Additionally, OCT systems can be incorporated into compact probes and catheters, making them well suited for imaging internal organs and diagnosing cancer.

Overall, the depth of our understanding of oncology depends largely on our ability to visualize and track the associated dynamic cellular changes. OCT provides appropriate spatiotemporal scales for non-destructive investigation of the complex dynamics of oncologic cells in vitro.

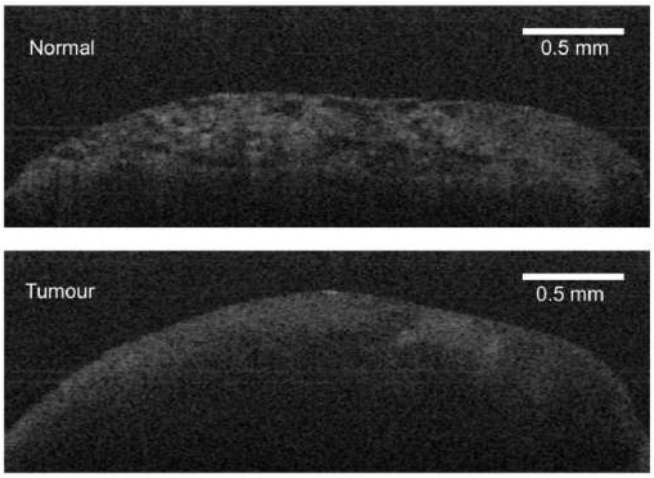


Figure 2.10: Typical OCT images from normal (top) and tumor (bottom) tissues [72].

Dermatology

Inflammatory skin diseases have been widely studied in vivo using OCT [73]. Studies have demonstrated that inflammation-related skin changes are clearly detectable in OCT images. For instance, irritant contact dermatitis is characterized by enlarged and more irregular surface skin folds. Epidermal thickening caused by spongiosis and acanthosis can also be identified, partly due to signal attenuation resulting from dilated blood vessels within the dermis. Spongiosis appears as thin, weakly backscattering clefts against the highly reflective background of the epidermis, while intercellular edema reduces backscattering from the cellular layers [74].

OCT is also applied in the assessment of blistering skin diseases (Figure 2.11). Both intradermal and subepidermal vesicles can be readily visualized in OCT images, as illustrated in Figure 2.11. Intraepidermal blisters can be differentiated from subepidermal ones by examining the location of the cleft at the lateral margin of the vesicle. Beyond determining blister depth, in vivo OCT can also provide information about blister content. Serous fluid shows low light scattering due to its high transparency and minimal cellular content, whereas purulent material contains numerous cells and therefore produces stronger scattering signals.

Overall, morphological features of both healthy skin and pathological abnormalities can be identified and compared. OCT enables non-invasive and reproducible observation of treatment effects over time during healing process.

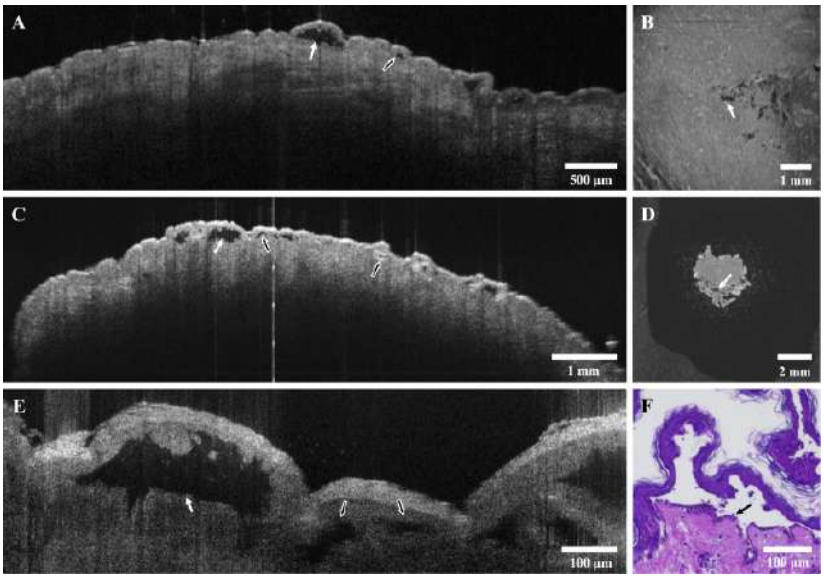


Figure 2.11: Comparison of OCT images of ex vivo skin grafts with induced intraepidermal blisters using different OCT systems. A-B) VivoSight Dx; C-D) MHz-OCT; E) mOCT. A, C, E) OCT B-scans (10x averaged); B, D) OCT en face cross sections at 90 µm depth; F) Histology (hematoxylin and eosin staining) of a similar region. Intraepidermal blisters are visible in all B-scans (white arrows) and also thin cleft formations are detectable (black arrows with white outline). In E and F, the suprabasal localization of the blister can be recognized by the typical tombstone pattern of the basal cells (black arrows). Field of view: A) 6×1.8 mm^2, B) 6×6 mm^2, C), 11×2.8 mm^2 D) 11×11 mm^2, E) 1×0.4 mm^2, F) 0.4×0.4 mm^2 [75].

Conclusions

Over last three decades optical coherence tomography has branched into various medical fields and became standard tool for non-invasive imaging. OCT provides fast retinal abnormalities detection, cancer diagnosis, high-resolution assistance in cardiovascular disease treatments and skin condition observation. In the end, optical coherence tomography becomes everyday equipment for many medical specialists.

3. FOURIER-DOMAIN FULL-FIELD OCT

3.1. Multimode fiber as a tool to reduce cross talk in Fourier-domain full-field optical coherence tomography

Fourier-domain full-field optical coherence tomography (FD-FF-OCT) is a viable and versatile tool for retinal imaging because fast imaging speed and stable phase information across the whole field of view. We show that a long multi mode fiber with a small core diameter can be used to reduce crosstalk in FD-FF-OCT. Furthermore, we demonstrate that both retina and choroid can be obtained in a single volume in vivo with reduced crosstalk and high contrast. This has been done in a passive mode – without fiber shaking or twisting, also without any additional active components such as holographic diffuser [37] or acoustic mode mixer.

Devices

While typical optical components, such as lenses, mirrors and optomechanical stages are commonly used and know, some of the equipment used in this research is less abundant in other fields. The next few paragraphs describe several devices and their working principles which may not be introduced outside OCT and microscopy fields. Before discussing this FF-FD-OCT setup, three main components used in our system should be addressed.

Swept Source Lasers

Swept source lasers are a type of tunable laser that can change its wavelength rapidly across a set range (Figure 3.1(a)), allowing for high-speed and high-resolution imaging. They are commonly used in various applications such optical coherence tomography (OCT) for medical diagnostics, fiber optic sensing, metrology and other biomedical imaging [76, 77].

The key difference from traditional lasers and Swept lasers is tunability. This ability enables laser to alter its wavelength over a given range in a controlled manner. Contrary to static lasers that emit a single wavelength, swept lasers can actively change their emission wavelength. The sweeping is usually synchronized with the measurement system, enabling real-time data collection over a wide spectral range. Such dynamic scanning is based on the sample interaction with different wavelengths of light which allows wider detection and analysis of biological tissues and other materials.

The operation of swept lasers is based on two main components: the tunable laser source and the wavelength sweeping mechanism. These components

combined make the core of the technology which enables high precision and versatility that make swept lasers invaluable in modern applications. The tunable laser source is the component responsible for generating the coherent light which can be adjusted in wavelength (frequency). This can be done in different ways, such as using a movable grating, integrated electro-optical modulator or temperature tuning. The wavelength sweeping mechanism is used for adjusting wavelength. This can be done Mechanically by physically altering the length of the laser cavity, typically by a movable mirror or a rotating diffraction grating. On the other hand, electronic tuning such as current injection in semiconductor lasers, changes the current which alters the refractive index and as a result the emitted wavelength of carrier-injection, or applying an electric field. Electronic tuning offers the advantage of high-speed tuning without the need for moving parts.

Selecting a swept source laser is usually based on a few criteria. Wavelength and wavelength range should be chosen for the field of research and samples to be analyzed, e.g. near infrared is preferable for biomedical sample imaging due to lower scattering and lower absorption. Wider scanning range results in higher axial resolution for FD-OCT systems [78]. Linewidth determines the imaging depth for FD-OCT applications. A narrower instantaneous linewidth increases coherence length and usable ranging depth [78]. Sweeping speed at which laser can sweep across the wavelength range directly results in imaging speed and fast sweeping enables real-time imaging [77]. Output power directly impacts how much light is delivered into the sample. Coherence in time is important for stable phase during measurements. Choosing output might seem simple, but sensitivity of a detector, losses in the system, phototoxicity to the sample and finally cost has to be taken into account choosing optimal power.

For our application in Fourier Domain Full-Field Optical Coherence Tomography (FD-FF-OCT) we have chosen a Broadsweeper BS-840-2-HP produced by Superlum. This laser has spectral range of 805 – 880 nm (tuning range is 75 nm). The Sweep Speed is adjustable between 100 and 100,000 nm/s. The Linewidth is 0.12 nm. According to the manufacturer [79], the optical part is based on an external fiber-optic ring cavity and a broadband Semiconductor Optical Amplifier (SOA), used as a gain medium. The wide bandwidth of the Semiconductor Optical Amplifier modules are used, and their high fiber-to-fiber gain enables wavelength tuning range of more than 50 nm at 3 mW of output power (20 mW can be achieved with an additional booster unit). For the wavelength tuning a specially developed narrowband Acousto-Optical Tunable Filter (AOTF) is used. In order to achieve high spectral stability of laser radiation The AOTF is actively thermally stabilized. The akinetic cavity design (no moving components inside) ensures high wavelength accuracy and wavelength reproducibility during sweeping. Due to the high quality AOTF tuning, the laser provides k-linear wavelength tuning over a wide spectral range.

Ultrafast Camera

In modern times on of the main tools for image registration is a 2D camera. The core element of a high-speed camera (Figure 3.1 (b)) is an imaging sensor capable of registering rapid sequences with high precision. These sensors are specially designed to handle high pixel data throughput. A CMOS (Complementary Metal-Oxide-Semiconductor) image sensor is a digital imaging device designed to obtain rapid sequences of images with minimal motion blur. It is much faster and energy efficient than conventional CCD (Charge-coupled device) sensor. In high-speed cameras the sensor has a fixed data throughput, typically measured in gigapixels per second (Gpixel/s). The Gpixel/s value of a sensor is a constant and defined by the sensor's architecture, which determines the maximum frame rate achievable at full resolution. By using a method called windowing, it is possible to boost the frame rate by decreasing resolution. More precisely, reducing the vertical and/or horizontal resolution results in the frame rate increase. Moreover, to achieve high-speed imaging, a high capacity and high-speed DDR RAM (double data rate random-access memory) is needed to quickly and safely store huge amounts of data while the synchronization between the sensor and memory has to be fast and precise in order not to lose any frames during high-speed image capturing [80]. Ultrafast cameras provide scientists both temporal and spatial resolution which can be altered by adjusting capture rate or resolution in favor of experiment requirements. Even though, high-speed cameras are typically used in automotive, industrial inspection [81], sports, entertainment, security or surveillance, they are important tools in scientific research of biological process analysis or in medical imaging where quickly capturing a wide field of a moving sample is important. Such cameras can obtain 20 000 frames per second at 1024 x 1024 pixel resolution or even 2 100 000 frames per second at 128 x 8 pixel resolution [82].

Multimode Fiber

Optical fibers belong to a wider category of optical structures called waveguides, which are based on total internal reflection (TIR) to confine and direct light inside a solid or liquid medium. Optical fibers are widely employed in applications such as illumination, telecommunications, sensors and spectroscopy [83]. Inside an optical fiber, a guided mode is an allowed electromagnetic field distribution of the fiber. There are two main types of optical fibers: single-mode fibers, which support only one guided mode, and multimode fibers (Fig. 3.1 (c), which allow the propagation of many modes simultaneously. The number of supported modes depends on parameters such as the core and cladding dimensions, the refractive index and the wavelength of the light. A fiber can support between a single mode to thousands of modes.

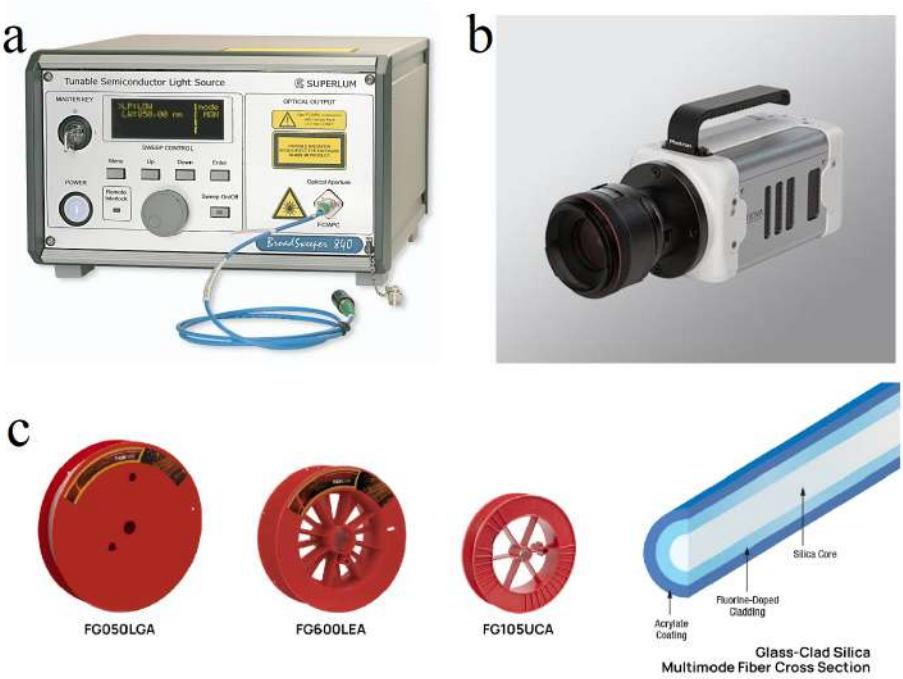


Figure 3.1: (a) Swept source laser [79], (b) Fastcam SA-Z, 2100K-M-16GB, Photron [82], (c) 0.22 NA (Silica)Core, Glass Clad Multimode Optical Fiber, Step Index [84]

First, after calculating fiber parameters (using formulas from [53, 85] to generate enough spatial modes, a fiber with numerical aperture $NA = 0.22$ and core radius of 25 µm has been chosen. At this setup:

$$N \approx \frac{2\pi^2 a^2 NA^2}{\lambda^2} \approx 840 \tag{3.1}$$

when wavelength $l = 840nm$ this fiber generates ≈ 840 guided modes which leads to crosstalk suppression of $\sqrt{840} \approx 29$ as suppression scales as a square root of number of modes $N^{1/2}$ [86]. Moreover, choosing fiber parameters is not only determined by core diameter as number of modes has to be balanced against the axial image range $\frac{\lambda}{NA_{ill}^2}$, where NA_{ill}^2 is NA of the illumination, n_1 is the fiber-core refractive index, but the length of the fiber is also important. We need a fiber minimum 100 m length

$$L_{min} = \frac{4l_c\pi^2 a^2 n_1}{\lambda^2} = 100m \tag{3.2}$$

[53, 85] to have all the excited spatial modes at the end of the tip add up incoherently and produce low speckle contrast. However, experiments have shown that optimal fiber length is 300 m as it induces lower speckle contrast

(Figure 3.4 (b)). While longer fiber separates [87] degenerate spatial modes with very similar group delays and propagation constants, longer fiber would attenuate power too much compared to reduction of speckle contrast.

FF-FD-OCT Setup

Our setup (Figure 3.2) has implemented real-time axial retinal imaging by using pupil plane splitting [88] and a line camera. (since the partial spatial coherence formed by the MM fiber occupies only a small portion of the conjugate pupil plane of the eye, and the backscattered light from the retina fills the whole pupil.) Such configuration enables retinal real-time preview in b-line mode and fine adjustments and eye alignment for final imaging as the ultrahigh-speed 2D camera cannot transfer images to the computer in real time. The FD-FF-OCT setup is shown in Figure 3.2 The laser light from a swept laser source (Broadsweeper BS-840-2-HP, Superlum) was coupled into the step-index MM fiber (300 m, 0.22 NA, low OH, Ø50 µm core, FG050LGA, Thorlabs). The light from the MM fiber was collimated by lens $L1$ ($f = 11$ mm); subsequently, lens $L2$ ($f = 50$ mm) imaged the tip of the MM fiber onto a small (1 mm diameter) 45° rod mirror (47-628, Edmund Optics).

The mirror reflected all of the illumination towards an interferometer, since the image from the fiber core that formed on the surface of the mirror was magnified (4.5×) to approximately 227 µm. A 50:50 non-polarizing beam splitter split the incoming light between the sample and reference arms with equal power. Lenses $L3$ ($f = 100$ mm) and $L4$ ($f = 50$ mm) reimaged the mirror, as well as the fiber tip, onto the pupil planes of the human eye in the sample arm and the microscope objective (Plan N, 10×, $NA = 0.25$, FN22, Olympus) in the reference arm.

The split light was collimated by the eye (on the sample arm) and the objective (on the reference arm). The back-scattered light from the retina and back-reflected beam from the reference mirror has been combined via the same beam splitter and split into two equal parts. The reflected light from beamsplitter was collected by lens $L5$ and focused by L6 onto ultrafast 2D camera (Fastcam SA-Z, 2100K-M-16GB, Photron). The magnification between reference mirror and ultrafast camera was 4.2 times and retina's pixel size was 3.3 µm. The remaining light, passed back through beamsplitter was obtained by a small 45° mirror and directed onto 1D (Alkeria, Necta N4K-7-F). line camera for fast preview and final adjustments before capturing retinal images via 2D camera. In standard OCT setup configuration this light is typically lost, however by tilting the reference mirror by about 1° this light could be collected and used to enable easier imaging. Even though such tilt produces a tilt in FD-FF-OCT volumes in z axis, this effect is not noticeable when imaging an eye and can be easily compensated computationally. The tube

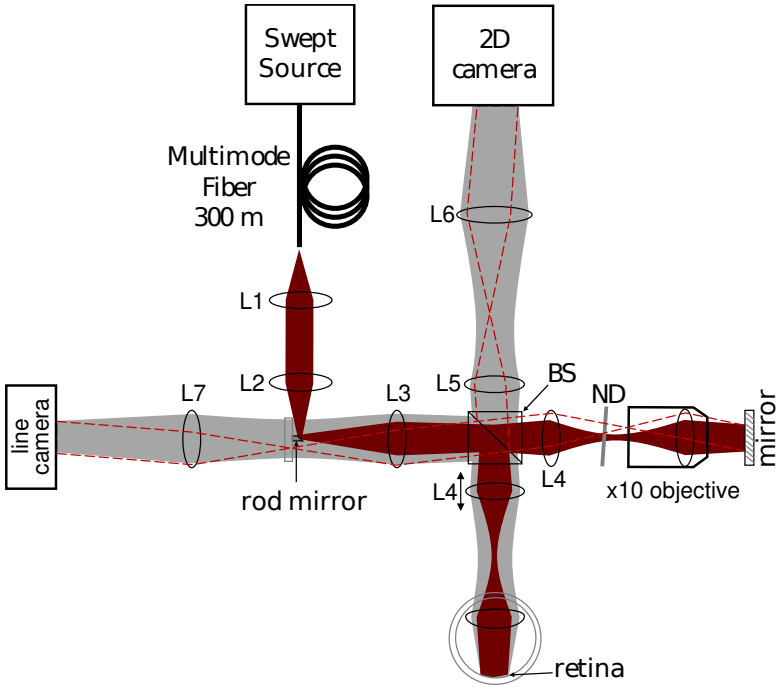


Figure 3.2: Schematic diagram of the FD-FF-OCT system with a MM fiber. The design also incorporates a line camera that is used to generate real-time axial images of the retina for quick visual feedback. ND: neutral density filter. $L1$–$L7$: lenses; BS: 50/50 beam splitter [89].

lens $L6$ was twice as long as $L7$ to match field of view for both cameras since pixel size of 1D camera was 10 µm while 2D camera had 20 µm pixels. Swept source laser was tuned at 8700 nm/s while both cameras were registering at 60 kHz. During one sweep 512 images with 0.15 nm wavelength shift between each other were acquired in total of 8.6 ms.

Experiment and analysis

The obtained multi-spectral interferometric retinal images (xyl) were converted into 3D volumes by postprocessing consisting of: subtracting the mean from each line (along l), apodizing with the Hamming window and applying fast Fourier transformation (FFT) to convert images from spectral domain to depth domain. The obtained en-face retinal images were spatially filtered to remove the MM fiber illumination induced low-frequency speckles [53] are filtered using a mask in Fourier space. Filtered and unfiltered B-scans of the retina are shown in Figure 3.3. Filtering was done in Fourier space using a block of

22 pixels (6.5 cycles/mm) to filter out periodic structures bigger than 80 µm (Figure 3.4). Chromatic dispersion correction was also applied together fixing any probable eye axial motion during each sweep. Despite using a partially spatially incoherent light source [90] the phase was stable across the whole image which enabled volumes to be corrected for depth-dependent defocus by using a sub-aperture approach [91].

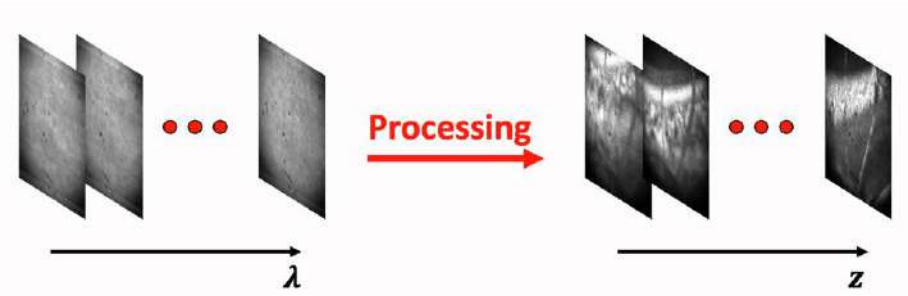


Figure 3.3: A representative illustration of the raw (left) and processed data (right). Interferometric images are Fourier transformed to produce volumetric image [89].

Finally, after aligning and processing volumes using a correlation based approach they were integrated incoherently in order to increase signal to noise ratio [50]. 21st Zernike polynomials (excluding piston, tip and tilt) were used correct aberrations in the photoreceptor image following by up-sampling with bi-cubic interpolation. The estimated lateral resolution of the FD-FF-OCT was 4.6 µm and assuming the spectrum as a Gaussian distribution, the measured axial resolution was 5.6 µm in the air over the 1.7 mm × 1.7 mm field of view (FOV). As nearly all of the spatial modes were temporally separated by differential modal group delays exceeding the source coherence time. at the end of the MM fiber, they did not interfere with each other, resulting in incoherent addition on the camera thus reducing in the fiber-induced speckle contrast.

The number of spatial modes N affecting the contrast C reduction can be estimated using $N = 1/C^2$, assuming all modes are spatially uncorrelated, non-interacting and have the same energy. Under these conditions, we estimated that $N \approx 250$, based on a contrast of $C = 0.06$, calculated using $C = \sigma/\langle I \rangle$, where σ is the standard deviation and $<I>$ is the average image intensity. To experimentally assess cross-talk suppression by the multimode fiber, a 100 µm thickness, strongly scattering latex phantom was imaged by both single-mode (SM) and multimode (MM) fibers using the FD-FF-OCT system, along with a scanning OCT system for comparison, as shown in Figure 3.5 (a).

When using SM fiber crosstalk noise can be seen outside the sample even though there should be no signal. The crosstalk noise suppression with the MM fiber can be estimated from these images by SM averaged A-scans by

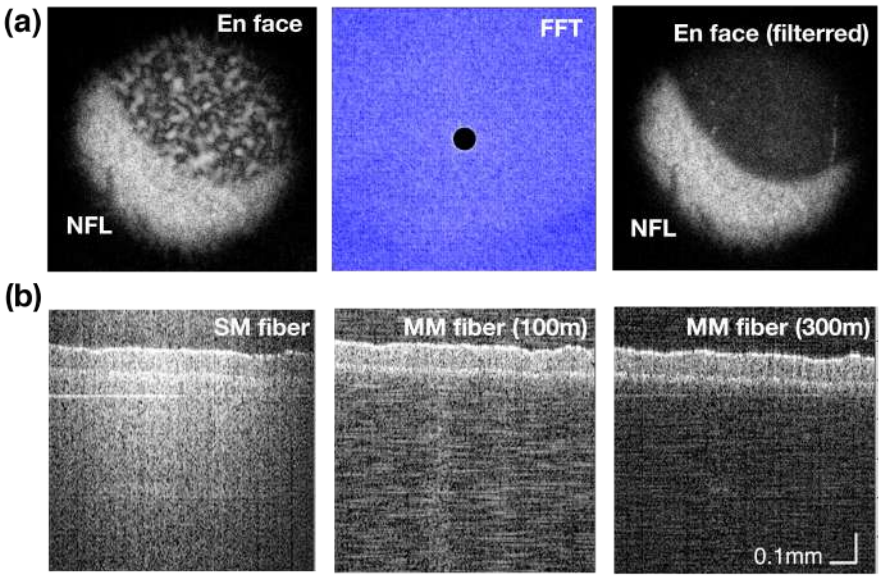


Figure 3.4: (a) Filtering out fiber-induced speckles in retinal OCT en-face images by using a block with a diameter of 22 pixels in the spatial frequencies. NFL: nerve fiber layer. (b) Unprocessed axial OCT images of a latex phantom acquired with different fibers show that a longer MM fiber features fewer fiber-induced speckles [89].

MM averaged A-scans, as shown in Figure 3.5 (b). As expected, The SM/MM curve reaches a maximum suppression value of approximately 15 (11.8 dB), since estimated 250 spatial modes in the fiber will reduce the cross talk by $N^{1/2} = 250^{1/2} \approx 15$ [86, 92]. The measured crosstalk suppression could also depend on sample-to-camera magnification, provided that the number of excited fibre modes remains unchanged. When the illumination is scaled to cover the camera field of view, increasing magnification reduces the illuminated area and the coherence-grain size at the sample, giving tighter spatial gating. Reducing magnification has the opposite effect and may lower the suppression in dB. However, larger coherence areas also retain more multiply scattered light, which can preserve depth-resolved structural information to some degree [93, 94]. A larger spatial-coherence volume has also been shown to increase penetration in FF-OCT [95]. Crosstalk suppression and imaging depth should therefore be considered separately. Overall, the decay of scanning OCT curve is comparable to MM curve suggesting FD-FF-OCT system is capable of similar cross-talk reduction [89].

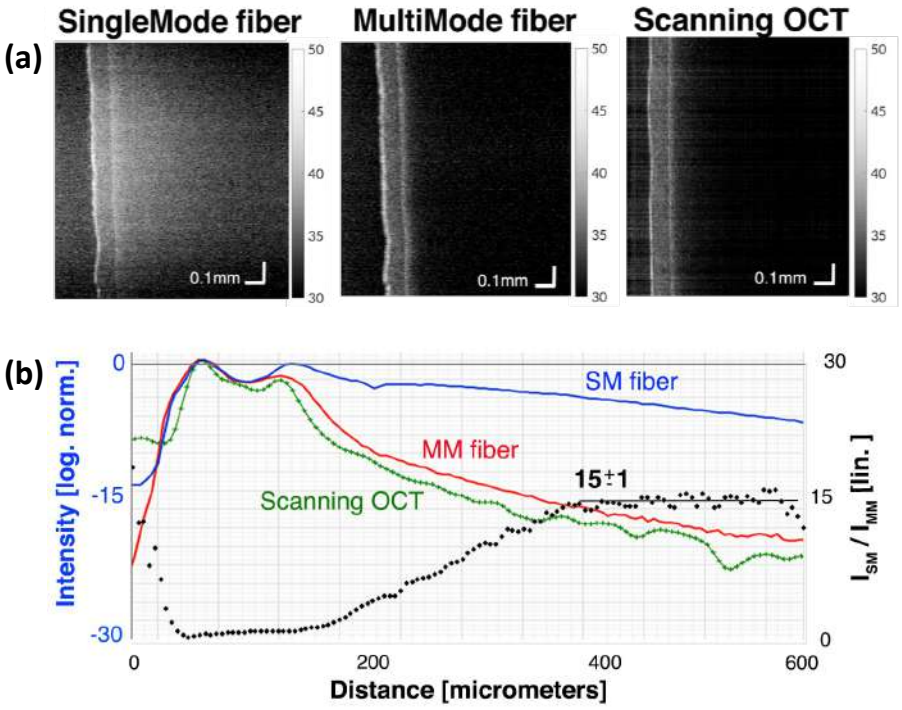


Figure 3.5: Demonstration of optical cross-talk suppression by the MM fiber on a latex phantom. (a) Axial FD-FF-OCT images acquired with a SM fiber and a 300 m MM fiber, as well as with a scanning OCT system. (b) Signal decay curves (averaged A-scans) as a function of depth, derived by summing all A-scan lines in the images. The black curve was derived by dividing SM curve by the MM curve [89].

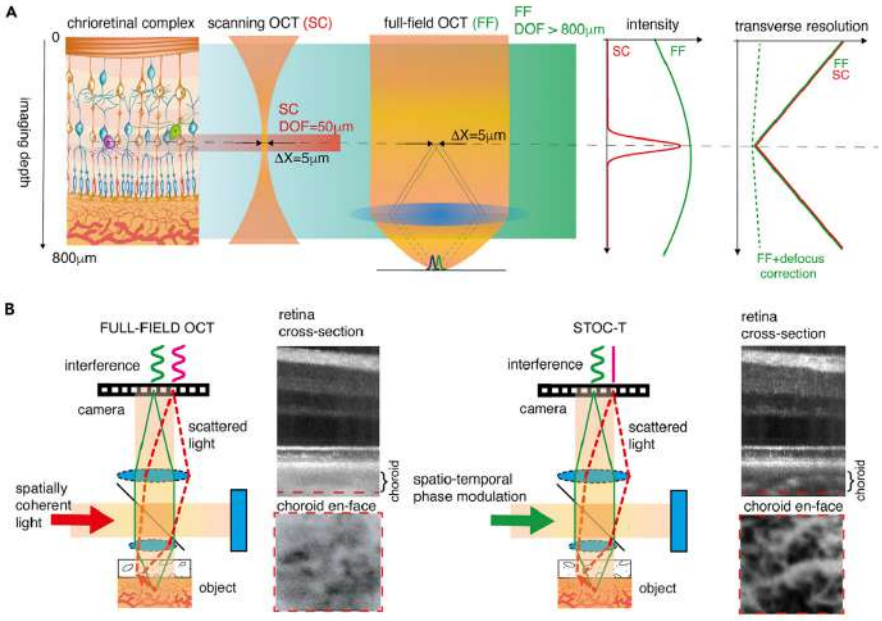


Figure 3.6: (A) In STOC-T (Spatio-Temporal Optical Coherence Tomography), the retina is probed with complex spatiotemporal light fields according to a wide-field imaging scheme (Full-Field OCT). As a result, there is no loss of light intensity with applied defocus, as is the case with confocal detection in scanning OCT methods. However, there is still image blurring associated with defocus. This blur, however, can be removed by the numerical defocus correction provided by the signals obtained with high-speed full-field interferometric registration. This preserves high (5 µm) lateral resolution with significant imaging depth, covering the entire extent of the chorioretinal complex (800 µm). (B) The complex spatiotemporal light fields guarantee the removal of the optical cross-talk effect created by scattered light in the sample. In STOC-T, scattered light that hits the camera pixels without recovering the original structure does not contribute to interference signals and thus to the volumetric reconstruction.

In Fourier domain Full-field OCT (FD-FF-OCT) the depth of focus (DOF) (the axial imaging range) does not depend the confocal parameter of Rayleigh range – a focused beam [37, 47, 96] but on the Rayleigh range of collimated beam illumination both sample and a reference mirror. In this interferometer the interference fringes will form over a long axial range of images but only in the very focus plane OCT images will be focused while others further away will be blurred. However, due to inherent FD-FF-OCT high phase stability images can be restored and deblured over great axial range by numerical defocus compensation as it was shown previously [36]. We have compared STOC-T (Spatio-Temporal Optical Coherence Tomography) to scanning OCT setup and demonstrated STOC-T advantages. First, we used a reflective USAF (United States Air Force) resolution target as a sample and imaged it with both scanning OCT and STOC-T systems. It was imaged along the optical axis acquiring images from each defocused position, as shown in Figure 3.7. We derived DOF curves from images and compared them (Figure 3.7). The DOF curve for STOC-T is broader than scanning OCT DOF curve by 2 orders of magnitude [97]. The same 10x objectives were used in both systems and the nominal resolution value was 3.4 µm.

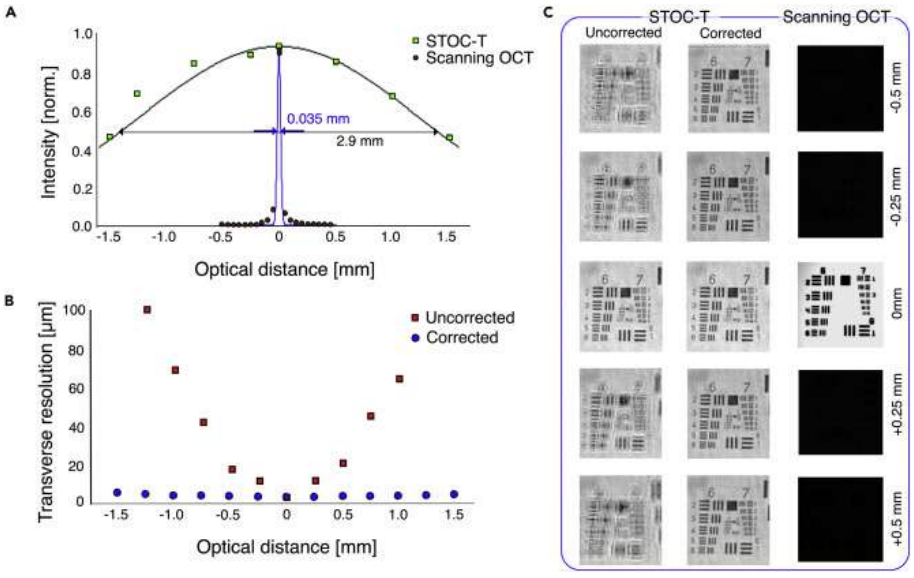


Figure 3.7: Measurement of DOF in STOC-T and scanning OCT, using a reflecting sample (USAF Test chart) (A–C) comparison of intensity attenuation for STOC-T and the scanning OCT, (B) effect of numerical defocus correction on transverse resolution loss in STOC-T, (C) Comparison of USAF test target images acquired with STOC-T and confocal scanning OCT at different defocus values.

In order to avoid errors and have replicable data, the 10x objective and USAF resolution target were used as a sample instead of human eye. The resolution target was made to be translatable along the optical axis. In the scanning OCT configuration the DOF had a fixed value of 35 µm (for the lateral resolution of 3.4 µm) and corresponded to the confocal parameter. By translating sample by 250 and 500 µm below or above focal plane, the signal dropped to 1 % and 0.5 % of it‘s maximum value, respectively. This drop in signal corresponds to -40dB in signal attenuation. On the other hand, in STOC-T such defocus (250 and 500 µm below or above focal plane) reduced signal to 95 % and 90 %, respectively. In this case signal is attenuated by only -1 dB. Even though by physically defocussing USAF targets leads to blurred STOC-T images (Figure 3.7 C), the resolution can be restored by computationally refocusing these images over whole imaging range of STOC-T (+-1.5 mm).

In order to show that broader DOF in STOC-T would provide a wider axial imaging range in real sample (3D), a strongly scattering phantom has been used. We have made a controlled volumetric phantom from a mixture of PDMS (polydimethylsiloxane) and TiO_2 as a scatterer [49]. Even though such phantom scatters light much more than a choroid or a retina, it could be used to compare STOC-T to scanning OCT and validate differences in imaging depth at the same lateral resolution as shown in Figure 3.8.

Signals acquired by both methods (in various sensitivities and illumination configurations were compared by normalizing the obtained volume reconstructions against the root-mean-square (RMS) of the noise. Figure 3.8 shows cross-sectional images which were used to derive signal decay graphs as depth functions. Yellow box shows are which parts were used to integrate signal along the x axis to produce these graphs. The curve of scanning OCT shows high level signal in the focal plane and substantially weakened signal in other planes of the scattering medium and corresponds consistently to OCT signal, obtained from sharply focused light in a scattering material, described literature [98, 99] and the signal from deeper layer of the scatterer is practically invisible.

On the other hand, the signal obtained via STOC-T setup is visible through entire thickness of 0.5 mm layer and the attenuation of the signal rises from the physical extinction processes in the scattering sample. By comparing en face image reconstruction between both techniques there is a noteworthy difference at different depths of the sample. The measurement with scanning OCT setup was conducted in enhanced depth imaging (EDI) configuration (zero optical path difference is located inside the sample) [100]. This configuration minimizes sensitivity drop-off in such system.

In conclusion, a crosstalk noise in FD-FF-OCT images can be greatly reduced by a small core diameter (50 µm) multimode fiber. Compared to a deformable membrane a MM fiber allows imaging both choroid and retina in high resolution at the same time. Moreover, obtained results are

repeatable and in high detail. Lastly, since MM fiber has no moving parts, it is a passive and failure resistant device that is suitable for routine use in medical applications and could spread FD-FF-OCT availability more clinics.

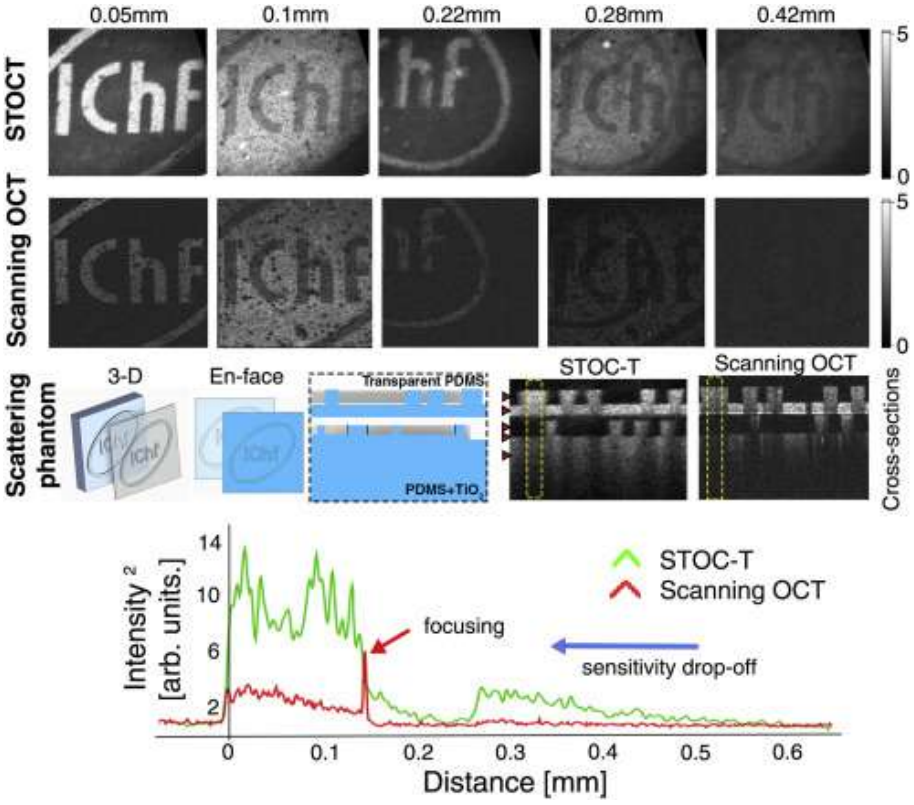


Figure 3.8: Signal decay as a function of depth in a volumetric scattering phantom Red arrows in the cross-sectional images denote the axial position of the en face images shown above. The curves were derived from the area indicated by the yellow dashed squares.

Overall, the results demonstrated two improvements to Fourier-domain Full-Field OCT for retinal imaging. First, coupling the illumination through a long multimode fiber was shown to suppress crosstalk without any moving parts. With an estimated $N \approx 250$ excited spatial modes, the multimode fiber reduced crosstalk by a factor of ≈ 15 (11.8 dB), matching the theoretically expected ($N^{1/2} = 250^{1/2} \approx 15$) value and reducing crosstalk close to a scanning OCT system used for comparison. Second, the full field imaging and high phase stability combined with digital defocus correction gave a DOF two orders of magnitude broader than scanning OCT at equal lateral resolution (3.4 µm): at 250–500 µm of defocus. In a volumetric scattering phantom, this translated into usable signal throughout the entire 0.5 mm sample thickness, whereas the scanning OCT signal from deeper layers was practically unrecoverable.

Finally, these results reduces the main limitations that have restricted FD-FF-OCT in retinal imaging: crosstalk from out-of-focus scattered light and shallow usable imaging depth. This is solved by using a purely passive fiber-based approach rather than mechanical or active beam-scrambling components. Since the multimode fiber has no moving parts, it is robust and well suited for routine clinical use. The extended DOF allows the entire chorioretinal complex to be imaged within a single acquired volume rather than requiring separate refocusing steps for retina and choroid. In conclusion, these improvements make FD-FF-OCT a more robust and clinically practical tool for wider adoption in ophthalmic imaging.

The key challenge of OCT is to image choriocapillaris (CC) as it has dense structure and short intercapillary distances (ICDs). Furthermore, the interference from the pigmentation of the RPE (retinal pigment epithelium) layer and choroidal melanocytes that strongly absorb and scatter light. Commercial OCT devices have been attempted to be used for choroidal imaging [101, 102] but system with 15-20 µm resolution cannot properly image 5-20 µm details of the ICD. Nevertheless, angio-OCT has been used extensively to image the CC [102–104] but, unlike the retinal microvasculature, the CC has a much denser capillary network and provides fewer signals. Recent studies has shown that different choroidal depth images registered via angio-OCT systems are very similar and it suggests that CC might be projected onto Sattler's and other retinal layers as this would explain phenomena of observed dense network deeper than 20 um from the RPE [105]. This lack of distinction between different choroidal layers renders quantitative analysis meaningless. Many experimental OCT setups have been used to image the choroid and choriocapillaris [106–108]. One of those setups would be ultrafast imaging with a 1060 nm swept-source laser which produced most promising results by balancing between lateral resolution and imaging depth [109–111]. Even though reconstructions of choriocapillaries were great, they were still limited by lateral resolution in reconstructing the morphology of the chorioretinal complex at different depths.

In Fourier domain Full-field OCT (FD-FF-OCT) the depth of focus (DOF) (the axial imaging range) does not depend the confocal parameter of Rayleigh range – a focused beam [37, 47, 96] but on the Rayleigh range of collimated beam illumination both sample and a reference mirror (Figure 3.2). In this interferometer the interference fringes will form over a long axial range of images but only in the very focus plane OCT images will be focused while others further away will be blurred. However, due to inherent FD-FF-OCT high phase stability images can be restored and deblurred over great axial range by numerical defocus compensation as it was shown previously [36].

Even though large DOF enables decent defocus compensation, the FD-FF-OCT is fundamentally limited by crosstalk [112], and the deeper tissue layers are imaged, the worse crosstalk becomes and limits imaging depth. Previously, crosstalk would be removed by rotating diffuser [37, 113] which therefore reduced axial imaging range. Recently, we have shown that spatial phase randomization tools, such as a long multimode fiber and fast deformable membrane can efficiently suppress crosstalk in FD-FF-OCT and provide large axial imaging range [3, 49, 50, 88–90, 114]. Spatial coherence of the light can be controlled by both tools eliminating crosstalk and by underfilling illumination pupils in both imaging and reference arms, a high lateral resolution and high DOF imaging can be achieved (Figure 3.6 (B)). We call the new method spatio-temporal

optical coherence tomography (STOC-T) to emphasize that the complex spatiotemporal light field (a combination of spatial and temporal coherence of light) defines its performance. Even though STOC-T and FD-FF-OCT can be used interchangeably and means the same setup, STOC-T highlights achieved noise reduction. We have demonstrated STOC-T system used without any mechanical scanning acquires retinal images with uniform resolution of 5 µm in all three dimensions, over the entire thickness of about 800 µm. We have also shown that STOC-T can obtain high-contrast volumetric chorioretinal images with reduced scattering effects. In order to process acquired data sets of retinal images and merge them into large field of view highly-corrected 3D images we used both known and our new developed algorithms. Thanks to all these advancements both retina and choroid became possible to be imaged with high transverse resolution at various depths. To our knowledge, this was the first demonstration when Haller‘s, Sattler‘s and choriocapillaris layers became possible to differentiate morphologically [97].

Results

FD-FF-OCT system was used to image two volunteers in vivo: one healthy 45 year old person and one 54 year old patient with photoreceptor degeneration. The volunteer's head was supported with a chin-rest place on a 3D translation stage to adjust eye to the imaging system. Previously mentioned 1D line camera provided real-time axial retinal images and guided system's alignment to find OCT signal and image desired spot of the retina. Lens L4 (Figure 3.2) was adjusted along the beam axis to compensate for refraction error of the eye. After all adjustments 2D ultrafast camera was used to obtain volumetric retinal data. Data processing is described in Figure 3.10.

The retinal and choroid images shown in Figure 3.9 were obtained from previously mentioned individuals in 0.17 s as 20 volumes were registered. The cross-sectional (axial) images show an axial span extending over all the major retinal and choroidal layers, reaching the choroid-scleral junction. Images of the first volunteer's retina, recorded 4° temporal from the macula with a dilated pupil, feature high-contrast details of internal limiting membrane (ILM), capillary plexuses (SCP, ICP, and DCP), and photoreceptors, as shown in Figure 3.9 (a). Individual photoreceptors are visible because of the aberration correction. Figure 3.9 (b) shows clearly visible blood vessels in Choroid (contrast inverted). The bottom row of Figure 3.9 (b) shows zoomed-in choroid. The en-face images are homogeneous and regular different from those in Ref. [3], where deformable membrane produced spatial modulation artifacts are apparent. The second volunteer's (patient's) images Figure 3.9 (c) show the thickening of the ROST (rod outer segment tips) layer and the irregular structure of COST (cone outer segment tips) are seen in the axial image are due to the degeneration of

photoreceptors. Likewise, the choroidal images show noticeable irregularity in layers closer to Bruch's membrane (20 µm and 50 µm below it).

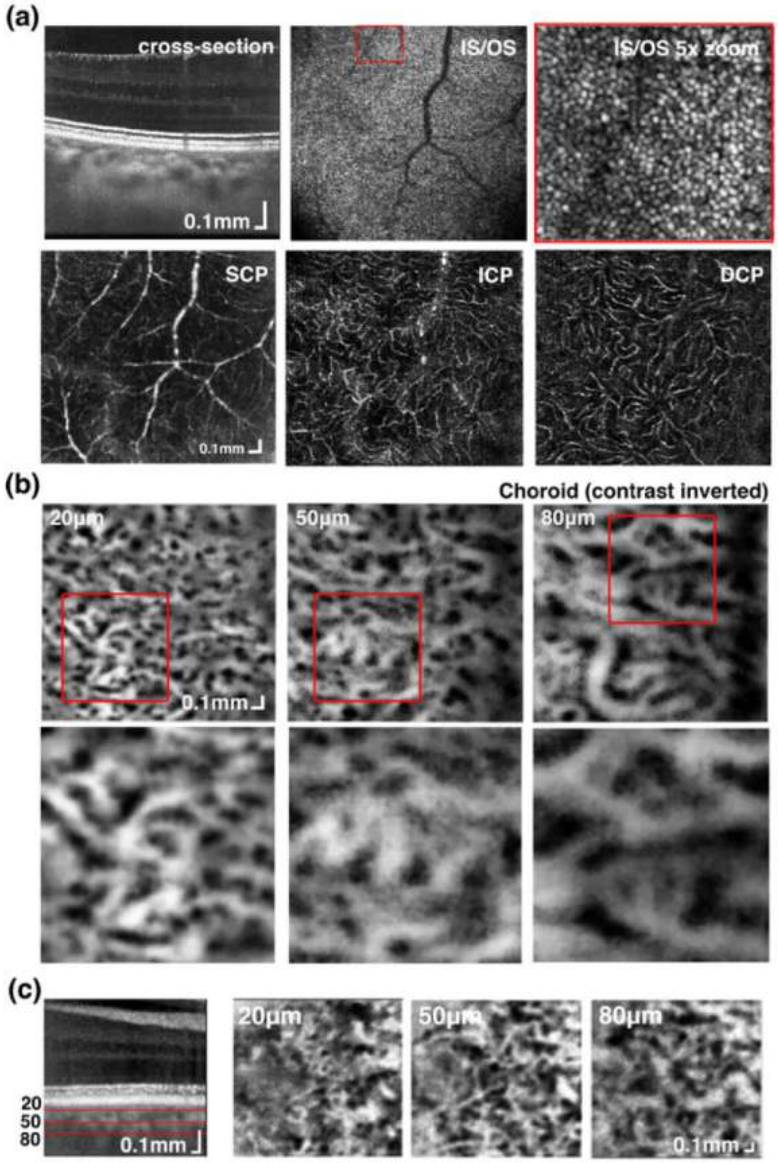


Figure 3.9: FD-FF-OCT images of (a) the retina and (b) the choroid of the first volunteer; (c) axial and en-face images of selected choroidal layers of the second volunteer with a photoreceptor degeneration condition. The choroidal images are contrast inverted to give a more realistic representation of the blood vessels. The distances shown in the choroidal images are those with respect to Bruch's membrane. SCP, ICP, DCP: superficial, intermediate, and deep capillary plexus, respectively; IS/OS: inner/outer segment junction.

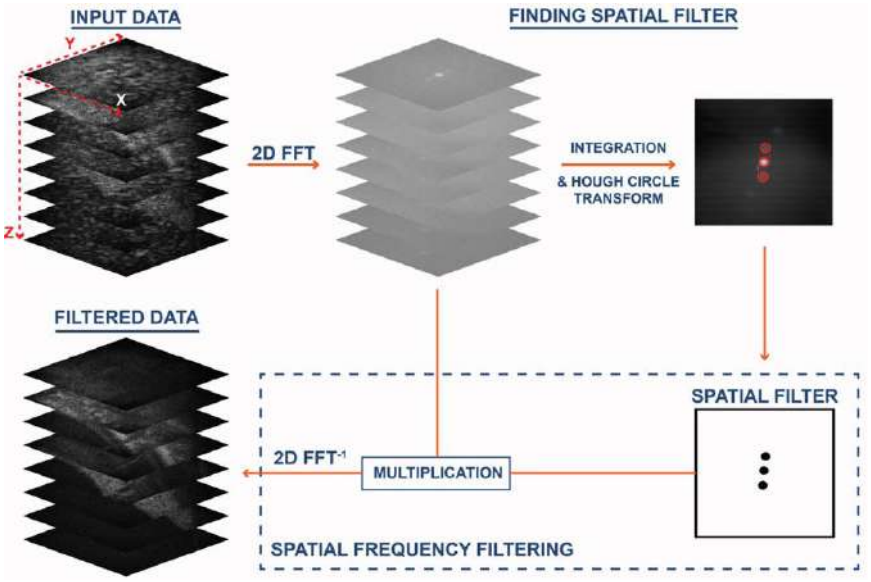


Figure 3.10: Spatial frequency filtering suppresses low-frequency speckles from the multi-mode fiber and reflections from camera glass. Each en face plane of the input data is 2D Fourier transformed to achieve a 3D stack of the spatial spectra. This stack is then integrated along Z to obtain the 2D image, which is subsequently processed with Hough Circle Transform to find circles. The resulting rings are employed to construct the mask multiplied by each XY plane in the spatial spectra stack. The resulting data is inverse Fourier-transformed to obtain filtered volume.

The utility of this setup for in vivo measurements of the human eye is best represented by choroid and retinal images. The visible high contrast and clarity is due to minimized crosstalk noise and reduced speckle size (compared to scanning OCT [3]). Fully opened pupil and computationally corrected aberrations leads to smaller speckles as retina backscatters light from a bigger pupil it generates smaller size speckles even with aberrations present [86].

The crosstalk noise could be suppressed even more by increasing the core size of MM fiber which increases the number of decorrelated speckle patterns [97]. However, this leads to reduced axial imaging range. The imaging speed could be increased even more, totaling less than a millisecond for whole volume (10 times faster than currently) but it is limited by the speed of swept source laser (compared to previously being limited by the membrane [3]).

In order to show improvements in penetration depth into the choroid we have compared our STOC-T system against two commercially available scanning OCT systems: Spectralis OCT with lateral resolution of 15 µm and depth of focus of 450 µm, and Triton OCT with lateral resolution of 20 µm and DOF of 600 µm Figure 3.11 (a). Due to parameter differences, such as scan densities, exposure times and number of averages, the signals were normalized with

respect to the reflectance values from the IS/OS layer and the hypo-reflective signal corresponding to the outer parts of the photoreceptors. Figure 3.11 (b) shows graphs on a logarithmic scale. STOC-T not only has almost 3-4 times higher resolution but also DOF is the normalized in-vivo signal-decay profile is similar to Triton OCT and substantially larger than Spectralis OCT. However, recent experimental analysis on commercial OCT systems have shown, that Spectralis and others have higher resolution (around 5 µm) than stated by manufacturers previously [115].

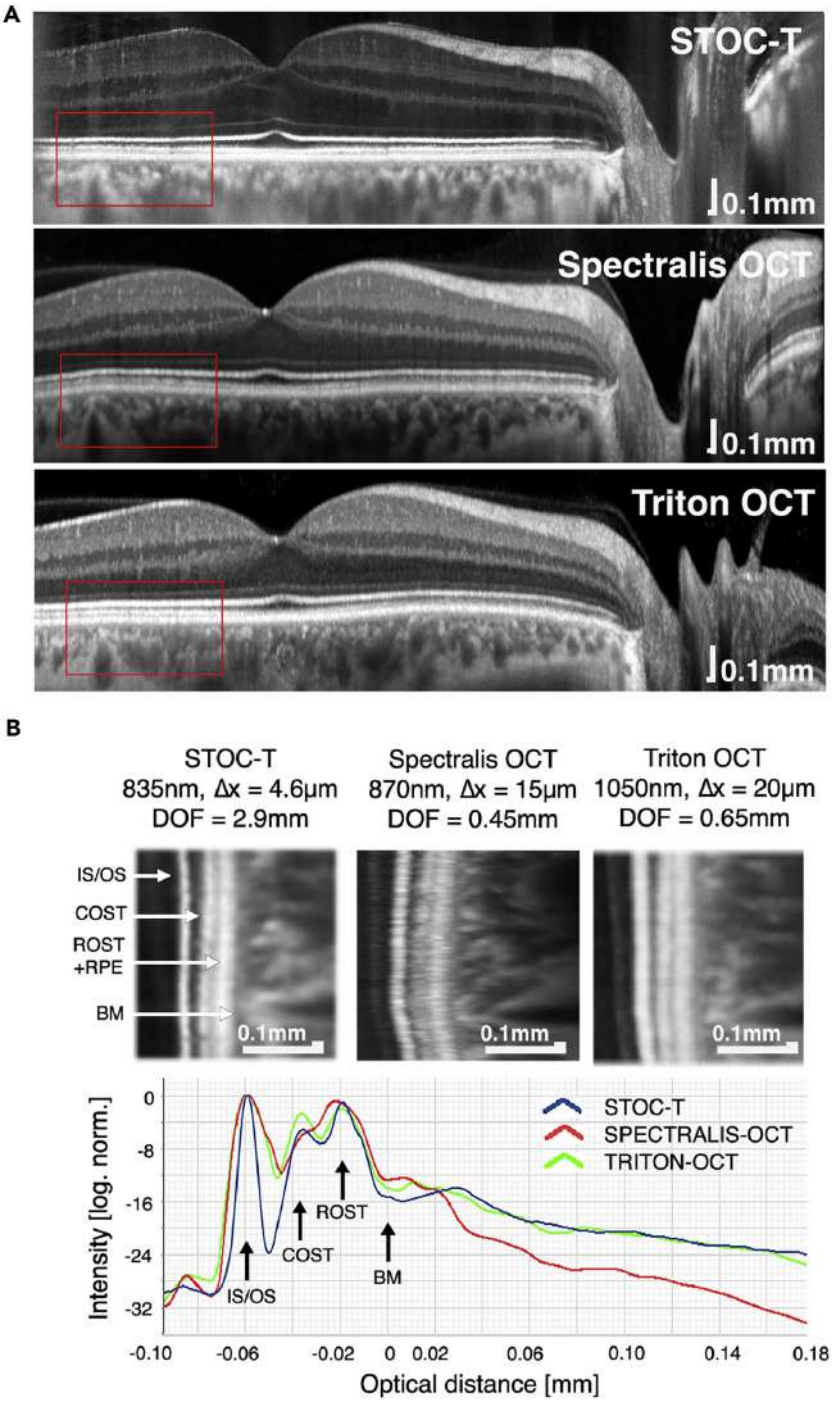


Figure 3.11: Comparison of the backscattered signal as a function of depth with STOC-T and two scanning OCT systems (Spectralis by Heidelberg Engineering and Triton by Topcon) (A and B) B-scans after averaging, (B) quantification of signal drop with imaging depth.

Our setup was used to image a larger area of the retina. Figures 3.12 (a) and 3.12(g) show en face and Figure 3.12 (b) shows axial images generated by stitching multiple images in the lateral plane. In order to produce these images we have acquired 30 volumes per single imaging location of 1.7 mm x 1.7 mm in size, within 260 ms. Volumes used for stitching were captured from 32 adjacent locations and final montage resulted in 9 mm by 4.6 mm image. By using STOC-T we are able to visualize en face view of the retina and see anatomical details without complex hardware. We have obtained impressive high resolution images of the structure of the thin Inner Limiting Membrane (ILM) that separates the nerve fiber layer (NFL) from the vitreous body. The structure of the membrane is shown in Figures 3.12 (c) and (f) while the architecture of individual nerve fibers can be seen in Figure 3.12 (d). Closer to the optic disk the ILM is less distinguishable as the nerve fibers dominate the area.

The transition between ILM layer and nerve fibers can be seen in Figure 3.12(f), panel (e) shows the ICP. By reconstructing retinal anatomy superficial, deep, and intermediate capillary plexuses (Figure 3.12(e)) layers can be seen without using OCT angiography. Furthermore, by incorporating numerical aberration correction [90] lateral resolution can be optimized to the diffraction limit making visualization of the photoreceptor mosaic possible (Figure 3.12(g)). After imaging photoreceptors we were able to evaluate the effective value of the lateral resolution of the images up-sampled and processed numerically. By using a signal of a single photoreceptor of a whole photoreceptor mosaic (Figure 3.12(g)) we have estimated lateral resolution to be 4.6 µm in terms of full-width half maximum (FWHM). In order to meet the Nyquist criteria for 4.6 µm resolution the sampling has to be done every 2.3 µm. However, our sampling was done every 3.3 µm as slight eye movements were taken into consideration and measurements were done by 8x numerical up-sampling and sub-pixel image registration of 30 volumes. This improved effective sampling beyond the single-frame Nyquist limit. Our method is similar to iterative weighted shift-and-add method [116] and an approach where the phase in the system pupil aperture is modulated by deformable mirror [117].

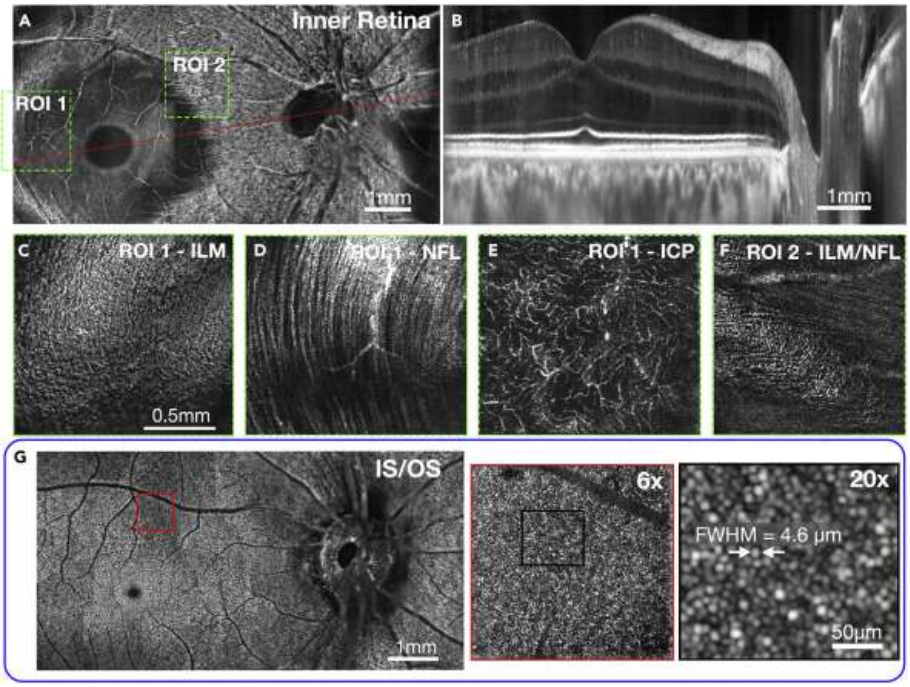


Figure 3.12: STOC-T imaging of retinal microstructure Montaged (stitched) retinal images (9 mm × 4.6 mm) of macula and optic nerve head; and panels with zoomed-in regions. (A) 15 µm en face projection of the inner retinal layers featuring the optic nerve discs, retinal nerve fiber layer (NFL), and retinal ganglion cell layer (GCL) in one image. (B) Cross-sectional image along the papillomacular axis of the human retina, indicated by red line in panel (A); (C–F) Details of the inner limiting membrane (ILM), NFL, and intermediate capillary plexus (ICP) are shown as thin layers (of 5 µm) and zoomed-in for the locations indicated by the dashed green boxes in (A); (G) STOC-T reconstruction of 15 µm thick coronal projection of the junction between inner and outer segments of photoreceptors (IS/OS); the red box in the IS/OS image is shown zoomed-in to various degrees on the right. The IS/OS reconstruction was numerically compensated for ocular aberrations revealing photoreceptor structure (22nd order Zernike polynomials).

Traditionally, choroid consists of three main layers at increasing depths: the choriocapillaris, Sattler's layer, and Haller's layer. While there is no clear division between Sattler's and Haller's layers [106], traditionally Sattler's layer contains medium-sized vessels whereas Haller's layer is considered as a volume of larger choroid vessels. Moreover, there is a significant variation layers thickness between the individuals and the area of the retina. Normally, subfoveal zone has thicker choroid while optic disk region has very thin choroid layer. Choroidal tissue has problematic imaging at different depths as choroid is heterogeneous optically (Figure 3.13).

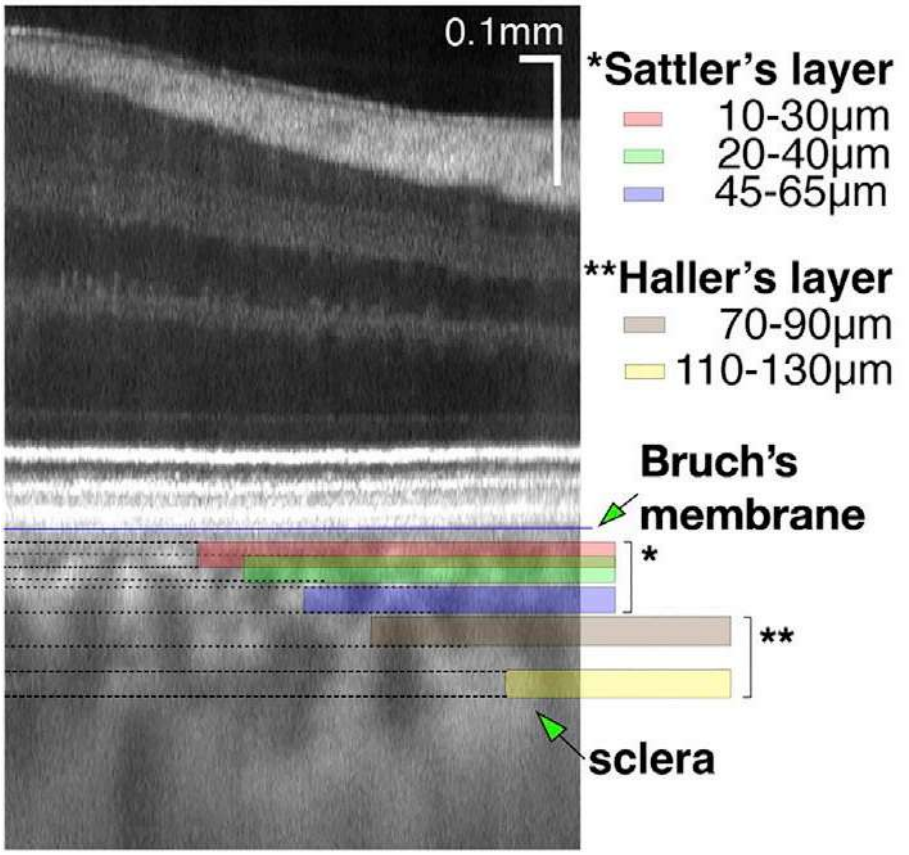


Figure 3.13: A representative cross-sectional image with the locations of arbitrarily selected projections from the choroid thickness

Another important use of light and imaging is blood flow monitoring. Laser Doppler Flowmetry (LDF) is a non invasive technique to assess tissue hemodynamics. It is based on analysis of frequency shifts which are produced when light is scattered from a moving particle [118]. Since LDF was invented, it was interesting subject for both research and development of new clinical tools [119]. It was shown, moving particle speed distribution can be calculated by analyzing Doppler spectrum of the laser [120]. Moreover, similarly Laser Doppler Holography (LDH) was used to visualize bloodflow in human retina label-free in vivo [121]. LDH detects backscattered and Doppler-shifted optical field from the retina. It is done by holographic or full-field interferometric setup. By bandpass filtering power spectral density of the signal blood flow images are calculated [122]. Typically, ultrafast 2D cameras are required for such data registration, but it is possible to use a slower camera [123]. Even though these techniques provide information about blood flow velocity, both LDF and LDH do not give depth-resolved flow information as they are based on fixed-wavelength illumination. Instead, they analyze the time-varying optical signal, which represents the combined contribution of scatterers from all depths. The signal can be written as:

$$U_{LDF,LDH}(x, y, t) = dzU(x, y, z, t) \tag{3.3}$$

The PSD is calculated from the temporal signal and is used to determine velocity of a scattered particle. By selecting PSD bands velocity shifted images are generated (instead of depth-resolved blood flow images).

Depth-selective blood-flow information can be obtained using multi-channel or multiwavelength Fourier-domain detection [124, 125], although conventional OCTA based on point-by-point scanning is limited by acquisition speed, eye motion, spatial resolution, and aberrations. Fourier-domain full-field OCT (FD-FF-OCT) [37] acquires the entire 2D field without beam scanning while preserving transverse phase stability, enabling high-speed in vivo retinal imaging [40] and extraction of blood-flow information from the same volumetric dataset. During STOC-T acquisition, optical frequency and time vary simultaneously, coupling depth-dependent structure and motion-induced phase; Fourier transformation of the spectrally resolved signal ($U_(x, y, \omega, t)$) provides depth-resolved data ($U_(x, y, z, t)$), while temporal signal variations reveal tissue dynamics. Phase correction suppresses static structures, while power spectral density (PSD) frequency gating isolates Doppler-broadened components produced by moving scatterers, enabling quantitative blood-flow estimation from a single volume. Unlike conventional Doppler OCT, which requires multiple sequential acquisitions [126], this approach can combine high-resolution structural retinal imaging with OCTA-, Doppler-OCT-, and laser-Doppler-

holography-like blood-flow information in a single-volume framework.

Wide-area MLDH blood-flow images were obtained by stitching measurements from multiple overlapping retinal locations (Figure 3.14), including the optic disc and macula, with 255 ms acquisition per location and 32 locations acquired in 8.2 s [127]. Compared with STOC-T, ICGA, and conventional OCTA, MLDH provides depth- and flow-sensitive contrast through frequency-gated power spectral density (PSD). The full 0–30 kHz band predominantly reveals inner-retinal flow, whereas gating 0–6 kHz enhances slower, larger choroidal vessels, 6–15 kHz highlights faster choroidal flow, and 10–30 kHz provides high-contrast visualization of the fastest flows [127]. Thus, frequency-selective MLDH can distinguish blood-flow components with different velocities and provide more comprehensive vascular information than OCTA or ICGA alone [127]. However, when compared to other experiments [128] the flow direction of should be taken into account. Retinal arteries and veins show axial flow in opposite directions, especially in the optic disk area [128]. This results in further need to optimize our data analysis.

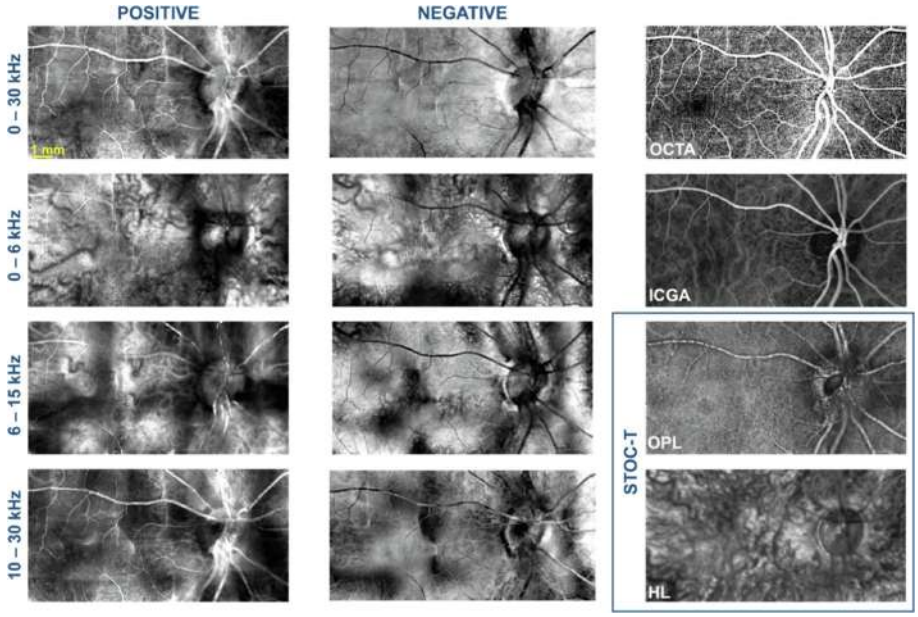


Figure 3.14: Wide-area blood flow images obtained from MLDH under variable frequency ranges are compared to conventional scanning OCTA (Optopol Revo), ICGA (Heidelberg Engineering), and STOC-T structural imaging [127].

Conclusions

This work demonstrated that spatio-temporal optical coherence tomography can image the entire chorioretinal complex with uniform 5 µm resolution in all three dimensions over the full 800 µm axial thickness without any mechanical scanning. Compared to two commercial scanning OCT systems, STOC-T achieved 3–4 times higher lateral resolution than both Spectralis and Triton while matching Triton's depth of focus (600 µm) and exceeding DOF of Spectralis (450 µm). This combination of high resolution and large DOF allowed, for the first time, morphological differentiation of Haller's layer, Sattler's layer, and the choriocapillaris within the same volumetric dataset. Furthermore, image processing enabled to resolve individual photoreceptors, and large-area (9 mm $\times$ 4.6 mm) montage was stitched from 32 adjacent locations which revealed retinal microstructure from the inner limiting membrane down to the capillary plexuses without additional hardware such as adaptive optics. The same STOC-T datasets were further shown to support Multiwavelength Laser Doppler Holography (MLDH), extracting depth- and velocity-gated blood flow information from a single volume acquisition rather than the multiple sequential measurements required by conventional Doppler OCT which enabled both slow choroidal circulation and fast retinal vessels be selectively visualized. However, this technique should be further improved to differentiate directional contrast between veins and arteries [128].

In conclusion, these results show that STOC-T provides a single, mechanically simple acquisition capable of resolving chorioretinal morphology better than it is achievable with commercial scanning OCT and at the same time obtaining blood-flow information that would otherwise require a separate imaging. This combination of high resolution and high depth setup makes STOC-T a promising research and diagnostic tool for chorioretinal diseases where both structural detail and vascular assessment are clinically important.

3.3. Deformable Membrane for modal noise reduction

OCT systems are built to constantly improve two main parameters: sensitivity and imaging speed. In this section an additional improvement to achieve higher sensitivity will be discussed. Sensitivity determines the image quality and is defined as the weakest signal that can still be detected above the noise floor [89]. In OCT, observable noise can generally be divided into three main types: detector noise, shot noise, and relative-intensity noise [129–131]. In the STOC-T technique that is based on use of multimode fibers, an extra source of noise appears. This noise is caused by the fluctuating interference between correlated transverse electromagnetic modes (TEMs) generated in the multimode fiber (MMF) [131]. The number of excited modes is inversely related to the generated speckle size observed at the output of a cylindrical optical fiber. For a set wavelength, by increasing the fiber's core diameter and numerical aperture the speckles reduce in size. With sufficient modal dispersion and fiber length, the TEMs can be separated in time. Though, when many modes are excited, some can degenerate, which lets them interfere and produce modal noise (multimode fiber induced speckle patterns that are not separated in time) [132,133] with a characteristic pattern [131,134]. Formula (3.4) shows how modal noise adds to other noises to the OCT signal:

$$\sigma^2_{noise} = \frac{1}{N}(\sigma^2_{shot} + \sigma^2_{receiver} + \sigma^2_{RIN} + \sigma^2_{modal}) \tag{3.4}$$

N is the number of statistically independent averaged realizations; the 1/N scaling is the ideal uncorrelated-noise case. Under ideal conditions, OCT systems are shot noise limited [129]. In this case, the sensitivity of an FD-OCT system can be calculated using 3.5 [135].

$$SNR_{FD-OCT} = \frac{\rho P_0 T}{e^-} \frac{\kappa_r \kappa_s R_r R_s}{(R_r + R_s)} \tag{3.5}$$

here: ρ is detector responsivity, T - the camera integration time, κ - unidirectional coupling coefficient of the beam splitter (optical losses included), and R - sample reflectivity. Therefore, an optimally designed OCT system should always minimize all other noise sources than shot noise. The detectors are normally constructed that receiver noise remains low enough to enable shot-noise-limited detection at standard illumination levels. It is possible to attenuate both modal noise and RIN using dual balanced-detection method [136, 137]. This method in Spectral Domain OCT achieves over 5dB SNR increase [137] registering three dimensional images in vivo by reducing autocorrelation artifacts and background noise. While this method requires precise calibration for 2 channel detection, it also becomes more expensive and complicated in full-field detection. A simple solution to use a light source which as lower intensity fluctuations than shot noise in detector cannot be applied as fluctuations are

generated by the MMF itself. This means that the modal noise 3.4 becomes dominant. It can be suppressed by using a dynamic diffraction element, such as grating, or agitating MMF as it is described in the literature [133, 138, 139]. When partial spatial coherence is generated in a long multimode fiber (MMF), by adding a reflective element that wobbles surface in front of the fiber input the speckle pattern will be altered . This variation causes multiple incoherent and quasi-stationary realizations of modal noise to be averaged. Thus, the noise fluctuation decreases, and the modal-noise variance is reduced. This is done by a phase-randomizing deformable mirror. When a multimode optical fiber of 0.22 NA is used, this can be done within a camera exposure of 20 µs [140]. Our aim here is the optimization of STOC-T systems detection performance by achieving shot noise limited detection which helps achieve higher dynamic range by multiple volume averaging. This setup is important for effective magnitude averaging taking into account eye movements. It attenuates speckle contrast, enhances dynamic range, and resulting in clearer images of cell bodies. To achieve this, we used a phase-randomizing deformable mirror to dynamically variate the distribution of illumination intensity in time. We applied a numerical averaging technique [141] which supported this approach, further increasing the signal-to-noise ratio (SNR). Finally, a healthy volunteer was used to test the new method and we have obtained improved cellular-resolution images.

Deformable Membrane

Deformable mirrors are mirrors which surface can be deformed (Figure 3.15), which enable light wavefront control and correction of optical aberrations. While there are many different approached to create a deformable mirrors, one of a typical approaches is to make a membrane mirrors based on electrostatics. Membrane mirrors are made by stretching a thin conductive and reflective membrane over a solid flat frame. It can be deformed electrostatically by applying different voltages to electrostatic electrode actuators which are typically positioned under the membrane [142]. Another type of membrane is based on a low-voltage piezoelectric ceramic actuator which vibrates a thin plate of reflective-coated glass, metal, or plastic. This vibration generates resonant modes and deforms the mirror surface relative to the motion of the actuator [143]. The deformable membrane or phase-randomizing deformable mirror has a continuous surface with relatively long correlation lengths. This can be explained as a created narrow-angle temporally-random divergence. Randomly-distributed deformations in the continuous surface at very high temporal frequencies produce many uncorrelated speckle patterns [144].

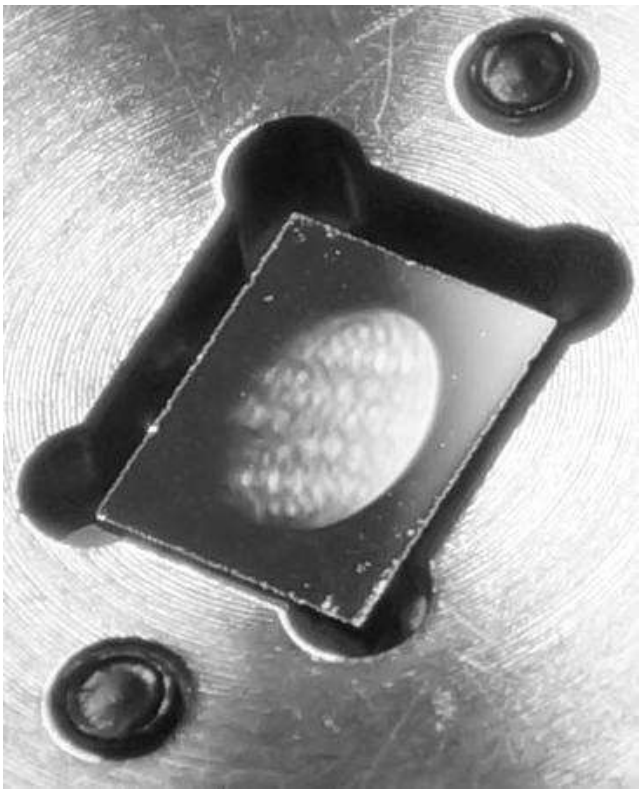


Figure 3.15: Deformable membrane capable to modulate surface up to 1.5 MHz, Dyoptica [144]

Experimental STOC-T setup and data processing

A schematic upgrade of the STOC-T experimental setup 3.2 is shown in Figure 3.16. The OCT system is used as described in Figure 3.2 with and additional setup for deformable membrane (Figure 3.16) where a 1.5m single mode fiber (MJ-3A3A-850-5/125-3-1, OZOptics) to gather light from a light source. SM fiber delivers light onto deformable mirror made by Dyoptika (operation speed 1.5 MHz), which modulates the pattern onto the multimode fiber (300 m, NA = 0.22, Φ50 µm circular core). The fibre supports approximately 840 guided modes; over 300 m, differential modal group delays exceeding the source coherence time reduce mutual coherence between many modes, although near-degenerate modes may remain coherent. Lenses l1-l4 (Figure 3.16) are used to collimate and focus light onto membrane and then reimage onto the tip of MM fiber. Such deformable mirror and multimode fiber combination loses up to 40%, mainly due to coupling.

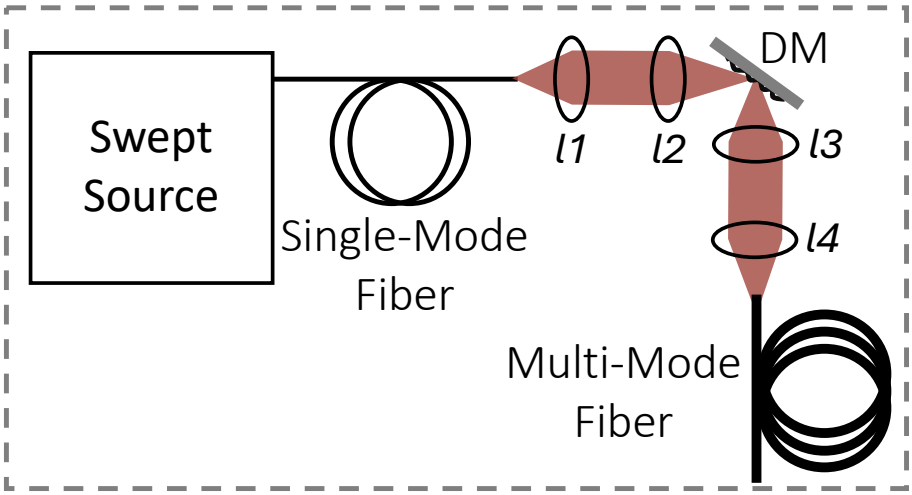


Figure 3.16: Additional scheme for deformable membrane for coherence noise reduction. Optimized configuration to focus light onto DM and then onto tip of MMF. Multimode fiber is coupled into the setup shown in Fig 3.2.

Spatially coherence reduced light from the MMF is collimated and then focused through a hole in mirror into interferometer. A 50/50 beamspliter is used to send half of the light onto the sample, another half is sent to reference mirror. An objective (PLN10X, Olympus) is used to match NA of an eye. Scattered light from the retina and reflected light from the mirror is then recombined with the same beamsplitter onto the high-speed camera (FASTCAM SA-Z, Photron) operating at 60 kFPS (60 000 frames per second) and which acquires 512 frames for each sweep of the laser. The deformable mirror (DM) induces changes in the speckle pattern in the fiber output when DM oscillates at about 1.5 MHz frequency. We capture these modulated image volumes using a high-speed camera and process them with standard OCT algorithms. A typical noise structure in the en face images is shown in Figure 3.17(b). By selecting and analyzing noise plane at a z-position, where there is no object information, and applying a 2D Fourier transform (2D-FFT), a noise distribution near the DC component is visible (Figure 3.17(c)). This noise can be reduced by applying 2D-FFT spatial filtering to remove the visible peaks (Figure 3.17(d)).

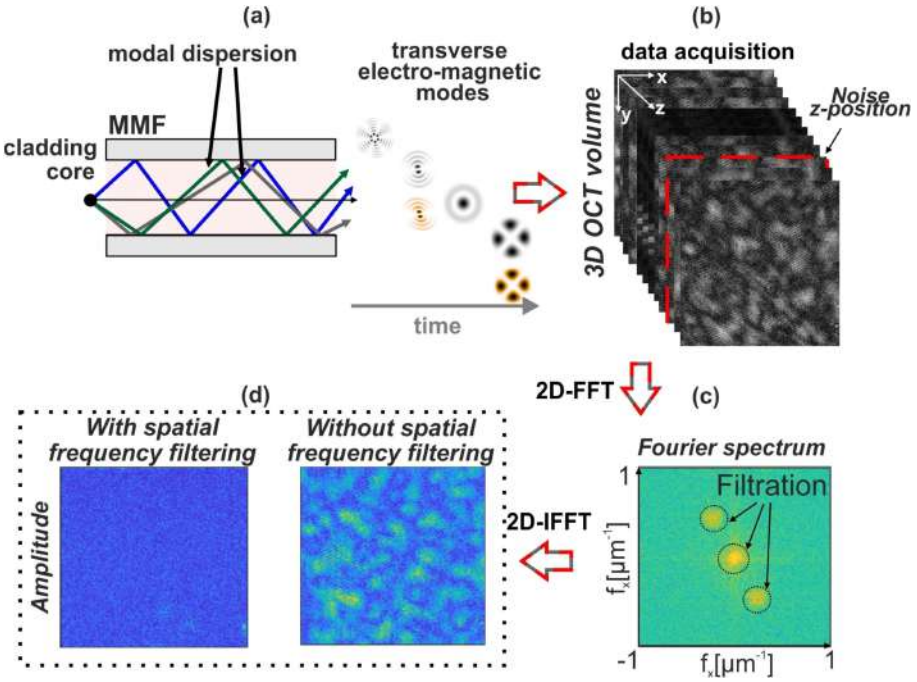


Figure 3.17: Diagram showing the generation and filtering of modal noise resulting from beating between degenerate modes in a long multimode fiber: (a) the formation of TEMs over time with degenerated modes that overlap and contribute to the modal noise; (b) 3D OCT volume with selected characteristic noise pattern in en face images at the z-position without object information; (c) Fourier spectrum with DC (direct current or zero-frequency) component and with marked visible peaks for 2D-FFT filtration (note: that extra filtering areas are used to filter out camera glass reflection); (d) resulting amplitude images with and without spatial frequency filtering.

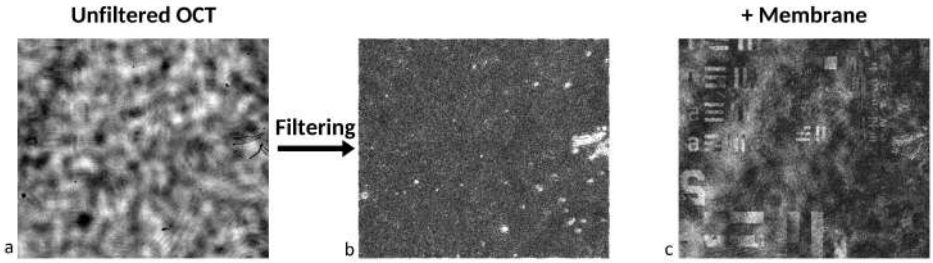


Figure 3.18: USAF target imaged behind ND filter. a) USAF is unrecognizable behind speckle pattern, (b) FFT filtering removes speckles together with reflective USAF target, (C) deformable membrane enabled, USAF is visible without FFT filtering.

We have tested how deformable membrane could be used imaging reflective samples. A STOC-T setup (Figure 3.17) was used to check speckle reduction [145]. A positive reflective USAF target behind ND filter. First, images without membrane were obtained. Figure 3.18 (a) shows overwhelming speckle pattern. Using spatial filtering in Fourier domain removed both speckle pattern and USAF entirely Figure 3.18 (b). When deformable membrane was turned on, obtained image of USAF target was visible without spatial filtering (Figure 3.18 (c)). Even though not all speckles were removed, membrane enabled imaging reflective image previously sunken in speckle noise.

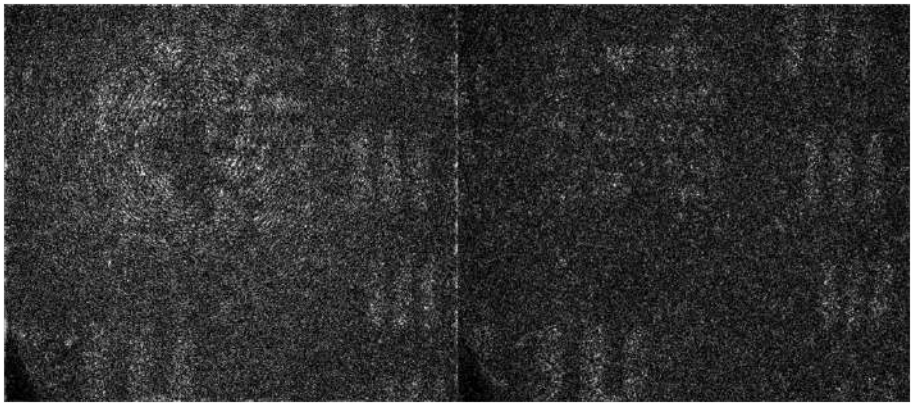


Figure 3.19: USAF target imaged behind ND filter and scattering layer. After cleaning speckles via FFT filtering there are still coherence artifacts cover part of USAF target (left). When deformable is used, these coherence artifacts are removed and center part of USAF is visible (right).

Further experiments were made with USAF target. USAF was placed behind strong OD (optical density) filter and scattering layer to produce barely registrable signal from the sample. When scattering layer was used, USAF was visible even after spatial filtering due to speckled appearance (thus high spatial frequencies which were not filtered). However, coherence noise was not possible to remove via Fourier space spatial filtering and part of USAF image was lost Figure 3.19 (left). When membrane was turned on, obtained and spatially filtered image revealed previously invisible structure of the USAF target Figure 3.19 (right). These results were promising and further investigation on biological sample fallowed.

A STOC-T setup (Figure 3.20) was used to check modal noise reduction on a cucumber cell sample. (Figure 3.21) Images of cells obtained using a multimode fiber-membrane system designed to reduce light coherence and coherent noise. Images captured with the membrane on and off in different slices are compared. As seen in the XZ and XY slices, the combination of fiber and membrane reduces noise and allows for higher contrast images. Since the experiment on cucumber cells gave positive results for noise reduction on pos-

sible SNR increase. It green-lit further development optimizing DM+MMF (deformable membrane and multimode fiber) configuration and conducting following experiments. Cucumber cell imaging provides rough estimation how system will behave imaging human retina.

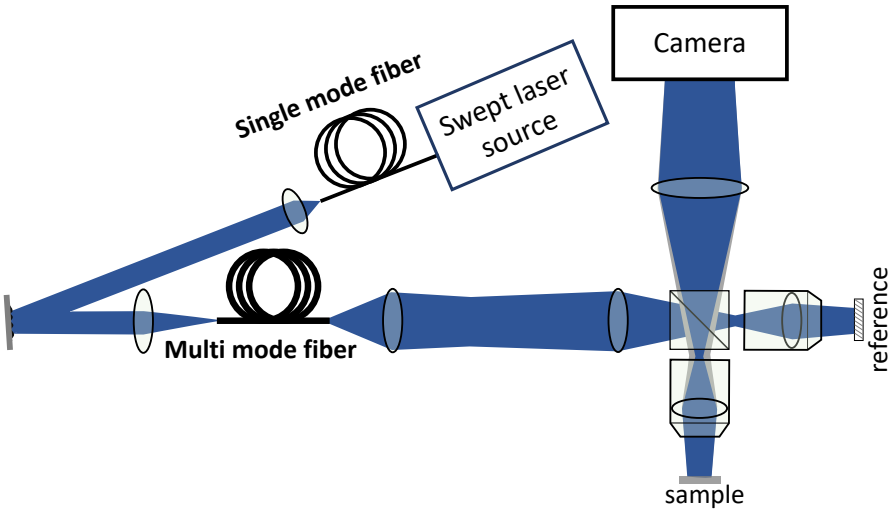


Figure 3.20: STOC-T system with a multimode fiber and deformable membrane for coherence noise reduction. For USAF and Cucumber experiments identical objectives were used in both sample arm and reference arm.

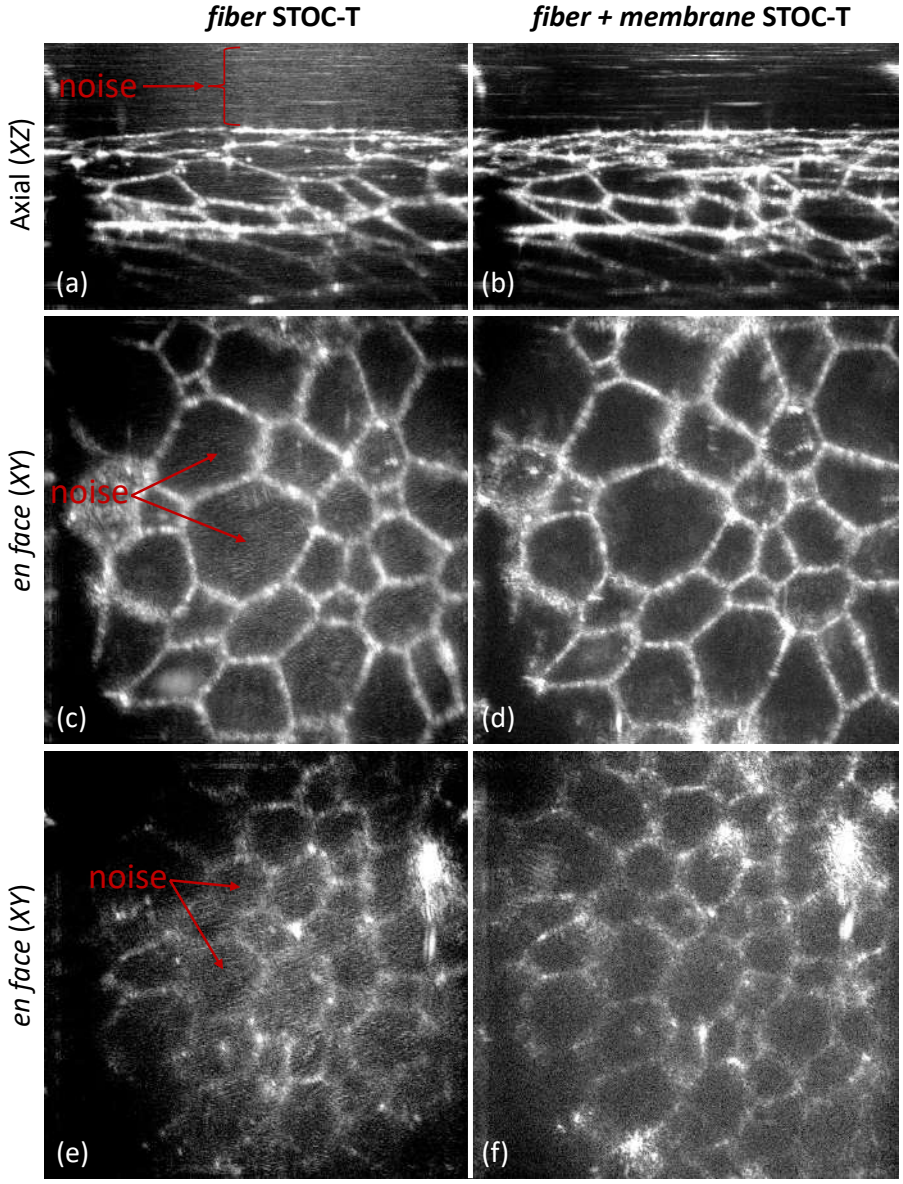


Figure 3.21: Cucumber cell images were obtained via STOC-T system using a multimode fiber (a, c, e) and its combination with a membrane (b, d, f) for coherent noise reduction. The combination helps to get rid of the coherent noise better as illustrated by the red arrows.

System sensitivity

The sensitivity of the STOC-T setup was measured using the standard method, assuming that the system is optimal and is limited by shot noise. Thus, sensitivity was calculated without averaging in order to have reliable information. The power output of swept source laser was limiting individual exposures. This is due to a lack of swept source lasers at 840 nm with higher power output and losses produced due to DM-MMF coupling. In such case measured SNR without averaging have lower coherent noise than shot noise. By averaging, SNR change differently than should be according to system parameters.

Sensitivity is typically measured from A-scan taking a peak value and comparing it to noise floor. Normally, experiment is made by measuring mirror attenuated with ND filter (which allows known attenuation). However, since in our system configuration we filter out low frequencies, a mirror is replaced by Ronchi grating with known reflectance value at non-zero order. Sensitivity is calculated using this formula:

$$Sens = 20log(\frac{I_{obj}}{\sigma_{noise}}) - 10log(T_{filt}^2) - 10log(R_{Ronchi}) \tag{3.6}$$

Figure 3.22 shows system sensitivity which shows what the lowest signal from an object that is detectable. X axis shows different filter attenuation in the reference arm while the sample arm filter remained the same. Y axis shows achievable sensitivity in comparison to noise calculated theoretically. As we can see, 2D FFT filtering modal noise (including zero order reflections from the grating) increases sensitivity by 5 dB up to theoretical value (80 dB) [145]. ND filters were tilted to avoid direct reflection onto the camera.

Moreover, not only FFT filtering, but also DM combination with MMF increases sensitivity and effectively achieves shot-noise limited measurement conditions. This DM addition to the system leads to ability to average multiple volumes linearly increasing SNR. Even though, even working near shot-noise limit, during averaging other noise, such as RIN or modal can arise from the noise floor and reduce SNR. For this reason we produced experiments with both reflective and scattering objects to test volume averaging influence to SNR.

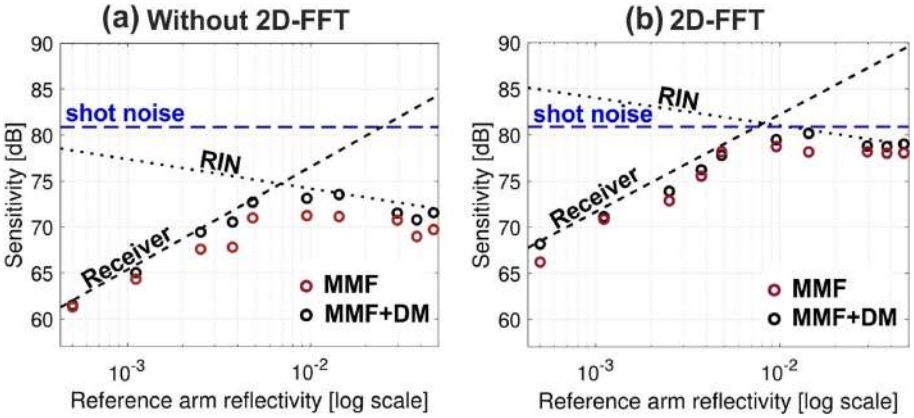


Figure 3.22: Evaluation of STOC-T sensitivity by using a Ronchi grating as reflecting object. Sensitivity is measured as a function of reference reflectivity when noise is reduced with the multimode fiber (MMF) and in combination with deformable mirror (MMF + DM), for (a) unfiltered data and (b) 2D-FFT filtered data, in the spatial frequency domain.

Magnitude averaging for reflecting and scattering objects

We can apply numerical magnitude averaging when system is shot noise limited. This condition enables linear sensitivity growth depending on averaged volumes (increasing total exposure time of the measurement). This is commonly used in OCT systems to achieved higher SNR [141, 146, 147].

$$M^{mag}(z,N) = \frac{1}{N}\sum_{n=0}^{N-1} M_n^{(1)}(z) \tag{3.7}$$

where N is the number of averaged samples. M is the magnitude-squared Fourier-transformed spectral fringes [147].

We first tested this method using Ronchi test target as a reflective sample. 30 volumes were recorded at the same target position, each containing 512 spectral points and 512 × 512 pixels. Acquisition time per volume was 8.6 ms. The data was processed with standard OCT algorithms, both with and without 2D-FFT spatial filtering. The results indicate that using a phase randomizing deformable mirror increases the SNR. The highest SNR enhancement obtained is 13.6 dB [145]. It is achieved by averaging using MMF+DM configuration and then averaging 30 volumes using 2D-FFT filtering. This result corresponds to the theoretical model for shot-noise reduction.

The second experiment was done to evaluate the MMF and MMF+DM configuration using a scattering phantom. The phantom was made to resemble complex scattering media, such as the retina of the eye or biological tissues, allowing to evaluate possible advantage of the MMF+DM setup. It was made of

transparent PDMS with two scattering layers composed of PDMS mixed with TiO_2 powder. Each layer contained "IChF" logotypes offset laterally. The upper layer was about 30 µm thick (90 µm with the logotypes). It was placed roughly 50 µm above the lower layer, which thickness was a few millimeters [49]. The magnitude averaging for 30 volumes is shown in Figure 3.23. Top shows data unprocessed with spatial filtering while bottom shows data where spatial filtering was applied. In this configuration, the MMF+DM setup with numerical filtering showed an SNR improvement of about 14 dB. Figures 3.23 b–f illustrate 3D imaging results for four variants: STOC-T with MMF and STOC-T with MMF+DM, each analyzed with and without 2D-FFT filtering. Figures 3.23 e and 3.23 f are visibly cleaned up by 2D-FFT filtering compared to unfiltered noisy 3.23 b and 3.23 c images. When multiple volumes are averaged, the negative influence of modal noise is clearly visible. In this case, 2D-FFT filtering alone increased the SNR by approximately 7 dB which is comparable to the improvement achieved with the deformable membrane. By combining both MMF+DM and 2D-FFT SNR increase dependence on averaged volumes fallows theoretical curve.

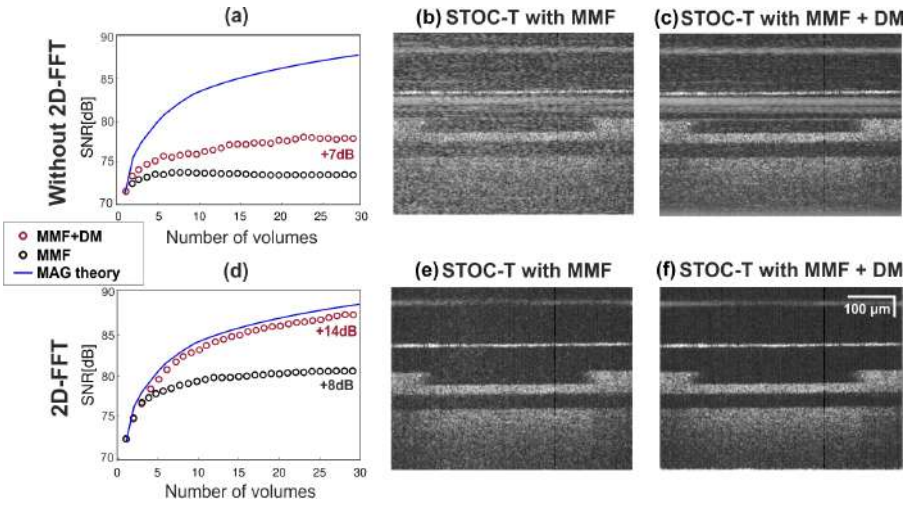


Figure 3.23: SNR as a function of the averaged volumes for the scattering object with multimode fiber (MMF), or with a combination of multimode fiber with deformable mirror (MMF+DM): (a, d) SNR is calculated after each volume iteration of averaging the magnitudes of 30 volumes; (b, e) reconstructed B-scans from measurements with only the multimode fiber (MMF); (c, f) B-scans obtained for the combination of multimode fiber with deformable mirror (MMF+DM). Solid blue line (MAG theory) represents theoretical increase of SNR with number of averaged volumes.

In vivo human retinal imaging

We tested our new STOC-T configuration in vivo to see actual improved capabilities imaging human retina. The retinal imaging was done in vivo on a healthy 49 year old volunteer with no retinal diseases. In order to avoid body movements, volunteers head was stabilized with a standard chin rest. For eye alignment a letter chard was placed in a conjugated plane to the high-speed camera (Figure 3.20). To find desired retinal location in real time a line camera was used [88].

Figure 3.24 compares in vivo retinal images obtained using two STOC-T configurations: a passive mode with only the MMF (Figure 3.24((a)) and a passive–active mode combining the DM and MMF (Figure 3.24(b)). The measurements were taken at a retinal location 5° temporal–superior to the macula. For this experiment only variation was a switch between MMF and DM+MMF. However, during the measurement retina's location slightly moved (as it is seen in the Figure 3.24(a) and (b) images). Each dataset consisted of 30 averaged volumes which were acquired in total 0.25 s (8.6 ms per volume, registering 512 spectral images in 512x512 pixel field of view at 60 000 fps). This short acquisition time minimized the influence of eye movements, which would blur speckle contrast even more. Figures 3.24(a) and (b) show B-scans (top) and en face images (bottom) of the inner nuclear layer (INL) for both setups (left MMF only, right DM+MMF). Figure 3.24(c) shows summed A-scans for both MMF and DM+MMF configurations. It is clearly visible, that noise levels in both configurations vary. The MMF+DM setup shows lower interlayer noise compared to the MMF-only configuration [145]. The choroidal layer appears slightly different in both averaged A-scans This is due to a small shift of retinal regions while imaging.

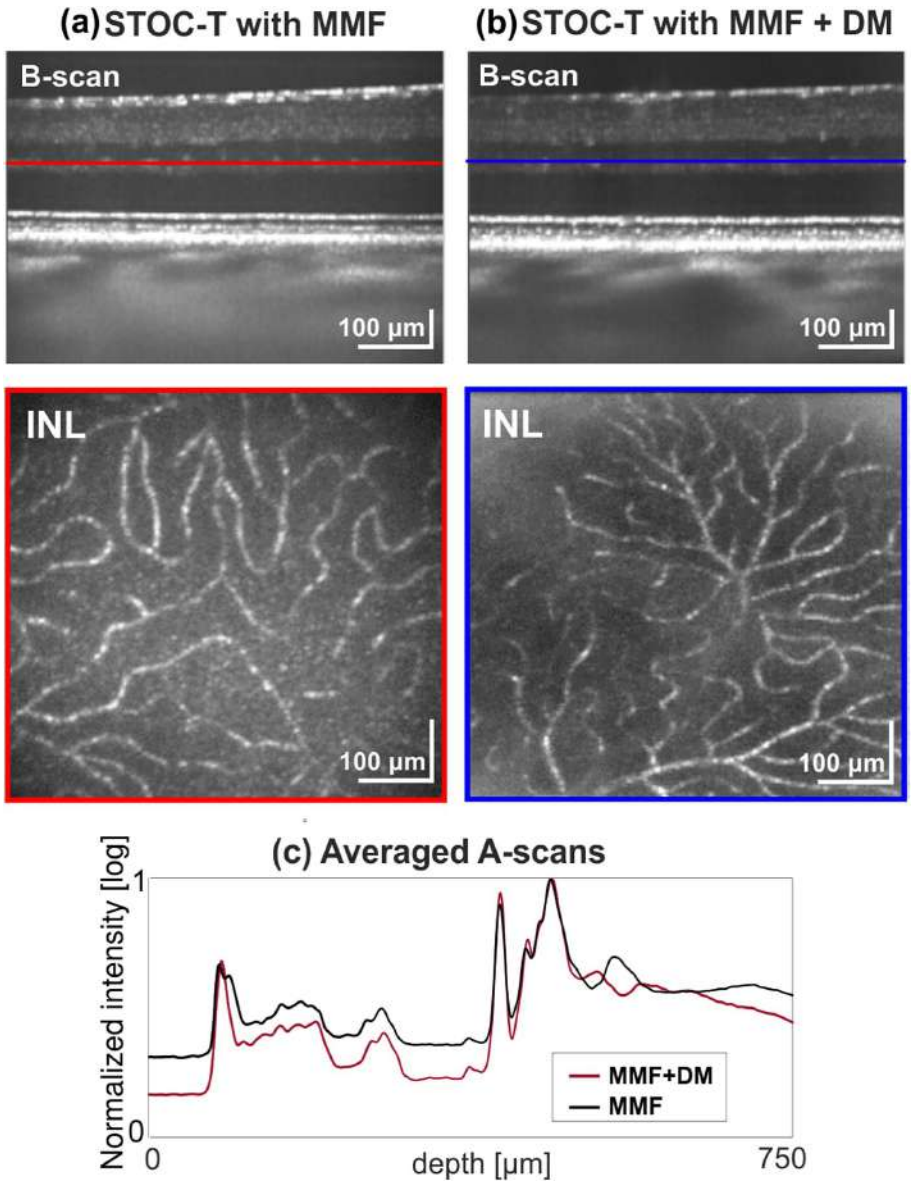


Figure 3.24: The comparison of in vivo measurement in STOC-T: (a) passive mode (only MMF) and (b) using a passive-active mode (DM+MMF), (c) averaged A-scans as a function of depth.

Overall, this approach to noise reduction in FF-OCT imaging resulted in development of combination of deformable membrane together with multimode fiber. This addition to STOC-T system led to improved images, reduced noise, high SNR and sensitivity reached approximately 80 dB. The use of DM+MMF combination can be applied for both reflective and scattering sample imaging. Furthermore, obtained high resolution retinal images in vivo had better than before contrast. Modal noise reduction enabled multiple volume averaging in quantities that were not possible before. In conclusion, this upgrade to STOC-T imaging may support future high-sensitivity retinal STOC-T development and as a new step reaching to maximize potential of OCT systems even further.

3.4. High-Throughput Spatio-Temporal Optical Coherence Tomography (STOC-T)

As discussed in previous section, crosstalk reduction and increase of SNR was achieved by combining a multimode fiber and a deformable membrane. However, OCT systems sensitivity is greatly affected by interferometer design [129] which enables another push for STOC-T development. The heart of every interferometer is the beamsplitter. In conventional systems where 50/50 beamsplitter is deployed, about 75 % of light is wasted. Photons traveling from a light source are split into two equal parts, and half of the light goes into the sample. Backscattered photons from the sample travel back to beamsplitter where 50 % of remaining photons are lost. Typically biomedical samples scatter only a few percent of light [15] and reference arm reflectivity has to be significantly attenuated (from almost 100 % to 1 %) to match sample arm. This means that light from the reference arm is almost entirely wasted. Usually, to collect more light with the camera illumination intensity is increased. However, imaging biomedical samples (especially in vivo) phototoxicity determines the power ceiling of the light source and limits photon budget. In confocal OCT the throughput problem is solved by a power-conserving fiber optical circulator [129], which can increase the sensitivity by > 4 dB [148]. The throughput in FF-OCT was increased by high-throughput dark-field (HTDF) interferometer design [32] which mainly consisted of 90/10 beamsplitter and a small pick-off mirror located in the pupil plane. In such setup, 90 % of light can be sent onto the sample and 10 % to the reference. Pick-off mirror enables detection through the same beamsplitter facet which is used to inject light into the interferometer. This way beamsplitter sends 90 % light backscattered from the sample to the camera. The pick-off mirror separated the illumination light from the scattered signal. However, this design in TD-FF-OCT forces to use low etendue light sources and also reduces lateral resolution due to the decrease in illumination pupil. The reported SNR increase there was due to the combination of a dark-field effect rejecting specular reflections and due to HT (high-throughput) design. Previously, a similar design was used in STOC-T setup with 50/50 beamsplitter where a pick-off mirror directed backreflected signal to another camera which was used for real-time imaging and aligning desired imaging area of the retina [88]. However, such use of pick-off mirror did not improve SNR and even though that system could use the second channel for another ultrafast camera theoretically, in practice this would double the price of whole setup and would require ultra precise alignment which may not even result actual improvement in imaging quality and sensitivity.

We have combined both advancements into a high-throughput (HT) STOC-T system which achieves up-to 3.5x higher SNR. We replaced 50/50 beamsplitter with 90/10 and used pick-off mirror to collect the signal through the same

beamsplitter facet that is used for illumination. Such configuration is possible when sample scatters light across a wide range of angles (typically, most biomedical tissue scatters light this way [149].

Methods

The idea behind HT STOC-T can be illustrated by simplifying interferometer into a single arm system. This lets simplify standard beamsplitter into 50 % mirror. By replacing said beamsplitter into normal 100 % mirror, all photons are sent from the light source into the sample and then backreflected through the same mirror into a camera. In such situation detector collects 4 times more photons than with 50 % mirror/beamsplitter. However, this is only true in ideal conditions where losses from the pick-off mirror are negligible. Moreover, considering signal-to-noise ratio (SNR), the SNR for regular FF OCT setup can be approximated $SNR_{regular} \propto 0.25NR_O$, where N is total number of photons and R_O – coherent reflectivity of sample, 0.25 comes from maximum interferometer efficiency when light passes 50/50 beamsplitter [32]. Meanwhile SNR for HT-STOC-T setup is approximated $SNR_{HT-STOC-T} \propto r^2NR_O$, where r is reflectivity of the beamsplitter's light inlet facet. As a result, and advantage ratio of SNR can be expressed such as:

$$\frac{SNR_{HT-STOC-T}}{SNR_{regular}} = 4r^2 \tag{3.8}$$

However, again this is only true for highly scattering low reflective biological samples (such as retina, cornea) where only a small part of light is scattered coherently and minimum signal from reference arm is sufficient and as in FF-OCT SNR can strongly depend on the reference, it can be shown that in the shot noise-limited detection – where the noise is dominated by the reference reflection– the SNR increase also scales as $4r^2$. It is clearly visible that the advantage of HT system approaches 4 when r reaches closer to 1 which happens when incoherent reflection is also comparable to zero but still present. However, when a highly reflective sample is imaged, it also requires a strong reference signal. In such case the benefit of HT configuration is lost and standard 50/50 beamsplitter becomes more efficient.

HT-STOC-T was combined with a Linnik interferometer (Figure 3.25). As a light source a swept source laser (Broadsweeper BS-840-2-HP, Superlum), tunable from 803nm to 878 nm at the maximal speed of 240000 nanometers per second was used. Laser light was coupled into a single mode (SM) fiber and imaged onto the ultrafast deformable membrane (Dyoptika) and refocused into a 300 meters of a step-index multimode (MM) fiber ($0.22NA$, Low-OH, Ø50 µm core, FG050LGA, Thorlabs). This configuration was used to distort spatial coherence and reduce modal noise in the MM fiber in order to increase

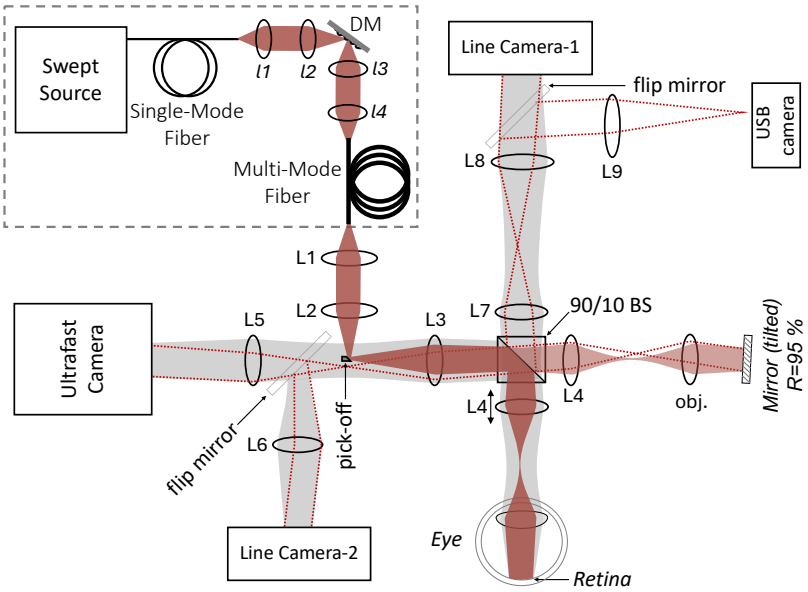


Figure 3.25: High-throughput STOC-T setup consisting of a light unit (inset) and an imaging system. In the light unit a swept laser source is coupled into the long multimode fiber after it is reflected off the deformable membrane (DM). The imaging system is based on a Linnik interferometer and three imaging cameras: one 2D ultrafast camera and two line cameras. A USB camera is an auxiliary camera used to image the pupil plane for the alignment purposes. $L1$-$L9$, achromatic lenses. Red beam shows illumination and the reference beam, whereas gray beams represent scattered light.

SNR after averaging multiple volumes [145].

Technical part

Here is detailed description of laser path through whole system. Swept source laser delivers light through SM fiber into „Light clean-up section“ (marked with dashed line in Figure 3.25). The tip is image onto the ultrafast membrane with a 1:1 ratio, forming a 5 µm spot, using lenses $l1$ (f=50 mm) and $l2$ (f=50 mm). Then the reflected-off from the membrane is reimaged onto the tip of MM fiber (again with a 1:1 ratio) using lenses $l3$ (f = 50 mm) and l4 (f = 50 mm). Light exiting MM fiber (and „cleaning section“) is collimate by lens $L1$ (f = 40 mm) and then focused by $L2$ (f = 75 mm) onto a 1 mm diameter 45° rod pick-off mirror (47-628, Edmund Optics) which was glued on the center of a glass window (B coated) located in the pupil-conjugate plane. Illumination is then reflected into interferometer and magnified 1.9× to 94 µm. Then both fiber tip and pick-off mirror is reimaged via lenses $L3$ (f

= 150 mm) and $L4$ (f = 75 mm) onto the pupil planes of the objective lenses (f = 30 mm) in the sample and reference arms or human eye in the sample arm. Light is divided into two parts via 90/10 beamsplitter which sends 90 % of the light onto a sample (5.9 mW) and another 10 % (0.74 mW) onto the reference mirror. Reference mirror made of silver reflects 95 % of light which is returned and optimally attenuated via second pass through beamsplitter to $\approx$ 1 % (0.07mW). Backscattered light is reflected back into beamsplitter and 90 % of it is reimaged with $L4$ and $L3$ lenses on the pupil-conjugate plane. Since we used the same beamsplitter facet for both illumination and detection we had to solve the problem of stray reflections hitting camera. To reduce back reflections from optical components, we deliberately selected lenses $L3$ and $L4$ based on both focal length and types of anti-reflection coatings. We also considered the beam paths in the system to circumvent any residual reflections from being imaged onto the camera.

The pupil plane of the objective lens is magnified twice in the conjugate plane which makes pick-off mirror to block less than 1 % of the light returning from interferometer (assuming even signal distribution across a wide range of angles). For image formation a tube lens $L5$ ($f = 100$ mm) made of two doublets (f = 200 mm) in Plösl configuration for better off-axis performance is used focus signal onto the 2D ultrafast camera (Fastcam Nova S16, Photron) with 512×448 resolution at 60 kHz rate and pixel size 20 µm. In order to replicate experiment and compare images with both 90/10 and 50/50 beamsplitters a replaceable kinematic beamsplitter cube (DFM1BS/M, Thorlabs) was used to switch between 2 beamsplitters. Furthermore, the system was equipped with two line cameras (raL2048-48gm, Basler) in order to obtain real time B-scan images and for retinal imaging. Both cameras were acquiring a line of 512 pixels at 60 kHz rate and were synchronized with the 2D ultrafast camera. The first line camera (camera-1 in Figure 3.25) was located in typical 2D ultrafast camera place for signal registration in the regular STOC-T setup – behind the output facet of the beamsplitter.

Lenses $L7$ (f=150 mm) and $L8$ (f=50 mm) were used to image both signal and reference onto the camera. The $L8$ was twice shorter than $L5$ to adjust field of view to a similar area as 2D camera because pixel size of line camera was 7 µm whereas 2D camera has 20 µm pixels. The second line camera shares the same light path as 2D camera – facing light inlet facet of the beamsplitter. In order to switch light path between line camera 2 and 2D camera a flip mirror is used. While all cameras are set at 60 kHz acquisition rate, the swept source is tuned to scan across wavelengths at 8700 nm/s. A single volume acquisition speed is 8.6 ms as 512 images are obtained during 0.15 nm change between each image. Acquired images form stacks of multispectral interferometric images (xyl) are converted into 3D volumes. To reconstruct data the mean is subtracted from each A-line along l

and apodization function (Hamming window) is applied. Then by using Fast Fourier transformation (FFT) spectral image sequence is converted into depth ($\lambda \rightarrow z$). In order to remove low-frequency speckles (induced by multimode fiber illumination [53]) en-face images are spatially filtered via 2D FFT. Meanwhile, B-scan images obtained via line camera were cleaned from speckles during FFT via 1D block mask in the center. Finally, whole volumes are corrected for image sharpness by using Kurtosis (also correcting accidental sample axial motion during measurement) and corrected for chromatic dispersion iteratively.

Sensitivity

We have measured sensitivity of the system with 50/50 beamsplitter and then with 90/10 beamsplitter. However, due to variation in beamsplitter cube holders (despite using magnetic cage to ensure repeatable positioning) the beam would deviate after switching from one to another beamsplitter. This would be fixed by tilting sample and reference to avoid clipping the light from the pick-off mirror changing the OCT signal which would affect sensitivity measurement. To track the position of the beam a USB camera (Figure 3.25) was installed and used to image the pupil plane. To measure if there is any sensitivity difference using two different beamsplitter facets, 2 line cameras were used. Camera-1 (Figure 3.25) was used in regular configuration whereas camera-2 (Figure 3.25) was used to measure the port for HT configuration. The measured sensitivity for both facets (using 50/50 beamsplitter) is equal to 74 dB. This means that there is no drawbacks in terms of sensitivity to use the port of the beamsplitter for both illumination and detection. For sensitivity measurements a blazed grating (150 Grooves, 500 nm ruled diffraction grating, #64-397, Edmund Optics) was used as a sample and placed behind ND filter (3.97 OD when measured in double pass). During measurements with 50/50 beamsplitter a 0.6 OD ND filter was used to attenuate reflection to achieve shot-noise-limited operation by operating the camera close to its saturation [150].

Sensitivity was estimated using a blazing grating by fallowing a procedure described in Ref. [145]. The estimation of sensitivity consisted of considering 50 % (3 dB) reflectance of the blazed grating at 850 nm and ND filter attenuation in the sample arm (39.7 dB). The sensitivity of a single volume for standard (50/50 beamsplitter) setup was evaluated as 81.2 dB while HT (90/10 beamsplitter) reached 86 dB. HT configuration increases sensitivity by 2.8x (4.5 dB) for a single volume acquisition. However, by averaging multiple volumes sensitivity increases up to 3.5x (4.5 dB). Sensitivity growth dependence on number of averaged volumes is shown in Figure 3.26. The system is shot noise limited and sensitivity increases linearly on a linear

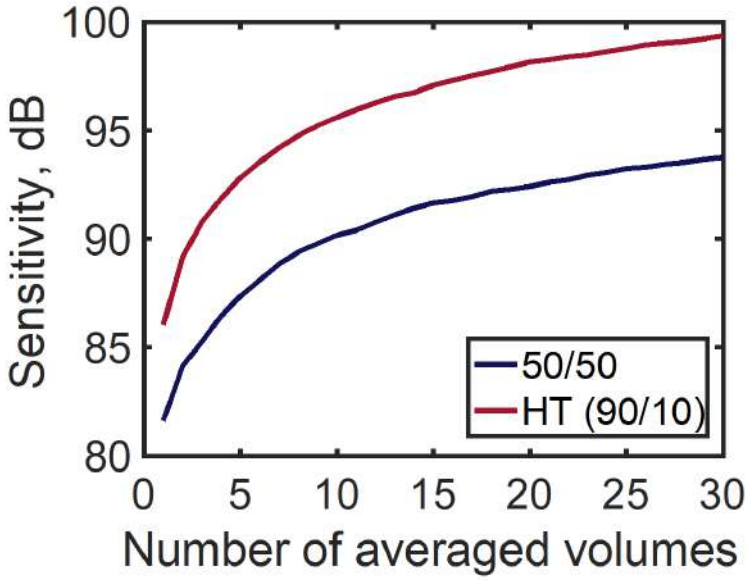


Figure 3.26: High-throughput STOC-T system demonstrates 3.5x SNR increase (∼5.4 dB sensitivity increase) over a regular STOC-T with high volume averaging.

non-logarithmic scale as in theory [141, 145]. The sensitivity measured with line camera was lower than sensitivity measured with the ultrafast 2D camera due to magnification, pixel size and integration time differences.

SNR

The SNR advantage using HT-STOC-T to image scattering samples was demonstrated by imaging a mounted USAF target behind a scattering layer (latex glove). Sample remained untouched during both standard and HT configuration measurements (USB camera was used for minor realignment). Registered volumes were converted from multispectral (xyl) to depth (xyz) images and then squared in order to make signal intensity in the images linearly proportional to the sample reflectivity which is needed to accurately measure SNR. In Figure 3.27 (a, b) we show en face (XY) images of the USAF target on the same linear scale, and in (c, d) axial images (XZ) are displayed on the same logarithmic scale. The difference of SNR between two configurations has been calculated and results in 3.2x (5.2 dB) increase when HT is used (Figure 3.27 (e)) [150] . To produce the line profile graph, whole images was summed at each layer (z). The visible signal below USAF target is produced by crosstalk of high laser coherence (even it is reduced as shown in Figure 3.25).

Finally, SNR improvement was demonstrated on retinal images acquired in vivo. For this experiment we took objective lens out and used a line camera-2 (Figure 3.25) to image retina of a healthy 46-year-old volunteer. Since camera is capable of recording for tens of seconds, beamsplitter was switched (therefore configuration was changed from regular to HT) during the retinal measurement and the imaging area was retained which led for better and objective comparison between two systems. The ultrafast 2D camera could not be used in this experiment as the whole has to be registered and only then B scan can be derived from obtained stack of images. Also, camera has only ∼3-4 second recording capacity (with internal memory of 64 GB) thus proper retinal imaging and beamsplitter switching becomes close to impossible. Volunteer's head was stationed by a chinrest mounted on a 3D positioning stage to achieve an alignment with the system. Lens L4 (in the sample arm, Figure 3.25) was adjusted axially to produce sharpest retinal images which meant successful correction of the eye's refractive error. B-scans (axial STOC-T images) obtained from the retina by a regular and HT setups and shown in Figure 3.28 on the same linear scale.

The images were produced by 20 averaged consecutive B-scans and show improved SNR when HT mode is used. For this experiment the line camera-1 could not be used in 90/10 configuration, as reflection from the beamsplitter would be 9 times stronger (9 % instead of 1 %) and a signal from the retina would be 9 times weaker. Figure 3.28 (a) and (b) only represents improved signal achieved by the HT configuration and not a total imaging potential combined with 2D ultrafast camera. Retinal cross-section images shown in Figure 3.29 are obtained via HT and 2D ultrafast camera combination. All the major retinal layers can be clearly identifiable in these images [150].

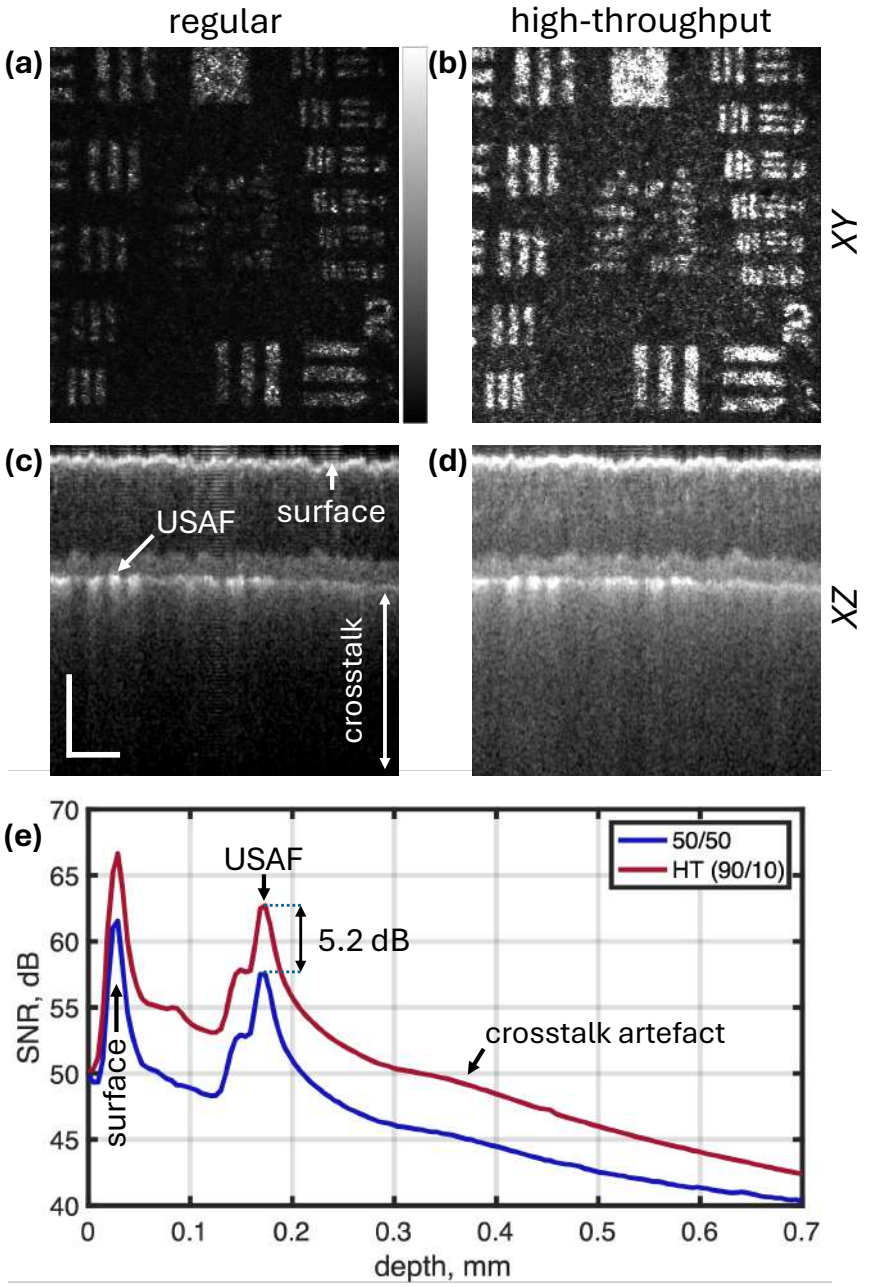


Figure 3.27: High-throughput configuration improves SNR by 3.2x (5.2 dB) as measured on a USAF target behind a scattering layer. (a, b) enface images of USAF target in regular and high throughput configurations, respectively. (c, d) axial images displayed in Logarithmic scale in regular and high throughput configurations, respectively. Signal that is depicted behind the USAF target is a crosstalk artifact. (e) depth profile of a sample derived by averaging A-scans. Scale bar XZ: 500 µm x 100 µm. XY and XZ images were derived by averaged 10 subsequent images.

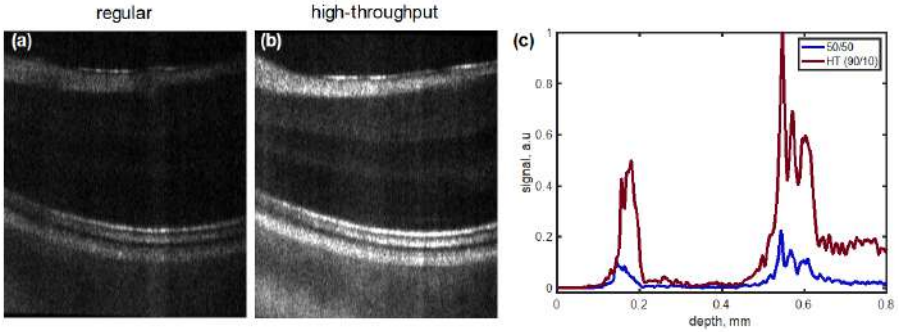


Figure 3.28: Comparison of retinal images acquired with line camera-2 in vivo in (a) regular and (b) HT modes, while (c) shows line profiles

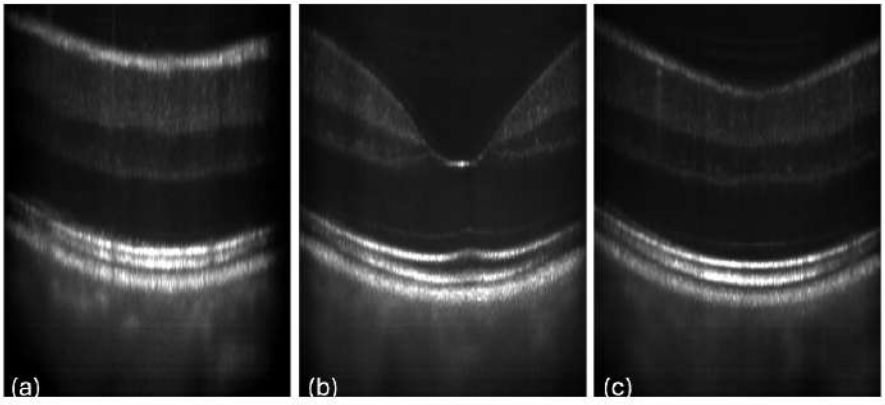


Figure 3.29: Retinal images acquired with ultrafast 2D camera in vivo in HT mode. Macula images taken from the same volume at different XZ location.

Dark field rejects autocorrelation artefacts from a coverslip

The HT scheme is more suitable to be implemented in FD-FF-OCT setups (e.g. STOC-T) because of the use of slightly spatially incoherent or completely coherent illumination which fills tiny part of the pupil plane. This enables efficient division between illumination and detection paths without discarding substantial part of the signal or illumination. Usually in FF-OCT in both illumination and detection pupil is filled fully which diminishes possible SNR advantage unless a small etendue light source is used [32]. We have used HT setup for TD-FF-OCT system with similar parameters [32] and measured x3.5 SNR increase. However, the main influencer was a pick-off mirror blocking reflection from glass window and freeing extra bandwidth for camera to detect actual signal thus improving SNR. Of course, STOC-T would benefit from dark-field effect for measuring reflective samples, but the setup would require tip-tilt stage for adjusting angle of the sample. We have then investigated dark-field effect on FD-FF-OCT imaging when biological sample is covered with a coverslip glass. A fresh, peeled and sliced cucumber, was chosen as a biological sample because of its known structure and transparency/scattering properties. The principle of dark field detection is based on the mechanical blocking of reflections that do not carry a useful signal. An opaque disc is placed in the pupil plane of the lens, which blocks directly reflected light and only lets diffused light through. This results in a higher-contrast image where fine details and structures are better seen. Figure 3.30 illustrates a portion of the STOC-T system that performs mechanical blocking of reflections in the conjugate pupil plane. For this experiment we used standard beamsplitter 50/50 configuration (Figure 3.30) to evaluate dark-field influence for autocorrelation artefact removal.

As shown in Figure 3.31, the dark field STOC-T system filters out some unwanted signals and noise. B scans (Figure 3.31 a, b) show that the reflections from coverslip glass introduces artefacts which are filtered with dark-field mask. Figure 3.31 c, d shows increased contrast in cellular details while Figures 3.31. e, f show cleaned-up coherence artefacts forming behind imaging sample.

As we can see, dark-field plays a strong role in eliminating autocorelation artefacts from reflective surfaces. HT-STOC-T incorporates this effect in some extent by having pick-off mirror in pupil plane. As mentioned previously, in order to have full control and efficiency, a Tip-Tilt stage should be integrated into the head mount for maximum reflection removal in retinal imaging. However, current setup is sufficient and reflection artefacts do not compromise final image.

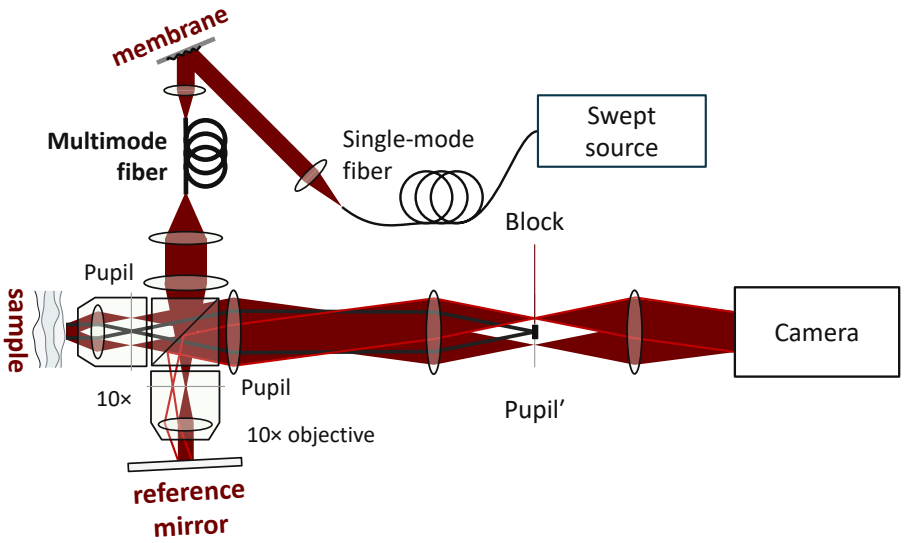


Figure 3.30: Dark-field STOC-T system for autocorrelation artefact removal showing insertable block in the pupil plane.

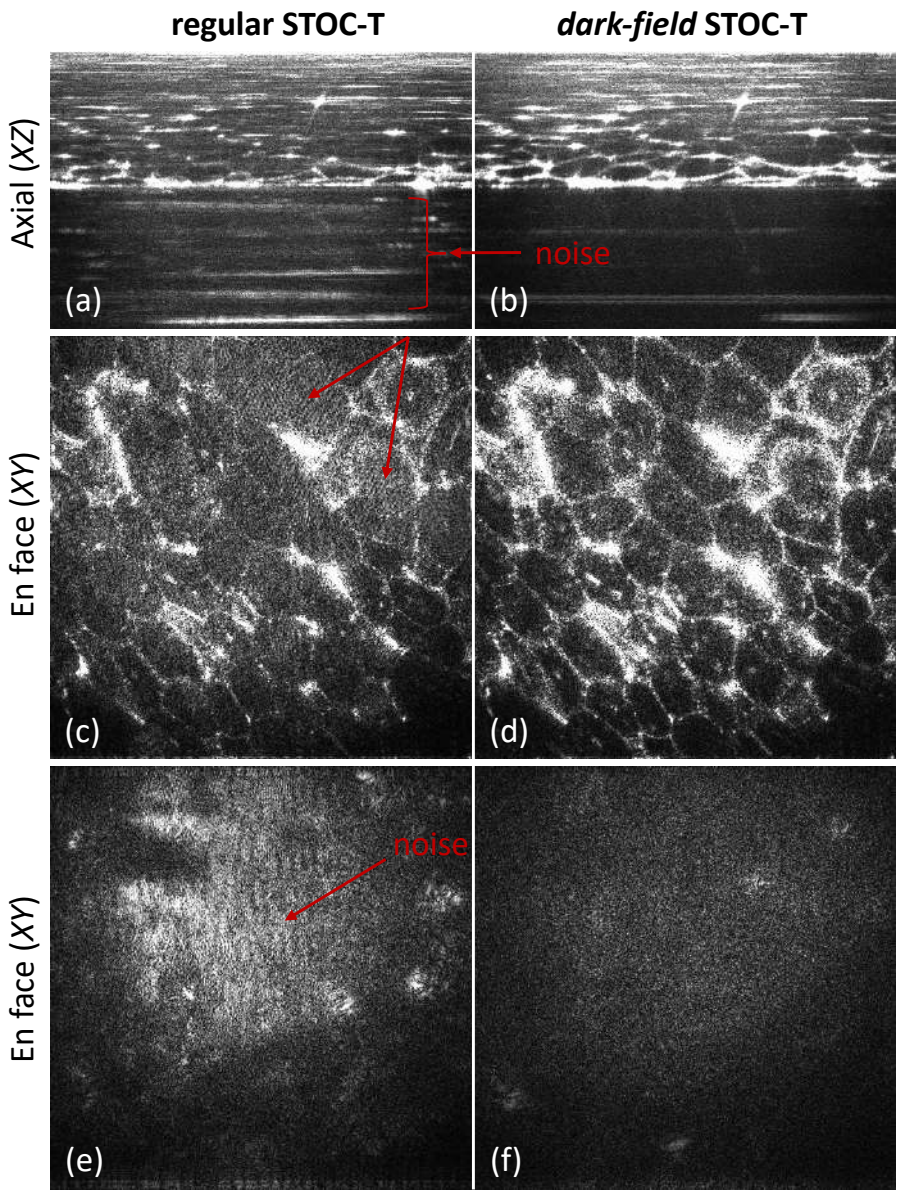


Figure 3.31: Cell images recorded with the conventional and dark-field STOC-T system. Axial image (a) shows reflection artefacts produced by cover glass, which are also visible in XY plane (c, e). The dark field STOC-T system is able to get rid most of the autocorelation artefacts (b, d, f) as shown by the red arrows.

The described high-throughput (HT) STOC-T setup reaches up to 3.5x (5.4 dB) increase in sensitivity after averaging 30 volumes. This improvement is achieved not only by changing beamsplitter and choosing another detection path by using pick-off mirror but also taking into account minor but very important details and adjustments of the system which led to minimize back-reflections (discussed in technical description part). Since reference signal is only 1 % any undesired reflection of similar magnitude would peril sensitivity. Thus, we have reduced residual reflections to less than 0.1 %. The achieved increased sensitivity graphs in Figure 3.26 compared to the sensitivity-optimized system in Ref. [145] show the superiority of the HT setup over a regular one. We have reached sensitivity of nearly 100 dB by averaging 30 volumes (equal to 0.3 seconds of acquisition time) which exceeds that reported in Ref. [145] and, as we are aware, suggests the highest sensitivity reported in the literature for FF-OCT. The selected beamsplitter ratio (90/10) optimizes SNR imaging low-reflective samples such as retina. In such case it is worth to prioritize delivering light to the sample arm while reduced light coming from reference arm less critical. However, further minimization of light coming from reference arm would cause an increase in autocorrelation noise thus increasing asymmetry of the beamsplitter diverges from ideal configuration to reach maximum SNR.

Overall, HT improves FD-FF-OCT usability for medical and research applications. By increasing obtained light from the sample a low-powered light source can be used to reduce phototoxicity risk, especially critical in ophthalmology. Furthermore, by increasing sensitivity, images can be registered with less averaging which minimizes motion artifacts during in vivo measurements.

4. TIME DOMAIN OCT

4.1. Time-domain full-field optical coherence tomography with a digital defocus correction

Time-domain full-field optical coherence tomography (TD-FF-OCT) is an interferometric technique used to obtain high-resolution biomedical images. By using temporally and spatially incoherent light source images can be acquired from deep tissue layers. However, image degrades when defocus or other optical aberrations are present, especially in deeper layers. We have implemented digital focus correction which is possible when both signal and reference arm lengths are matched. Defocus correction can be applied both on scattering and reflective samples and defocus compensation can be achieved up to 1mm.

While FD-FF-OCT with swept-source laser provides fast imaging method, it has reduced lateral resolution due to underfilling illumination pupil, low numerical aperture (NA) objective and coherence noise which is produced by spatially coherent laser. Moreover, phase stability of swept source enables efficient computational aberration correction [36, 151] which is greatly reduced in scanning confocal OCT systems [152, 153]. By reducing spatial coherence of swept source [49], coherence noise (cross talk) can be attenuated while maintaining aberration correction [90]. However, by using fully spatially incoherent light source in Time Domain (TD) FF-OCT produced images achieve higher resolution. This allows using cheaper light source in exchange of the need of axial sample scanning which increases data acquisition time [23]. Although TD-FF-OCT cannot computationally compensate for chromatic dispersion between sample arm and reference, since obtained signal is complex (has both amplitude and phase information), it is possible to computationally correct for the blur due to confocal and coherence gate separation [154] caused by refractive index mismatches between thick sample and reference mirror in air. Even though, manual correction of the sample in TD-FF-OCT is usually possible, it is often inconvenient or, especially, in retinal imaging may not be possible. Such scenario asks for computational aberration correction.

A TD-FF-OCT system was built to demonstrate digital aberration correction. As illumination source An incoherent white LED (MNWHL4, Thorlabs) was used. Setup was based on Linnik interferometer which had a pair of identical dry-immersion 10x microscope objectives ($NA = 0.25$, Plan N, Olympus). Illumination was directed onto the he objectives' pupil planes using lenses in 4f configuration (Figure 4.1). Standard 50:50 beamsplitter was used to split light into sample and reference arms. Returning light from sample and reference arms were combined with the same beamsplitter and registered via 1440x1440 pixel (pixel size 12 µm) CMOS camera (Q-2HFW-CXP, Adimec).

A composition of 2 achromatic lenses (f = 75 cm) in Plösl configuration was used as a tube lens (f = 37.5cm), which resulted in 20.8 times magnification while sample was sampled every 0.576 µm. Both sample arm and reference arm were equipped with stepper motors (T-NA08A25-S, Zaber). This enabled sample axial scanning and moving whole reference arm (green in Figure 4.1). By reducing optical path difference between sample and reference to temporal coherence length, the interference pattern was obtained via camera. To even out signal and reference power, a 0.6 OD neutral density (ND) filter was inserted into reference arm resulting of 6 % of returning signal. To compensate for chromatic dispersion, 0 OD but the same thickness ND filter was inserted into sample arm. Phaseshifting was implemented by mounting a piezo element (STr-25, Piezomechanik) on the reference mirror holder [155].

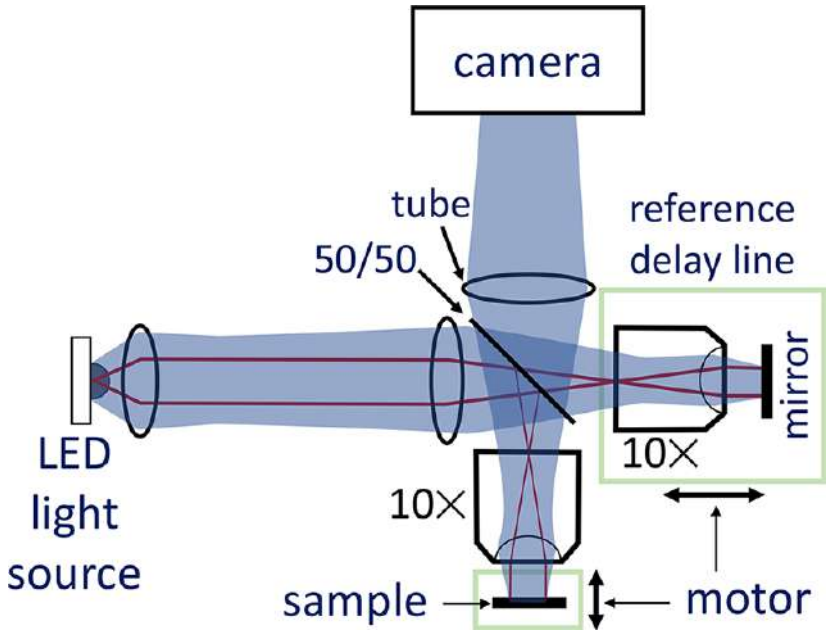


Figure 4.1: Principal scheme of the FF-OCT system. Dark blue represents the spatially incoherent LED illumination path, red—spatially coherent laser. Green boxes indicate translation stages equipped with stepping motors.

Method

To reconstruct a TD-FF-OCT amplitude image A from registered phase-shifted images formula

$$A = \sqrt{(I_3 - I_1)^2 + (I_4 - I_2)^2} \tag{4.1}$$

is used, where I_1, I_2, I_3, I_4 are 4 raw images obtained at 0°, 90°, 180° and 270° phase shifts which were done by piezo element in the reference arm. These raw images could be used to calculate [156] the phase image

$$\phi = arctan\frac{(I_4 - I_2)}{(I_3 - I_1)}. \tag{4.2}$$

In order to do digital refocusing a 2D Fourier transformation in transverse plane is made on a complex TD-FF-OCT image $\bar{A} = Ae^{-i\phi}$ and complex field in the pupil plane is obtained. Then it is multiplied by quadratic phase distortion function $e^{-i\Delta l(f_x^2+f_y^2)}$ where delta l is the defocus-phase coefficient, f_x and f_y are spatial frequencies. Then refocus TD-FF-OCT image $\bar{A}_{refoc}$ is calculated by applying inverse Fourier transformation of the pupil plane

$$\bar{A}_{refoc} = FFT^{-1}\{FFT(\bar{A})e^{-i\Delta l(f_x^2+f_y^2)}\} \tag{4.3}$$

The most in focus image was selected by visual inspection from a range of delta l values.

The benefit of such selection method is that neither plane location or any other parameter is not needed to find correct Δl value.

Experiment

It was noticed that by defocusing sample an optical path length mismatch between sample and reference arms is introduced which results in loss of signal. To overcome this issue, whole reference arm reference optical distance has to be matched. It was found that whole reference arm (not only mirror but also objective) has to be translated for defocus compensation. To demonstrate defocus correction, a high-resolution U.S. Air Force (USAF) resolution test chart (Highres-2, Newport) was used. Here defocus correction was done up to 1mm of defocus. Figure 4.2 shows conventional microscopy (bright-field) images recorded by blocking the reference arm and FF-OCT images recorded at various defocus values as well as their refocused counterparts. First, one can see that FF-OCT images are already less sensitive to defocus compared to the conventional bright-field images shown in Figures 4.2 a–d, which has been pointed out before in the literature[8]. Even FF-OCT becomes blurry with larger defocus values as shown in Figures 4.2 e–h. Finally, computational defocus correction can be used to refocus FF-OCT images as shown in Figures 4.2 i–l.

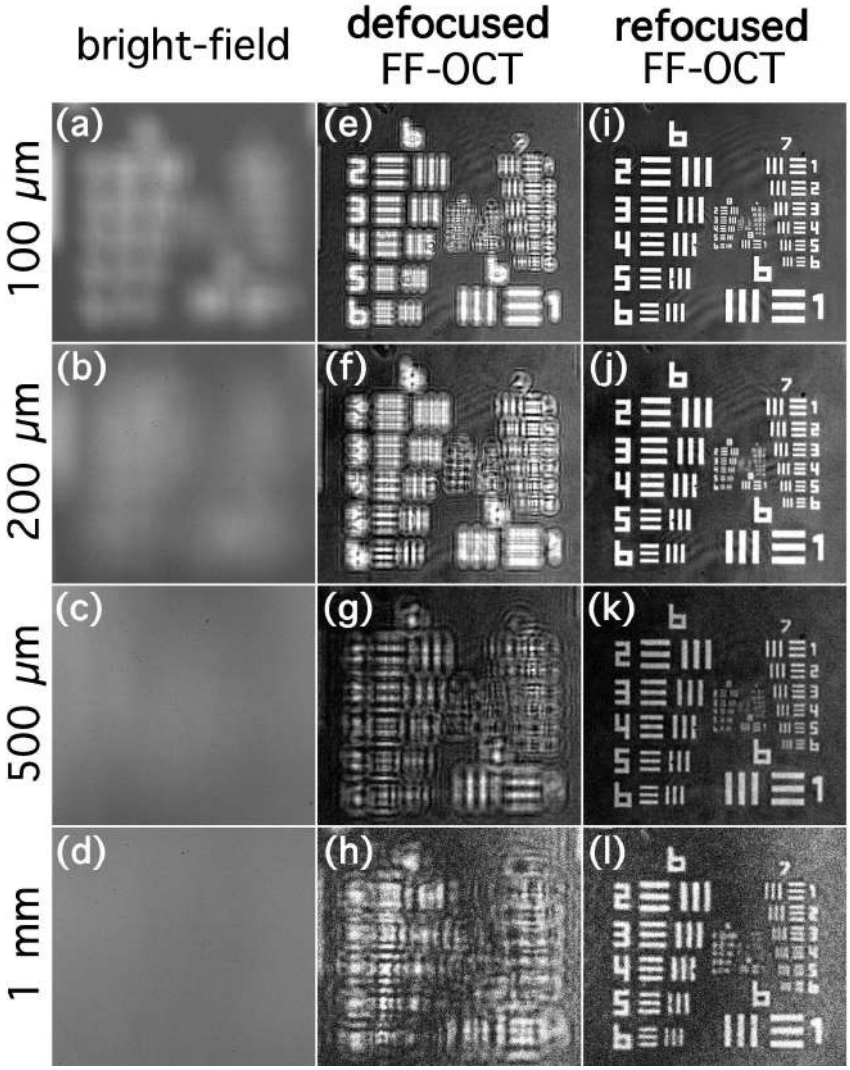


Figure 4.2: Demonstration of digital defocus correction of FF-OCT images of USAF target recorded at progressively increasing defocus values of 100 µm, 200 µm, 500 µm and 1 mm. (a–d) conventional bright-field images recorded with blocked reference arm. (e–h) FF-OCT images. (i–l) defocus-corrected FF-OCT images.

A dimensionless optical coordinate unit $u = 4kznsin^2(\frac{\alpha}{2})$ was used to avoid dependence of NA of the objective and wavelength, where k is the wave vector, z is the distance along the optical axis, n is the refractive index of sample medium, and a is the semi-angle of the light cone forming the focus. Measured depth of field is 10 µm (u = 6.76) which is 100 smaller than defocus of 1 mm (u = 676.4).

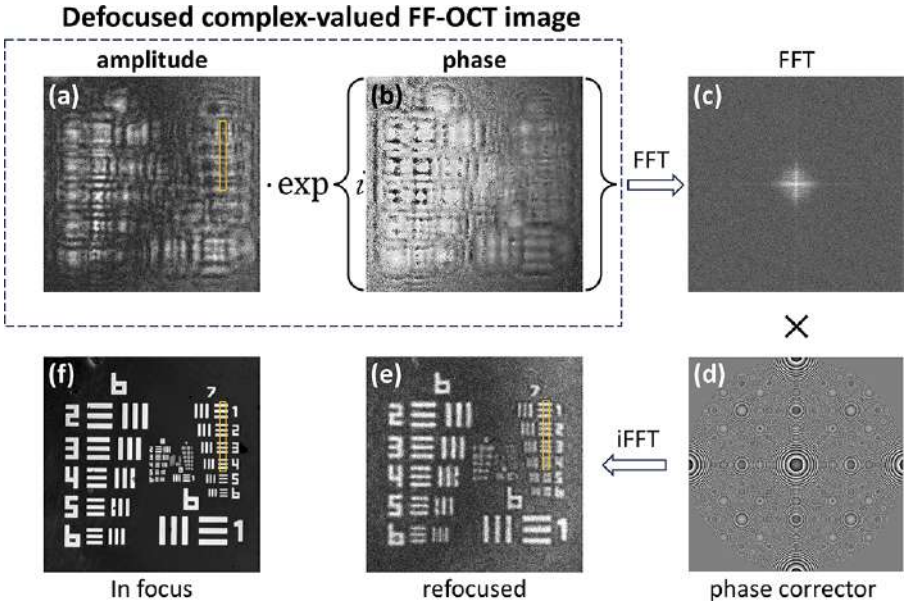


Figure 4.3: Digital defocus correction of a complex-valued TD-FF-OCT image of the USAF target defocused by 1mm (u = 676.4). The complex-valued signal, consisting of amplitude (a) and phase (b), is Fourier-transformed (c), then multiplied by a quadratic phase function (d), and subsequently inverse Fourier-transformed, resulting in a refocused image (e). An in-focus image is provided in (f) for comparison.

Figure 4.3 (a) shows that by manually defocusing sample bars become too blurred to be individually identifiable. As shown in Figure 4.3 (e), by applying digital defocus correction image can be restored back in-focus. However, compared to focused image (Figure 4.3 (f)), spatial resolution of refocused image is reduced. In order to find out how defocusing sample manually and refocusing digitally affects spatial resolution, line profiles over the 1–4 elements in group number 7 of USAF bars (Figure 4.2) were derived for in-focus, defocused and refocused images (Figure 4.3).

The refocused bars of group 7 element 4 (181 lines/mm (l pm) corresponding to spatial frequency of 0.181 μm^{-1}) are almost irresolvable which is seen not only in Figure 4.3 (e) but also in Figure 4.4 (a) line profiles. Meanwhile, neither defocused images nor line profiles of this group are resolvable. Figure 4.4 (b) shows the change of spatial frequencies dependence on image refocusing depth [155].

To create graph shown in Figure 4.4 (b) both defocused and refocused images were Fourier-transformed and rotational averaging applied in Fourier space. Then the Fourier spectrum of refocused image was divided by Fourier spectrum of the defocused image. It was done at 3 different defocus depths: 100, 500, and 1000 µm. The fallowing values of highest recoverable spatial

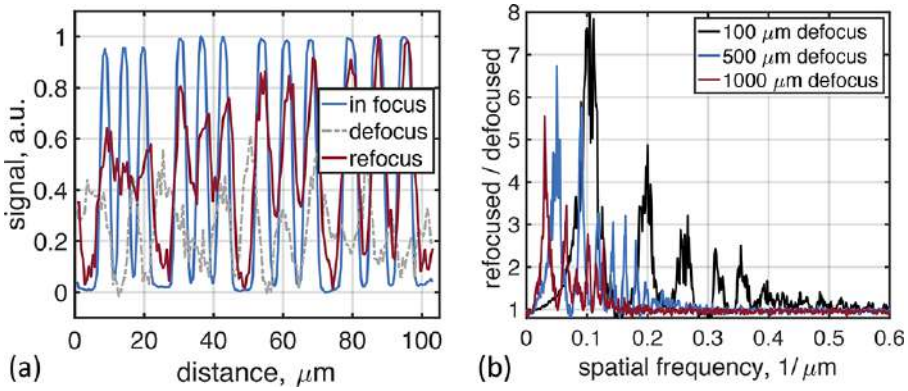


Figure 4.4: (a) Line profiles derived over the bars in elements 1–4, group number 7 (demarcated by yellow box), for in focus, defocused, and refocused images, shown in Figure 4.3 (b) Ratio (refocused/defocused) of spatial frequencies at three different defocus values: 100 µm (u = 67.6), 500 µm (u = 338.2), and 1000 µm (u = 676.4).

frequencies are 0.55 μm^{-1} for 100 µm defocus, 0.25 μm^{-1} for the 500 µm defocus and 0.15 µ m^{-1} for the 1000 *micro*m defocus, which is close to previously evaluated smallest recoverable 0.181 µ m^{-1} for the 1000 µm defocus from the image. Moreover, not only higher spatial frequencies decay after refocusing but signal deteriorates too.

Such degradation is caused by fringe contrast reduction due to reference arm translation to compensate the induced defocus. Even though optical paths are matched, high defocus values introduce differences in optical fields. In order to investigate changes in defocused FF-OCT signal two stepper motors for both sample and reference arms were used. For each sample position, whole reference arm (mirror+objective) was translated in the same axial direction by the same size steps in the range from -1 to 1 mm for each defocus value. TD-FF-OCT images were calculated at each defocus position and a line profile was taken along the axial direction of the image stack. Three different samples were used in this experiment (Figure 4.5 (a)): one reflective (USAF) and two scattering samples (used in Figures 4.5 and 4.9).

For Digital refocusing the Fresnel propagator: $exp(-j\pi\lambda\Delta z[f_x^2 + f_y^2])$ was used. While sample was defocused by Δz, digital refocus had to be calculated using a value of $\Delta z/2$ when LED was used as illumination source. This phenomena was studied by applying two layers of scotch tape on the USAF target and using this sample with both illumination sources: spatially coherent SLD (SLD850S-A20W, Thorlabs) and LED (M850L3, Thorlabs). Both sources had central wavelength at 850 nm and were filtered with the same spectral bandwidth filter resulting 10 nm bandwidth. When laser is used as source of illumination, induced physical defocus Δz need digital refocus propagation of

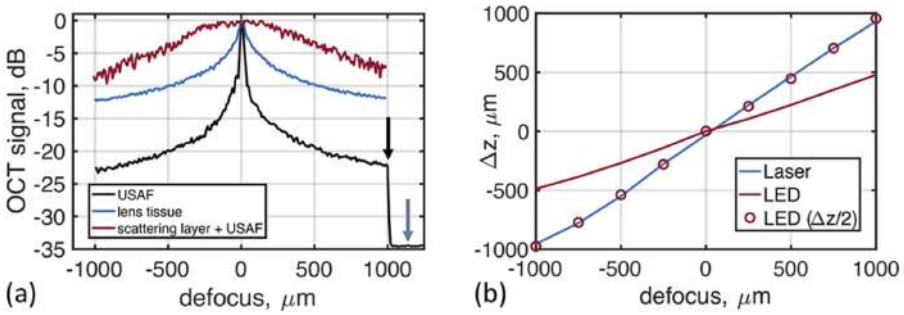


Figure 4.5: (a) FF-OCT signal as a function of sample defocus for three different samples (reflective, scattering and highly scattering). Black arrow indicates a position where the reference motor was stopped in order to deliberately mismatch the optical path length of the reference and sample arms. Blue arrow shows the signal background appearing from the mismatch. (b) Digital refocusing as a function of physical defocusing using LED and laser illumination.

Δz as well. However, when LED is used as illumination source, for the same physical defocus Δz only a half ($\Delta z/2$) of digital propagation is needed for refocusing (Figure 4.5 (b)). These results were double-checked by calculating the standard deviation value on all the pixels in the image as the image sharpness metric and could be explained by difference in PSF (point spread function) for coherent and incoherent light [157].

Two different scattering samples were made for digital refocusing capability demonstration. First sample was a folded lens tissue (MC-5, Thorlabs) behind a highly scattering media. The second sample was USAF target (R1DS1P, Thorlabs) which was also place behind the a strong scatterer. A combination of LED (M625L4, Thorlabs) and $NA = 0.3$ water-immersion objective (UMPLFLN10XW, Olympus) with $f = 18$ cm tube lens (SWTLU-C, Olympus) was used for imaging the first sample. Figure 4.6 shows images of a sample 100 µm below the surface. Sample was defocused by 500 µm. To compensate for the change of optical paths, the reference arm was translated too [155]. However, since silicone oil was used as an immersion medium for the sample, reference arm had to be translated by n x 500 µm, where n is the refractive index of the silicone oil. Obtained defocused image shown in Figure 4.6 (b) is blurred and the most of tissue strands is indistinguishable. However, by applying digital defocus correction those fibers become visible again (Figure 4.6 (c)). As expected from previous results, image is not completely restorable and higher spatial frequencies are lost (Figure 4.6 (d)).

The digital aberration correction scheme is shown in Figure 4.7, using a pair of defocused nanoparticles as an example. The procedure does not require the knowledge of the focal plane location or the refractive index change in the

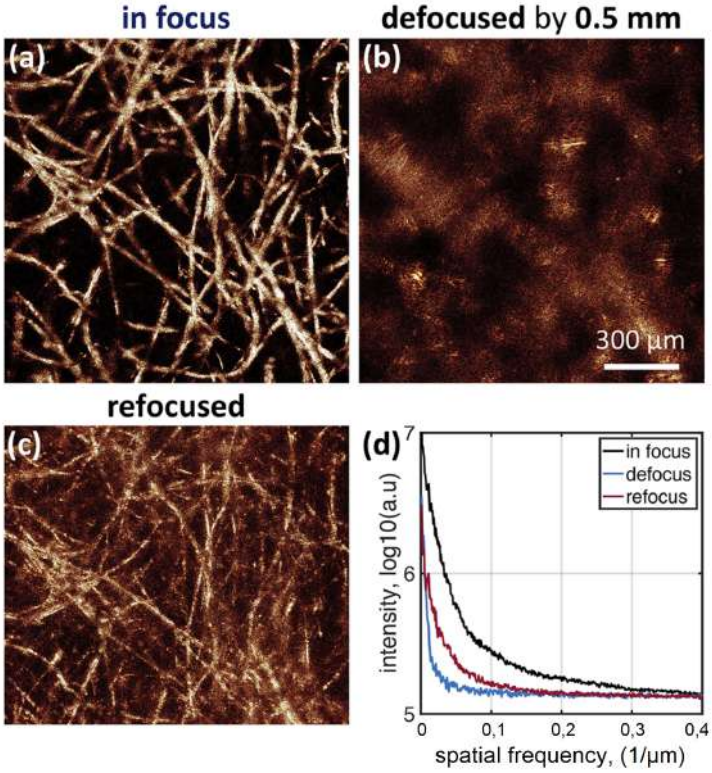


Figure 4.6: Digital defocus correction of FF-OCT images acquired 100 µm beneath the lens' tissue surface. (a) In-focus FF-OCT image, (b) FF-OCT image physically defocused by 500 µm. (c) Digitally refocused FF-OCT image. (d) Spatial frequency spectra for three images displayed in (a), (b) and (c). The images are normalized, whereas curves in (d) are produced from (non-normalized) FF-OCT images.

sample, or any other system parameter. The figure demonstrates how the two severely defocused nanoparticles can be resolved after digital defocus correction using Equation 4.3. It also illustrates that phase is recorded together with the amplitude which gives rise to a complex-valued FF-OCT. The line profiles taken along the same pixels in defocused and refocused images of the nanoparticles show dramatic signal increase.

Another experiment was made to demonstrate digital defocus correction for point-like objects. It was tested on a low-scattering phantom consisting of sub-diffraction FeO nanoparticles suspended in a transparent matrix of polyurethane. The magnification was doubled by replacing the tube lens with two achromatic lenses arranged in Plosl configuration to give the focal length $f = 37.5$ cm (instead of the original 18 cm). Viscous silicone oil was used as an immersion medium to ensure that any unintentional floaters in the immer-

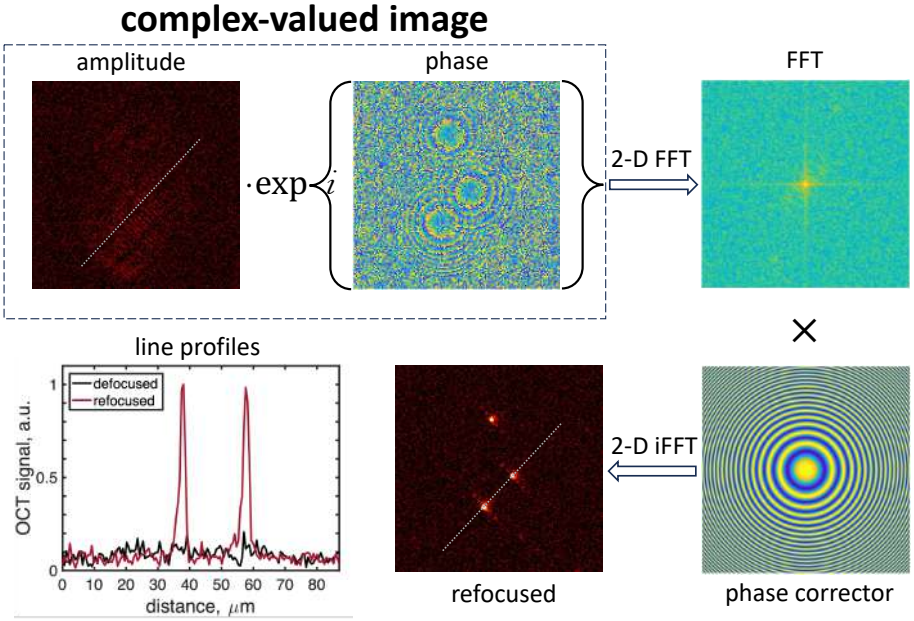


Figure 4.7: Digital defocus correction using complex-valued FF-OCT signal and quadratic phase function on sub-diffraction FeO nanoparticles. The complex-valued signal is Fourier-transformed and multiplied by a quadratic phase function (phase corrector) and then inverse Fourier-transformed, which results in a refocused image when a phase corrector is used. An image quality metric was used to find the optimal phase corrector.

sion medium will be slowed down and, therefore, will not generate significant image artifacts. Figure 4.8 (a) shows an en face FF-OCT image of nanoparticles recorded 1.5 mm away from the surface of the sample. The image shows significant blurring that visually looks like defocus. However, the blur appears not because of defocusing of the sample but because of the refractive index mismatch between the immersion medium and the sample, which causes the focal and coherence planes to separate. 'Coherence plane' can be defined as a plane inside a sample that is at the same optical distance from a camera as the reference mirror. When imaging inside a sample that has different refractive index (n_1) than immersion medium (n_2), the focal plane shifts forward by z n_1/n_2 and the coherence plane and backward by z n_2/n_1 , where z is distance from sample surface [156].To realign the planes one can move the delay line in the reference arm [158].

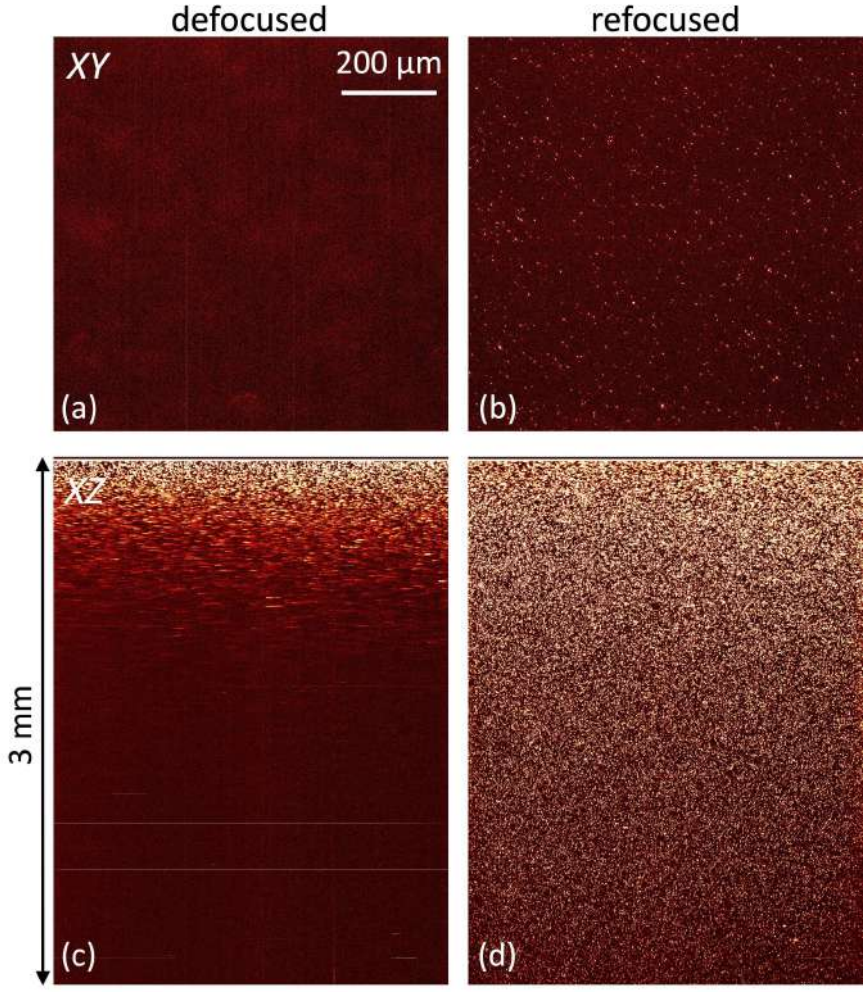


Figure 4.8: Blurred (a, c) and digitally refocused (b, d) FF-OCT images of FeO nanoparticles embedded in polyurethane. (a, b) enface FF-OCT and (c, d) axial (B-scan) images derived from acquired stack of images. (a) en face FF-OCT images recorded at the depth of 1.5 mm featuring a severely blurred image of nanoparticles, which is corrected in (b). (c) axial (XZ) image of nanoparticles showing in-focus nanoparticles at the top of the image and progressively defocused nanoparticles below that are corrected in (d). XY (en face) and XZ (axial) images were derived by maximum projection of 30 and 1,440 adjacent images, respectively.

However, it is possible to try to correct for the blur computationally using the same Equation 4.3 as in the previous two examples [155]. The difference, however, is that the correction coefficient z will vary for each plane. This is because the sample does not scatter light strongly; therefore, we can image deeper over a couple of millimeters which causes significant refractive index

mismatch changes and, hence, increasingly stronger blur. Thus, the amount of blur will change as a function of depth, requiring that the correction coefficient z in Equation 4.3 be adjusted for each plane separately when a stack of images is acquired at different axial positions. To this end, we automated the process of finding optimal z for each plane by estimating image quality for a broad range of z values. We chose the standard deviation of all the pixels in the image as the image quality metric.

Figure 4.8 (b) shows an en face FF-OCT image of nanoparticles after digital refocusing the defocused image shown in Figure 4.8 (a). Axial images, shown in Figures 4.8 (c and d), were derived by performing the maximum projection of the whole stack of 1,440 images before and after refocusing. One can notice a clear limitation of the imaging depth in Figure 4.8 (c) due to the nanoparticles appearing so defocused that it results in almost homogeneous background beyond 1 mm depth. Therefore, digital aberration correction extends the usable imaging depth and produces a sharp image of nanoparticles that were previously submerged in noise.

Last experiment was conducted to demonstrate advantage of a LED over a spatially coherent laser in the FF-OCT. Sample used was USAF target behind 400 µm scattering medium. First, as illumination source LED was used in combination of microscope objective and tube lens. Imaged in-focus USAF target is visible with some artefacts due to thick scatterer (Figure 4.9 (a)). However using laser as illumination source in the same conditions reveal only cross-talk noise which eradicates FF-OCT signal (Figure 4.9 (b)). By physically defocusing sample (lit by LED) by 1 mm we lose all distinguishable features (Figure 4.9 (c)). However, after applying digital decofus correction, while USAF target becomes visible again, images is degraded and lost smaller features (Figure 4.9 (d)). The deterioration of spatial frequencies after refocusing is shown in graphs in Figures 4.9 (e) and (f). Refocusing recovered spatial frequencies below approximately $\sim 0.03 \mu m^{-1}$ higher frequencies were not recovered and were lower than imaged USAF target without scattering media because resolution and contrast is suppressed by multiply scattered photons.

By physically defocusing and digitally defocusing it was noticed the decrease of the signal attenuation by increasing sample scattering. While typically multiply scattered photons are considered as a negative aspect to OCT signal, in these experiment they provided a benefit [159]. Comparing lost signal by manually defocusing sample and then digitally refocusing it was noticed that imaged USAF target without any scatterer suffered 20 dB loss of the signal after refocusing, lens tissue sample lost 10 dB and USAF target put behind 400 µm thickness scatterer lost only 5 dB of the signal. This suggests that multiply scattered photons in the media carry OCT signal. The temporal delay of these photons is shorter than the coherence time of the illumination source which leads to contribution to the FF-OCT signal [158].

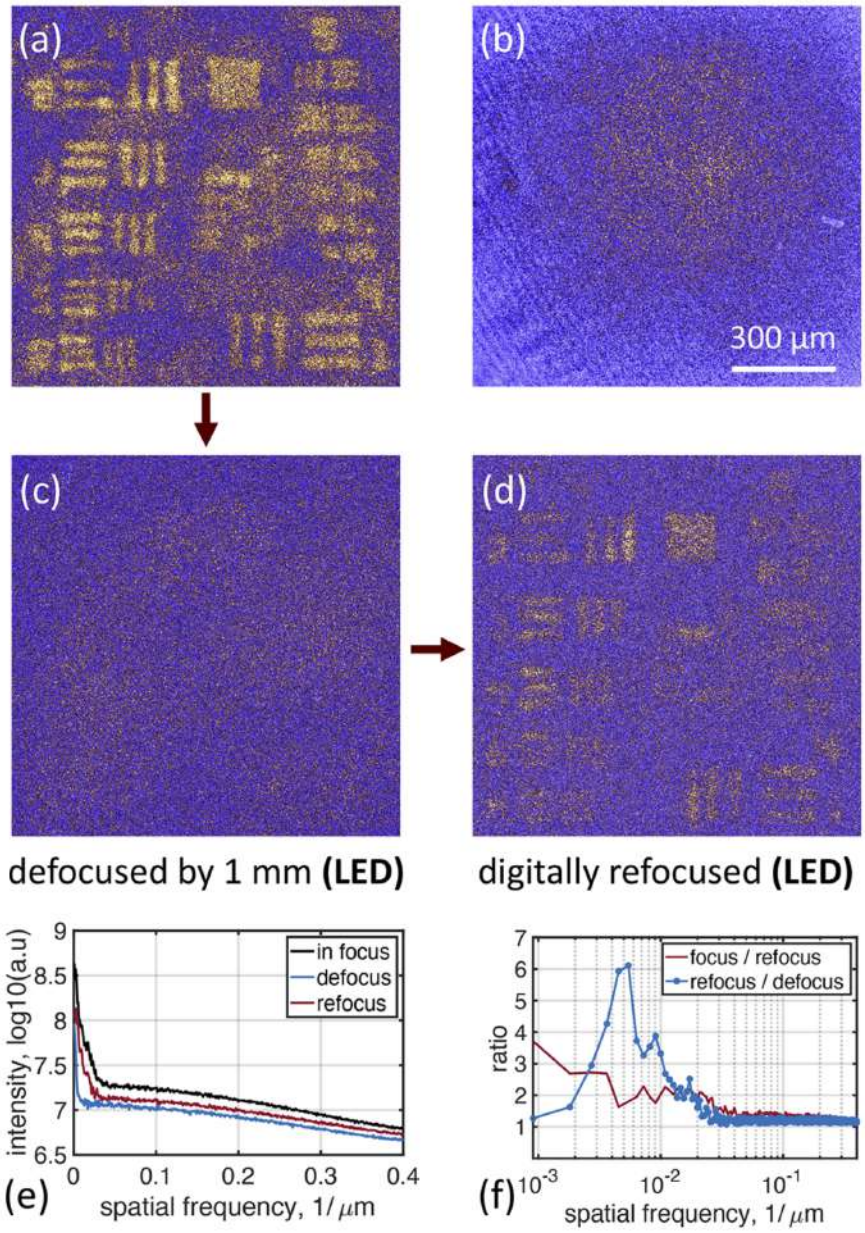


Figure 4.9: Digital defocus correction in FF-OCT imaging through highly scattering media: a demonstration using a USAF target beneath 400 µm of a scattering material. (a) In-focus image of the USAF target. (b) Same image as in (a) but acquired with a laser. (c) USAF target image defocused by 1 mm. (d) Computationally refocused defocused USAF target. (e) Spatial frequency plots for the USAF target's in-focus, defocused, and refocused images. (f) Ratio plots of normalized spatial frequencies.

Overall, these experiments demonstrated that phase stability of the complex-valued TD-FF-OCT signal allows strongly defocused images to be digitally refocused, provided that the optical path lengths of the sample and reference arms are re-matched after the sample is physically defocused. Digital refocusing has shown that the usable imaging depth could be extended to 500–1000 µm, about two orders of magnitude beyond the 10 µm physical depth of focus of the imaging objective. It was done on both reflective (USAF target) and scattering (paper tissue, nanoparticle sample) samples. The correction was found to depend on the coherence of the illumination source: only a spatially incoherent LED illumination allows usable digital refocusing through strongly scattering media compared to coherent laser illumination which is dominated by cross-talk noise and defocus correction is unusable. Refocused images lost signal value by roughly 20 dB in free space and up to 5 dB behind a 400 µm -thick scattering layer. High spatial frequencies (above ≈ 0.15–0.55 µm$^{-}1$, depending on defocus depth) were not recoverable which suggests that multiply scattered photons within the coherence gate contribute usefully to the refocused signal. In conclusion, these results are particularly significant because they remove the need for mechanical refocusing or repeated sample re-scanning when imaging through scattering media. This is especially important for imaging deep or heterogeneous tissue where manual refocusing is difficult or impractical. This method is also applicable to in vivo retinal imaging, where physical refocusing is difficult.

4.2. Time-Domain Full-Field Confocal Optical Coherence Tomography with Digital Scanning

Optical coherence tomography can be split into scanning and Full-field OCT. Full-Field OCT without the need of transverse scanning quickly obtains high resolution images via 2D detectors, such as CMOS cameras and is optimal of in vivo en face retinal imaging. However, the main drawback of such systems is the lack of confocal gating thus shallower imaging depth and reduced sensitivity is observed. Confocal gating reduces the incoherent signals that reach the detector and worsens signal to noise ratio (SNR) [33]. The sensitivity of FF-OCT system can be increased by using dark-field detection [31, 32] which rejects specular reflections but multiply scattered light is still left unfiltered. Confocal scanning OCT can be sped up by increasing the number of scanning spots on the sample [160, 161]. One of traditional approach to achieve fast parallelization is to use Nipkow disk for illumination and a camera instead of light sensor for detection thus achieving 1 kHz confocal imaging rate [162]. This can be applied to interferometric imaging [163]. Another way of parallelization is to implement Digital micromirror devices (DMDs).

DMD

DMDs (Figure 4.10) are flexible and accessible tools that are able to generate arbitrary illumination patterns, such as multiple spots [164] and are used in confocal microscopy both for illumination and detection using individual mirrors as pinholes for confocal effects [165, 166].

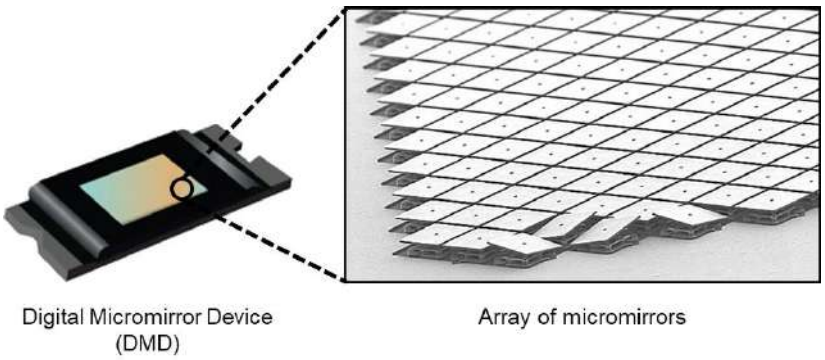


Figure 4.10: Digital Micromirror Device consists of an array of individually addressable mirrors [167].

The Digital micromirror device (DMD) is a part of devices known as micro electromechanical systems (MEMS) and work as a light switch (Figure 4.11). Accelerometers, pressure sensors, and micro-actuators also belong to MEMS. The DMD is monotonically created during CMOS-like processes on a CMOS

memory. Every "pixel" is a light switch made as an aluminum mirror, (a few micrometer size) which reflects light in one of two directions. The direction depends on the memory state. By introducing voltage difference between the mirror and the memory cell, electrostatic force enables mirror rotation [168]. Typical rotation of the mirror is +/-10 degrees. Image shows micromirror device in detail. DMD usually come in a large number pixel array and provide high modulation speed (typically several tens of kHz). DMDs are used in real-time applications, such as for high-resolution microscopy where illumination shaping and scanning is required [169]. DMD combined with camera using rolling shutter was used to obtain OCT images previously [33]. Comparable DMD use for line sectioning was later demonstrated in Flood-Illumination Ophthalmoscope [170]. Similarly to DMD line scanning, illumination line scanning combined with camera in rolling shutter mode was later applied in Adaptive Optics Rolling Slit Ophthalmoscope for phase contrast imaging [171].

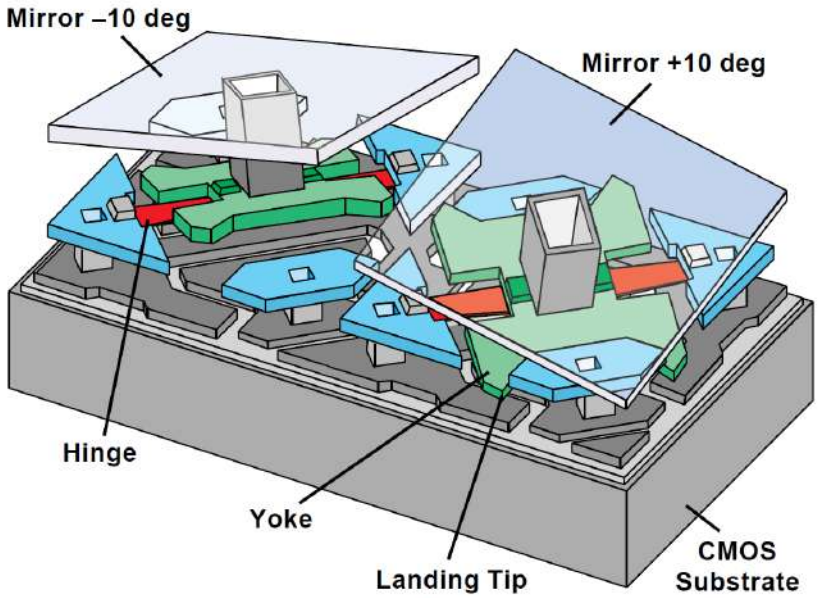


Figure 4.11: Two DMD pixels (mirrors are displayed as transparent) shown in detail in "on" and "off" positions simultaneously [168].

DMD can activate every N^{th} micromirror to generate multiple spots thus enabling scanning by displaying N^2 DMD patterns per camera frame, totaling N^2 patterns. This technique is popular in fluorescence confocal microscopy, but imaging weakly reflective images in reflectance configuration is challenging. Fluorescence imaging can easily solve the main DMD problem – backscattering from DMD itself [172]. It is done by using spectral filters. However, there is

no such option in reflectance microscopy. This is still applicable for highly reflective samples [165, 173, 174] as the signal from the surface is stronger than backscattered noise. On the other hand, the use back-reflections from the DMD add shot noise which can bury low reflected details in the image.

Setup

We have constructed Full Field OCT system with confocal optical sectioning which uses DMD by creating one array of confocal illumination spots and another array confocal pinholes which rejects light coming out of focal plane. DMD is used in double pass [175] configuration but both illumination and detection paths are split onto different halves of the DMD chip where illumination spots and pinholes [176] are generated. The utilization of DMD in regular double-pass setup for FF-OCT is limited due to backreflected and scattered light coming from sub-structure of the micromirrors is stronger than obtained light from sample itself. This leads to lack of utilization of DMD as a convenient spatial light modulator for FF-OCT systems. However, we have found and patented [177] a way to go around such limitation and separate confocal illumination and spatially filter registered signal. Our patented invention shown in Figure 4.12 is described as reflective confocal microscope which uses a DMD with a divided working area: one sub area used for sample illumination, another dedicated for signal detection.

The patented confocal microscope setup was transformed into FF-OCT microscopy system (Figure 4.13) which enabled to examine it's benefits further. The setup is built around Linnik interferometer which uses two identical objective lenses (10×/0.25, Plan N, Olympus, Tokyo, Japan) for sample and reference arms achieving 1.6 µm lateral resolution. A DMD – digital micromirror device (V-7001, Vialux, Chemnitz, Germany) is used to create illumination and detection patterns. The DMD is made of individually addressable 13.7 µm × 13.7 µm micromirrors in 1024x768 array. The micromirrors can flip at 22.7 kHz rate (dead time 44 µs) between "on" (+12°) and "off" (-12°) positions and produce controlled illumination pattern. Due to flipping axis of micromirrors, the DMD is mounted at a 45° angle relative to the optical table in order to have both illumination beam and reflected light pass parallel to the table. As a light source, a 660 nm LED (M660L4, Thorlabs, Mölndal, Sweden) is used with a spectral bandwidth of 20 nm (FWHM). In order to achieve even illumination on the DMD surface and reduce scattered light in the system a Köhler illumination configuration was built (not shown in Figure 4.13). In FF-OCT such configuration significantly increases signal-to-noise ratio. By determining temporal coherence (using relation $\Delta z = (2ln2/\pi)\lambda_0^2/\Delta\lambda \approx 9.6\mu m$ in air) gating we have estimated it to be 9.6 µm.

Illumination light is incident on the DMD at a 24° angle relative to its

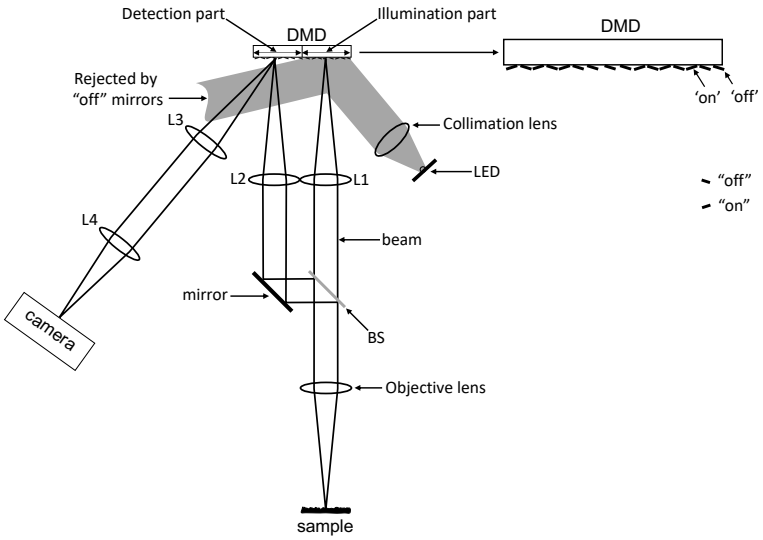


Figure 4.12: Only one beam (and a light spot on the sample) is shown for illustrative purposes. The LED-emitted light beam is collimated by a lens and the resulting collimated light is delivered onto the illumination part of the DMD device. Beamsplitter used for such microscope naturally leads to further development of interferometer for OCT implementation [177].

surface normal. Each micromirror is tilted such that its normal forms a 12° angle with the direction of the incident or reflected beam. In multi-spot mode, a defined subset of micromirrors on one half of the DMD (region A in Figure 4.13) is switched to the "on" state, while the rest remain "off," producing an array of illumination spots. This illumination pattern is directed onto the sample by lens $L2$ ($f = 200$ mm) in combination with the objective lens ($f = 18$ mm). A non-polarizing 50/50 beam splitter has dual use. First, it divides the source light between the sample and reference arms. Second, it recombines the backscattered light from the sample and light reflected from the reference mirror.

The recombined beam is then projected by lens $L3$ ($f = 200$ mm) onto the second half of the DMD (region B in Figure 4.13). On this half, a digital pinhole array is generated by setting micromirrors corresponding to pinhole locations "off" and the remaining micromirrors "on." This forms a confocal detection scheme, ensuring that only light originating from the illuminated sample spots passes through the pinholes to the camera. Back-reflections produced in region A when illuminated by the LED are directed back toward the source and are prevented from reaching the camera, contrary to alternative configurations.

In order to ensure high image quality, lenses $L2$ and $L3$ each are made of two $f = 400$ mm achromatic doublets arranged in a Plössl configuration, which preserves high resolution across whole field of view by minimizing off-

axis aberrations. The interference pattern formed on the DMD half containing the digital pinholes is reimaged onto a CMOS camera (acA2040-180kmNIR, Basler, Ahrensburg, Germany) using lenses $L4$ ($f = 150$ mm) and $L5$ ($f = 100$ mm). The camera has a resolution of 2048 × 2048 pixels, each 5.5 µm in size, with a full well capacity of 11.9 ke-. When operated with a 512 × 512 pixel region of interest (ROI), it can reach up to 700 frames per second. Under these conditions, the resulting field of view was 380 µm × 380 µm. The reflectance of the reference mirror was set to 2 % to match R_{inc} (the incoherent sample's reflectivity). And using Formula 4.4, where ξ_{sat} is full well capacity (FWC) of the camera, the sensitivity of the system was calculated as:

$$sensitivity = \frac{3}{4} N \xi_{sat} \frac{1}{R_{inc}} \tag{4.4}$$

A three-axis translation stage driven by a stepper motor (T-NA08A25-S, Zaber, Vancouver, BC, Canada) was used for sample mounting. This allowed imaging at different focal depths, enabling depth scanning and 3D reconstruction of the image. The entire reference arm was placed on an independent translation stage, serving as a time-delay line for precise adjustment of the optical path length between the sample and reference arms. To phase-shift and acquire images, the reference mirror was mounted on a piezoelectric actuator (STr-25, Piezomechanik, München, Germany), which introduced controlled phase shifts to the reference beam. The final FF-OCT image was reconstructed from these phase-shifted frames according to

$$E_{OCT} = (E_1 - E_2)^2 + (E_1 - E_3)^2 + (E_2 - E_3)^2 \tag{4.5}$$

E_1, E_2 and E_3 are the camera intensities acquired at phase shifts of 0°, 120° and 240°.

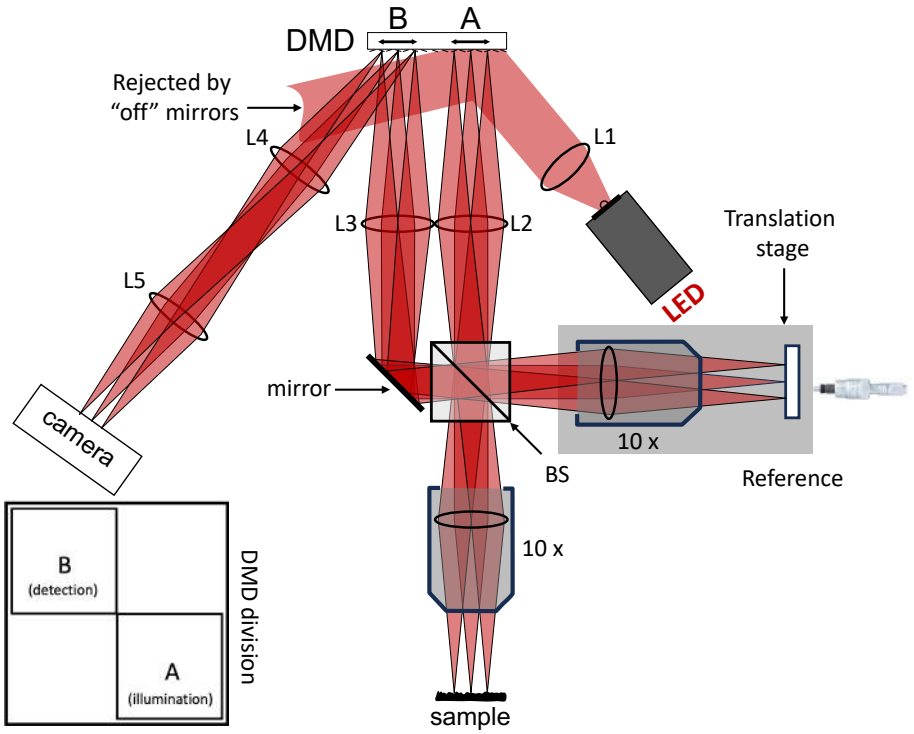


Figure 4.13: Principle scheme of the FF-OCT system with confocal gating implemented with the help of DMD. $L1$—aspheric collimator ($f = 16$ mm); $L2$–$L3$—achromatic lenses ($f = 200$ mm); $L4$—achromatic lens ($f = 150$ mm); $L5$—achromatic lens ($f = 100$ mm); BS—non-polarizing 50/50 beamsplitter; DMD—digital mirror device; LED—light-emitting diode. A mirror is mounted on a tip-and-tilt mount in order to adjust it such that two parts of the DMD are conjugated. The optical path of only three beams is shown for the sake of simplicity. Inset shows the arrangement of the illumination (A) and detection (B) parts of the DMD. The parts are arranged such that they are as far apart from each other as possible.

The system could also be run in full-field illumination mode by setting all micromirrors to the "on" state on the illumination side of the DMD, while switching all micromirrors "off" on the imaging side. This configuration made a uniform illumination field. For multi-spot illumination only specifically selected micromirrors on the illumination half of the DMD were activated, generating an array of separate light spots. The light reflected from the sample then passed through the imaging half of the DMD, where a matching pattern of micromirrors was turned "off" to form digital confocal pinholes, sending the signal toward detection. Using a mirror mounted on a tip–tilt stage accurate alignment between illumination spots and pinholes was achieved (Figure 4.13), and ensured out-of-focus light was suppression while light from each illuminated spot passed through its corresponding pinhole.

To scan the entire field of view of the sample, the DMD displayed a sequence of various micromirror patterns within a single exposure of the CMOS camera. This approach enabled rapid multi-spot imaging without requiring synchronization between the DMD and the camera. Every illumination spot was made of one "on" micromirror, while the corresponding detection pinholes were combined from 2×2 blocks of "off" micromirrors on the imaging side of the DMD. The spacing between spots and pinholes was varied to balance optical sectioning capability, imaging speed and cross-talk. In particular, spacings of 15, 7, and 4 for micromirrors to be set as a spot/pinhole were tested, requiring 225, 49, and 16 different DMD patterns in order to image whole sample. For each spacing, all patterns were displayed during a single camera exposure. As the number of patterns increased, the illumination time had to be decreased for each individual pattern. Because of the limited output power of the light source, this led to weaker signals per pattern, showing the trade-off between the acquisition speed of the camera and the strength of the registered OCT signal [175].

We did not only multi-spot scanning but also employed a multi-line scanning method. Instead of generating arrays of individual spots, alternative DMD patterns were used to form line-shaped illumination and detection regions. As in the multi-spot experiment, the illumination lines had width of one micromirror, while the detection lines had width of two micromirrors and a spacing of 15 micromirrors between each line. Since the pattern is periodic in only one direction, such line-scanning approach shortens acquisition time by reducing the number of required DMD patterns. For instance, only 15 patterns were needed, compared to 225 for multi-spot scanning with the same spacing. Fewer patterns make it possible to capture images faster within a single camera exposure. The drawback is that line illumination and detection achieve only partial confocal sectioning, suppressing out-of-focus light in one direction but not the other. In

order to demonstrate the benefit of using a multi-spot/multi-line scanning in FF-OCT, we first measured the axial response, otherwise called the "optical sectioning curve" (Figure 4.14), by placing a mirror in the sample arm and moving it along the optical axis while the reference arm was blocked.

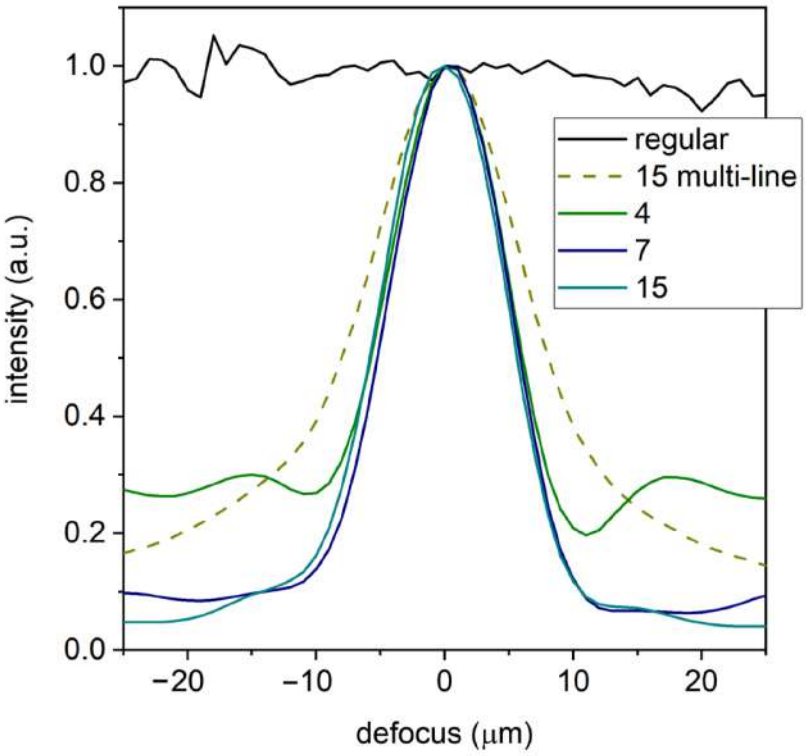


Figure 4.14: Optical sectioning curves in regular, multi-line, and multi-spot FF-OCT microscopy with different pinhole spacings, which are specified in the number of micromirrors.

Experiments were performed with different pinhole spacings. The measured intensity profile showed a peak with a non-zero baseline, caused by cross-talk between neighboring spots or pinholes. This baseline increased for smaller pinhole spacings, since cross-talk starts appearing at smaller defocus values. However, the curve shape and the full width at half maximum (FWHM) remained nearly constant at about 12 µm for all spacings.

Contrary to an experiment in the multi-spot mode with the same pinhole spacing, for the multi-line mode the sectioning curve was broader and did not decrease as sharply. This behavior is expected and agrees with results from line-scanning FF-OCT using a rolling shutter camera which was done previously [33]. During our experiment in standard full-field mode, the intensity showed almost no variation over the same axial range (Figure 4.14). The advantages of multi-spot scanning for FF-OCT imaging were further demon-

strated on a scattering sample made of a US Air Force (USAF) resolution target (R1DS1P, Thorlabs) placed beneath a 160 µm thick scattering layer of polydimethylsiloxane (PDMS) with embedded TiO_2 nanoparticles (Figure 4.15).

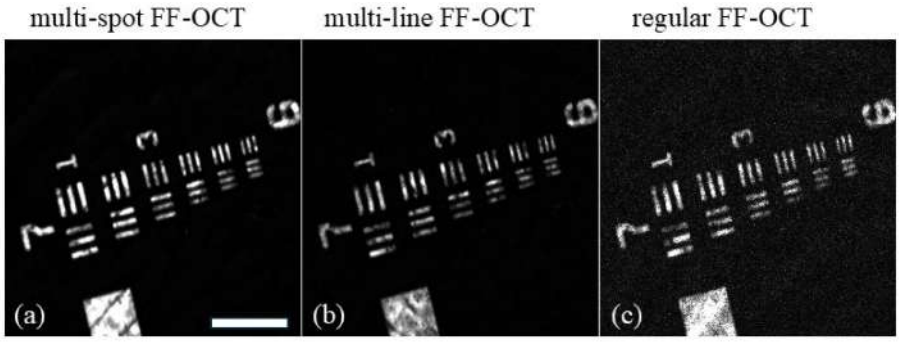


Figure 4.15: FF-OCT images of the sample composed of a USAF target mounted beneath a scattering layer acquired in (a) multi-spot, (b) multi-line, and (c) regular modes. Scale bar, 50 µm. Images are presented using different intensity scales for comparison: (a) 0–10,000, (b) 0–2000, and (c) 0–200.

By mixing Sylgard 184 silicone elastomer with its curing agent (Dow Corning, Midland, MI, USA) in a 10:1 volume-to-volume (v/v) ratio The PDMS film was prepared. Titanium dioxide (TiO_2, 14027, Sigma-Aldrich, St. Louis, MO, USA) was then added at 1 % weight/volume (w/v) and mixed until uniform consistency. In order to eliminate bubbles, the mixture was centrifuged for 1 min at 20,238×g and further degassed under vacuum for 30 min. A PDMS sheet was produced by placing 20 µL of the mixture between two coverslides while a coverslip was used as a spacer. This "sandwich" was cured at 80 °C for 1 h [175]. Figure 4.15 shows a comparison of FF-OCT images recorded in different modes. For demonstration, the multi-spot mode was operated with a relatively long camera exposure of 200 ms, resulting frame rate of only 5 Hz . In contrast, both the multi-line and conventional full-field modes were recorded with 20 ms exposure time, resulting 50 Hz frame rate. To make the comparison consistent, the conditions of the experiment were tuned. First, as described earlier, the highest SNR is obtained when the reflectivity of the reference arm matches the level of incoherent light returning from the sample.

As it changes between each imaging mode, different reflectors on the reference arm were used. Specifically, for the measurements in the full-field mode an absorptive neutral density filter functioned as the reference reflector. During imaging in both the multi-spot and multi-line OCT modes a lower-reflectivity color filter was used as a reflector. This ensured optimal reference reflectivity during each experiment. Second, illumination intensity was adjusted so that the detector received the same amount of signal in all modes. In practice, the

multi-spot mode required the maximum available LED power, whereas for the multi-line and full-field modes, the illumination was reduced to match the signal intensity from the sample arm. The FF-OCT signal is much stronger in confocal scanning mode (multi-spot) in comparison to the standard full-field mode (shown in Figure 4.15(a)). This improvement happens because the confocal gate (12 µm (FWHM) aligned with the USAF target plane) suppresses light from out-of-focus planes (scattering layer above). As a result, more illumination light reaches the target, and more of the scattered signal from the target is collected. In line-scanning mode, the intensity of FF-OCT signal is between that of the multi-spot and standard full-field configurations. This can be explained by the presence of partial confocal sectioning, which is less effective than in the multi-spot regime. To evaluate the upgrade in image quality, the signal-to-noise ratio (SNR) was estimated for each image. SNR was defined using

$$SNR = (\frac{\sqrt{signal}}{std(\sqrt{background})})^2, \tag{4.6}$$

where the signal corresponds to the OCT signal intensity on the USAF target bars, and the background is taken by misaligning coherence gate and measuring OCT signal there. For the standard FF-OCT image (Figure 4.15(c)), the SNR was 67. In comparison, confocal scanning (Figure 4.15(a)) yielded an SNR of 1914, which improved 29 times. Meanwhile, the line-scanning configuration produced results in between as an SNR was 529.

The confocal sectioning is further demonstrated by the optical sectioning curve in Figure 4.14, which has an FWHM of 12 µm. For instance, a signal coming from 10 µm deeper (or higher) compared to the focal plane would be reduced about tenfold during confocal scanning, while it would remain unaffected in conventional FF-OCT. This suppression of scattered light out of confocal plane accounts for the substantial SNR increase using with confocal detection.

In order to illustrate the benefits of multi-spot imaging, a biological sample was imaged at multiple depths. Figure 4.16 clearly displays maximum intensity signal derived from resliced image stacks of a cucumber, obtained using both multi-spot and regular full-field. The stack was imaged from 20 µm beneath the sample surface to a depth of 1 mm, with an axial increment of 1 µm between successive frames. Across the entire depth range, the multi-spot setup reveals a greater amount of structural detail. At depths exceeding approximately 400 µm, structural features are no longer visible in the standard imaging mode. However, the multi-spot approach still enables imaging sample structures down to nearly 800 µm deep in the tissue [175]. This example shows that the increased SNR provided by multi-spot imaging produces a qualitative improvement in image content when confocal effect rejects incoherent background signals.

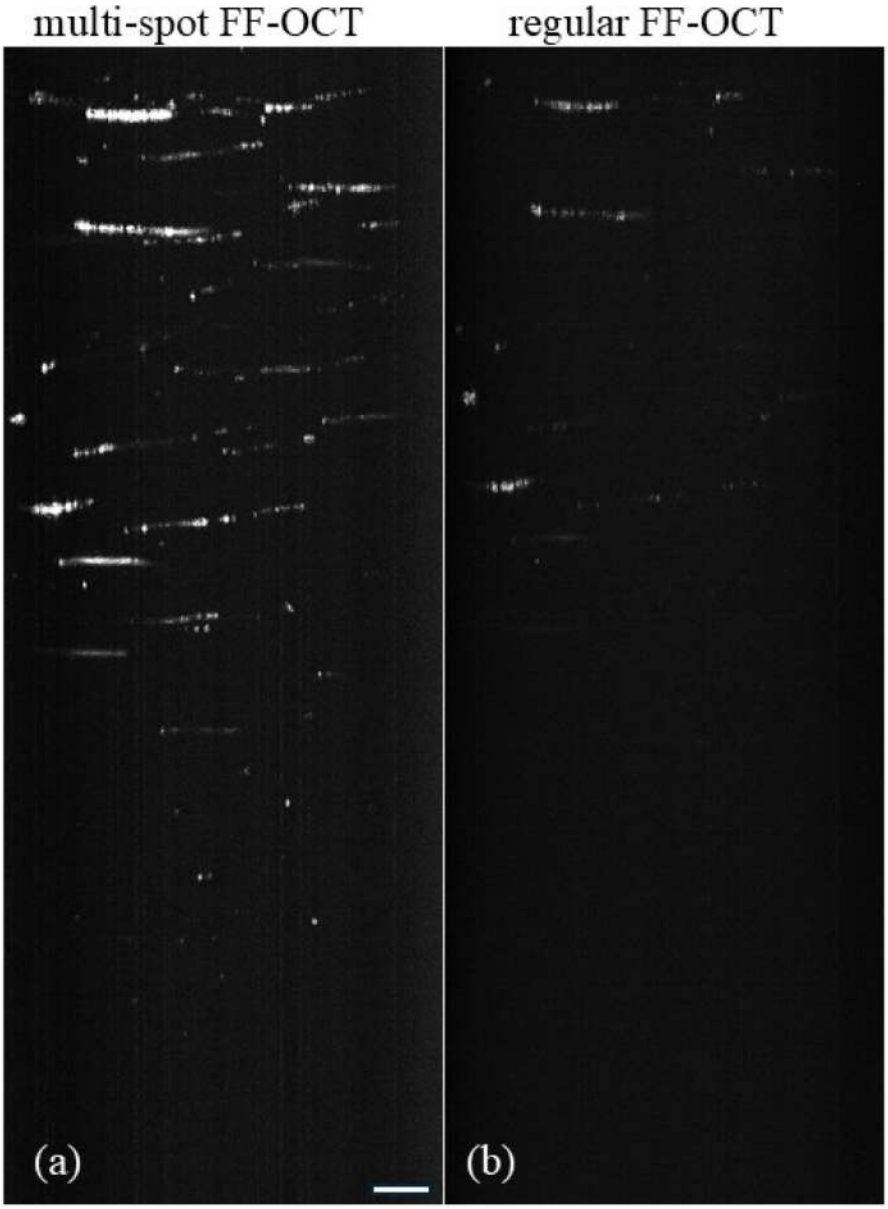


Figure 4.16: Axial images (XZ) of a cucumber acquired in (a) multi-spot and (b) regular modes. Maximum intensity projections were performed on 512 images. Scale bar 50 µm.

In conclusion, the presented confocal FF-OCT system operates in multi-spot and multi-line scanning modes. The system uses a reworked and patented double-pass geometry implemented to digital micromirror device (DMD) for confocal detection in reflection mode. Signal-to-noise ratio (SNR) was improved by reducing the amount of incoherent light reaching the detector. Multi-spot illumination combined with digital pinholes creates confocal sectioning in full-field imaging which strongly suppresses out-of-focus light, which results in increased SNR. By using one half of the DMD for illumination spots and another half to form confocal pinholes, we eliminate backreflections that previously limited the use of DMDs in FF-OCT. This method provides benefits for imaging scattering samples, assuming that the light source has enough brightness. The digital pinholes block unwanted light and improve SNR. The programmable DMD allows simple adjustment of all parameters: spot size, pinhole size and spacing between both of them, which is not possible in other confocal techniques such as Nipkow disk systems. The setup can be simply changed between standard full-field and adjustable confocal modes without adjusting setup mechanically. Moreover, the system does not need big moving parts, which normally cause vibrations and result in reduced image quality. Despite these advantages, the method has limitations. Only a fraction of the illumination is used when sparse multi-spot illumination patterns are applied. Denser patterns improve illumination source efficiency but introduce cross-talk between different spots. For this reason a stronger light source is needed to fully utilize the system. A broadband laser combined with a microlens array could make illumination more efficient and improve light delivery to the sample. By applying these modifications, such system could be used for highly scattering tissue imaging, such as the brain or adapted for in vivo measurements, such as retinal imaging.

CONCLUSIONS

During this work several conclusions were drawn:

1. Coherence noise in FD-FF-OCT can be substantially reduced using a passive, small-core multimode fiber which allows simultaneous high-resolution imaging of the retina and full-thickness choroid in vivo.

2. A fast deformable membrane combined with the multimode fiber further suppresses modal noise, increases STOC-T sensitivity enough to resolve retinal ganglion cells and photoreceptors.

3. High-Throughput interferometer design (90/10 beamsplitter with pupil-plane pick-off mirror) further increases STOC-T sensitivity which enables use of lower power illumination and reduces volume averaging.

4. In TD-FF-OCT computational defocus correction extends usable imaging depth beyond the physical depth of focus of the objective.

5. A setup based on DMD design that uses one half of the mirror array for illumination spots and the other half as digital confocal pinholes solves backreflection problem and combines confocal microscopy benefits with Full-Field OCT speed.

5. SANTRAUKA LIETUVIŲ KALBA

Įvadas

Pirmąjį lazerį sukurė Theodoras Maimanas "Hughes Research Laboratories" tyrimų centre 1960 m. Šis įvykis optikos srityje savo reikšme prilygsta ugnies atradimui žmonijos istorijoje. Lazerio atsiradimas paskatino spartų daugelio sričių vystymąsi, tarp jų – ir mediciną. Vėliau, be lazerių, buvo tobulinami ir komerciškai prieinami šviesos diodai (LED, angl. light-emitting diodes), kas dar labiau išplėtė šviesos šaltinių pasirinkimą. Šiuolaikinė medicina neįsivaizduojama be diagnostinių metodų, pagrįstų šviesos generavimu, įvedimu ir detekcija. Vienas iš tokių metodų yra optinė koherentinė tomografija (OKT), kuri priskiriama prie tokių svarbių vaizdinimo technologijų kaip rentgenografija, kompiuterinė tomografija (KT), magnetinio rezonanso tomografija (MRT), ultragarsinis vaizdinimas ir terahercinis (THz) vaizdinimas.

Optinė koherentinė tomografija (OKT) yra neinvazinė diagnostinė technologija, leidžianti realiuoju laiku gauti didelės skiriamosios gebos (gylio atžvilgiu) trimačius vaizdus. Pirmą kartą OKT metodas aprašytas 1991 m. žurnale Science [1]. Naudojant superliuminescencinį diodą (SLD), vienmodį optinį šviesolaidį ir fotodiodą, buvo išmatuota žmogaus tinklainė in vitro. Nuo to laiko atsirado daugybė OKT metodų ir jų variacijų: nuo klasikinės vieno taško skenavimo laikinė (Time-Domain) OKT iki greitų pilnojo lauko Furjė (angl. Fourier-Domain) OKT metodo, taip pat Doplerio OKT, dviejų ašių OKT, poliarizacijai jautrios OKT ir kt. Šiandien OKT yra sėkmingo biofotonikos mokslo taikymo klinikinėje praktikoje pavyzdys [2]. Ši technologija plačiai paplito įvairiose medicinos srityse, sudarydama galimybes detaliai vaizdinti tyrimo objektus oftalmologijoje, kardiologijoje, onkologijoje, dermatologijoje ir kitose disciplinose.

Vis dėlto skirtingos OKT taikymo sritys kelia ir naujus technologinius iššūkius. Pavyzdžiui, in vivo tinklainės vaizdinimui būtina itin sparti signalo registracija, tam kad butų išvengta vaizdo suliejimo dėl nevalingų akies judesių. Kita vertus, fiksuotų audinių tyrimuose prioritetas teikiamas didesnei erdvinei skiriamajai gebai ir vaizdinimo gyliui, prailginant matavimo laiką. Pereinant nuo laikinės (Time-Domain) prie Furjė (Fourier-Domain) OKT, vienų parametrų gerinimas dažnai vyksta kitų parametrų sąskaita, todėl būtini nuoseklūs abiejų konfigūracijų tobulinimai. Dėl šios priežasties pilnojo lauko OKT (Full-Field OCT) metodų vystymas leidžia pasiekti ne tik didelę skiriamąją gebą ir didelį vaizdinimo gylį, bet ir išlaikyti didėjantį vaizdinimo greitį [3]. Tai užtikrina komfortišką tyrimų trukmę klinikinėse sąlygose bei aukštą gaunamų vaizdų kokybę.

Darbo tikslas

Darbo tikslas – sukurti ir eksperimentiškai patikrinti optinius bei skaitmeninio duomenų apdorojimo metodus, skirtus Furjė erdvės ir laikinės viso lauko optinės koherentinės tomografijos vaizdų kokybei gerinti ir vaizdinimo gyliui didinti, mažinant koherentinio persiklojimo ir modų interferencijos triukšmą, didinant interferometro optinį pralaidumą, taikant skaitmeninę defokuso korekciją ir programuojamą konfokalinį filtravimą.

Sprendžiami uždaviniai

Darbo tikslui įgyvendinti buvo išsikelti uždaviniai:

1. Sukurti Furjė erdvės viso lauko OKT sistemą, ištirti ilgo daugiamodžio šviesolaidžio ir greitos deformuojamosios membranos taikymą koherentinio persiklojimo bei modų interferencijos triukšmui slopinti ir įvertinti tinklainės bei gyslainės vaizdinimo galimybes.

2. Sukurti didesnio optinio pralaidumo STOC-T (angl. spatio-temporal optical coherence tomography) interferometrą ir įvertinti jo jautrį bei signalo ir triukšmo santykį.

3. Sukurti ir eksperimentiškai patikrinti laikinės viso lauko OKT skaitmeninės defokuso korekcijos ir programuojamo konfokalinio filtravimo metodus, skirtus geriau išskirti struktūras ir išplėsti naudingą vaizdinimo intervalą sklaidančiuose bandiniuose.

Mokslinis naujumas

1. Furjė erdvės viso lauko OKT sistemoje pritaikytas pasyvus koherentinio persiklojimo triukšmo slopinimas ilgu, mažo šerdies skersmens daugiamodžiu šviesolaidžiu. Tai sudarė sąlygas viename in vivo užregistruotame tūryje atvaizdinti tinklainę ir visą gyslainės storį.

2. STOC-T sistemoje suderinti ilgas daugiamodis šviesolaidis ir greita deformuojamoji membrana. Šis derinys sumažino modų interferencijos triukšmą, pagerino tinklainės vaizdų kokybę ir sumažino triukšmą tarp tinklainės sluoksnių.

3. Sukurta didelio optinio pralaidumo STOC-T interferometro sistema su 90:10 pluošto dalikliu ir vyzdžio plokštumoje esančiu nukreipiamuoju veidrodėliu. Ji padidino silpnai atspindinčių, plačiu kampų diapazonu šviesą sklaidančių bandinių registravimo jautrį; vidurkinant 30 tūrių pasiektas beveik 100 dB jautris.

4. Pademonstruota, kad skaitmeninė defokusavimo korekcija laikinės pilnojo lauko OKT sistemoje leidžia refokusuoti vaizdus, kurie yra toliau už fizinio objektyvo fokusavimo gylį. Korekcijos efektyvumas priklauso nuo šviesos šaltinio koherentiškumo, todėl galima padidinti vaizdinimo gylį sklaidantiems audiniams ex vivo, pakartotinai neskenuojant ar mechaniškai refokusuojant.

5. Užpatentuota mikroveidrodėlių sistemos (DMD) dvigubo praėjimo konfiguracija, kurioje viena mikroveidrodžių matricos pusė naudojama apšvietimo taškams, o kita panaudojama skaitmeninėms konfokalinėms apertūroms formuoti. Taip pašalinama DMD atgalinių atspindžių problema, anksčiau ribojusi jo taikymą pilnojo lauko OKT sistemose. Tokiu būdu tampa įmanoma programiškai keisti apšvietimo taškų ir apertūrų dydį bei atstumą tarp jų.

Ginamieji teiginiai

1. Ilgas (300 m), mažo šerdies diametro (50 µm) daugiamodis šviesolaidis pasyviai slopina koherentinį triukšmą Furjė pilnojo lauko OKT (FD-FF-OKT) sistemoje iki 11,8 dB. Šio slopinimo pakanka, kad viename užregistruotame in vivo vaizdų rinkinyje galima išskirti tiek tinklainę, tiek viso storio gyslainę (gyslainės kapiliarų, Sattlerio ir Hallerio sluoksnius).

2. Daugiamodžio šviesolaidžio ir greitai veikiančios deformuojamos membranos derinys papildomai slopina modų triukšmą, padidindamas STOC-T sistemos jautrį iki maždaug 80 dB ir signalo triukšmo santykį iki 13,6 dB, lyginant su tik pasyvia konfigūracija. Tai leidžia vaizdinti in vivo tinklainės ganglijinių ląstelių sluoksnį ir fotoreceptorių vidinius bei išorinius segmentus.

3. Interferometro konstrukcija, pagrįsta didelio pralaidumo (90/10) pluošto dalikliu ir vyzdžio plokštumoje esančiu nukreipiančiuoju veidrodžiu, padidina STOC-T sistemos jautrį 3,5 karto (5,4 dB), lyginant su standartine šviesolaidžio ir deformuojamos membranos konfigūracija. Atlikus 30 vaizdų rinkinių vidurkinimą (registravimo trukmė 0,3 s), pasiekiamas beveik 100 dB jautris, todėl galima naudoti mažesnę apšvietimo galią ir sumažinti tinklainės vaizdinimo metu in vivo judesio sukeltų trikdžių suvidurkinimo poreikį.

4. Laikinėje pilnojo lauko OKT sistemoje skaitmeninė defokusavimo korekcija leidžia atkurti sufokusuotus vaizdus iš duomenų, užregistruotų 500–1000 µm atstumu nuo fokusavimo plokštumos, t. y. maždaug 100 kartų toliau už fizinį vaizdinimo objektyvo fokusavimo gylį. Ši korekcija gali būti taikoma tiek šviesą sklaidantiems, tiek atspindintiems ex vivo bandiniams, be papildomo mechaninio refokusavimo.

5. Patobulinta dvigubo praėjimo skaitmeninio mikroveidrodinio prietaiso (DMD) geometrija leidžia laikinėje pilnojo lauko OKT sistemoje programiškai valdyti konfokališkumą, kuris leidžia naudoti daugiataškį ir daugialinijinį skenavimo režimus. Esant atskirai optimizuotoms registravimo sąlygoms, signalo ir triukšmo santykis padidinamas iki 29 kartų (14,6 dB, nuo 67 s.v. iki 1914 s.v.), lyginant su standartiniu pilnojo lauko detektavimu, o tinkamas vaizdinimo gylis šviesą sklaidančiame audinyje padidinamas nuo 400 iki 800 µm.

Autoriaus indelis

Autorius kūrė, statė OKT sistemas, atliko eksperimentus, analizavo rezultatus. Autorius taip pat bendradarbiavo su bendraautoriais rangdamas publikacijas. Važiavo į konferencijas, kuriose pristatinėjo naujus pasiekimus. Taip pat populiarino OCT žiniasklaidoje.

Optinė koherentinė tomografija (OKT) yra neinvazinė ir bekontaktė vaizdinimo technika, pagrįsta išsklaidytos atgaline kryptimi šviesos intensyvumo matavimu. Ji pirmą kartą aprašyta 1991 m. [1] ir tapo vienu pagrindinių medicininio vaizdinimo įrankių. OKT galima palyginti su ultragarsiniu vaizdinimu, kai ultragarso banga siunčiama į audinį, o atspindėtų signalų vėlinimai registruojami kaip gylio informacija. Tačiau, kadangi OKT pagrįsta šviesos atspindžiu, nėra pakankamai greitų elektroninių sistemų, galinčių registruoti tokius trumpus laiko intervalus tarp šviesos atspindžių. Todėl OKT remiasi interferometriniu vaizdinimu (pvz., naudojant Michelsono interferometrą). Naudojant mažo koherentiškumo plačiajuostį (broadband) šviesos šaltinį, interferencija vyksta tik tada, kai bandinio ir atraminės šakos optiniai keliai sutampa. Ši sąlyga leidžia atlikti audinio gylinį matavimą (priklausomai nuo atstumo ir signalo stiprumo).

Pirmosiose šios technikos realizacijose buvo naudojami vienmačiai gylio profiliai (A-scan), gaunami skenuojant atraminę šaką ašine kryptimi ir registruojant signalo stiprumo pokyčius priklausomai nuo atstumo. Tokia technika vadinama laiko srities OKT (TD-OCT). Tačiau ankstyvosios laikinės OKT (TD-OCT) sistemos buvo labai lėtos (net ir naujesnės sistemos pasiekia tik šimtus vienmačių gylio profilių per sekundę) [5], todėl pilno vaizdo gavimas užtrukdavo ilgai. Dėl to atsirado kita OKT rūšis – Furjė OKT (FD-OCT). Pirmosios FD-OCT sistemos pademonstruotos po kelių metų: spektrinė OKT (SD-OCT) sistema – 1995 m. [6], o spektrą skenuojančio šaltinio (SS-OCT) – 1997 m. [7].

Pagrindinė OKT savybė yra interferometrinė atgal išsklaidytos šviesos detekcija. Gylis nustatomas matuojant vienąkart atgal išsklaidytos šviesos iš bandinio interferenciją su atspindžiu nuo atraminėje šakoje esančio veidrodžio. Ašinė skiriamoji geba priklauso nuo šviesos šaltinio koherentiškumo ilgio l_c:

$$l_c = \frac{2ln2(\lambda_0^2)}{\pi\Delta\lambda}. \tag{5.1}$$

λ_0 – centrinis bangos ilgis, o $\Delta\lambda$ – spektro plotis (pilnas plotis ties puse maksimumo (FWHM)). Taigi, siekiant didelės ašinės skiriamosios gebos, paprastai naudojami plačiajuosčiai šviesos šaltiniai (superliuminescenciniai diodai, plačiajuosčiai lazeriai). Skersinė skiriamoji geba priklauso nuo sufokusuoto pluošto dydžio ir vaizdinimo lęšio skaitinės apertūros. Tai leidžia pasiekti aukštą skiriamąją gebą net tais atvejais, kai negalima naudoti didelės skaitinės apertūros optikos (pvz., tinklainės tyrimuose). Tačiau skersinė skiriamoji geba ribojama vaizdinimo gyliu. Fokusavimo gylis b gali būti apskaičiuojamas:

$$b = \pi\frac{(\Delta x^2)}{2\lambda} \tag{5.2}$$

o dėmės dydis Δx:

$$\Delta x = \frac{4\lambda f}{\pi d}, \tag{5.3}$$

kur f yra židinio nuotolis d yra apertūros diametras.

Ašinės ir skersinės skiriamosios gebos atskyrimas leidžia kurti įvairias specifinėms užduotims pritaikytas OKT sistemas. Pagrindinis interferometro (taigi ir OKT sistemos) elementas yra pluošto daliklis, kuris padalija šviesą į bandinio ir atraminę šakas. Atspindėta šviesa sujungiama tame pačiame daliklyje ir registruojama detektoriumi. Yra daug OKT modifikacijų, tačiau dvi pagrindinės kryptys – laiko ir Furjė OKT.

Laikinėse OKT sistemose ašinė informacija gaunama skenuojant atraminį veidrodį optinio vėlinimo linija [8]. Interferencija registruojama detektoriumi tik tada, kai optinių kelių skirtumas patenka į koherentiškumo ilgio ribas, todėl skenuojant veidrodį gaunamas laikinis signalas, atitinkantis bandinio ašinę struktūrą. Furjė OKT sistemose registruojamas ne laikinis, o spektrinis interferencijos signalas [10]. Tokiu būdu išvengiama lėtos vėlinimo linijos, kuri pakeičiama spektrometru arba skenuojamo spektro lazeriu. Užregistruotos spektrininės interferogramos naudojant inversinę Furjė transformaciją paverčiamos į ašinius profilius. Nors laikinės OKT sistemos yra paprastesnės ir pigesnės, Furjė OKT pasižymi didesniu vaizdo registravimo greičiu ir geriau tinka in vivo tyrimams.

Pagrindiniai OKT vaizdų terminai:

A-scan – gylio profilis;

B-scan –tomografinio pjūvio vaizdas (xz arba yz);

en face – dvimatis (xy) pasirinkto sluoksnio vaizdas.

Furjė OKT skirstoma pagal detekciją:

spektrinė OKT – naudojamas plataus spektro šaltinis ir spektrometras; spektrą skenuojančio šaltinio OKT – naudojamas greitai derinamas lazeris ir taškinis detektorius.

Abiem atvejais registruojami atspindėti spektrai, iš kurių rekonstruojamas gylio profilis [13]. Vienam bangos ilgiui signalas suteikia informaciją apie lūžio rodiklio periodinių pokyčių amplitudę, kuri susijusi su banginiu vektoriumi $k = 2p/\lambda$. Sujungus skirtingų bangos ilgių signalus ir pritaikius Furjė transformaciją, randamas gylio profilis, nes informacija užkoduota dažninėje (k) erdvėje. Šie metodai padidino ne tik greitį, bet ir signalo bei triukšmo santykį (SNR).

Pilno lauko OKT

Pilno lauko optinė koherentinė tomografija (PL-OKT) pirmą kartą buvo pademonstruota 1998 m. [14]. Pagrindinis skirtumas tarp įprastinių OKT sistemų ir PL-OKT yra tas, kad PL-OKT leidžia registruoti vaizdus be skersinio

skenavimo. Tradicinėje OKT vaizdinimas atliekamas registruojant gylio profilį, kuri gali būti gaunama naudojant taškinį arba linijinį detektorių. Tuomet šviesos spindulys skenuojamas ant bandinio taškas po taško ir formuojami tomografinio pjūvio vaizdai ir vėliau tridimensiniai vaizdai. Pilnojo lauko optinė koherentinė tomografija (PL-OKT) yra interferometrinis metodas. Interferenciniai signalai registruojami kamera, kuri gali registruoti signalą visame vaizdo lauke [14–16]. PL-OKT geriausiai žinoma dėl didelės skyros vaizdų, kuriuose koherentiniai artefaktai yra labai menki arba jų visai nėra [15, 17]. Tokie vaizdai praktiškai neturi dėmelių (angl. speckle) ir persiklojimo (angl. crosstalk) artefaktų, nes naudojami erdviškai ir laikiškai nekoherentiški šviesos šaltiniai, pavyzdžiui, elektros lanko lempos ar šviesos diodai (LED).

Pilnojo lauko konfigūracija veikia kitaip. Vietoj bandinio skenavimo taškas po taško, dvimatė kamera registruoja visą dvimatį en face vaizdą pasirinktame gylyje. Tūrinis vaizdas vėliau atkuriamas perkeliant vaizdinimo plokštumą išilgine kryptimi ir apdorojant vaizdus skirtinguose bandinio gyliuose. Abiejais vaizdinimo metodais optinio pjūvio storį pagrinde lemia apšvietimo šaltinio laikinio koherentiškumo ilgis, kuris yra atvirkščiai proporcingas jo spektrinės juostos pločiui. Sumažinus dvimatį nuskaitymą iki vienmačio nuskaitymo išilgine kryptimi (z ašimi), atsiranda tiek privalumų, tiek naujų techninių iššūkių [18]. Pastaruoju metu ši metodika pradėta vadinti laikine pilnojo lauko optine koherentine tomografija (laikinė PL-OKT, angl. TD-FF-OCT), siekiant ją atskirti nuo toliau aptariamos dažninės (Furjė) pilnojo lauko optinės koherentinės tomografijos (Furjė PL-OKT, angl. FD-FF-OCT), dar vadinamos PL-OKT su derinamu dažnio šaltiniu (angl. SS-FF-OCT). Laikinėje PL-OKT vaizdų registravimo spartą riboja kameros kadrų dažnis, todėl vieno kadro registravimo trukmė paprastai viršija 1 ms. Palyginimui, kai kurios skenuojančios OKT sistemos šiuo metu gali registruoti daugiau kaip 100 000 gylio prifilių per sekundę [20].

Skenuojančioje OKT kiekvienas vaizdo pikselis registruojamas nuosekliai skirtingais laiko momentais nuskaitymo metu. Tačiau PL-OKT atveju visi pikseliai užregistruojami vienu metu, kai kamera veikia globalaus registravimo (angl. global shutter) režimu. Dėl šios priežasties judančių bandinių OKT vaizduose gali atsirasti judesio sukelti artefaktai. Skenuojančioje OKT optinė fazė gali būti tiesiogiai apskaičiuojama iš dviejų gretimų taškų z ašyje [21], tačiau PL-OKT sistemoje optinei fazei atkurti būtina atlikti kelis matavimus, registruotus esant skirtingiems fazės poslinkiams. Laikinė PL-OKT leidžia pasiekti didelę skersinę ir išilginę skyrą. Pirmiausia todėl, kad PL-OKT sistemoje fokusavimo gylis nėra ribojamas taip, kaip, pavyzdžiui, Furjė OKT sistemose, todėl vaizdinimui galima naudoti didelės skaitinės apertūros objektyvus. Ilgą laiką objektyvų skaitinė apertūra, o kartu ir pasiekiama skyra, buvo ribota maždaug iki 1 µm, nes Linnik tipo interferometruose, kurie yra dažniausiai naudojama PL-OKT sistemose, sudėtinga suderinti dispersiją tarp interferometro

bandinio atšakos ir atraminės atšakos. Didelę išilginę skyrą (apie 1 µm) yra nesunku pasiekti, nes PL-OKT sistemose galima naudoti plataus spektro baltosios šviesos šaltinius, pavyzdžiui, ksenoninę išlydžio lempą. Pastaruoju metu didelės skaitinės apertūros objektyvai buvo sėkmingai panaudoti PL-OKT vaizdams su statiniu ir dinaminiu kontrastu formuoti [22–24]. Rekordinė maždaug 280 nm skersinė skyra neseniai buvo pademonstruota naudojant objektyvą, kurio skaitinė apertūra siekė $NA = 1{,}25$ [25].

Vis dėlto, norint suformuoti trimačius duomenų rinkinius (trimačius vaizdus), būtina išilgine kryptimi stumdyti patį bandinį arba atraminį veidrodį. Šis reikalavimas, kartu su konfokalinio vartų efekto nebuvimu PL-OKT sistemose bei greitų kamerų, kurios turėtų didelę pikselių krūvio kaupimo talpą (angl. full well capacity, FWC), trūkumu, ilgą laiką ribojo PL-OKT taikymą gyvų bandinių (in vivo) vaizdinimą. Nepaisant lygiagrečios OKT signalo registracijos, sistema buvo pernelyg lėta daugeliui in vivo taikymų, todėl daugiausia naudota tik negyvų (ex vivo) akių vaizdinimui [26–29] arba primigdytų žiurkių akių in vivo tyrimams [30]. Konfokalinio efekto nebuvimas PL-OKT sistemose kelia didesnius reikalavimus kameroms, nes jos registruoja visą nefokusuotą šviesą, kuri nėra koherentiška su atraminės atšakos signalu tačiau pasiekia detektorių. Ši nekoherentinė šviesa neprisideda prie naudingo OKT signalo formavimo ir taip padidina foninį signalą bei užima reikšmingą detekcijos dinaminio diapazono dalį. Dėl šios priežasties sumažėja bendras sistemos jautris. Kai kurias nekoherentinės šviesos dedamąsias, pavyzdžiui, atspindžius nuo lęšių ar bandinio paviršių, galima slopinti naudojant tamsaus lauko detekciją (angl. dark-field detection) [31, 32] arba papildomą konfokalinį filtravimą [33], tačiau didžiąją dalį ateinančios iš bandinio daugkartinai išsklaidytos šviesos kamera vis tiek užregistruoja. Dėl šių priežasčių tūrinis in vivo vaizdinimas laikinės PL-OKT sistemomis išlieka sudėtingas uždavinys. Nepaisant to, buvo parodyta, kad ne ašinio išdėstymo laikinė PL-OKT (angl. off-axis TD-FF-OCT), kurioje vietoje lėtesnio fazių poslinkių metodo naudojama vienašūvė registracija (angl. single-shot acquisition), gali maždaug per 1 sekundę suformuoti tinklainės tomografinius skerspjūvius [34, 35]. Tačiau dėl erdviškai koherentiško lazerinio šaltinio ir kameros detekcijos sukuriamo didelio persiklojimo (angl. crosstalk) triukšmo vaizdinimo gylis tinklainėje išlieka stipriai apribotas. Todėl siekiant išspręsti laikinės PL-OKT sistemoms būdingas problemas ir įgalinti spartų in vivo vaizdinimą, buvo sukurta Furjė pilnojo lauko optinė koherentinė tomografija (Furjė PL-OKT, angl. FD-FF-OCT) [3].

Furjė pilnojo lauko optinėje koherentinėje tomografijoje vietoje plataus spektro nekoherentinio apšvietimo, naudojamo laikinėje FF-OKT, taikomas greitai keičiamo bangos ilgio lazerinis šaltinis, dažniausiai vadinamas derinamo dažnio lazeriu (angl. swept-source) [3]. Šiuo atveju signalas registruojamas dažninėje (Furjė) erdvėje. Derinant tokį detektavimo metodą su lygiagrečiu vaizdų registravimu kamera, galima pasiekti maždaug 10 GHz vokselių registravimo spartą [36]. Dėl to Furjė PL-OKT yra vienas sparčiausių optinės koherentinės tomografijos tūrinio vaizdinimo metodų, kartu išlaikantis santykinai didelį jautrį. Dar vienas svarbus šio metodo privalumas yra iš registruotų duomenų atkuriamos optinės fazės stabilumas. Furjė PL-OKT sistemoje fazė išlieka stabili visame regėjimo lauke, priešingai nei skenuojančioje OKT, kur A-skenai registruojami nuosekliai. Stabili fazės informacija OKT sistemose yra ypač vertinga, nes leidžia taikyti skaitmeninę aberacijų korekciją, kuri pagerina galutinio vaizdo kokybę [36]. Furjė pilnojo lauko optinė koherentinė tomografija (angl. FD-FF-OCT) yra perspektyvus ir universalus akių vaizdinimo metodas dėl didelės vaizdų registravimo spartos ir galimybės gauti stabilią fazės informaciją visame regėjimo lauke. Tačiau nevisos akies dalys yra lengvai vaizdinamos, pavyzdžiui, gyslainės vaizdinimą dažniausiai riboja persiklojimo (angl. crosstalk) triukšmas. Gyslainės vaizdinimas yra svarbus, nes suteikia informacijos apie įvairių galinio akies segmento ligų patogenezę, kadangi pagrindinė gyslainės funkcija yra aprūpinti išorinę tinklainės dalį deguonimi. Plataus lauko detekcija kartu su erdviškai koherentišku lazeriniu šaltiniu sukelia persiklojimo triukšmą, kuris blogina vaizdo kokybę, palaipsniui mažindamas skersinę skyrą vaizdinant gilesnius audinių sluoksnius. Vienas iš būdų sumažinti persiklojimo triukšmą yra naudoti erdviškai nekoherentišką šviesos šaltinį, kuris leidžia vidurkinti skersine kryptimi išsklaidytus fotonus. Pirmoji erdviškai nekoherentiška, derinamo bangos ilgio lazerinė sistema, skirta Furjė PL-OKT, buvo sukurta 2006 m. [37].

Tačiau ši sistema buvo sudėtinga, pasižymėjo ribotu išilginiu vaizdinimo diapazonu, o užregistruotuose vaizduose buvo persiklojimo triukšmo. Kita vertus, ši sistema veikė be fotoelastinio dvigubo lūžio moduliatoriaus [15] ar pjezo elemento [38], todėl tokia sistema tapo pagrindu Furjė PL-OKT sistemoms, kokias jas suprantame šiandien. Didėjant derinamo dažnio lazerių bei didelės spartos vaizdo kamerų prieinamumui, Furjė OKT tapo vis praktiškesniu vaizdinimo metodu. Tačiau derinamo dažnio lazerių veikimo principas yra toks, kad siaura spektrinė linija yra skenuojama plačiame spektro ruože. Dėl to neišvengiamai atsiranda ryškūs koherentiniai artefaktai, pavyzdžiui, dėmelės (speckle). Dėmelės yra nepageidaujami interferenciniai dariniai, susidarantys dėl daugkartinai bandinyje išsklaidytos šviesos (Paveikslas 2.4), kurie blogina vaizdo kokybę [39]. Kuo didesnis šviesos šaltinio koherentiškumas, tuo didesnį poveikį OKT vaizdui daro koherentinis triukšmas. Dėl šios priežasties didelė dalis Furjė PL-OKT technologijos vystymo yra orientuota į šio koherentinio

triukšmo mažinimą. Dar vienas svarbus PL-OKT vystymosi etapas buvo pasiektas 2010 m., kai pirmą kartą pavyko atlikti žmogaus tinklainės vaizdinimą in vivo [40]. Tam buvo panaudotas derinamo dažnio lazerinis šaltinis ir didelės spartos CMOS kamera, galinti registruoti 640 × 24 pikselių sritį 100 000 kadrų per sekundę dažniu. Eksperimentą ribojo šviesos šaltinio galia, todėl registruojama plotas turėjo būti apribotas iki linijos, kuriai gauti buvo panaudoti cilindriniai lęšiai. Sistema statyta Maikelsono interferometru, o koherentinis apšvietimas į interferometrą buvo nukreiptas vienmodžiu šviesolaidžiu. Gauti B-skenų vaizdai turėjo koherentinio triukšmo bei susiliejimo artefaktų dėl judesių (1 pav. 2.5). Vis dėl to, tokios sistemos veikimo galimybės buvo įrodytos ir pademonstruotos tolesnio sistemos optimizavimo perspektyvos. Siekiant sumažinti koherentinį triukšmą, 2013 m. buvo pademonstruotas interferometrinis erdvinis ir laikinis optinės koherencijos valdymas (angl. spatiotemporal optical coherence, STOC) [41]. Šis terminas literatūroje naudojamas kalbant apie pilno lauko Furjė erdvės OKT sistemas, kuriose galimas erdvinio koherentiškumo valdymas. Šioje konfiguracijoje Maikelsono interferometre vietoje bandinio buvo panaudotas erdvinis šviesos moduliatorius (angl. spatial light modulator, SLM), leidžiantis valdyti interferencinių juostų struktūrą keičiant šviesos fazę. Šis eksperimentas parodė naują būdą mažinti koherentinį triukšmą biomedicininėse OKT sistemose keičiant fazę. Vėliau lazerio erdviniam koherentiškumui sumažinti buvo panaudotas besisukantis difuzorius [42]. Siekiant apeiti šio metodo ribojimus, vėliau buvo pasiūlyti siaurajuosčių VCSEL (vertical-cavity surface-emitting laser) lazerių masyvai [43] bei itin greitai veikianti deformuojamoji membrana. Šie metodai pranašesni tuo, kad besisukantys difuzoriai yra per lėti naudoti su didelės spartos kameromis ir negali pakankamai sumažinti erdvinio koherentiškumo per trumpą kameros ekspozicijos laiką, todėl riboja vaizdų registravimo spartą.

Vėliau, panaudojus gerokai spartesnę kamerą tinklainės kraujagyslių dinamikai tirti bei išnaudojus tai, kad fazė išlieka stabili visame regėjimo lauke [44], buvo pasiektas didesnio regėjimo lauko vaizdinimas. Tai ne tik leido atlikti tūrinį tinklainės vaizdinimą in vivo, bet ir pasiekti iki tol didžiausią OKT registravimo spartą – apie 10 GHz vokselių dažnį [36], išlaikant santykinai didelį jautrį. Nors panaši tūrinio vaizdinimo sparta teoriškai gali būti pasiekta ir laikinėje PL-OKT [45], jos jautris daug mažesnis. Kaip ir Furjė OKT sistemose, taip ir Furjė PL-OKT sistemose bandinio ir atraminės atšakų chromatinės dispersijos neatitiktis bei judėjimas z ašimi registruojamame interferencijos spektre pasireiškiantis kaip dažnio moduliacija (angl. chirp) yra neišvengiama vaizdininant in vivo, bet tai gali būti kompensuojama skaitmeniniais metodais. Tokia kompensacija laikinėje PL-OKT sistemoje nėra galima. Tačiau didelė Furjė PL-OKT tūrinio vaizdinimo sparta ir nuskaitymo nereikalaujantis dizainas pasiekiami mažinant galimą skersinę skyrą, nes būtina užtikrinti pakankamai didelį fokusavimo gylį, kad būtų galima kelias išilgines plokštu-

mas registruoti per labai trumpą laiko tarpą. Vis dėlto ilgą laiką Furjė PL-OKT sistemų taikymą ribojo persiklojimo triukšmas (crosstalk noise), atsirandantis dėl erdviškai koherentinio lazerinio šaltinio ir pilnojo lauko detekcijos [36, 40, 44], [46–48]. Šis triukšmas susidaro dėl daugkartinai išsklaidytų fotonų, kurie, išlikdami koherentiški su atraminės atšakos spinduliu, kameroje atvaizduojami į artimas vaizdo vietas. Persiklojimo triukšmas riboja vaizdinimo gylį tinklainėje ir trukdo aiškiai atvaizduoti gyslainės struktūrą. Vienas iš šios problemos sprendimo būdų buvo ne-ašinės (angl. off-axis) Furjė PL-OKT konfigūracijos panaudojimas [48]. Buvo parodyta, kad tokia konfiguracija sumažina dėl lazerinio šaltinio atsirandantį koherentinį autokoreliacijos triukšmą, tačiau tai pasiekiama sumažinant skersinę skyrą arba regėjimo lauką.

Kitas būdas sumažinti erdvinį koherentiškumą yra panaudoti deformuojamą membraną [49], [3]. Naudojant tokį metodą lazerio spindulys yra nukreipiamas į deformuojamąją membraną, kuri chaotiškai virpa iki 500 000 kartų per sekundę dažniu. Šie spartūs virpesiai visame šviesos pluošte sukuria atsitiktinius, tarpusavyje nekoreliuotus fazės pokyčius, vykstančius gerokai didesniu dažniu nei atvirkštinė kameros ekspozicijos trukmė. Dėl to šviesos pluoštas praranda erdvinį koherentiškumą. Paprastai deformuojamoji membrana įrengiama prieš interferometrą, todėl identiški fazės pasiskirstymai projektuojami tiek į bandinio, tiek į atraminę atšakas. Tokia konfigūracija išsaugo interferencines juostas, susidarančias dėl vienkartinai atgal išsklaidytų fotonų. Tačiau deformuojamoji membrana nėra optimalus sprendimas, nes jos taikymas riboja vaizdinimo gylį [3,50] ir vaizduose atsiranda artefaktai, kuriuos sudėtinga pašalinti. Kitas būdas sumažinti erdvinį koherentiškumą yra naudoti daugiamodį (MM) šviesolaidį, kuris erdviškai koherentišką šviesą suskaido į daugybę erdvinių modų ir taip sumažina koherentinius artefaktus. Šis principas plačiai taikomas lazerinėse projekcinėse vaizdo sistemose [51]. Be to, plataus spektro lazerinę spinduliuotę galima įvesti į daugiamodį šviesolaidį, kad būtų suformuotas iš dalies erdviškai koherentiškas apšvietimas, tinkamas laikinei pilnojo lauko optinei koherentinei tomografijai (angl. TD-FF-OCT). Toks sprendimas buvo pritaikytas vaizdinant vaisinę muselę [38] bei aliuminio plokštelę [52]. Nors laikinėje PL-OKT gali būti naudojami didelės galios šviesos diodai (LED) ir kiti alternatyvūs šviesos šaltiniai, šiuo metu nėra alternatyvų, galinčių generuoti iš dalies erdviškai koherentišką, siauro momentinio spektro pločio ($\sim$ 0,1 nm) ir kelių dešimčių nanometrų diapazone derinamą spinduliuotę. Artimiausia komerciškai prieinama alternatyva yra derinamo dažnio lazeris. Tačiau naudojant tokį lazerį siauro spektrinio pločio spindulys, įvestas į trumpą daugiamodį šviesolaidį, šviesolaidžio išėjime suformuoja didelio kontrasto dėmelių (speckle) struktūrą.

Vėliau buvo nustatyta, kad ilgas daugiamodis šviesolaidis, turintis gan mažą šerdies skersmenį, taip pat gali būti naudojamas lazerio erdviniam koherentiškumui sumažinti ir turi tam tikrų pranašumų lyginant su deformuojamosios

membranos metodu [53]. Visų pirma, naudojant šį metodą gaunami vaizdai pasižymi mažesniu artefaktų kiekiu, o pats šviesolaidis veikia kaip pasyvus optinis elementas – jo nereikia lankstyti ar sukti. Tai pasiekiama nepaisant to, kad naudojama labai siauro momentinio spektro pločio ($\sim$ 0,1 nm) spinduliuotė. Nors tokia siauro spektro spinduliuotė daugiamodžio šviesolaidžio išėjime ir PL-OKT vaizduose sukuria dėmelių struktūrą, ją galima veiksmingai pašalinti taikant skaitmeninį filtravimą [53], kurio metu neprarandamas naudingas signalas.

Triukšmas

Eksperimentinės sąlygos visada yra neidealios – ne tik atskiri komponentai gali turėti trūkumų, bet ir visa sistema dažniausiai nėra tobula. Viena iš dažniausių problemų vaizdinime yra triukšmas. Išskiriamos penkios pagrindinės triukšmo rūšys: šūvio triukšmas, modinis triukšmas, koherentinis/persiklojimo (cross-talk) triukšmas, detektoriaus triukšmas ir santykinio intensyvumo triukšmas.

Šūvio triukšmas yra fundamentali optinio intensyvumo svyravimų riba. Nors istoriškai jis buvo siejamas su fotodetekcija (atsitiktiniais įvykiais, kai fotonas sugeriamas detektoriuje), iš tikrųjų tai yra pačios šviesos lauko savybė [54]. Šūvio triukšmas paprastai aprašomas kaip kvantinis triukšmas, paklūstantis Puasono statistikai. Jo pašalinti neįmanoma, tačiau signalo ir triukšmo santykį angl. (SNR) galima gerinti didinant šviesos šaltinio galią, mažinant optinius nuostolius, naudojant didesnio kvantinio efektyvumo detektorius bei ilginant integracijos laiką. Kadangi šūvio triukšmas didėja proporcingai aptiktų fotonų skaičiaus kvadratinei šakniai [55], SNR išreiškiamas kaip $SNR = N/\sqrt{N} = \sqrt{N}$, todėl padidinus signalą 100 kartų, triukšmas padidėja tik 10 kartų.

Santykinio intensyvumo triukšmas (angl. RIN) apibūdina lazerio optinės galios svyravimus, normalizuotus vidutinei galiai [56]. Paprastai jis charakterizuojamas galios spektrine tankio funkcija (angl. PSD), nusakančia triukšmo stiprį tam tikrame dažnių diapazone. Pagrindiniai šio triukšmo šaltiniai puslaidininkiniuose lazeriuose yra spontaninė emisija ir elektronų–skylių rekombinacijos šūvio triukšmas [57].

Modinis triukšmas atsiranda daugiamodžiuose šviesolaidžiuose, kai koherentiniai arba dalinai koherentiniai šviesos šaltiniai sužadina daug modų, turinčių netolygų pasiskirstymą. Dėl to šviesolaidžio išėjime susidaro dėmelių struktūra, kurios svyravimai sukelia galios fluktuacijas. Modinis triukšmas yra atvirkščiai proporcingas lazerio spektrinėa linijos pločiui (angl. linewidth) [57]. Norint sumažinti modinį triukšmą yra mažinamas šviesos koherentiškumas, pavyzdžiui, plečiant spektrą arba mechaniškai judinant šviesolaidį skaidula, kad būtų išmaišytos modos.

Detektoriaus triukšmą daugiausia sudaro šiluminis triukšmas ir tamsiosios srovės triukšmas. Net ir nesant šviesos, fotodiode teka tamsioji srovė, kuri atsiranda dėl termiškai generuojamų elektronų–skylių porų p–n sandūroje. Be to, dėl atsitiktinio elektronų judėjimo apkrovos varžoje atsiranda papildomas šiluminis triukšmas [57]. Šiuos efektus galima sumažinti aušinant detektorių.

Koherentinis/persiklojimo (angl. cross-talk) triukšmas dažniausiai pasireiškia PL-OCT sistemose dėl daugybinio šviesos sklaidos. Interferometre interferencija vyksta tik koherentiškumo ilgio ribose, o keičiant atraminės atšakos padėtį galima pasirinkti skirtingus mėginio gylius. Tačiau naudojant didelio koherentiškumo šaltinį kelis kart išsklaidytas fotonas, gali interferuoti taip pat, kaip fotonas atėjęs iš gilesnių bandinio sluoksnių, taip sukeldamas nepageidaujamą persiklojimo triukšmą [4]. Šis efektas paprastai mažinamas naudojant mažesnio koherentiškumo šviesos šaltinius.

Medicininės taikymo sritys

Neinvazinių medicininio vaizdinimo metodų poreikis yra itin svarbus sparčiai vystantis ligų diagnostikai ir gydymui, ypač tiriant jautrius organus. Optinės koherentinės tomografijos (OKT) raida sukėlė reikšmingą proveržį akių priežiūros srityje. Priekiniai ir galiniai akies audiniai dabar gali būti tiriami neinvaziškai, o tai leidžia gydytojui greičiau ir tiksliau priimti sprendimus, remiantis objektyvia struktūrine informacija [58]. Oftalmologijoje OKT suteikia galimybę vaizdinti įvairias akies struktūras, įskaitant rageną, tinklainę, rainelę, bei regos nervą [59]. Taip pat naudojama OKT angiografija, leidžianti vizualizuoti kraujotaką be kontrastinių medžiagų. Kardiologijoje OKT naudojama vainikinių arterijų vaizdinimui, pasižymi $\sim$ 10–15 µm skiriamąja geba ir leidžia detaliai analizuoti kraujagyslių struktūrą, onkologijoje OKT padeda atskirti sveikus ir navikinius audinius, dermatologijoje OKT taikoma odos ligų diagnostikai, leidžia stebėti uždegimus, pūslelių susidarymo ir gydymo eigą in vivo. OKT šiandien yra plačiai naudojamas ir nepakeičiamas daugelio medicinos specialistų įrankis.

Furjė pilnojo lauko optinė koherentinė tomografija

Buvo surinkta Furjė pilnojo lauko optinės koherentinės tomografijos (angl. FD-FF-OCT) sistema tinklainės vaizdinimui (paveikslas 5.1). Sistemoje realizuotas išilginių tinklainės pjūvių registravimas realiuoju laiku, naudojant vyzdžio plokštumos padalijimo metodą [88] ir linijinę kamerą. Kadangi daugiamodžio šviesolaidžio suformuotas dalinai erdviškai koherentiškas apšvietimas užima tik nedidelę akies konjuguotos vyzdžio plokštumos dalį, o nuo tinklainės atgaline kryptimi išsklaidyta šviesa užpildo visą vyzdį, tokia konfigūracija leidžia realiu laiku stebėti tinklainę B-skenų režimu. Tai suteikia galimybę tiksliai suderinti sistemą ir akies padėtį naudojantis klinijine kamera prieš galutinį vaizdų registravimą, nes itin didelės spartos dvimatė kamera negali perduoti duomenų į kompiuterį realiuoju laiku.

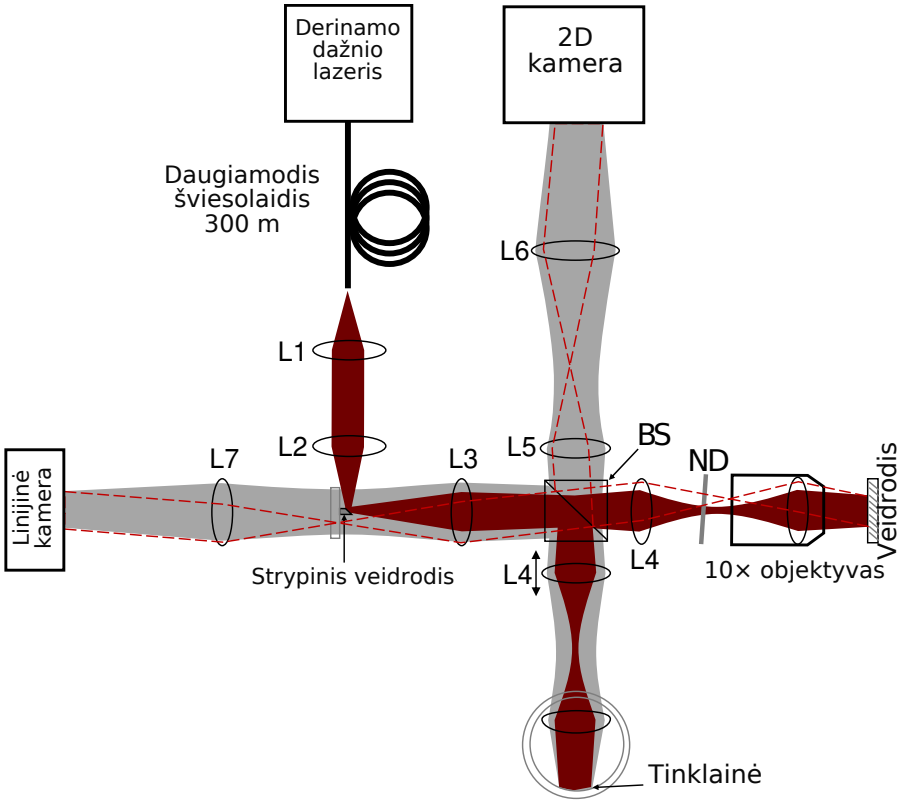


Figure 5.1: Furjė pilnojo lauko OKT sistema.

Derinamo dažnio lazerinio šaltinio (Broadsweeper BS-840-2-HP, Superlum) spinduliuotė buvo įvesta į 300 m ilgio laiptinio lūžio rodiklio profilį turintį daugiamodį šviesolaidį (0,22 NA, 50 µm šerdies skersmens, FG050LGA, Thorlabs). Iš šviesolaidžio sklindanti šviesa buvo nukreipta į Maichelsono interferometrą, kuriame 50/50 pluošto daliklis nukreipė šviesą į bandinio ir atraminę atšakas.

Nuo tinklainės atgaline kryptimi išsklaidyta šviesa ir nuo atraminio veidrodžio atsispindėjusi šviesa buvo sujungtos tuo pačiu pluošto dalikliu ir padalytos į dvi dalis. Dalis šviesos buvo nukreipta į itin didelės spartos dvimatę kamerą (Fastcam SA-Z, Photron), o likusi dalis nukreipta į linijinę kamerą (Alkeria Necta N4K-7-F), skirtą greitam vaizdo stebėjimui ir galutiniam sistemos suderinimui prieš registruojant tinklainės vaizdus. Įprastinėse OKT sistemose ši šviesa paprastai prarandama, tačiau apie 1° pakreipus atraminį veidrodį ją galima panaudoti bandinio stebėjimui realiu laiku. Toks pakreipimas sukelia nedidelį tūrinio vaizdo pakrypimą z kryptimi, tačiau jis akių vaizdinimo metu yra nereikšmingas ir lengvai kompensuojamas skaitmeniniais metodais.

Lazerinis šaltinis spektrą skenavo 8700 nm/s greičiu, o abi kameros registravo duomenis 60 kHz dažniu. Lazeriui praskenuojant visą spektrą buvo užregistruoti 512 vaizdų, kurių bangos ilgio žingsnis siekė 0,15 nm, o bendra vieno tūrinio vaizdo registravimo trukmė buvo 8,6 ms.

Yra du pagrindiniai optinių šviesolaidžių tipai: vienmodžiai šviesolaidžiai, kurie palaiko tik vienos modos sklidimą, ir daugiamodžiai šviesolaidžiai, kuriuose vienu metu gali sklisti daug modų. Šviesolaidžiu galinčių sklisti modų skaičius priklauso nuo tokių parametrų kaip šerdies ir apvalkalo matmenys, lūžio rodiklis bei šviesos bangos ilgis. Šviesolaidis gali palaikyti nuo vieno iki kelių tūkstančių modų. Pirmiausia, apskaičiavus šviesolaidžio parametrus pagal [53, 85] pateiktas formules ir siekiant sužadinti pakankamą erdvinių modų skaičių, buvo pasirinktas šviesolaidis, kurio skaitinė apertūra $NA = 0{,}22$, o šerdies spindulys 25 µm. Esant tokiai konfigūracijai (3.1 formulė), kai bangos ilgis $\lambda = 840$ nm, šviesolaidyje sužadinama apie 840 modų, todėl persiklojimo triukšmas sumažėja maždaug $\sqrt{(840)} \approx 29$ kartus, nes slopinimo efektyvumas yra proporcingas modų skaičiaus kvadratinei šakniai $N^{1/2}$ [86]. Be to, siekiant užtikrinti, kad visos sužadintos erdvinės modos šviesolaidžio gale susidėtų nekoherentiškai ir sudarytų mažo kontrasto dėmelių struktūrą, reikalingas ilgesnis nei 100 m ilgio šviesolaidis. Tačiau eksperimentiniai tyrimai parodė, kad optimalus šviesolaidžio ilgis yra 300 m, nes toks ilgis užtikrina dar mažesnį dėmelių kontrastą.

Siekiant eksperimentiškai įvertinti daugiamodžio šviesolaidžio gebėjimą slopinti persiklojimo triukšmą, naudojant Furjė pilnojo lauko optinės koherentinės tomografijos sistemą buvo vaizdinamas 100 µm storio stipriai sklaidantis latekso bandinys, eksperimente naudojant vienmodį ir daugiamodį šviesolaidžius. Rezultatai palyginti su skenuojančia OKT sistema, kaip parodyta 5.2 (a).

Naudojant vienmodį šviesolaidį, persiklojimo triukšmas aiškiai matomas už bandinio ribų, nors šioje srityje neturėtų būti jokio naudingo signalo. Persiklojimo triukšmo slopinimo efektyvumas, naudojant daugiamodį šviesolaidį, buvo įvertintas apskaičiuojant santykį tarp vienmodžiu ir daugiamodžiu šviesolaidžiais užregistruotų suvidurkintų ašinių profilių (Paveikslas 5.2 (b)).

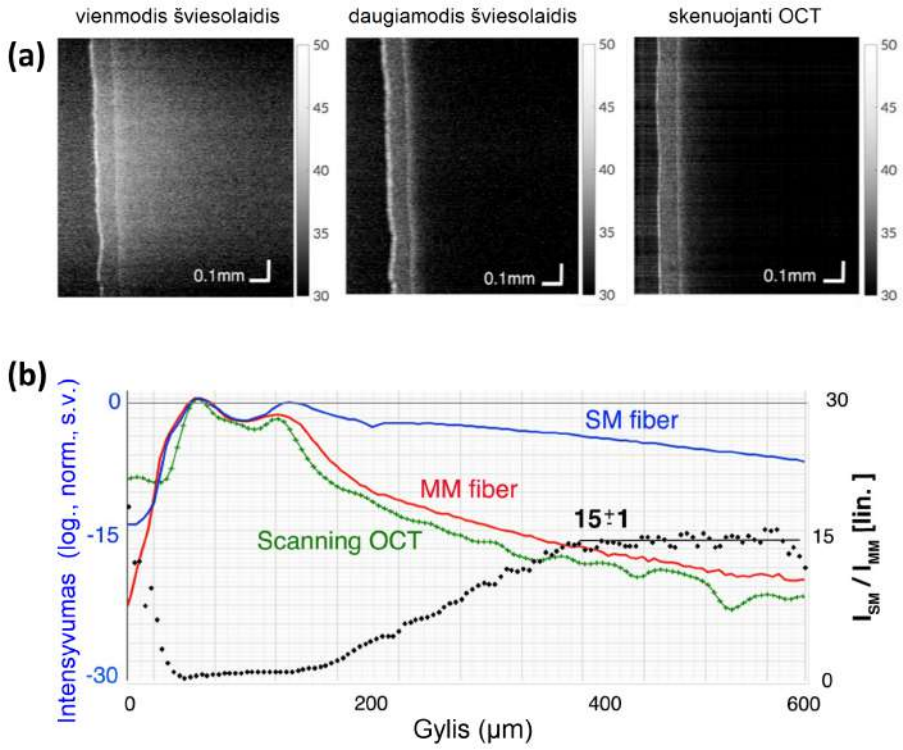


Figure 5.2: (a) Tomografiniai skerspjūviai, gauti naudojant vienmodį šviesolaidį, 300 m ilgio daugiamodį šviesolaidį ir skenuojančią OKT sistemą. (b) Signalo kreivės, priklausančios nuo gylio ir gautos susumavus ašinių profilių vertes. Juoda kreivė gauta padalijus vienmodžio šviesolaidžio kreivę iš daugiamodžio šviesolaidžio kreivės [89].

Kaip ir buvo tikėtasi, SM/MM kreivė pasiekia maždaug 15 kartų (11,8 dB) persiklojimo triukšmo slopinimą, nes šviesolaidyje sužadintos maždaug 250 erdvinių modų sumažina persiklojimo triukšmą $N^{1/2} = 250^{1/2} \approx 15$ kartų [86, 92]. Skenuojančios OKT kreivės slopimo pobūdis yra panašus į daugiamodžio šviesolaidžio kreivę, o tai rodo, kad Furjė PL-OKT sistema gali užtikrinti panašų persiklojimo triukšmo slopinimo lygį.

Furjė pilnojo lauko optinėje koherentinėje tomografijoje fokusavimo gylis (angl. DOF), t. y. išilginis vaizdinimo diapazonas, nepriklauso nuo sufokusuoto pluošto konfokalinio parametro arba Reilėjaus nuotolio [37, 47, 96]. Jį lemia kolimuoto apšvietimo pluošto Reilėjaus nuotolis tiek bandinio, tiek

atraminio veidrodžio atšakose. Tokioje sistemoje interferencinės juostos susidaro dideliame išilginiame vaizdinimo diapazone, tačiau tik židinio plokštumoje užregistruoti OKT vaizdai yra ryškūs, o nuo židinio plokštumos nutolę vaizdai tampa išsilieję. Tačiau dėl Furjė PL-OKT sistemoms būdingo didelio fazės stabilumo vaizdai gali būti atkuriami skaitmeniniais metodais kompensuojant defokusavimą, todėl ryškūs vaizdai gali būti gaunami dideliame išilginiame diapazone, kaip prieš tai buvo parodyta ankstesniuose tyrimuose [36].

Tokią konfiguraciją, kurioje naudojamas ilgas multimodinis šviesolaidis erdviniam koherentiškumui mažinti pavadinome STOC-T (angl. Spatio-Temporal Optical Coherence Tomography). Buvo atlikti tolesni eksperimentai palyginti STOC-T su skenuojančia OKT sistema. Kitame eksperimente kaip bandinys buvo naudojama atspindintis USAF skiriamosios gebos taikinys, kuris buvo vaizdinamas tiek skenuojančia OKT, tiek STOC-T sistemomis. Bandinys buvo perstumiamas išilgai optinės ašies, registruojant vaizdus kiekvienoje defokusuotoje padėtyje, kaip parodyta paveiksle 5.3. Iš užregistruotų vaizdų buvo apskaičiuotos fokusavimo gylio kreivės ir jos tarpusavyje palygintos (paveikslas 5.3). Matome, kad STOC-T sistemos fokusavimo gylio kreivė yra dviemis eilėmis platesnė nei skenuojančios OKT sistemos fokusavimo gylio kreivė. Abiejose sistemose buvo naudojami tie patys 10× objektyvai, kurių skersinė skyra buvo 3,4 µm.

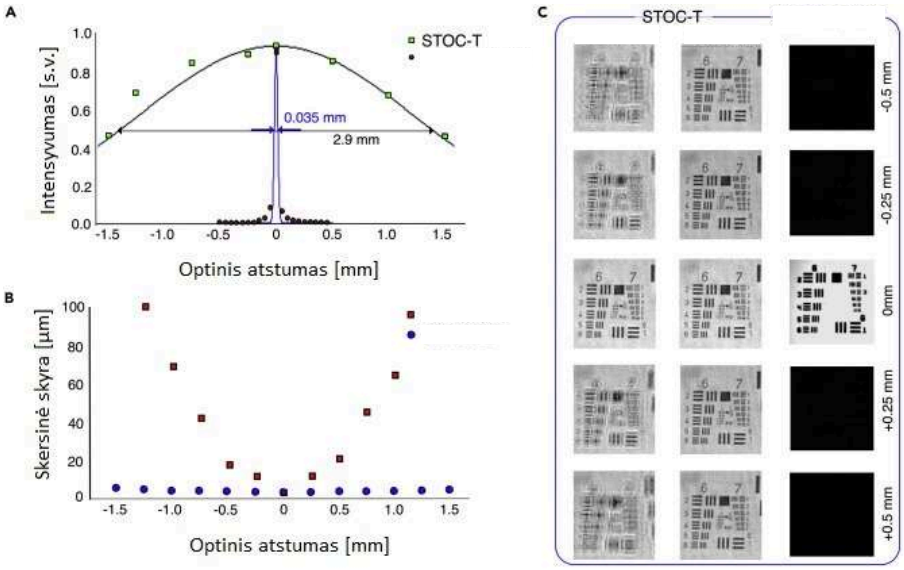


Figure 5.3: Fokusavimo gylio matavimas STOC-T ir skenuojančioje OKT sistemoje, naudojant atspindintį bandinį (USAF taikinį). (A–C) STOC-T ir skenuojančios OKT sistemos intensyvumo mažėjimo palyginimas, (B) skaitmeninės defokuso korekcijos poveikis skersinės skyros praradimui STOC-T sistemoje, (C) naudojant STOC-T ir konfokalinę skenuojančią OKT sistemą skirtingomis defokusavimo vertėmis gautų USAF bandinio vaizdų palyginimas.

Apibendrinant galima teigti, kad Furjė pilnojo lauko optinės koherentinės tomografijos vaizduose persiklojimo triukšmas gali būti reikšmingai sumažintas naudojant mažo šerdies diametro (50 µm) daugiamodį šviesolaidį. Daugiamodis šviesolaidis leidžia vienu metu didelės skiriamosios gebos režimu vaizdinti tiek tinklainę, tiek gyslainę. Be to, gauti rezultatai pasižymi geru pasikartojamumu. Galiausiai, kadangi daugiamodis šviesolaidis neturi judančių dalių, jis yra pasyvus ir mechaniniam nusidėvėjimui atsparus optinis elementas, tinkamas įprastiniam naudojimui medicininėse sistemose ir galintis prisidėti prie platesnio Furjė PL-OKT technologijos taikymo klinikinėje praktikoje.

Furjė PL-OKT sistemos panaudojimas in vivo vaizdinimui

Furjė pilnojo lauko optinės koherentinės tomografijos (PL-OKT) sistema buvo panaudota dviejų savanorių tinklainės vaizdinimui in vivo: vieno sveiko 45 metų asmens ir vieno 54 metų paciento, kuris serga fotoreceptorių degeneracija. Savanorio galva buvo fiksuojama smakro atrama, sumontuota ant trimatės transliacinės postūmio sistemos, kuri leido tiksliai suderinti akies padėtį su vaizdinimo sistema. Anksčiau aprašyta vienmatė linijinė kamera realiuoju laiku registravo išilginius tinklainės pjūvius ir buvo naudojama sistemos derinimui. Tai leido aptikti OKT signalą ir pasirinkti norimą tinklainės sritį. Lęšio $L4$ padėtis (1 pav. 5.1) buvo reguliuojama išilgai optinės ašies, siekiant kompensuoti akies lūžio rodiklio skirtumus. Atlikus visus sistemos suderinimo veiksmus, tūriniai tinklainės duomenys buvo registruojami didelės spartos dvimate kamera.

Pirmojo savanorio tinklainės vaizduose, užregistruotuose 4° toliau nuo geltonosios dėmės, kai vyzdys yra išsiplėtęs, aiškiai matomos didelio kontrasto vidinės ribinės membranos (angl. ILM), paviršinio, tarpinio ir giliojo kapiliarinių rezginių (angl. SCP, ICP ir DCP) bei fotoreceptorių struktūros, kaip parodyta paveikslo 5.4 (a). Atskiri fotoreceptoriai yra aiškiai matomi dėl taikytos aberacijų kompensacijos. 5.4 (b) taip pat aiškiai matomos gyslainės kraujagyslės (kontrastas invertuotas).

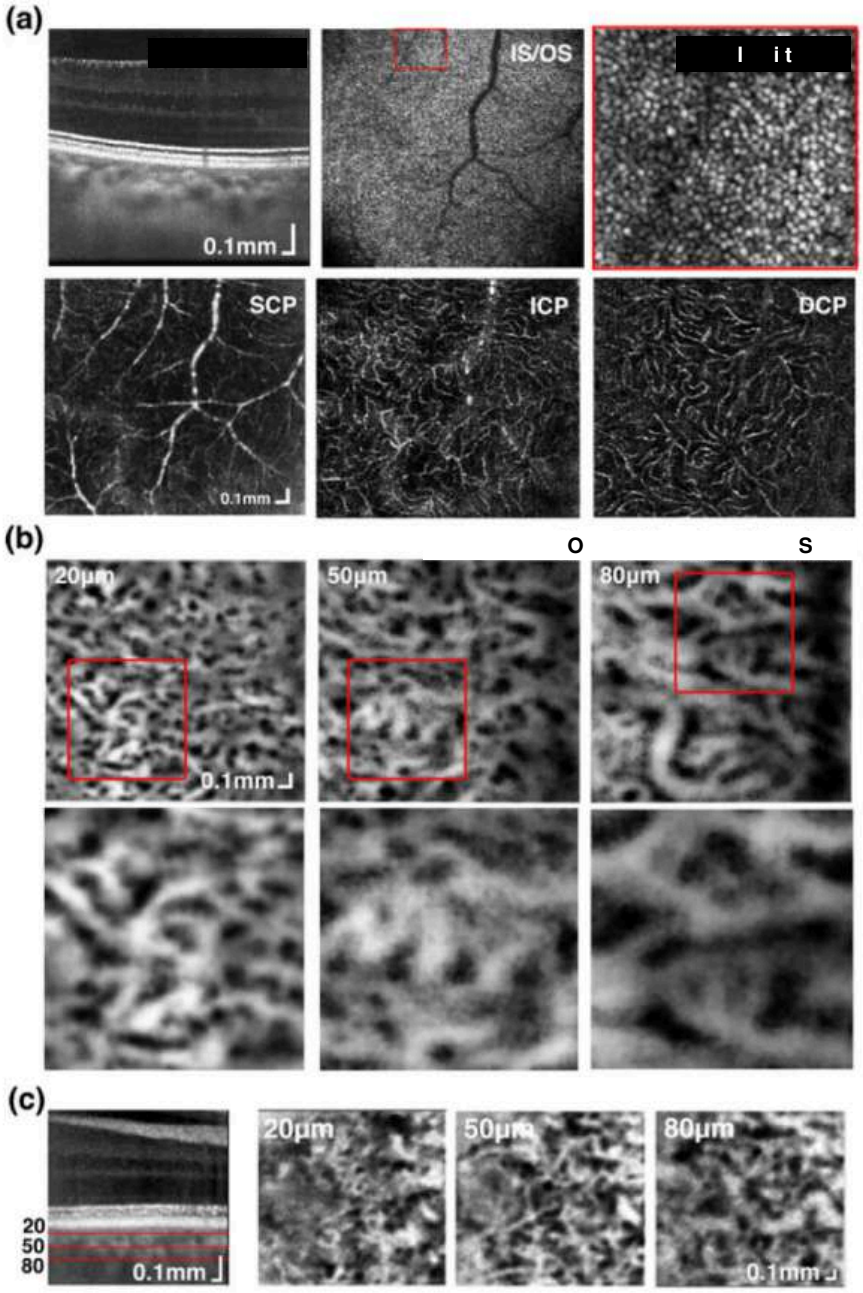


Figure 5.4: Furjė viso lauko optinės koherentinės tomografijos vaizdai: (a) pirmojo savanorio tinklainė ir (b) gyslainė; (c) antrojo savanorio, kuriam nustatyta fotoreceptorių degeneracija, pasirinktų gyslainės sluoksnių išilginiai ir en face vaizdai. Gyslainės vaizdų kontrastas yra invertuotas, kad būtų aiškiau matomos kraujagyslės. Gyslainės vaizduose nurodyti atstumai yra matuojami nuo Brucho membranos. SCP, ICP, DCP – atitinkamai paviršinis, tarpinis ir gilusis kapiliarų rezginiai; IS/OS – vidinio / išorinio segmento sandūra.

Užregistruoti tinklainės ir gyslainės vaizdai parodo, kad sistema yra tinkama vaizdinimui in vivo [89] [97]. Ryškūs ir didelio kontrasto vaizdai gaunami dėl stipriai sumažinto persiklojimo triukšmo ir mažesnio dėmelių dydžio, lyginant su skenuojančia OKT [3]. Pilnai išplėstas vyzdys ir skaitmeniniu būdu kompensuojamos aberacijos leidžia sumažinti dėmelių dydį, nes nuo tinklainės atgaline kryptimi išsklaidyta šviesa sklinda per didesnę vyzdžio apertūrą, todėl susidaro smulkesnės dėmelės net ir esant akies aberacijoms [86].

Siekdami įvertinti vaizdinimo gylio pagerėjimą gyslainėje, STOC-T sistemą palyginome su dviem komercinėmis skenuojančios OKT sistemomis: Spectralis OCT, kurios skersinė skyra yra 15 µm, fokusavimo gylis yra 450 µm, ir Triton OCT, kurios skersinė skyra yra 20 µm, fokusavimo gylis yra 600 µm (Pav. 5.5 (a)). Dėl sistemų parametrų skirtumų, tokių kaip matavimų dažnis, registracijos trukmė ir vidurkinimų skaičius, signalai buvo sunormuoti pagal IS/OS sluoksnio atspindžio vertes ir signalą nuo išorines fotoreceptorių. Paveiksle 5.5 (b) pateiktos kreivės logaritminėje skalėje. STOC-T sistema pasižymi ne tik maždaug 3–4 kartus didesne skersine skyra, bet ir fokusavimo gyliu, kuris yra panašus į Triton OCT sistemos fokusavimo gylį ir gerokai didesnis nei Spectralis OCT sistemos fokusavimo gylis.

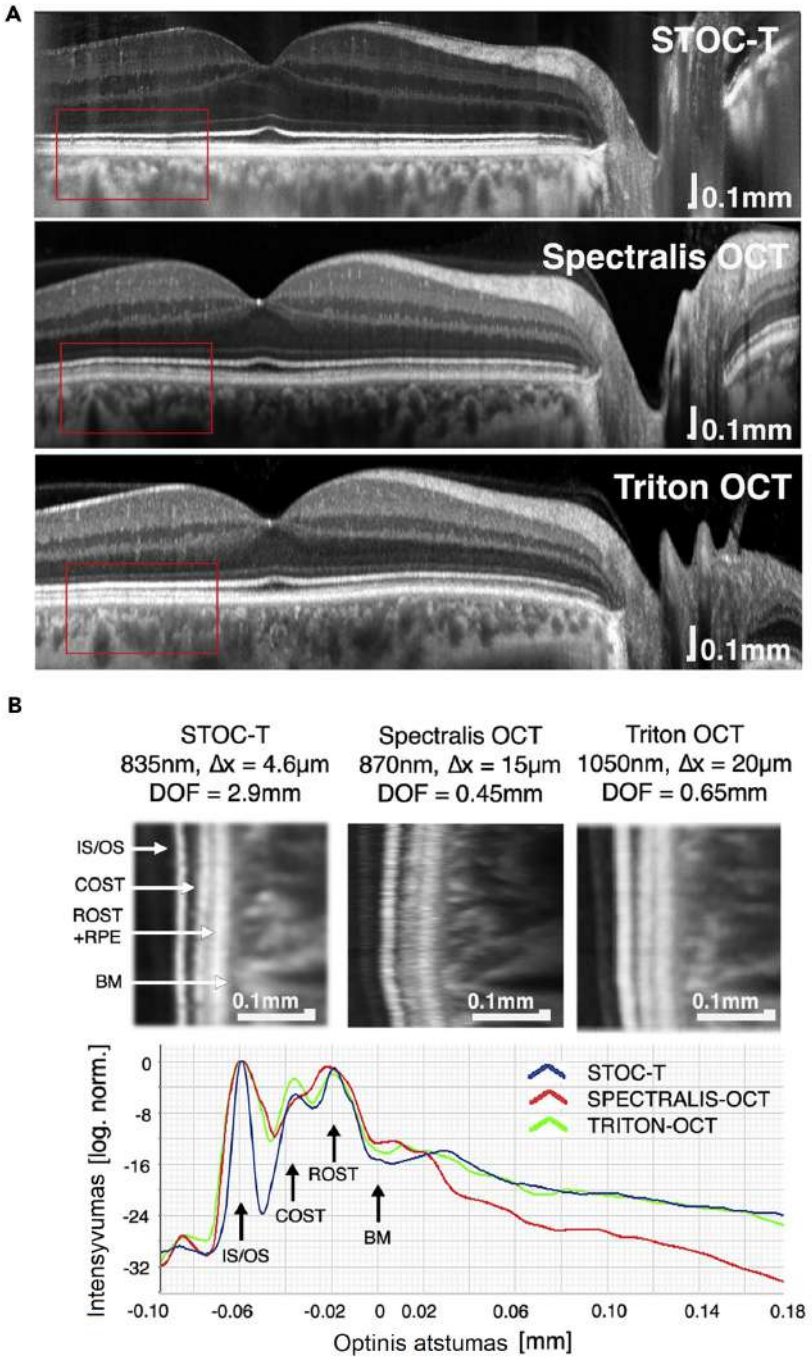


Figure 5.5: Atgal išsklaidyto signalo priklausomybė nuo gylio naudojant STOC-T ir dvi skenuojančias OKT sistemas („Spectralis“, „Heidelberg Engineering“ ir „Triton“, „Topcon“): (A ir B) tomografiniai skerspjūviai po vidurkinimo, (B) signalo susilpnėjimas nuo vaizdinimo gylio.

Gylio atžvilgiu selektyvi informacija apie kraujo tėkmę gali būti užregistruojama naudojant daugiakanalį arba kelių bangos ilgių Furjė erdvės detekciją [124, 125], tačiau įprastinė taškas po taško skenavimu pagrįsta OKT angiografija (OCTA) yra ribojama registravimo spartos, akies judesių, erdvinės skyros ir aberacijų. Furjė pilnojo lauko optinė koherentinė tomografija [37] leidžia registruoti visą dvimatį vaizdą be spindulio skenavimo. Taip skersinė fazė išlieka stabili, todėl galima atlikti didelės spartos tinklainės vaizdinimą in vivo [40] ir iš to paties tūrinio duomenų rinkinio išgauti informaciją apie kraujo tėkmę [127].

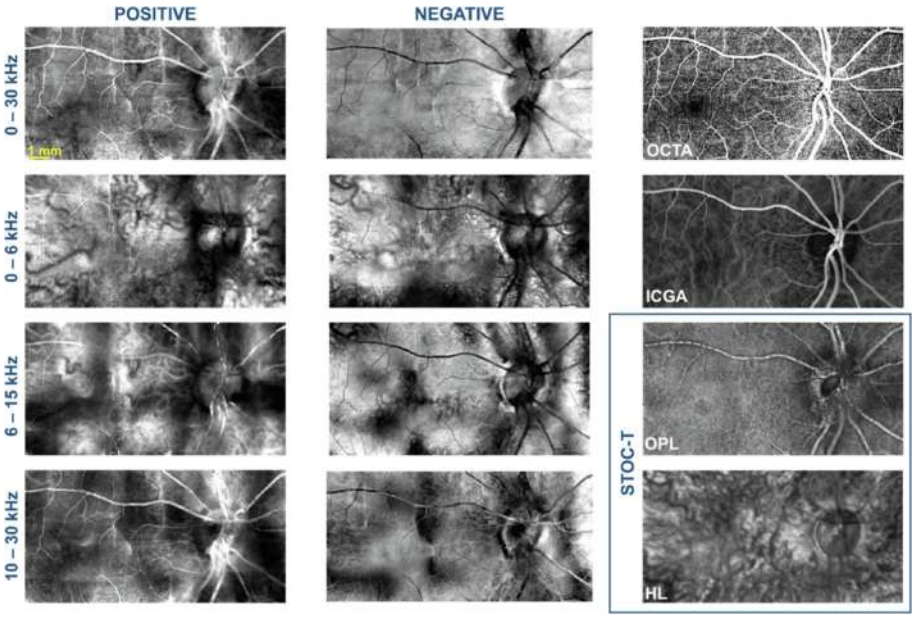


Figure 5.6: Didelio ploto kraujo tėkmės vaizdai, gauti naudojant MLDH skirtinguose dažnių diapazonuose, palyginami su įprastine skenuojančia OKT angiografija (Optopol Revo), ICGA (Heidelberg Engineering) ir STOC-T struktūriniu vaizdinimu [127].

Didelio ploto MLDH (kelių bangos ilgių lazerinė Doplerio holografija; angl. multiwavelength laser Doppler holography) kraujo tėkmės vaizdai buvo gauti sujungiant matavimus iš kelių persidengiančių tinklainės sričių (paveikslas 5.6), įskaitant optinį diską ir geltonąją dėmę. Kiekvienos vietos registravimo trukmė buvo 255 ms, o 32 vietos buvo įregistruotos per $\approx$ 8,2 s [127]. Lyginant su STOC-T, ICGA (angl. indocyanine green angiography) ir įprastine OCTA, MLDH užtikrina nuo gylio ir kraujo tėkmės priklausantį kontrastą, naudojant dažninį galios spektrinio tankio (angl. PSD) atrinkimą. Visas 0–30 kHz diapazonas daugiausia atskleidžia vidinių tinklainės sluoksnių kraujo tėkmę, o 0–6 kHz diapazonas išryškina lėtesnės tekmės, stambesnes gyslainės kraujagysles, 6–15 kHz diapazonas išryškina greitesnę kraujo tėkmę gyslainėje, o 10–30 kHz

diapazonas leidžia dideliu kontrastu vizualizuoti greičiausią kraujo tėkmę [127]. Taigi, dažninė MLDH atranka leidžia atskirti skirtingo greičio kraujo tėkmės komponentus ir suteikia išsamesnę informaciją apie kraujagyslių struktūrą nei vien tik OCTA ar ICGA [127].

Deformuojamosios membranos nauda Furjė PL-OKT sistemoje

Norėdami dar labiau padidinti Furjė pilnojo lauko optinės koherentinės tomografijos sistemos jautrį, į optinę schemą buvo integruota deformuojamoji membrana. Deformuojamos membranos priedas prie STOC-T sistemos 5.1 matomas paveiksle 5.7. OKT sistema veikė pagal 5.1 pav. aprašytą konfigūraciją, kurios pradžioje buvo deformuojamosios membranos posistemė 5.7. Šviesa iš šaltinio buvo atvedama 1,5 m ilgio vienmodžiu šviesolaidžiu (MJ-3A3A-850-5/125-3-1, OZOptics). Lazerio spinduliuotė buvo nukreipiama į deformuojamąją membraną, kuri moduliavo fazės pasiskirstymą ir projektavo jį į daugiamodį šviesolaidį (300 m ilgio, $NA = 0{,}22$, 50 µm šerdies diametro). Toks šviesolaidis sužadina apie 840 modų, kurios laike atskiriamos didesniu atstumu nei apšvietimo šaltinio koherentiškumo ilgis. Sumažinto erdvinio koherentiškumo šviesa, išeinanti iš daugiamodžio šviesolaidžio buvo nukreipta į interferometrą.

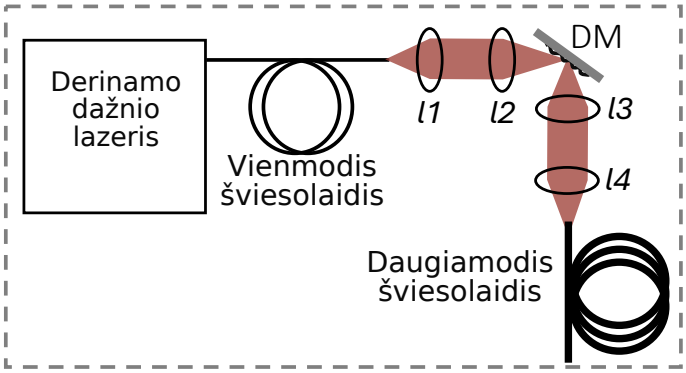


Figure 5.7: Papildoma deformuojamos membranos schema triukšmo mažinimui. Šviesa fokusuojama į DM, o po to fokusuojama į šviesolaidį.

Deformuojamosios membranos įtaka buvo išbandyta vaizdinant atspindinčius bandinius. Kaip bandinys buvo naudojama atspindinti USAF skiriamosios gebos taikinys, prieš kurį buvo ND filtras. Pirmiausia buvo registruojami vaizdai be deformuojamosios membranos. Paveikslas 5.8 (a) matomas ryškus dėmelių triukšmas, visiškai užgožiantis bandinio struktūrą. Naudojant erdvinį filtravimą Furjė erdvėje buvo pašalintas ne tik dėmelių triukšmas, bet ir visas USAF taikinio vaizdas (Paveikslas 5.8 (b)). Įjungus deformuojamąją membraną, USAF taikinio vaizdas tapo aiškiai matomas netaikant erdvinio

filtravimo (1 pav. 5.8 (c)). Nors ne visos dėmelės buvo pašalintos, deformuojamoji membrana leido atvaizduoti atspindintį bandinį, kuris prieš tai buvo visiškai užgožtas dėmelių triukšmo .

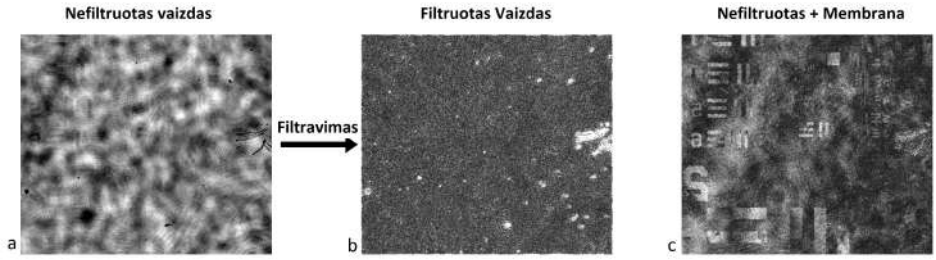


Figure 5.8: USAF taikinys už ND filtro. a) USAF taikinio nesimato už dėmelių, (b) Furjė filtavimas išvalo dėmeles kartu su atspindinčiu USAF taikiniu, (C) kai naudojama membrana, USAF taikinys matomas be papildomo filtravimo.

Kitame eksperimente modų triukšmo mažinimui buvo panaudotas agurko ląstelių bandinys. Paveiksle 5.9 pateikti ląstelių vaizdai, užregistruoji naudojant daugiamodžio šviesolaidžio ir deformuojamosios membranos kombinaciją, skirtą šviesos koherentiškumui ir koherentiniam triukšmui mažinti. Palyginę vaizdus, užregistruotus įjungus ir išjungus deformuojamąją membraną, matome, kad daugiamodžio šviesolaidžio ir deformuojamosios membranos derinys sumažina triukšmą ir leidžia užregistruoti didesnio kontrasto vaizdus tiek XZ, tiek XY pjūviuose.

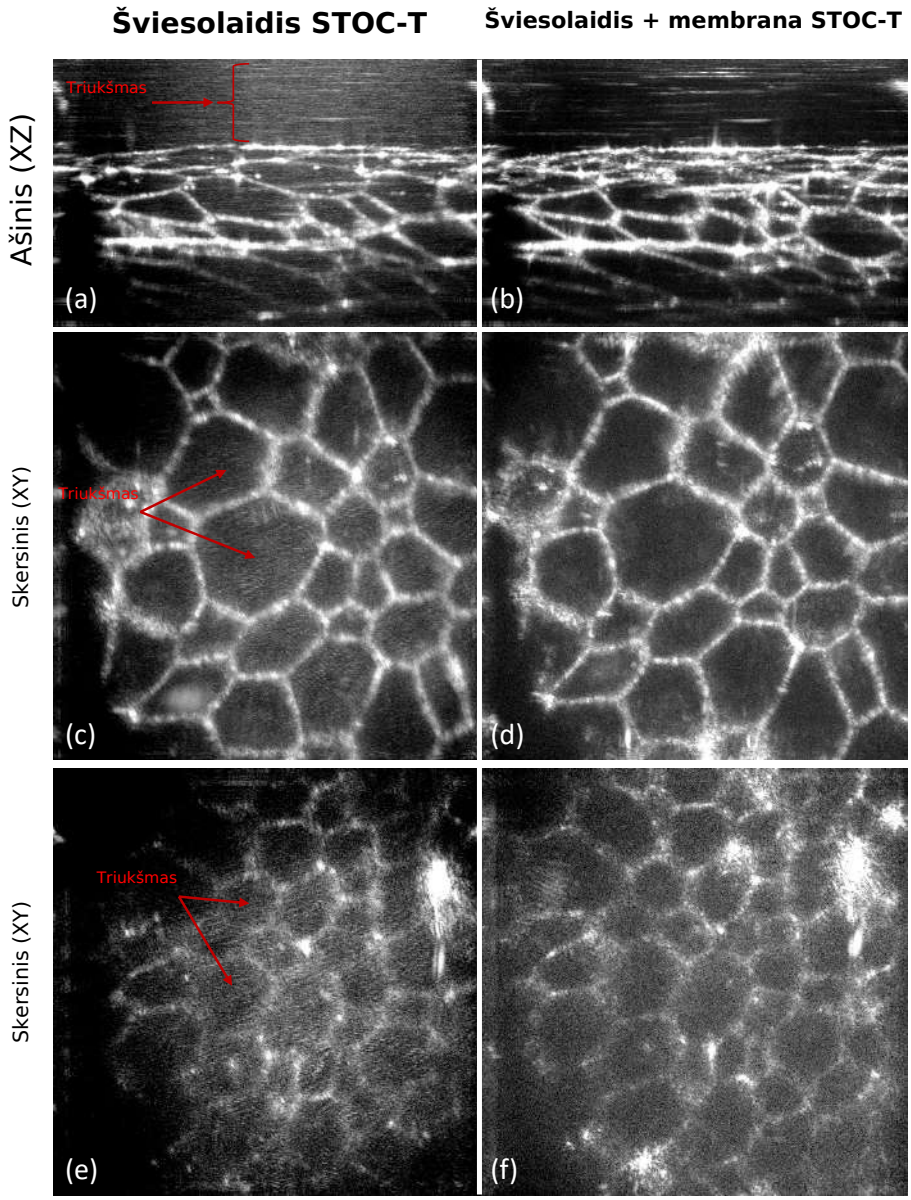


Figure 5.9: Agurko ląstelių vaizdai, gauti naudojant multimodinį šviesolaidį (a, c, e) ir jį kartu su membrana (b, d, f). Šis derinys leidžia efektyviau pašalinti koherentinį triukšmą.

STOC-T sistemos jautris buvo išmatuotas pagal standartinį metodą, darant prielaidą, kad sistema yra optimizuota ir jos veikimą riboja tik šūvio (shot) triukšmas. Todėl jautris buvo apskaičiuotas be vidurkinimo, siekiant gauti patikimą sistemos charakteristiką. Matavimų trukmę ribojo derinamo dažnio lazerinio šaltinio galia. Taip yra dėl tokio tipo lazerinių šaltinių galios trūkumo

bei dėl deformuojamosios membranos ir daugiamodžio šviesolaidžio nuostolių. Be vidurkinimo išmatuotas signalo ir triukšmo santykis buvo labiau ribojamas šūvio triukšmo nei koherentinio triukšmo, todėl vidurkinant signalo ir triukšmo santykis kito kitaip, nei būtų galima tikėtis pagal teorinius skaičiavimus. Jautris paprastai nustatomas iš gylio profilio (angl. A-scan), lyginant didžiausią signalo amplitudę su triukšmo lygiu. Įprastai tam naudojamas nuo veidrodžio atsispindėjęs signalas, susilpnintas neutralaus tankio filtru, kurio slopinimas yra žinomas. Tačiau mūsų sistemoje taikomas žemųjų dažnių filtravimas, todėl vietoje veidrodžio buvo naudojama Ronchi gardelė, kurios atspindžio vertė yra žinoma.

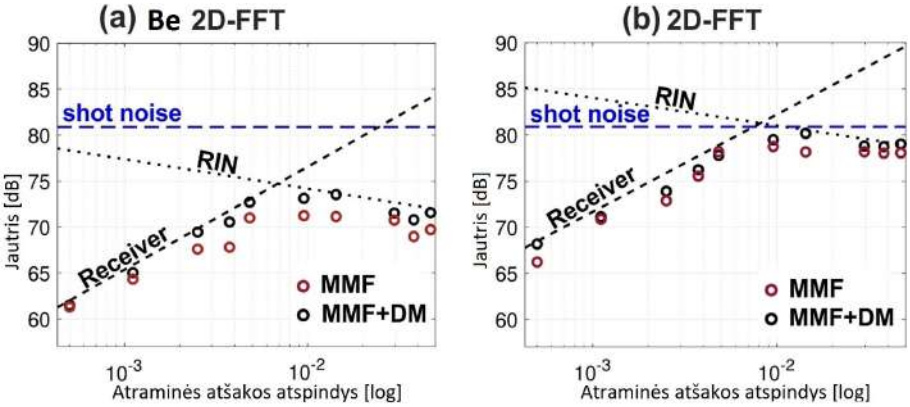


Figure 5.10: STOC-T sistemos jautrio įvertinimas naudojant Ronchi gardelę kaip atspindintį bandinį. Jautris matuojamas kaip atraminio atspindžio funkcija kai triukšmas yra sumažintas su šviesolaidžiu ir šviesolaidžio ir membranos kombinacija. (a) be Furjė filtro (b) su Furjė filtru.

Paveiksle 5.10 pateiktas sistemos jautrio įvertinimas, rodantis mažiausią sistemos užregistruojamą signalą. X ašyje pateiktas skirtingas atraminės atšakos filtro slopinimas, o bandinio atšakos filtro slopinimas išliko pastovus. Y ašyje atvaizduotas pasiekiamas jautris bei teoriškai apskaičiuotas triukšmo lygis. Matome, kad modų triukšmo slopinimas taikant dvimatį Furjė filtravimą padidina jautrį maždaug 5 dB ir leidžia pasiekti teorinę 80 dB ribą. Neutralaus tankio filtrai buvo įdėti kampu, tam kad į kamerą nepatektų tiesioginis atspindys nuo filtro paviršiaus.

Siekdami įvertinti naujos STOC-T sistemos galimybes, buvo atliktas eksperimentas vaizdinant žmogaus tinklainę in vivo [145].

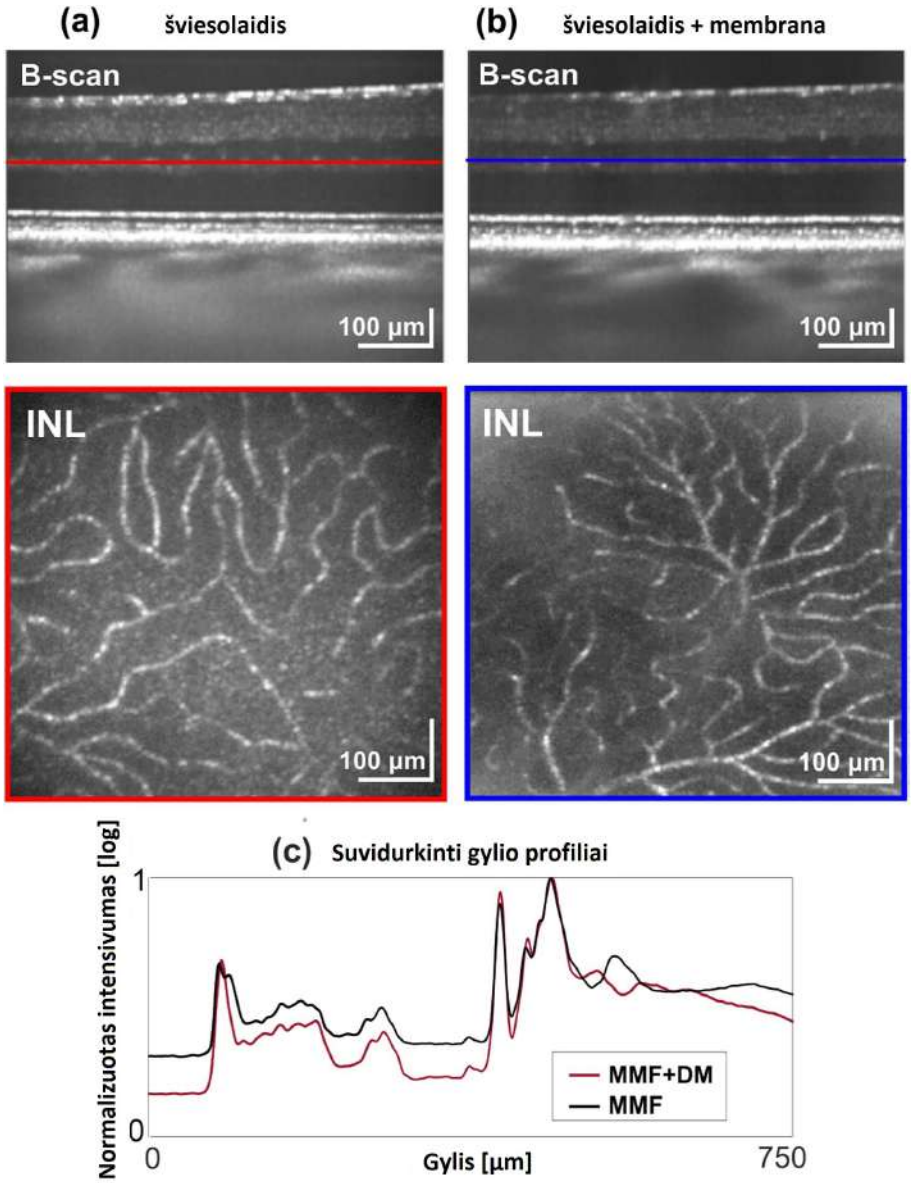


Figure 5.11: Tinklainės vaizdų palyginimas (a) tik multimodinis šviesolaidis (b) multimodinis šviesolaidis ir deformuojamoji membrana, (c) suvidurkintų gylio profilių funkcija nuo gylio.

Paveiksle 5.11 palyginami in vivo tinklainės vaizdai, užregistruoti naudojant dvi STOC-T sistemos konfigūracijas: tik multimodinis šviesolaidis (paveikslas 5.11(a)), ir multimodinis šviesolaidis kartu su deformuojamąja membrana (paveikslas. 5.11(b)). Vaizdai buvo registruojami tinklainės dalyje, esančioje 5°

virš geltonosios dėmės. Dėl vaizdo atsikartojamumo, eksperimento metu buvo tik įjungiama/išjungiama deformuojamoji membrana. Tačiau registravimo metu dėl neišvengiamų akies judesių vaizdinama tinklainės pajudėjo (paveikslai 5.11(a) ir (b)).

Rezultatai rodo, kad triukšmas abiejose konfigūracijose skiriasi. Šviesolaidžio ir membranos konfigūracijoje koherentinis triukšmas yra mažesnis nei naudojant vien tik multimodinį šviesolaidį. Vidurkintų gylio profilių palyginimas taip pat rodo nedidelius gyslainės sluoksnio skirtumus, kurie atsirado dėl nedidelio tinklainės vietos poslinkio matavimo metu. Taigi, koherentinio triukšmo sumažinimas parodo deformuojamosios membranos ir šviesolaidžio kombinacijos efektyvumą. Šis priedas leido pagerinti vaizdų kokybę, sumažinti triukšmą, padidinti signalo ir triukšmo santykį bei padidinti sistemos jautrį iki 80 dB.

Didelio pralaidumo Furjė PL-OKT

Pagrindinis kiekvieno interferometro elementas yra pluošto daliklis. Įprastai, optinėse sistemos naudojamas 50:50 pluošto daliklis, kuris praranda apie 75 % šviesos. Norėdami padidinti sistemos efektyvumą, 50:50 pluošto daliklį pakeistėme 90:10 pluošto dalikliu, o signalą nukreipti į kamerą buvo panaudotas nukreipiantis veidrodis (pick-off mirror), leidžiantis registruoti signalą iš tos pačios pluošto daliklio pusės, iš kurios ateina apšvietimas [150]. Tokia konfigūracija yra įmanoma tada, kai bandinys išsklaido šviesą plačiais kampais, kas yra įprasta biologiniams audiniams [149].

Didelio pralaidumo STOC-T (HT-STOC-T) sistema buvo sujungta su Linniko interferometru (paveikslas 5.12).

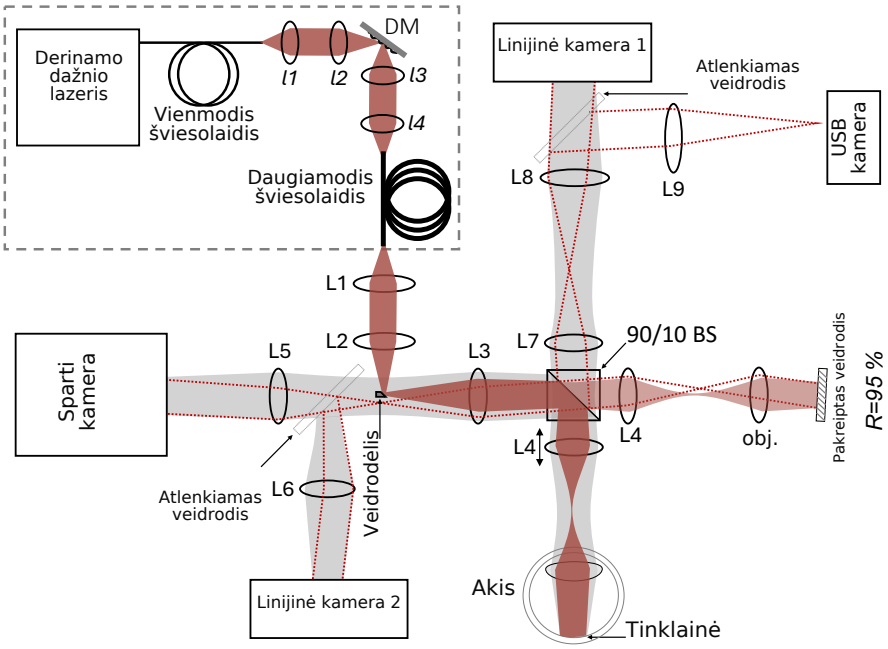


Figure 5.12: Didelio pralaidumo STOC-T sistema, sudaryta iš apšvietimo posistemės su deformuojamąja membrana ir vaizdinimo sistemos. Apšvietimo posistemėje lazerio spinduliuotė, atsispindėjusi nuo deformuojamosios membranos, nukreipiama į ilgą daugiamodį šviesolaidį. Vaizdinimo sistema pagrįsta Linniko interferometru ir keturiomis vaizdo kameromis: viena 2D ypač didelės spartos kamera ir dviem linijinėmis kameromis. USB kamera yra pagalbinė kamera, naudojama sistemai sulygiuoti. $L1$–$L9$ – achromatiniai lęšiai. Raudona spindulio trajektorija žymi apšvietimo ir atraminį spindulį, o pilkos spindulio trajektorijos žymi išsklaidytą šviesą.

Pirma buvo išmatuotas sistemos jautris naudojant 50:50 pluošto daliklį, o vėliau 90:10 pluošto daliklį. Jautrio matavimams buvo naudojama difrakcinė gardelė (150 griovelių, 500 nm žingsnio, 64-397, Edmund Optics), uždengta ND filtru (3,97 optinis tankis spinduliui praeinant pirmyn ir atgal). Sistemos jautris buvo nustatytas naudojant šią gardelę pagal metodiką, aprašytą [145].

Nustatyta, kad standartinės sistemos su 50:50 pluošto dalikliu vieno tūrio jautris siekė 81,2 dB, o didelio pralaidumo sistemos su 90:10 pluošto dalikliu buvo 86 dB [150]. Taigi didelio pralaidumo OCT sistema pasiekė 2,8 karto (4,5 dB) didesnį registravimo jautrį. Vidurkinant kelis tūrius jautris padidėjo iki 3,5 karto (4,5 dB). Jautrio priklausomybė nuo vidurkinimo matoma paveiksle 5.13. Sistema veikė šūvio triukšmo ribojamo režimu, todėl jautris didėjo tiesiškai, kaip ir rašoma teorijoje [141, 145].

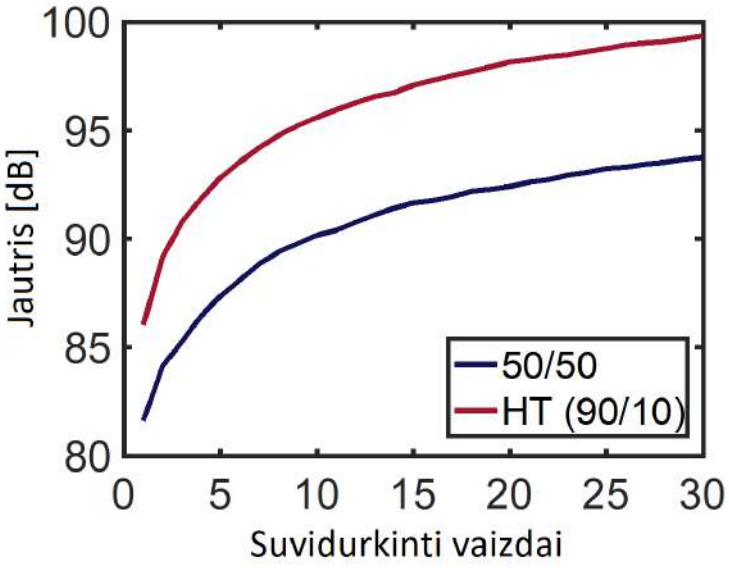


Figure 5.13: Didelio pralaidumo STOC-T sistema pasiekia 3,5x signalo ir triukšmo santykio padidėjimą ($\sim$ 5,4 dB jautrumo padidėjimą) lyginant su įprasta STOC-T.

Toliau naujosios sistemos pranašumas buvo pademonstruotas vaizdinant šviesą sklaidančius bandinius. Tam buvo naudojama USAF taikinys, ant kurio buvo uždėta lateksinė pirštinė, kuri sklaidė šviesą. Apskaičiuotas signalo ir triukšmo santykio skirtumas tarp paprastos ir didelio pralaidumo sistemos parodė, kad sistema su 90:10 pluošto dalikliu pasiekia signalo ir triukšmo santykį 3,2 kartus (5,2 dB) didesnį nei įprasta konfiguracija paveikslas 5.14).

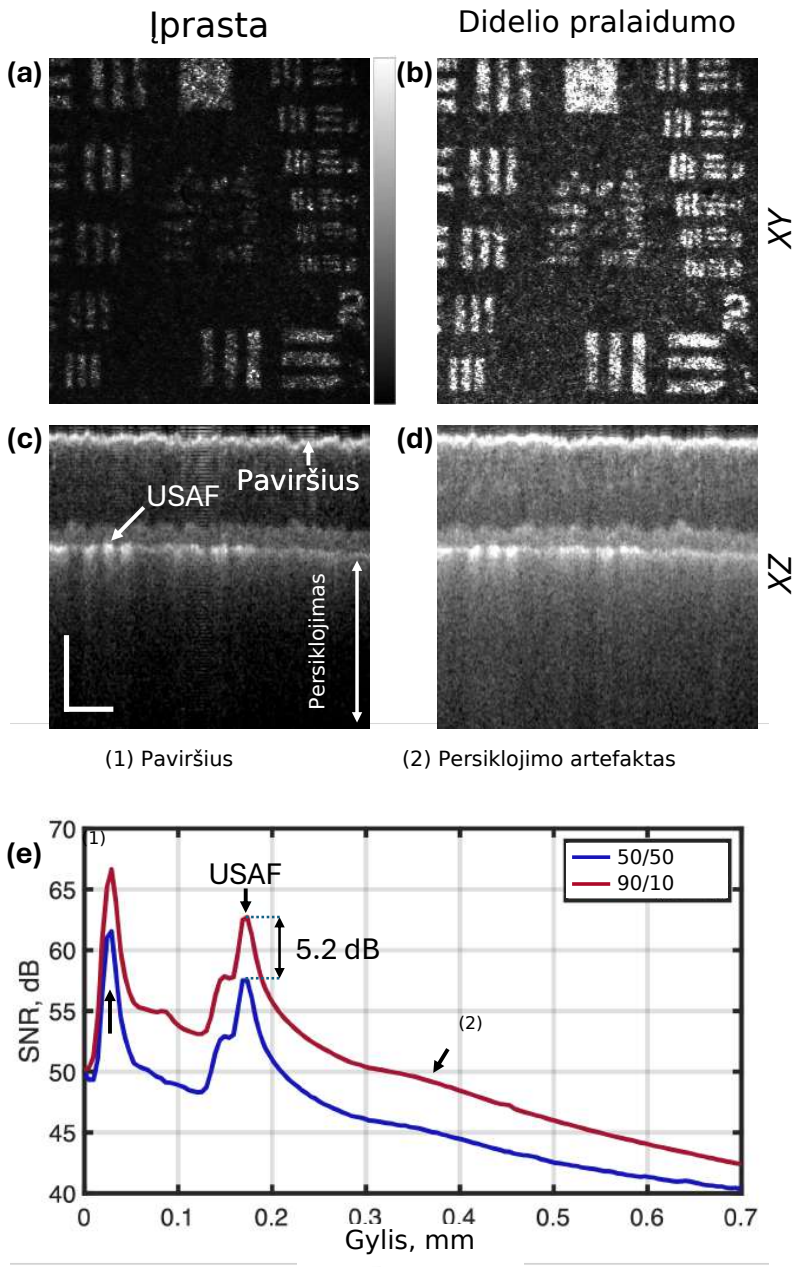


Figure 5.14: Didelio pralaidumo sistema pagerina signalo ir triukšmo santykį 3,2 karto (5,2 dB) vaizdinant USAF taikinį už sklaidančio sluoksnio. (a, b) USAF taikinio en face vaizdai, užregistruoti naudojant įprastą ir didelio pralaidumo konfigūracijas. (c, d) Tomografiniai skerspjūviai, pateikti logaritminėje skalėje, gauti atitinkamai naudojant įprastą ir didelio pralaidumo konfigūracijas. Už USAF taikinio pavaizduotas signalas yra koherentinio triukšmo artefaktas. (e) kreivė, gauta vidurkinant gylio profilius.

Galiausiai signalo–triukšmo santykio pagerėjimas buvo parodytas vaizdinant žmogaus tinklainę in vivo. Tinklainės vaizdinimui buvo naudojama antroji linijinė kamera. Eksperimente buvo vaizdinama sveiko 46 metų savanorio tinklainė. Vaizdai buvo suformuoti vidurkinant 20 nuosekliai užregistruotų tomografinio pjūvio vaizdų (angl. B-scan). Rezultatai rodo didelį signalo ir triukšmo santykio pagerėjimą naudojant didelio pralaidumo sistemą. Paveikslas 5.15 (a) ir (b) pateiktas tik didelio pralaidumo konfigūracijos gaunamas signalo pagerėjimas. Tinklainės skerspjūvio vaizdai, pateikti paveiksle 5.16, buvo užregistruoti naudojant didelės spartos dvimatę kamera. Šiuose vaizduose aiškiai atskiriami pagrindiniai tinklainės sluoksniai.

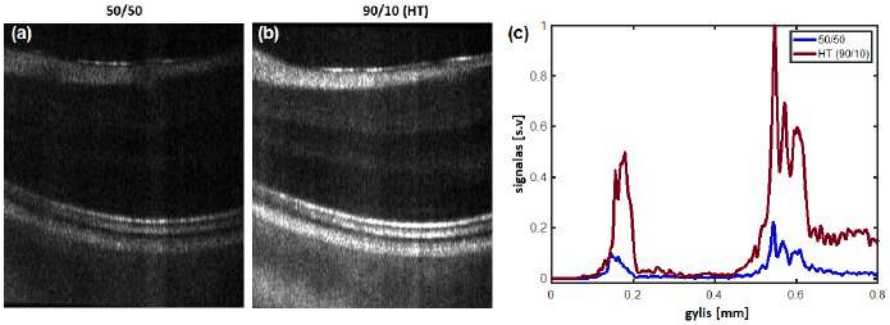


Figure 5.15: Tinklainės vaizdų palyginimas vaizdinant linijine kamera: (a) įprasta sistema, (b) didelio pralaidumo sistema, (c) linijiniai profiliai.

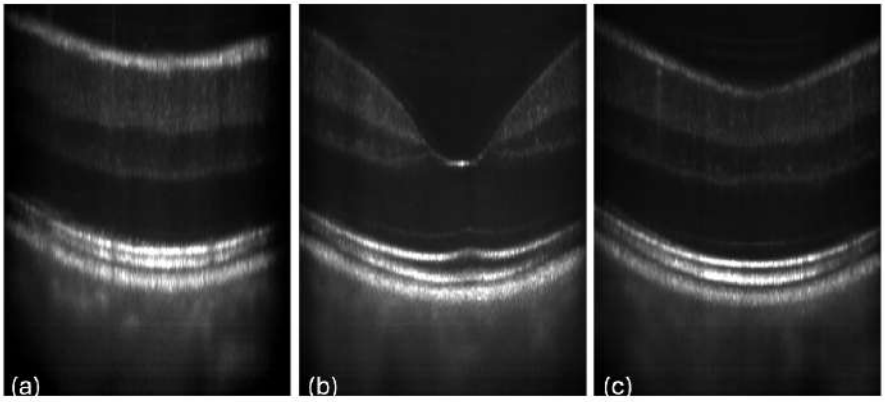


Figure 5.16: Tinklainės vaizdai registruoti greita 2D kamera.

Taigi, didelio pralaidumo konfigūracija gali pagerinti Furjė pilnojo lauko OKT sistemos panaudojimą medicininiams ir moksliniams tyrimams. Galėdami detektuoti didesnį šviesos kiekį nuo bandinio, galima naudoti mažesnės galios šviesos šaltinį ir taip sumažinti fototoksiškumo riziką, kuri yra ypač

svarbi oftalmologiniuose tyrimuose. Be to, padidėjęs jautris leidžia registruoti vaizdus naudojant mažesnį vidurkinimų skaičių, todėl sumažėja judesio artefaktų įtaka in vivo matavimų metu.

Laikinė pilnojo lauko optinė koherentinė tomografija

Defokuso korekcija

Laikinė viso lauko optinė koherentinė tomografija (TD-FF-OCT) yra interferometrinis metodas, naudojamas registruoti aukštos skiriamosios gebos biomediciniinius vaizdus. Naudojant laikiškai ir erdviškai nekoherentišką šviesos šaltinį, galima registruoti audinių vaizdus dideliame gylyje. Tačiau esant defocusui arba kitoms optinėms aberacijoms, vaizdo kokybė blogėja, ypač vaizdinant gilesnius sluoksnius. Sukūrėme skaitmeninę fokusavimo korekciją, kuri veikia, kai bandinio ir atraminės atšakų optiniai keliai yra vienodi. Fokusavimo korekcija gali būti taikoma tiek sklaidantiems, tiek atspindintiems bandiniams, o defokuso korekcija veikia iki 1 mm gylio.

Skaitmeninei aberacijų korekcijai pademonstruoti buvo sukurta laikinė pilnojo lauko optinės koherentinės tomografijos (angl. TD-FF-OCT) sistema. Apšvietimui naudotas mažo erdvinio koherentiškumo baltosios šviesos LED šaltinis (MNWHL4, Thorlabs). Sistema buvo pagrįsta Linnik interferometru, kuriame naudoti du identiški objektyvai (paveikslas 5.17). Interferometre buvo naudojamas įprastas 50/50 pluošto daliklis.

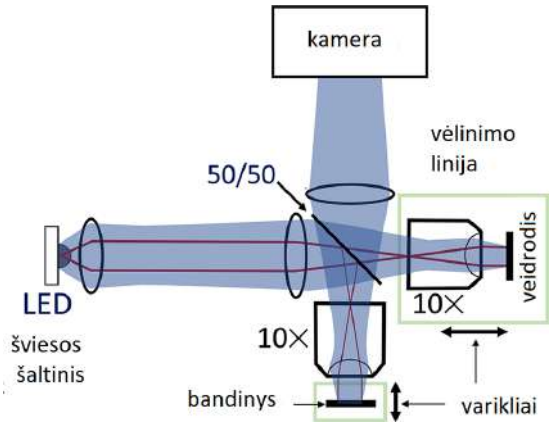


Figure 5.17: Principinė pilno lauko OKT sistema. Mėlyna - nekoherentiška LED šviesa, raudona - koherentiška lazerio šviesa.

Tiek bandinio, tiek atraminėje atšakose buvo naudojamos vėlinimo linijos (T-NA08A25-S, Zaber). Jos leido atlikti bandinio išilginį skenavimą ir stumdyti visą atraminę atšaką (žalia spalva 4.1 pav.). Sumažinus optinio kelio skirtumą tarp bandinio ir atraminės atšakų iki šviesos šaltinio koheren-

tiškumo nuotolio, interferencinis vaizdas buvo registruojamas kamera. Siekiant sulyginti bandinio ir atraminės atšakų signalų galias, atraminėje atšakoje buvo įterptas 0,6 OD optinio tankio (ND) filtras, dėl kurio grįžtančio signalo galia sumažėjo iki 6 %. Chromatinei dispersijai kompensuoti bandinio atšakoje buvo įdėtas 0 OD tokio paties storio ND filtras. Fazės poslinkis buvo sukuriamas ant atraminio veidrodžio laikiklio pritvirtinus pjezoelektrinį elementą (STr-25, Piezomechanik). Siekiant pademonstruoti defokuso korekciją, buvo naudojamas didelės skiriamosios gebos USAF taikinys (Highres-2, Newport). Defokuso korekcija buvo atlikta iki 1 mm defokusavimo [155]. Paveiksle 5.18 pateikti įprastinės mikroskopijos (šviesaus lauko) vaizdai, užregistruoti užblokavus atraminę atšaką, taip pat PL-OKT vaizdai, užregistruoti esant skirtingoms defokusavimo vertėms, ir atitinkami jų skaitmeniškai refokusuoti vaizdai. Matome, kad PL-OKT vaizdai yra mažiau jautrūs defokusavimui, lyginant su įprastinės šviesaus lauko vaizdais, pateiktais paveikslo 5.18 a–d dalyse. Šis PL-OKT atsparumas defokusavimui jau buvo aprašytas ankstesniuose literatūros šaltiniuose [8]. Vis dėlto, didinant defokusavimo atstumą, PL-OKT vaizdai taip pat tampa neryškūs (5.18 e–h). Naudojant skaitmeninę defokuso korekciją, PL-OKT vaizdai gali būti refokusuojami, kaip parodyta paveikslo 5.18 i–l dalyse.

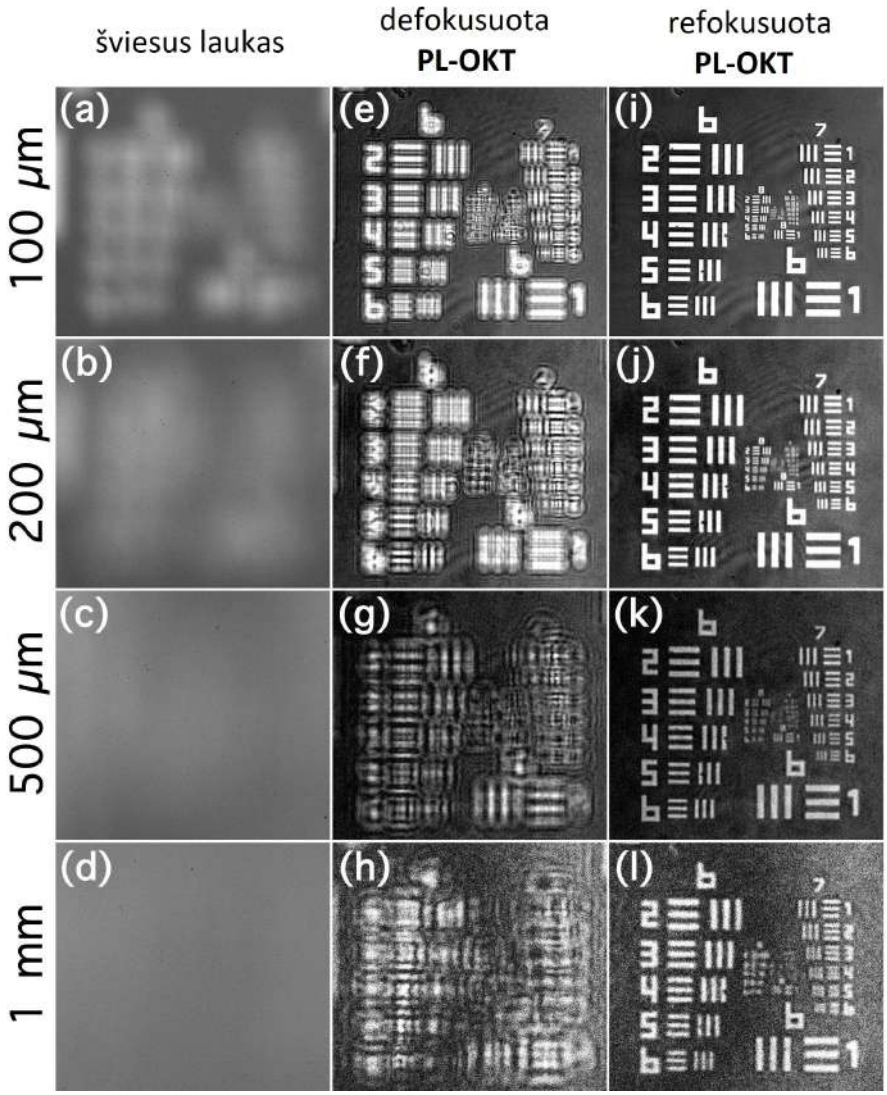


Figure 5.18: Skaitmeninio defokusavimo korekcijos demonstravimas PL-OKT USAF taikinio vaizduose, užregistruotuose palaipsniui didinant defokusavimo gylį: 100 µm, 200 µm, 500 µm ir 1 mm. (a–d) Įprasti šviesaus lauko vaizdai, užregistruoti užblokavus atraminę atšaką. (e–h) PL-OKT vaizdai. (i–l) PL-OKT vaizdai, kuriuose atlikta skaitmeninė defokusavimo korekcija.

Siekiant išvengti priklausomybės nuo objektyvo NA ir bangos ilgio, buvo naudojamas bedimensis koordinatinis vienetas $u = 4kznsin^2(\frac{\alpha}{2})$, kur k yra bangos vektorius, z – atstumas išilgai optinės ašies, n – bandinio lūžio rodiklis, o α – šviesos kūgio, formuojančio fokusą, pusinis kampas. Išmatuotas objektyvo fokusavimo gylis yra 10 µm ($u = 6,76$), t. y. 100 kartų mažesnis už 1 mm defokusavimą ($u = 676,4$).

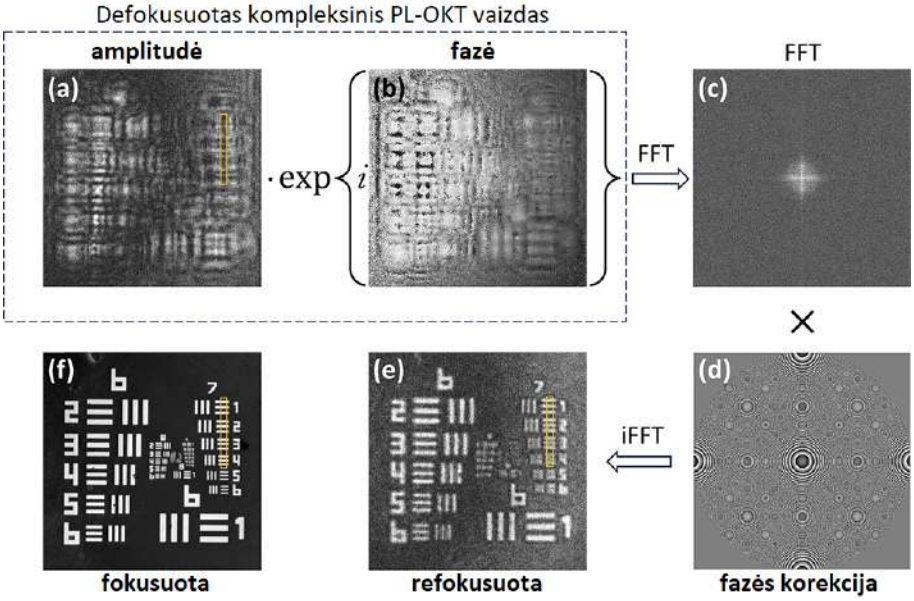


Figure 5.19: Skaitmeninė USAF taikinio, defokusuoto 1 mm (u = 676,4), korekcija. Kompleksinis signalas, kurį sudaro amplitudė (a) ir fazė (b), Furjė transformacija (c), dauginimas iš kvadratinės fazės funkcijos (d) atvirkštinė Furjė transformacija, refokusuotas vaizdas (e). Palyginimui pateiktas sufokusuotas vaizdas (f).

Paveikslo 5.19 (a) dalyje parodyta, kad rankiniu būdu defokusavus bandinį, taikinio juostelės tampa tokios neryškios, kad jų nebeįmanoma individualiai atskirti. Kaip parodyta paveikslo 5.19 (e) dalyje, pritaikius skaitmeninę defokuso korekciją, vaizdas gali būti atkurtas ir vėl sufokusuotas. Tačiau, lyginant su sufokusuotu vaizdu, pateiktu paveikslo 5.19 (f) dalyje, perfokusuoto vaizdo erdvinė skyra yra mažesnė.

Norėdami nustatyti, kaip rankinis bandinio defokusavimas ir skaitmeninis refokusavimas veikia erdvinę skyrą, buvo paimti linijiniai profiliai einantys per USAF taikinio 7-osios grupės 1–4 elementus (paveikslas 5.18). Linijiniai profiliai buvo gauti sufokusuotiems, defokusuotiems ir skaitmeniniu būdu refokusuotiems vaizdams (paveikslas 5.19).

Siekiant ištirti PL-OKT signalo pokyčius defokusavimo metu, buvo naudojami du žingsniniai varikliai, skirti atitinkamai bandinio ir atraminei atšakoms. Kiekvienai bandinio padėčiai visa atraminė atšaka (veidrodis ir objektyvas) buvo stumdoma ta pačia kryptimi ir tokio paties dydžio žingsniais (išilgai optinės ašies) Matavimai atlikti nuo nuo -1 iki 1 mm kiekvienai defokusavimo vertei [155].

Kiekvienoje defokuso padėtyje buvo užregistruoti laikinės PL-OKT vaizdai, o iš vaizdų rinkinio buvo išskirtas linijinis gylio profilis.

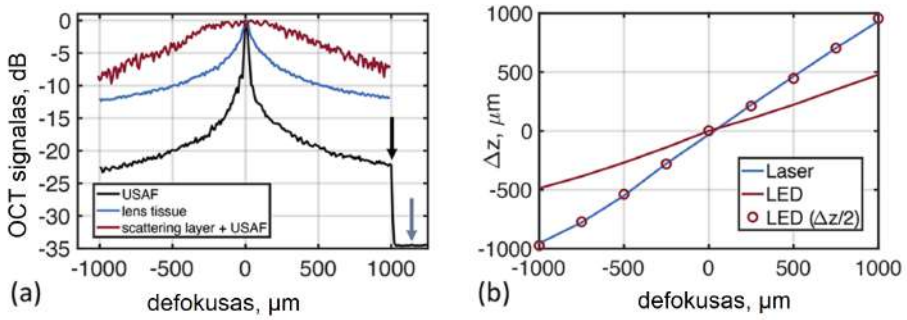


Figure 5.20: (a) PL-OKT signalas priklausomai nuo bandinio defokusavimo, gautas naudojant tris skirtingus bandinius. Juoda rodyklė nurodo padėtį, kurioje buvo sustabdytas atraminės atšakos variklis, siekiant sąmoningai sukurti atraminės ir bandinio atšakų optinių kelių ilgių skirtumą. Mėlyna rodyklė žymi dėl šios neatitikties atsirandantį signalo foną. (b) Skaitmeninio refokusavimo priklausomybė nuo fizinio defokusavimo, naudojant LED ir lazerinį apšvietimą.

Šiame eksperimente buvo naudojami trys skirtingi bandiniai (paveikslas 5.20 (a)): vienas atspindintis (USAF) ir du sklaidantieji bandiniai.

Skaitmeniniam refokusavimui buvo naudojamas Frenelio sklidimo operatorius: $exp(-j\pi\lambda\Delta z[f_x^2 + f_y^2])$. Kai bandinys buvo defokusuotas per Δz, naudojant LED kaip apšvietimo šaltinį, skaitmeninis refokusavimas turėjo būti apskaičiuojamas naudojant $\Delta z/2$ reikšmę. Šis reiškinys buvo pastebėtas ant USAF taikinio užklijavus du matinės lipniosios juostos sluoksnius. Toks bandinys buvo naudotas atliekant eksperimentą su abiem apšvietimo šaltiniais: erdviškai koherentišku lazeriu (SLD850S-A20W, Thorlabs) ir LED šviestuku (M850L3, Thorlabs). Abiejų šaltinių centrinis bangos ilgis buvo 850 nm, o naudojant tą patį spektrinio pločio filtrą abiejų šaltinių spektrinis juostos plotis buvo sumažintas iki 10 nm. Naudojant lazerį ir defokusavus bandinį Δz reikalinga tokio pat dydžio skaitmeninio refokusavimo vertė Δz. Tačiau naudojant LED kaip apšvietimo šaltinį, tam pačiam defokusavimui Δz refokusuoti reikia tik pusės skaitmeninio sklidimo nuotolio $\Delta z/2$ (paveikslas 5.20(b)). Šie rezultatai buvo papildomai patikrinti apskaičiuojant visų vaizdo pikselių standartinį nuokrypį, kuris buvo vaizdo ryškumo matmuo. Šį reiškinį galima paaiškinti koherentinei ir nekoherentinei šviesai būdingų galios skėsties funkcijų (angl. PSF) skirtumu [157]. Refokuso galimybes buvo pademonstruotos už stipriai sklaidančio sluoksnio padėjus sulankstyto lęšių valymo servetėlės bandinį (MC-5, Thorlabs). Paveiksle 5.21 pateikti vaizdai, gauti 100 μm gylyje žemiau bandinio paviršiaus. Bandinys buvo defokusuotas 500 μm. Siekiant kompensuoti optinio kelio pokytį, taip pat buvo stumdoma atraminė atšaka. Kadangi bandinys buvo panardintas silikoninėje alyvoje, atraminę atšaką reikėjo perstumti $n \cdot 500\ \mu m$, kur n yra silikoninės alyvos lūžio rodiklis.

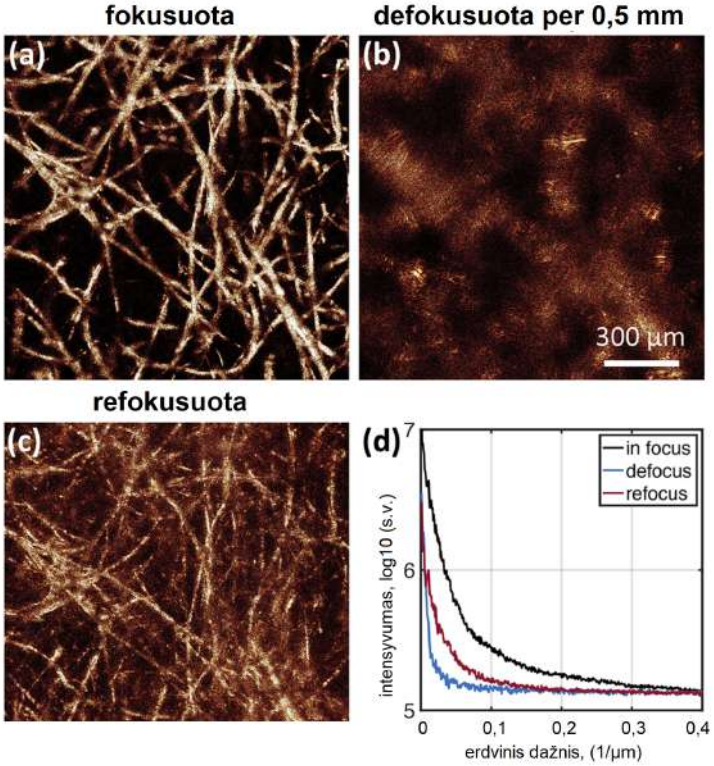


Figure 5.21: PL-OKT vaizdų, gautų 100 µm gylyje nuo servetėlės paviršiaus, skaitmeninė defokusavimo korekcija (Vaizdai normalizuoti). (a) Sufokusuotas PL-OKT vaizdas, (b) PL-OKT vaizdas, fiziškai defokusuotas 500 µm. (c) Refokusuotas PL-OKT vaizdas. (d) Erdvinio dažnio spektrai, gauti iš trijų vaizdų, pateiktų (a), (b) ir (c), (d) kreivės gautos iš nenormalizuotų FF-OKT vaizdų.

Gautas defokusuotas vaizdas, parodytas paveikslo 5.21 (b) dalyje, yra neryškus, todėl daugumos audinio plaušų neįmanoma išskirti. Tačiau pritaikius skaitmeninę defokuso korekciją, šie plaušai vėl tampa matomi (paveikslo 5.21 (c) dalis). Kaip ir buvo galima tikėtis remiantis ankstesniais rezultatais, vaizdo visiškai atkurti nepavyksta, o aukštesnieji erdviniai dažniai prarandami (paveikslo 5.21 (d) dalis).

Daugiataškis vaizdinimas panaudojant skaitmeninį mikroveidrodžių prietaisą

Optinę koherentinę tomografiją galima suskirstyti į skenuojamąją ir viso lauko OKT. Viso lauko OKT, nenaudojant skersinio skenavimo, registruoja didelės skiriamosios gebos vaizdus naudojant dvimačius detektorius (kameras). Tačiau pagrindinis tokių sistemų trūkumas yra konfokalinio sekcionavimo nebuvimas, todėl sumažėja vaizdinimo gylis ir jautris. Konfokalinis sekcionavi-

mas sumažina į detektorių patenkančios nefokusuotos šviesos kiekį bei pagerina signalo ir triukšmo santykį (SNR) [33]. PL-OKT sistemos jautris gali būti padidintas naudojant tamsaus lauko detekciją [31, 32], kuri slopina dėmelių triukšmą, tačiau kelis kartus išsklaidyta šviesa tokiu būdu nėra išfiltruojama. Konfokalinės skenuojamosios OKT spartą galima padidinti didinant vienu metu bandinyje skenuojamų taškų skaičių [160, 161]. Siekiant sujungti skenuojamosios ir viso lauko OKT sistemų privalumus, buvo panaudotas skaitmeninis mikroveidrodžių prietaisas (angl. DMD). Skaitmeninis mikroveidrodžių prietaisas gali generuoti įvairius apšvietimo struktūras, pavyzdžiui, daugiataškę struktūrą [164]. Skaitmeninis mikroveidrodžių prietaisas taip pat naudojamas konfokalinėje mikroskopijoje tiek apšvietimui, tiek detekcijai, kai atskiri mikroveidrodžiai naudojami kaip konfokalinės diafragmos, užtikrinančios konfokalinį efektą [165, 166].

Sukonstravome viso lauko OKT sistemą su konfokaliniu optiniu sekcionavimu. Sistemoje naudojamas skaitmeninis mikroveidrodžių prietaisas taip, kad viename jo plote generuojama konfokalinių apšvietimo taškų matrica, o kitame – konfokalinių diafragmų matrica, slopinanti iš fokuso plokštumos sklindančią šviesą. DMD naudojamas dvigubo praėjimo [175] konfigūracijoje, tačiau apšvietimo ir detekcijos keliai nukreipiami į skirtingas skaitmeninio mikroveidrodžių prietaiso lusto puses, kuriose atitinkamai generuojami apšvietimo taškai ir diafragmos [176]. Skaitmeninio mikroveidrodžių prietaiso naudojimą įprastoje dvigubo praėjimo konfigūracijoje PL-OKT sistemose riboja tai, kad nuo mikroveidrodžių lusto antrinių elementų atgal atsispindėjusi ir išsklaidyta šviesa yra stipresnė už iš paties bandinio gaunamą šviesą. Dėl šios priežasties skaitmeninio mikroveidrodžių prietaiso negalima patogiai naudoti kaip erdvinio šviesos moduliatoriaus PL-OKT sistemose. Tačiau mums pavyko sukurti ir užpatentuoti metodą, leidžiantį išvengti šio apribojimo. Šis metodas gali atskirti konfokalinį apšvietimą ir erdviškai filtruoti užregistruotą signalą. Mūsų patentuotas išradimas [177], aprašomas kaip atspindžio konfokalinis mikroskopas, kuriame naudojamas DMD su padalyta darbine sritimi: viena dalis skirta bandiniui apšviesti, o kita – signalui detektuoti. Panaudojant tokia konfiguraciją, buvo surinkta OKT sistema Linnik interferometro pagrindu (Paveikslas 5.22), kuriame bandinio ir atraminėje atšakose naudojami du identiški objektyvai (10×/0.25, Plan N, Olympus, Tokyo, Japan), užtikrinantys 1,6 µm skersinę skyrą.

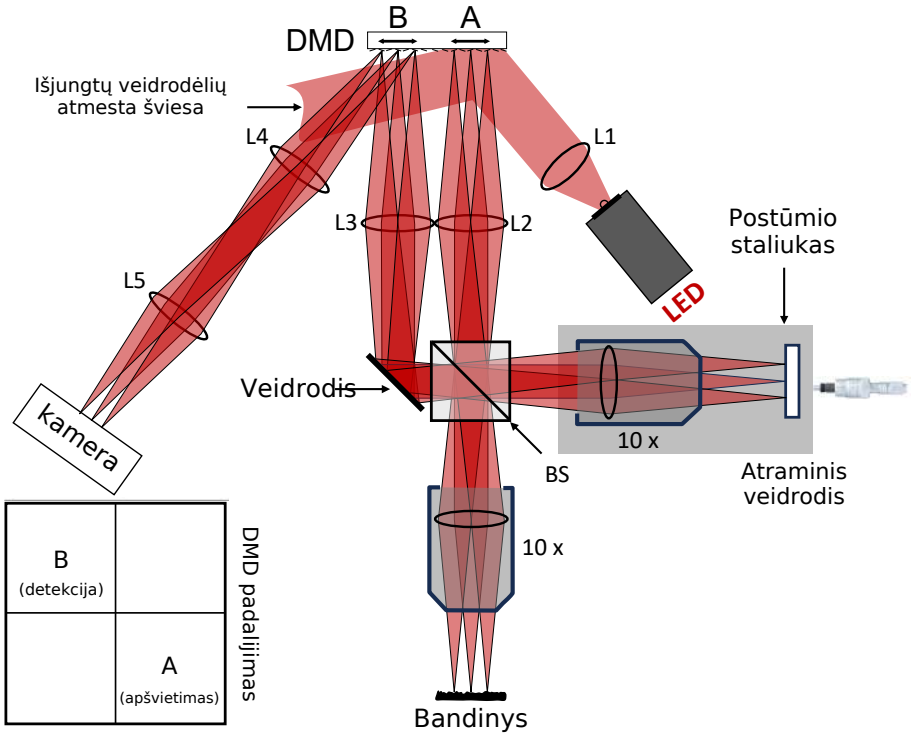


Figure 5.22: Principinė PL-OKT sistemos schema su skaitmeninių veidrodėlių prietaisu.

Siekiant nuskenuoti visą bandinį, CMOS (angl. complementary metal-oxide-semiconductor) kameros vieno išlaikymo metu skaitmeninio mikroveidrodžių prietaisu buvo generuojamos įvairių mikroveidrodžių struktūrų sekos [175]. Toks metodas leido greitai atlikti keliataškį vaizdinimą, nereikalaujant skaitmeninio mikroveidrodžių prietaiso ir kameros sinchronizavimo. Kiekvieną apšvietimo tašką sudarė vienas „įjungtas“ (angl. „on“) mikroveidrodis, o atitinkamos detekcijos diafragmos skaitmeninio mikroveidrodžių prietaiso vaizdinimo pusėje buvo suformuotos iš 2×2 „išjungtų“ (angl. „off“) mikroveidrodžių blokų. Atstumai tarp apšvietimo taškų ir detekcijos diafragmų buvo keičiami siekiant subalansuoti optinio sekcionavimo galimybes, vaizdinimo spartą ir persiklojimo triukšmą.

Taip pat, po keliataškio skenavimo buvo taikomas ir kelialinijinis skenavimo metodas [175]. Vietoje atskirų taškų matricų generavimo buvo naudojami alternatyvios skaitmeninio mikroveidrodžių prietaiso struktūros, formuojančios linijines apšvietimo ir detekcijos sritis. Kaip ir daugiataškio eksperimento atveju, apšvietimo linijų plotis buvo vieno mikroveidrodžio, o detekcijos linijų plotis buvo dviejų mikroveidrodžių. Atstumas tarp gretimų linijų buvo 15 mikroveidrodžių.

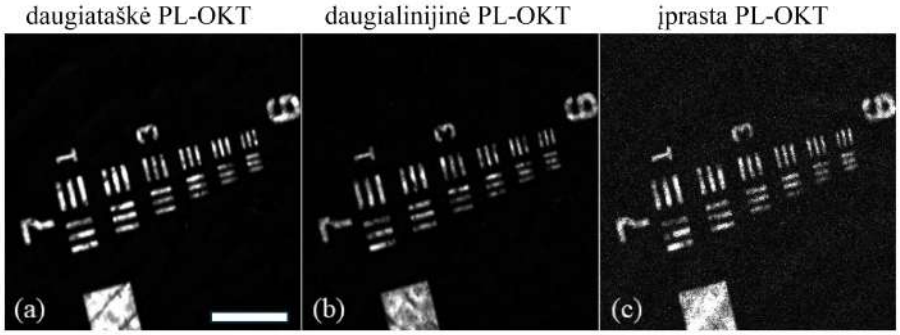


Figure 5.23: PL-OKT bandinio, pagaminto iš po sklaidančiuoju sluoksniu pritvirtinto USAF (angl. United States Air Force) taikinio, vaizdai, užregistruoti naudojant (a) kelių taškų (angl. multi-spot), (b) kelių linijų (angl. multi-line) ir (c) įprastą režimus. Mastelio juosta – 50 µm. Palyginimui vaizdai pateikti naudojant skirtingas intensyvumo skales: (a) 0–10 000 s.v., (b) 0–2000 s.v. ir (c) 0–200 s.v.

Paveiksle 5.23 pateiktas PL-OKT vaizdų, užregistruotų skirtingais režimais, palyginimas. Demonstracinio eksperimento metu keliataškis režimas veikė naudojant santykinai ilgą, 200 ms trukmės kameros ekspoziciją, todėl kadrų registravimo sparta siekė tik 5 Hz. Priešingai, tiek kelialinijinės, tiek įprastinės viso lauko OKT režimų vaizdai buvo registruojami naudojant 20 ms išlaikymo trukmę, todėl kadrų registravimo sparta siekė 50 Hz. Norint užtikrinti palyginamų rezultatų registravimą, eksperimento sąlygos buvo atitinkamai suvienodintos.

Konfokalinio skenavimo režimu (daugybės taškų) PL-OKT signalas yra gerokai stipresnis nei standartins viso lauko režimas, paveikslas 5.23(a). Toks pagerėjimas pasiekiamas todėl, kad konfokalinis sekcionavimas (12 µm (FWHM), sutampantis su USAF taikinio plokštuma) slopina iš nefokusuotų plokštumų sklindančią šviesą (nuo virš taikinio esančio sklaidančiojo sluoksnio). Dėl to daugiau šviesos pasiekia taikinį ir surenkama daugiau nuo taikinio išsklaidytos šviesos.

Linijinio skenavimo režimu PL-OKT signalo intensyvumas yra tarp kelių taškų konfiguracijos ir viso lauko konfigūracijos signalų intensyvumo. Tai galima paaiškinti daliniu konfokaliniu optiniu sekcionavimu, kuris yra mažiau efektyvus neidaugiataškiu režimu.

Vertinant vaizdo kokybės pagerėjimą, kiekvienam vaizdui buvo apskaičiuotas signalo ir triukšmo santykis (SNR). SNR buvo apibrėžtas taip:

$$SNR = \left(\frac{\sqrt{signal}}{std(\sqrt{background})}\right)^2 \tag{5.4}$$

čia signalas atitinka OKT signalo intensyvumą USAF taikinio juostelėse, o fonas nustatomas nesuderinus koherentinio sekcionavimo plokštumos su ban-

dinio plokštuma ir ten matuojant OKT signalą.

Standartinio FF-OKT vaizdo, pateikto paveikslo 5.23(c) dalyje, SNR buvo 67 s.v. Konfokalinio skenavimo režimu (paveikslo 5.23(a) dalis) gautas SNR siekė 1914 s.v., (padidėjo 29 kartus, 14,6 dB). O linijinio skenavimo konfigūracijos SNR buvo tarpinis ir siekė 529 s.v. Norėdami pademonstruoti daugiataškės konfiguracijos vaizdinimo privalumus, biologinį bandinį vaizdinome skirtinguose gyliuose. Paveiksle 5.24 pateikti agurko vaizdų skerspjūviai, gauti persluoksniuojant registruotus vaizdus, didžiausio intensyvumo signalai, užregistruoti naudojant daug taškų režimą ir vieno taško vaizdinimo režimą. Vaizdų rinkinys buvo registruojamas nuo 20 µm gylio po bandinio paviršiumi iki 1 mm gylio, o tarp gretimų vaizdų buvo 1 µm išilginis poslinkis. Visame matuotame gylių diapazone naudojant daugiataškę konfigūraciją galima išskirti daugiau bandinio struktūrinių detalių. Kai vaizdinimo gylis viršija 400 µm, standartiniu vaizdinimo režimu bandinio struktūros nebeužregistruojamos. Tačiau daug taškų vaizdinimo metodas leidžia užregistruoti bandinio struktūras beveik iki 800 µm gylio bandinyje. Šis pavyzdys rodo, kad dėl daugiataškio vaizdinimo padidėjęs signalo ir triukšmo santykis pagerina vaizdo kokybę, nes konfokalinis efektas slopina nekoherentinę foninę šviesą.

Apibendrinant, pristatyta konfokalinė-pilnojo lauko OKT sistema veikia daugiataškiu ir daugialinijiniu skenavimo režimais. Sistemoje naudojama mūsų patentuota dvigubo praėjimo geometrija pritaikyta skaitmeniniam mikroveidrodžių prietaisui. Tai įgalina konfokalinį vaizdinimą atspindžio režimu. Signalo ir triukšmo santykis buvo pagerintas sumažinus detektorių pasiekiančios nekoherentinės šviesos kiekį. Daugiataškis apšvietimas, derinamas su skaitmeninėmis apertūromis, pilnojo lauko vaizdinimo sistemoje užtikrina konfokalinį sekcionavimą ir stipriai slopina nefokusuotą šviesą, dėl ko padidėja signalo ir triukšmo santykis [175]. Viena skaitmeninio mikroveidrodžių prietaiso pusė naudojama apšvietimo taškams formuoti, o kita skirta konfokalinėms apertūroms. Taip pašalinami atgaliniai atspindžiai anksčiau ribotą skaitmeninio mikroveidrodinio prietaiso taikymą PL-OKT sistemose. Šis metodas ypač naudingas vaizdinant šviesą stipriai sklaidančius bandinius, jei naudojamas pakankamo skaisčio šviesos šaltinis.

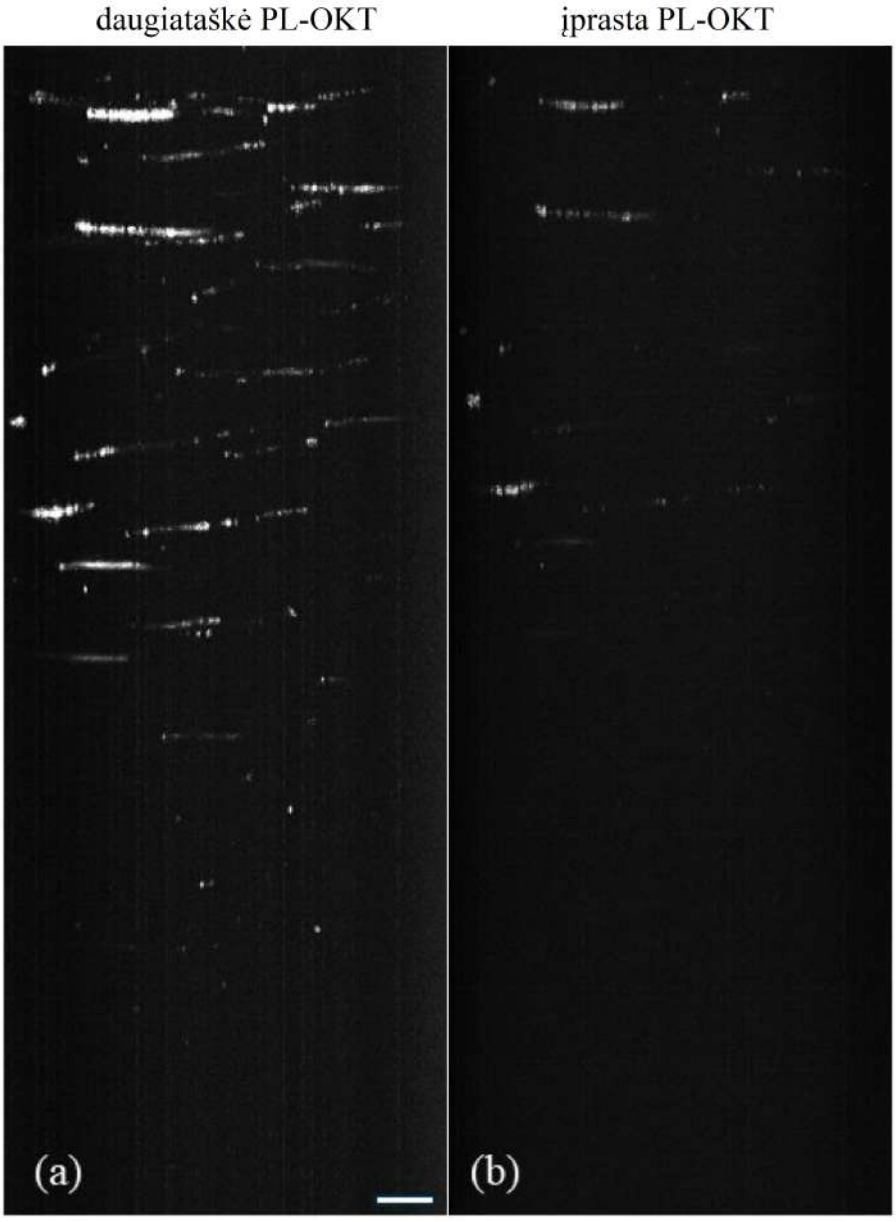


Figure 5.24: Agurko ašiniai vaizdai (XZ), užregistruoti naudojant (a) kelių taškų ir (b) įprastą režimus. Mastelio juosta – 50 µm.

Išvados

Atliekant darbą buvo padarytos tokios išvados:

1. Koherentinis triukšmas Furjė pilnojo lauko optinės koherentinės tomografijos sistemoje gali būti reikšmingai sumažintas naudojant pasyvų mažo šerdies skersmens daugiamodį šviesolaidį. Tai leidžia in vivo vienu metu užregistruoti didelės skyros tinklainės ir gyslainės vaizdus.

2. Greitai veikianti deformuojamoji membrana, kartu su daugiamodžiu šviesolaidžiu, papildomai slopina modinį triukšmą ir padidina erdvines ir laikines koherencijos optinės tomografijos sistemos jautrį tiek, kad galima išskirti tinklainės ganglijines ląsteles ir fotoreceptorius.

3. Didelio pralaidumo interferometro konstrukcija, pagrįsta 90/10 pluošto dalikliu ir vyzdžio plokštumoje esančiu atskiriamuoju veidrodžiu, dar labiau padidina erdvines ir laikines koherencijos optinės tomografijos sistemos jautrį. Tai leidžia naudoti mažesnės galios šviesos šaltinį ir sumažinti vaizdų rinkinių vidurkinimo poreikį.

4. Laikinės pilnojo lauko optinės koherentinės tomografijos sistemoje skaitmeninė defokusavimo korekcija leidžia išplėsti tinkamą vaizdinimo gylį už fizinio objektyvo vaizdinimo gylio ribų.

5. Skatmeniniu mikroveidrodžių prietaisu pagrįsta sistema, kurioje viena mikroveidrodžių matricos pusė naudojama apšvietimo taškams, o kita – skaitmeninėms konfokalinėms apertūroms formuoti, išsprendžia atgalinių atspindžių problemą ir sujungia konfokalinės mikroskopijos privalumus su pilnojo lauko optinės koherentinės tomografijos vaizdų registravimo sparta.

BIBLIOGRAPHY

[1] D. Huang, E. A. Swanson, C. P. Lin, J. S. Schuman, W. G. Stinson, W. Chang, M. R. Hee, T. Flotte, K. Gregory, C. A. Puliafito, J. G. Fujimoto, Optical coherence tomography, Science **254**(5035), 1178–1181 (1991), https://doi.org/10.1126/science.1957169.

[2] R. Chopra, S. K. Wagner, P. A. Keane, Optical coherence tomography in the 2020s-outside the eye clinic, Eye **35**(1) (2021), https://doi.org/10.1038/s41433-020-01263-6.

[3] E. Auksorius, D. Borycki, M. Wojtkowski, Crosstalk-free volumetric in vivo imaging of a human retina with fourier-domain full-field optical coherence tomography, Biomed. Opt. Express **10**(12), 6390–6407 (2019).

[4] B. Karamata, M. Leutenegger, T. Lasser, *Handbook of Full-Field Optical Coherence Microscopy* (Jenny Stanford Publishing, 2016).

[5] Y. Yasuno, Optical coherence tomography – principles, implementation, and applications in ophthalmology (2022), https://arxiv.org/abs/2212.04380.

[6] A. Fercher, C. Hitzenberger, G. Kamp, S. El-Zaiat, Measurement of intraocular distances by backscattering spectral interferometry, Optics Communications **117**(1), 43–48 (1995), https://doi.org/10.1016/0030-4018(95)00119-S.

[7] S. R. Chinn, E. A. Swanson, J. G. Fujimoto, Optical coherence tomography using a frequency-tunable optical source, Opt. Lett. **22**(5), 340–342 (1997), https://doi.org/10.1364/OL.22.000340.

[8] J. Zhang, V. Mazlin, K. Fei, A. C. Boccara, J. Yuan, P. Xiao, Time-domain full-field optical coherence tomography (td-ff-oct) in ophthalmic imaging, Therapeutic Advances in Chronic Disease **14**, 20406223231170146 (2023), https://doi.org/10.1177/20406223231170146.

[9] R. Su, M. Kirillin, P. Ekberg, L. Mattsson, Three-dimensional metrology of embedded microfeatures in ceramics by infrared optical coherence tomography – advantages and limitations (2015).

[10] R. Paschotta, Optical coherence tomography, RP Photonics Encyclopedia (2019), https://www.rp-photonics.com/optical_coherence_tomography.html.

[11] R. Su, P. Ekberg, M. Leitner, L. Mattsson, Accurate and automated image segmentation of 3d optical coherence tomography data suffering from low signal-to-noise levels, J. Opt. Soc. Am. A **31**(12), 2551–2560 (2014), https://doi.org/10.1364/JOSAA.31.002551.

[12] D. Le, T. Son, J. I. Lim, X. Yao, Quantitative optical coherence tomography reveals photoreceptor change in diabetic retinopathy, Investigative Ophthalmology and Visual Science **62**(8) (2021).

[13] A. F. Fercher, W. Drexler, C. K. Hitzenberger, T. Lasser, Optical coherence tomography - principles and applications, Reports on Progress in Physics **66**(2), 239 (2003), https://doi.org/10.1088/0034-4885/66/2/204.

[14] E. Beaurepaire, A. C. Boccara, M. Lebec, L. Blanchot, H. Saint-Jalmes, Full-field optical coherence microscopy, Opt. Lett. **23**(4), 244–246 (1998), https://doi.org/10.1364/OL.23.000244.

[15] A. Dubois, L. Vabre, A.-C. Boccara, E. Beaurepaire, High-resolution full-field optical coherence tomography with a linnik microscope, Appl. Opt. **41**(4), 805–812 (2002), https://doi.org/10.1364/AO.41.000805.

[16] L. Vabre, A. Dubois, A. C. Boccara, Thermal-light full-field optical coherence tomography, Opt. Lett. **27**(7), 530–532 (2002), https://doi.org/10.1364/OL.27.000530.

[17] A. Dubois, K. Grieve, G. Moneron, R. Lecaque, L. Vabre, C. Boccara, Ultrahigh-resolution full-field optical coherence tomography, Appl. Opt. **43**(14), 2874–2883 (2004), https://doi.org/10.1364/AO.43.002874.

[18] O. Thouvenin, C. Apelian, A. Nahas, M. Fink, C. Boccara, Full-field optical coherence tomography as a diagnosis tool: Recent progress with multimodal imaging, Applied Sciences **7**(3) (2017), https://doi.org/10.3390/app7030236.

[19] S. M. S. Kazmi, R. K. Wu, A. K. Dunn, Evaluating multi-exposure speckle imaging estimates of absolute autocorrelation times, Opt. Lett. **40**(15), 3643–3646 (2015), https://doi.org/10.1364/OL.40.003643.

[20] B. Potsaid, I. Gorczynska, V. J. Srinivasan, Y. Chen, J. Jiang, A. Cable, J. G. Fujimoto, Ultrahigh speed spectral / fourier domain oct ophthalmic imaging at 70,000 to 312,500 axial scans per second, Opt. Express **16**(19), 15149–15169 (2008), https://doi.org/10.1364/OE.16.015149.

[21] S. Song, Z. Huang, T.-M. Nguyen, E. Y. Wong, B. Arnal, M. O'Donnell, R. K. Wang, Shear modulus imaging by direct visualization of propagating shear waves with phase-sensitive optical coherence tomography, Journal of Biomedical Optics **18**(12), 121509 (2013), https://doi.org/10.1117/1.JBO.18.12.121509.

[22] K. Groux, A. Verschueren, C. Nanteau, M. Clémençon, M. Fink, J.-A. Sahel, C. Boccara, M. Paques, S. Reichman, K. Grieve, Dynamic full-field optical coherence tomography allows live imaging of retinal pigment epithelium stress model, Communications Biology **5**(1), 575 (2022), https://doi.org/10.1038/s42003-022-03479-6.

[23] T. Monfort, S. Azzollini, J. Brogard, M. Clémençon, A. Slembrouck-Brec, V. Forster, S. Picaud, O. Goureau, S. Reichman, O. Thouvenin, K. Grieve, Dynamic full-field optical coherence tomography module adapted to commercial microscopes allows longitudinal in vitro cell culture study, Communications Biology **6**(1), 2399–3642 (2023), https://doi.org/10.1038/s42003-023-05378-w.

[24] J. Scholler, K. Groux, O. Goureau, J.-A. Sahel, M. Fink, S. Reichman, C. Boccara, K. Grieve, Dynamic full-field optical coherence tomography: 3d live-imaging of retinal organoids, Light: Science & Applications **9**(1) (2020), https://doi.org/10.1038/s41377-020-00375-8.

[25] E. Tarvydas, A. Trečiokaitė, E. Auksorius, High-resolution dynamic full-field optical coherence microscopy: illuminating intracellular activity in deep tissue, npj Imaging **4**(1) (2026), https://doi.org/10.1038/s44303-026-00153-y.

[26] K. Grieve, M. Paques, A. Dubois, J. Sahel, C. Boccara, J.-F. Le Gargasson, Ocular tissue imaging using ultrahigh-resolution, full-field optical coherence tomography, Investigative Ophthalmology and Visual Science **45**(11), 4126–4131 (2004), https://doi.org/10.1167/iovs.04-0584.

[27] M. Akiba, N. Maeda, K. Yumikake, T. Soma, K. Nishida, Y. Tano, K.-P. Chan, Ultrahigh-resolution imaging of human donor cornea using full-field optical coherence tomography, Journal of Biomedical Optics **12**(4) (2007), https://doi.org/10.1117/1.2764461.

[28] E. Auksorius, Y. Bromberg, R. Motiejūnaitė, A. Pieretti, L. Liu, E. Coron, J. Aranda, A. M. Goldstein, B. E. Bouma, A. Kazlauskas, G. J. Tearney, Dual-modality fluorescence and full-field optical coherence microscopy for biomedical imaging applications, Biomed. Opt. Express **3**(3), 661–666 (2012), https://doi.org/10.1364/BOE.3.000661.

[29] W. Ghouali, K. Grieve, S. Bellefqih, O. Sandali, F. Harms, L. Laroche, M. Paques, V. Borderie, Full-field optical coherence tomography of human donor and pathological corneas, Current Eye Research **40**(5), 526–534 (2015), https://doi.org/10.3109/02713683.2014.935444.

[30] K. Grieve, A. Dubois, M. Simonutti, M. Paques, J. Sahel, J.-F. L. Gargasson, C. Boccara, In vivo anterior segment imaging in the rat eye with high speed white light full-field optical coherence tomography, Opt. Express **13**(16), 6286–6295 (2005), https://doi.org/10.1364/OPEX.13.006286.

[31] E. Auksorius, A. C. Boccara, Dark-field full-field optical coherence tomography, Opt. Lett. **40**(14), 3272–3275 (2015), https://doi.org/10.1364/OL.40.003272.

[32] E. Auksorius, A. C. Boccara, High-throughput dark-field full-field optical coherence tomography, Opt. Lett. **45**(2), 455–458 (2020), https://doi.org/10.1364/OL.381888.

[33] D. Rutkauskas, E. Auksorius, Time-domain full-field optical coherence tomography with digital confocal line scanning, Opt. Lett. **48**(13), 3539–3542 (2023), https://doi.org/10.1364/OL.488431.

[34] H. Sudkamp, P. Koch, H. Spahr, D. Hillmann, G. Franke, M. Münst, F. Reinholz, R. Birngruber, G. Hüttmann, In-vivo retinal imaging with off-axis full-field time-domain optical coherence tomography, Opt. Lett. **41**(21), 4987–4990 (2016), https://doi.org/10.1364/OL.41.004987.

[35] C. von der Burchard, M. Moltmann, J. Tode, C. Ehlken, H. Sudkamp, D. Theisen-Kunde, I. König, G. Hüttmann, J. Roider, Self-examination low-cost full-field oct (selff-oct) for patients with various macular diseases, Graefe's Archive for Clinical and Experimental Ophthalmology **259**(6), 1503–1511 (2021), https://doi.org/10.1007/s00417-020-05035-6.

[36] D. Hillmann, H. Spahr, C. Hain, H. Sudkamp, G. Franke, C. Pfaeffle, C. Winter, G. Hüttmann, Aberration-free volumetric high-speed imaging of in vivo retina, Scientific Reports **6**(35209) (2016), https://doi.org/10.1038/srep35209.

[37] B. Považay, A. Unterhuber, B. Hermann, H. Sattmann, H. Arthaber, W. Drexler, Full-field time-encoded frequency-domain optical coherence tomography, Opt. Express **14**(17), 7661–7669 (2006), https://doi.org/10.1364/OE.14.007661.

[38] A.-H. Dhalla, J. V. Migacz, J. A. Izatt, Crosstalk rejection in parallel optical coherence tomography using spatially incoherent illumination with partially coherent sources, Opt. Lett. **35**(13), 2305–2307 (2010), https://doi.org/10.1364/OL.35.002305.

[39] J. M. Schmitt, S. H. Xiang, K. M. Yung, Speckle in optical coherence tomography, Journal of Biomedical Optics **4**(1), 95–105 (1999), https://doi.org/10.1117/1.429925.

[40] T. Bonin, G. Franke, M. Hagen-Eggert, P. Koch, G. Hüttmann, In vivo fourier-domain full-field oct of the human retina with 1.5 million a-lines/s, Opt. Lett. **35**(20), 3432–3434 (2010), https://doi.org/10.1364/OL.35.003432.

[41] D. Borycki, M. Nowakowski, M. Wojtkowski, Control of the optical field coherence by spatiotemporal light modulation, Opt. Lett. **38**(22), 4817–4820 (2013), https://doi.org/10.1364/OL.38.004817.

[42] Y. Choi, P. Hosseini, J. W. Kang, S. Kang, T. D. Yang, M. G. Hyeon, B.-M. Kim, P. T. C. So, Z. Yaqoob, Reflection phase microscopy using spatio-temporal coherence of light, Optica **5**(11), 1468–1473 (2018), https://doi.org/10.1364/OPTICA.5.001468.

[43] B. Redding, Y. Bromberg, M. A. Choma, H. Cao, Full-field interferometric confocal microscopy using a vcsel array, Opt. Lett. **39**(15), 4446–4449 (2014), https://doi.org/10.1364/OL.39.004446.

[44] H. Spahr, D. Hillmann, C. Hain, C. Pfäffle, H. Sudkamp, G. Franke, G. Hüttmann, Imaging pulse wave propagation in human retinal vessels using full-field swept-source optical coherence tomography, Opt. Lett. **40**(20), 4771–4774 (2015), https://doi.org/10.1364/OL.40.004771.

[45] A. Nahas, M. Tanter, T.-M. Nguyen, J.-M. Chassot, M. Fink, A. C. Boccara, From supersonic shear wave imaging to full-field optical coherence shear wave elastography, Journal of Biomedical Optics **18**(12), 121514 (2013), https://doi.org/10.1117/1.JBO.18.12.121514.

[46] D. Hillmann, T. Bonin, C. Lührs, G. Franke, M. Hagen-Eggert, P. Koch, G. Hüttmann, Common approach for compensation of axial motion artifacts in swept-source oct and dispersion in fourier-domain oct, Opt. Express **20**(6), 6761–6776 (2012), https://doi.org/10.1364/OE.20.006761.

[47] D. Hillmann, H. Spahr, C. Pfäffle, H. Sudkamp, G. Franke, G. Hüttmann, In vivo optical imaging of physiological responses to photostimulation in human photoreceptors, Proceedings of the National Academy of Sciences **113**(46), 13138–13143 (2016), https://doi.org/10.1073/pnas.1606428113.

[48] D. Hillmann, H. Spahr, H. Sudkamp, C. Hain, L. Hinkel, G. Franke, G. Hüttmann, Off-axis reference beam for full-field swept-source oct and holoscopy, Opt. Express **25**(22), 27770–27784 (2017), https://doi.org/10.1364/OE.25.027770.

[49] P. Stremplewski, E. Auksorius, P. Wnuk, Ł. Kozoń, P. Garstecki, M. Wojtkowski, In vivo volumetric imaging by crosstalk-free full-field oct, Optica **6**(5), 608–617 (2019), https://doi.org/10.1364/OPTICA.6.000608.

[50] E. Auksorius, D. Borycki, P. Stremplewski, K. Liżewski, S. Tomczewski, P. Niedźwiedziuk, B. L. Sikorski, M. Wojtkowski, In vivo imaging of the human cornea with high-speed and high-resolution fourier-domain full-field optical coherence tomography, Biomed. Opt. Express **11**(5), 2849–2865 (2020), https://doi.org/10.1364/BOE.393801.

[51] J. G. Manni, J. W. Goodman, Versatile method for achieving 1% speckle contrast in large-venue laser projection displays using a stationary multimode optical fiber, Opt. Express **20**(10), 11288–11315 (2012), https://doi.org/10.1364/OE.20.011288.

[52] J. Kim, D. T. Miller, E. K. Kim, S. Oh, J. H. Oh, T. E. Milner, Optical coherence tomography speckle reduction by a partially spatially coherent source, Journal of Biomedical Optics **10**(6), 064034 (2005), https://doi.org/10.1117/1.2138031.

[53] E. Auksorius, D. Borycki, M. Wojtkowski, Multimode fiber enables control of spatial coherence in fourier-domain full-field optical coherence tomography for in vivo corneal imaging, Opt. Lett. **46**(6), 1413–1416 (2021), https://doi.org/10.1364/OL.417178.

[54] R. Paschotta, Shot noise, RP Photonics Encyclopedia (2005), https://www.rp-photonics.com/shot_noise.html.

[55] ICO Optics, Noise sources in image intensifiers: Shot noise and dark current explained (2025), https://www.ico-optics.org/noise-sources-in-image-intensifiers-shot-noise-and-dark-current/.

[56] R. Paschotta, Relative intensity noise (2007), https://www.rp-photonics.com/relative_intensity_noise.html.

[57] W. Shieh, I. Djordjevic, Chapter 3 - optical communication fundamentals, in W. Shieh, I. Djordjevic (eds.), *OFDM for Optical Communications* (Academic Press, Oxford, 2010), 53–118.

[58] A. Singh, M. Dogra, B. Moharana, R. Singh, Posterior segment optical coherence tomography in uncooperative paediatric patients using exo-illumination and microscope-integrated optical coherence tomography, Cureus **14**(12) (2022), https://doi.org/10.7759/cureus.32994.

[59] M. Zeppieri, S. Marsili, E. S. Enaholo, A. O. Shuaibu, N. Uwagboe, C. Salati, L. Spadea, M. Musa, Optical coherence tomography (oct): A brief look at the uses and technological evolution of ophthalmology, Medicina **59**(12) (2023), https://doi.org/10.3390/medicina59122114.

[60] R. Rocholz, F. Corvi, J. Weichsel, S. Schmidt, G. Staurenghi, J. F. Bille, *OCT Angiography (OCTA) in Retinal Diagnostics* (Springer, 2019).

[61] J. H. Yeo, R. Oh, J. Y. Lee, J.-G. Kim, Y. H. Yoon, Y. J. Kim, Optical coherence tomography angiographic findings of lamellar macular hole: Comparisons between tractional and degenerative subtypes, Scientific Reports **10**(1), 13331 (2020), https://doi.org/10.1038/s41598-020-70254-0.

[62] M. Hope-Ross, L. A. Yannuzzi, E. S. Gragoudas, D. R. Guyer, J. S. Slakter, J. A. Sorenson, S. Krupsky, D. A. Orlock, C. A. Puliafito, Adverse reactions due to indocyanine green, Ophthalmology **101**(3), 529–533 (1994), https://doi.org/10.1016/S0161-6420(94)31303-0.

[63] A. Koustenis, A. Harris, J. Gross, I. Januleviciene, A. Shah, B. Siesky, Optical coherence tomography angiography: an overview of the technology and an assessment of applications for clinical research, British Journal of Ophthalmology **101**(1), 16–20 (2017), https://doi.org/10.1136/bjophthalmol-2016-309389.

[64] Cleveland Clinic, Optical coherence tomography (oct), last updated September 24, 2024 (2024), https://my.clevelandclinic.org/health/diagnostics/optical-coherence-tomography-oct.

[65] P. Anvari, M. Ashrafkhorasani, A. Habibi, K. Ghasemi Falavarjani, Artifacts in optical coherence tomography angiography, Journal of Ophthalmic and Vision Research **16**(2), 271–286 (2021), https://doi.org/10.18502/jovr.v16i2.9091.

[66] W. Rosamond, K. Flegal, K. Furie, A. Go, K. Greenlund, N. Haase, S. M. Hailpern, M. Ho, V. Howard, B. Kissela, S. Kittner, D. Lloyd-Jones, M. McDermott, J. Meigs, C. Moy, G. Nichol, C. O'Donnell, V. Roger,

P. Sorlie, J. Steinberger, T. Thom, M. Wilson, Y. Hong, Heart disease and stroke statistics—2008 update, Circulation **117**(4), e25–e146 (2008), https://doi.org/10.1161/CIRCULATIONAHA.107.187998.

[67] M. Terashima, H. Kaneda, T. Suzuki, The role of optical coherence tomography in coronary intervention, The Korean journal of internal medicine **27**(1) (2012), https://doi.org/10.3904/kjim.2012.27.1.1.

[68] B. Hiram, Intravascular oct in pci, American College of Cardiology (2016).

[69] I. K. Jang, B. E. Bouma, D. H. Kang, S. J. Park, S. W. Park, K. B. Seung, K. B. Choi, M. Shishkov, K. Schlendorf, E. Pomerantsev, S. L. Houser, H. Aretz, G. J. Tearney, Visualization of coronary atherosclerotic plaques in patients using optical coherence tomography: comparison with intravascular ultrasound, Journal of the American College of Cardiology **39**(4) (2002), https://doi.org/10.1016/s0735-1097(01)01799-5.

[70] D. G. Bragg, State-of-the-art assessment. Diagnostic oncologic imaging, Cancer **64**(1) (1989), https://doi.org/10.1002/1097-0142(19890701)64:1+<261::AID-CNCR2820641316>3.0.CO;2-F.

[71] J. Wang, Y. Xu, S. A. Boppart, Review of optical coherence tomography in oncology, Journal of biomedical optics **22**(12) (2017), https://doi.org/10.1117/1.JBO.22.12.121711.

[72] P. C. Ashok, B. B. Praveen, N. Bellini, A. Riches, K. Dholakia, C. S. Herrington, Multi-modal approach using raman spectroscopy and optical coherence tomography for the discrimination of colonic adenocarcinoma from normal colon, Biomed. Opt. Express **4**(10), 2179–2186 (2013), https://doi.org/10.1364/BOE.4.002179.

[73] T. Gambichler, V. Jaedicke, S. Terras, Optical coherence tomography in dermatology: technical and clinical aspects, Archives of dermatological research **303**(7) (2011), https://doi.org/10.1007/s00403-011-1152-x.

[74] N. D. Gladkova, G. A. Petrova, N. K. Nikulin, S. G. Radenska-Lopovok, L. B. Snopova, Y. P. Chumakov, V. A. Nasonova, V. M. Gelikonov, G. V. Gelikonov, R. V. Kuranov, A. M. Sergeev, F. I. Feldchtein, In vivo optical coherence tomography imaging of human skin: norm and pathology, Skin Research and Technology **6**(1) (2000), https://doi.org/doi.org/10.1034/j.1600-0846.2000.006001006.x.

[75] M. Göb, L. Ha-Wissel, C. Jacobi, J. E. Hundt, R. Huber, Megahertz dynamic optical coherence tomography of blisters in human skin, Biomedical Optics Express **16**(10), 4063–4078 (2025), https://doi.org/10.1364/BOE.571621.

[76] E. T. Corp, Ss-oct lasers and systems (2019), https://www.excelitas.com/product-category/ss-oct-lasers-and-systems.

[77] FindLight, Swept lasers: An in-depth buying guide for technical applications (2023), https://www.findlight.net/blog/swept-lasers-an-in-depth-buying-guide-for-technical-applications/.

[78] Szewczyk, Olga, Łaszczych, Zbigniew, Soboń, Grzegorz, Narrow–linewidth tunable laser source for long-wavelength optical coherence tomography at 1700 nm, EPJ Web Conf. **309**, 07012 (2024), https://doi.org/10.1051/epjconf/202430907012.

[79] Superlum, Benchtop wavelength-swept tunable semiconductor lasers (2025), https://www.superlumdiodes.com/broadsweeper-benchtop.htm.

[80] AOS Technologies Logo in White, What makes a camera "high speed" (2025), https://www.aostechnologies.com/blog/what-makes-a-camera-high-speed/.

[81] Biz Dynamics MRI, What is high speed cmos image sensor? uses, how it works top companies (2025), https://www.linkedin.com/pulse/what-high-speed-cmos-image-sensor-uses-how-works-top-shmsc/.

[82] PHOTRON, Photron technical datasheet (2025), https://photron.com/wp-content/uploads/2016/11/SA-Z-REV16.10.27_LowRes.pdf.

[83] Thorlabs Inc., Multimode fiber tutorial (2026), https://www.thorlabs.com/multimode-fiber-tutorial?tabName=MM%20Fiber%20Tutorial.

[84] Thorlabs Inc., 0.22 na silica core, glass clad multimode optical fiber, step index (2026), https://www.thorlabs.com/0.22-na-silica-core-glass-clad-multimode-optical-fiber-step-index?CurrencySelect=Dollar&tabName=Overview.

[85] J. Senior, M. Jamro, *Optical Fiber Communications: Principles and Practice* (Pearson Education, 2009), 3rd edition.

[86] J. W. Goodman, *Speckle Phenomena in Optics: Theory and Applications* (Roberts Company, 2007).

[87] A. Efimov, Different measures of speckle and coherence at the output of a multimode optical fiber, J. Opt. Soc. Am. A **36**(1), 1–11 (2019), https://doi.org/10.1364/JOSAA.36.000001.

[88] E. Auksorius, Fourier-domain full-field optical coherence tomography with real-time axial imaging, Opt. Lett. **46**(18), 4478–4481 (2021), https://doi.org/10.1364/OL.435104.

[89] E. Auksorius, D. Borycki, P. Wegrzyn, I. Žičkienė, K. Adomavičius, B. L. Sikorski, M. Wojtkowski, Multimode fiber as a tool to reduce cross talk in fourier-domain full-field optical coherence tomography, Opt. Lett. **47**(4), 838–841 (2022), https://doi.org/10.1364/OL.449498.

[90] D. Borycki, E. Auksorius, P. Węgrzyn, M. Wojtkowski, Computational aberration correction in spatiotemporal optical coherence (stoc) imaging, Opt. Lett. **45**(6), 1293–1296 (2020), https://doi.org/10.1364/OL.384796.

[91] L. Ginner, A. Kumar, D. Fechtig, L. M. Wurster, M. Salas, M. Pircher, R. A. Leitgeb, Noniterative digital aberration correction for cellular resolution retinal optical coherence tomography in vivo, Optica **4**(8), 924–931 (2017), https://doi.org/10.1364/OPTICA.4.000924.

[92] B. Redding, M. Choma, H. Cao, Speckle-free laser imaging using random laser illumination, Nature Photonics **6**(6), 355–359 (2012), https://doi.org/10.1038/nphoton.2012.90.

[93] A. Badon, A. C. Boccara, G. Lerosey, M. Fink, A. Aubry, Multiple scattering limit in optical microscopy, Optics Express **25**(23), 28914–28934 (2017), https://doi.org/10.1364/OE.25.028914.

[94] R. Fang, I. Rubinoff, H. F. Zhang, Multiple forward scattering reduces the measured scattering coefficient of whole blood in visible-light optical coherence tomography, Biomedical Optics Express **13**(9), 4510–4527 (2022), https://doi.org/10.1364/BOE.459607.

[95] T.-S. Ho, M.-R. Tsai, C.-W. Lu, H.-S. Chang, S.-L. Huang, Mirau-type full-field optical coherence tomography with switchable partially spatially coherent illumination modes, Biomedical Optics Express **12**(5), 2670–2683 (2021), https://doi.org/10.1364/BOE.422622.

[96] D. Hillmann, C. Lührs, T. Bonin, P. Koch, G. Hüttmann, Holoscopy - holographic optical coherence tomography, Opt. Lett. **36**(13), 2390–2392 (2011), https://doi.org/10.1364/OL.36.002390.

[97] E. Auksorius, D. Borycki, P. Węgrzyn, B. L. Sikorski, K. Liżewski, I. Žičkienė, M. Rapolu, K. Adomavičius, S. Tomczewski, M. Wojtkowski, Spatio-temporal optical coherence tomography provides full thickness imaging of the chorioretinal complex, iScience **25**(12), 105513 (2022), https://doi.org/10.1016/j.isci.2022.105513.

[98] J. A. Izatt, M. R. Hee, G. M. Owen, E. A. Swanson, J. G. Fujimoto, Optical coherence microscopy in scattering media, Opt. Lett. **19**(8), 590–592 (1994), https://doi.org/10.1364/OL.19.000590.

[99] A. Curatolo, et al., Quantifying the influence of bessel beams on image quality in optical coherence tomography, Scientific Reports **6**, 23483 (2016), https://doi.org/10.1038/srep23483.

[100] R. F. Spaide, H. Koizumi, M. C. Pozonni, Enhanced depth imaging spectral-domain optical coherence tomography, American Journal of Ophthalmology **146**(4), 496–500 (2008), https://doi.org/10.1016/j.ajo.2008.05.032.

[101] E. Borrelli, D. Sarraf, K. B. Freund, S. R. Sadda, Oct angiography and evaluation of the choroid and choroidal vascular disorders, Progress in Retinal and Eye Research **67**, 30–55 (2018), https://doi.org/10.1016/j.preteyeres.2018.07.002.

[102] F. Corvi, L. Su, S. R. Sadda, Evaluation of the inner choroid using oct angiography, Eye **35**, 110–120 (2021), https://doi.org/10.1038/s41433-020-01217-y.

[103] D. Ferrara, N. K. Waheed, J. S. Duker, Investigating the choriocapillaris and choroidal vasculature with new optical coherence tomography technologies, Progress in Retinal and Eye Research **52**, 130–155 (2016), https://doi.org/10.1016/j.preteyeres.2015.10.002.

[104] Z. Chu, G. Gregori, P. J. Rosenfeld, R. K. Wang, Quantification of choriocapillaris with optical coherence tomography angiography: A comparison study, American Journal of Ophthalmology **208**, 111–123 (2019), https://doi.org/10.1016/j.ajo.2019.07.003.

[105] G. Ledesma-Gil, P. Fernández-Avellaneda, R. F. Spaide, Swept-source optical coherence tomography angiography imaging of the choriocapillaris, Retina **41**(7), 1373–1378 (2021), https://doi.org/10.1097/IAE.0000000000003109.

[106] M. Esmaeelpour, S. Ansari-Shahrezaei, C. Glittenberg, S. Nemetz, M. F. Kraus, J. Hornegger, J. G. Fujimoto, W. Drexler, S. Binder, Choroid, Haller's, and Sattler's layer thickness in intermediate age-related macular degeneration with and without fellow neovascular eyes, Investigative Ophthalmology Visual Science **55**(8), 5074–5080 (2014), https://doi.org/10.1167/iovs.14-14646.

[107] D. Y. Kim, J. Fingler, R. J. Zawadzki, S. S. Park, L. S. Morse, D. M. Schwartz, S. E. Fraser, J. S. Werner, Optical imaging of the chorioretinal vasculature in the living human eye, Proceedings of the National Academy of Sciences **110**(35), 14354–14359 (2013), https://doi.org/10.1073/pnas.1307315110.

[108] W. Choi, K. J. Mohler, B. Potsaid, C. D. Lu, J. J. Liu, V. Jayaraman, A. E. Cable, J. S. Duker, R. Huber, J. G. Fujimoto, Choriocapillaris and choroidal microvasculature imaging with ultrahigh speed OCT angiography, PLOS ONE **8**(12), 1–8 (2013), https://doi.org/10.1371/journal.pone.0081499.

[109] B. Marsh-Armstrong, J. Migacz, R. Jonnal, J. Werner, Quantification of choriocapillaris structure in high-resolution octa images, Investigative Ophthalmology & Visual Science **60**(9), 3089, aRVO meeting abstract (2019).

[110] I. Gorczynska, J. V. Migacz, R. J. Zawadzki, A. G. Capps, J. S. Werner, Comparison of amplitude-decorrelation, speckle-variance and phase-variance oct angiography methods for imaging the human retina and choroid, Biomed. Opt. Express **7**(3), 911–942 (2016), https://doi.org/10.1364/BOE.7.000911.

[111] J. V. Migacz, I. Gorczynska, M. Azimipour, R. Jonnal, R. J. Zawadzki, J. S. Werner, Megahertz-rate optical coherence tomography angiography improves the contrast of the choriocapillaris and choroid

in human retinal imaging, Biomed. Opt. Express **10**(1), 50–65 (2019), https://doi.org/10.1364/BOE.10.000050.

[112] B. Karamata, M. Laubscher, M. Leutenegger, S. Bourquin, T. Lasser, P. Lambelet, Multiple scattering in optical coherence tomography. I. Investigation and modeling, J. Opt. Soc. Am. A **22**(7), 1369–1379 (2005), https://doi.org/10.1364/JOSAA.22.001369.

[113] A. Grebenyuk, A. Federici, V. Ryabukho, A. Dubois, Numerically focused full-field swept-source optical coherence microscopy with low spatial coherence illumination, Appl. Opt. **53**(8), 1697–1708 (2014), https://doi.org/10.1364/AO.53.001697.

[114] M. Wojtkowski, P. Stremplewski, E. Auksorius, D. Borycki, Spatio-temporal optical coherence imaging - A new tool for in vivo microscopy, Photonics Letters of Poland **11**(2), 44–49 (2019), https://doi.org/10.4302/plp.v11i2.905.

[115] R. F. Spaide, T. Otto, S. Caujolle, J. Kübler, S. Aumann, J. Fischer, C. Reisman, H. Spahr, A. Lessmann, Lateral resolution of a commercial optical coherence tomography instrument, Translational Vision Science & Technology **11**(1), 28 (2022), https://doi.org/10.1167/tvst.11.1.28.

[116] N. Meitav, E. N. Ribak, Improving retinal image resolution with iterative weighted shift-and-add, J. Opt. Soc. Am. A **28**(7), 1395–1402 (2011), https://doi.org/10.1364/JOSAA.28.001395.

[117] P. Zhang, S. K. Manna, E. B. Miller, Y. Jian, R. K. Meleppat, M. V. Sarunic, E. N. Pugh, R. J. Zawadzki, Aperture phase modulation with adaptive optics: a novel approach for speckle reduction and structure extraction in optical coherence tomography, Biomed. Opt. Express **10**(2), 552–570 (2019), https://doi.org/10.1364/BOE.10.000552.

[118] M. D. Stern, In vivo evaluation of microcirculation by coherent light scattering, Nature **254**, 56–58 (1975), https://doi.org/10.1038/254056a0.

[119] J. Micheels, B. Aisbjorn, B. Sorensen, Laser doppler flowmetry. A new non-invasive measurement of microcirculation in intensive care?, Resuscitation **12**(1), 31–39 (1984), https://doi.org/10.1016/0300-9572(84)90056-X.

[120] A. Liebert, N. Żołek, R. Maniewski, Laser-doppler spectrum decomposition for measurement of distribution of speed of particles, in *Biomedical Optics, Technical Digest (CD)* (Optica Publishing Group, 2006), SH69.

[121] L. Puyo, M. Paques, M. Fink, J.-A. Sahel, M. Atlan, Waveform analysis of human retinal and choroidal blood flow with laser doppler holography, Biomed. Opt. Express **10**(10), 4942–4963 (2019), https://doi.org/10.1364/BOE.10.004942.

[122] L. Puyo, M. Paques, M. Fink, J.-A. Sahel, M. Atlan, In vivo laser doppler holography of the human retina, Biomed. Opt. Express **9**(9), 4113–4129 (2018), https://doi.org/10.1364/BOE.9.004113.

[123] L. Puyo, M. Paques, M. Atlan, Reverse contrast laser doppler holography for lower frame rate retinal and choroidal blood flow imaging, Opt. Lett. **45**(14), 4012–4015 (2020), https://doi.org/10.1364/OL.393712.

[124] A. Liebert, M. Leahy, R. Maniewski, Multichannel laser-doppler probe for blood perfusion measurements with depth discrimination. Medical biological engineering computing, Medical and Biological Engineering and Computing **36**(6), 740 – 747 (1998), https://doi.org/10.1007/BF02518878.

[125] D. Borycki, O. Kholiqov, S. P. Chong, V. J. Srinivasan, Interferometric near-infrared spectroscopy (inirs) for determination of optical and dynamical properties of turbid media, Opt. Express **24**(1), 329–354 (2016), https://doi.org/10.1364/OE.24.000329.

[126] Y. Li, J. Chen, Z. Chen, Advances in doppler optical coherence tomography and angiography, Translational Biophotonics **1**(1-2), e201900005 (2019), https://doi.org/10.1002/tbio.201900005.

[127] D. Borycki, E. Auksorius, P. Węgrzyn, K. Liżewski, S. Tomczewski, I. Žičkienė, K. Adomavičius, K. Karnowski, M. Wojtkowski, Multiwavelength laser doppler holography (mldh) in spatiotemporal optical coherence tomography (stoc-t), Biocybernetics and Biomedical Engineering **44**(1), 264–275 (2024), https://doi.org/10.1016/j.bbe.2024.03.002.

[128] L. Puyo, M. Paques, M. Atlan, Retinal blood flow reversal quantitatively monitored in out-of-plane vessels with laser doppler holography, Scientific Reports **11**, 17828 (2021), https://doi.org/10.1038/s41598-021-96877-5.

[129] A. M. Rollins, J. A. Izatt, Optimal interferometer designs for optical coherence tomography, Opt. Lett. **24**(21), 1484–1486 (1999), https://doi.org/10.1364/OL.24.001484.

[130] M. A. Choma, M. V. Sarunic, C. Yang, J. A. Izatt, Sensitivity advantage of swept source and fourier domain optical coherence tomography, Opt. Express **11**(18), 2183–2189 (2003), https://doi.org/10.1364/OE.11.002183.

[131] R. E. Epworth, Modal noise – causes and cures, Laser Focus **17**(9), 109–115 (1981).

[132] M. Bass (ed.), *Handbook of Optics: Fiber Optics and Nonlinear Optics*, volume IV (McGraw-Hill, 2001), 2nd edition.

[133] J. Baudrand, G. A. H. Walker, Modal noise in high-resolution, fiber-fed spectra: A study and simple cure, Publications of the Astronomical Society of the Pacific **113**(785), 851–858 (2001).

[134] D. P. Sablowski, D. Plüschke, M. Weber, K. G. Strassmeier, A. Järvinen, Comparing modal noise and frd of circular and non-circular cross-section fibres, Astronomische Nachrichten **337**(3), 216–225 (2016), https://doi.org/10.1002/asna.201412299.

[135] M. Wojtkowski, High-speed optical coherence tomography: basics and applications, Appl. Opt. **49**(16), D30–D61 (2010), https://doi.org/10.1364/AO.49.000D30.

[136] A. Bradu, A. G. Podoleanu, Fourier domain optical coherence tomography system with balance detection, Opt. Express **20**(16), 17522–17538 (2012), https://doi.org/10.1364/OE.20.017522.

[137] W.-C. Kuo, C.-M. Lai, Y.-S. Huang, C.-Y. Chang, Y.-M. Kuo, Balanced detection for spectral domain optical coherence tomography, Opt. Express **21**(16), 19280–19291 (2013), https://doi.org/10.1364/OE.21.019280.

[138] S. Mahadevan, S. Halverson, L. Ramsey, N. Venditti, Suppression of fiber modal noise induced radial velocity errors for bright emission-line calibration sources, The Astrophysical Journal **786**(1), 18 (2014), https://doi.org/10.1088/0004-637x/786/1/18.

[139] R. R. Petersburg, T. M. McCracken, D. Eggerman, C. A. Jurgenson, D. Sawyer, A. E. Szymkowiak, D. A. Fischer, Modal noise mitigation through fiber agitation for fiber-fed radial velocity spectrographs, The Astrophysical Journal **853**(2), 181 (2018), https://doi.org/10.3847/1538-4357/aaa487.

[140] F. Shevlin, High-Frequency Homogenization of Laser Illumination Through Stationary 0.22 N.A. Multimode Optical Fiber, in *The 12th Laser Display and Lighting Conference (LDC2023)* (LDC2023, Yokohama, Japan, 2023).

[141] M. Szkulmowski, M. Wojtkowski, Averaging techniques for oct imaging, Opt. Express **21**(8), 9757–9773 (2013), https://doi.org/10.1364/OE.21.009757.

[142] K. Bush, D. German, B. Klemme, A. Marrs, M. Schoen, Electrostatic membrane deformable mirror wavefront control systems: Design and analysis (2004), volume 5553, 28–38.

[143] J. Wallace, Anti-speckle technique uses dynamic optics (2009), https://www.laserfocusworld.com/optics/article/16566181/anti-speckle-technique-uses-dynamic-optics.

[144] DYOPTYKA, Anti-speckle technology (2025), https://dyoptyka.com/.

[145] M. Mikuła-Zdańkowska, D. Borycki, P. Węgrzyn, K. Adomavičius, E. Auksorius, M. Wojtkowski, Imaging of retinal ganglion cells and photoreceptors using spatio-temporal optical coherence tomography (stoc-t) without hardware-based adaptive optics, Biocybernetics and Biomedical Engineering **45**(1), 52–61 (2025), https://doi.org/10.1016/j.bbe.2025.01.001.

[146] L. Thrane, S. Gu, B. J. Blackburn, K. V. Damodaran, A. M. Rollins, M. W. Jenkins, Complex decorrelation averaging in optical coherence

tomography: a way to reduce the effect of multiple scattering and improve image contrast in a dynamic scattering medium, Opt. Lett. **42**(14), 2738–2741 (2017), https://doi.org/10.1364/OL.42.002738.

[147] B. Baumann, C. W. Merkle, R. A. Leitgeb, M. Augustin, A. Wartak, M. Pircher, C. K. Hitzenberger, Signal averaging improves signal-to-noise in oct images: But which approach works best, and when?, Biomed. Opt. Express **10**(11), 5755–5775 (2019), https://doi.org/10.1364/BOE.10.005755.

[148] B. E. Bouma, G. J. Tearney, Power-efficient nonreciprocal interferometer and linear-scanning fiber-optic catheter for optical coherence tomography, Opt. Lett. **24**(8), 531–533 (1999), https://doi.org/10.1364/OL.24.000531.

[149] J. Xia, G. Yao, Angular distribution of diffuse reflectance in biological tissue, Appl. Opt. **46**(26), 6552–6560 (2007), https://doi.org/10.1364/AO.46.006552.

[150] K. Adomavičius, A. Trečiokaitė, E. Tarvydas, E. Auksorius, High-throughput spatio-temporal optical coherence tomography (stoc-t), Opt. Continuum **4**(9), 2099–2106 (2025), https://doi.org/10.1364/OPTCON.564109.

[151] A. Kumar, W. Drexler, R. A. Leitgeb, Subaperture correlation based digital adaptive optics for full field optical coherence tomography, Opt. Express **21**(9), 10850–10866 (2013), https://doi.org/10.1364/OE.21.010850.

[152] S. G. Adie, B. W. Graf, A. Ahmad, P. S. Carney, S. A. Boppart, Computational adaptive optics for broadband optical interferometric tomography of biological tissue, Proceedings of the National Academy of Sciences **109**(19), 7175–7180 (2012), https://doi.org/10.1073/pnas.1121193109.

[153] N. D. Shemonski, F. A. South, Y.-Z. Liu, S. G. Adie, P. S. Carney, S. A. Boppart, Computational high-resolution optical imaging of the living human retina, Nature Photonics **9**(7), 440–443 (2015), https://doi.org/10.1038/nphoton.2015.102.

[154] G. Min, J. W. Kim, W. J. Choi, B. H. Lee, Numerical correction of distorted images in full-field optical coherence tomography, Measurement Science and Technology **23**(3), 035403 (2012), https://doi.org/10.1088/0957-0233/23/3/035403.

[155] A. Trečiokaitė, K. Adomavičius, E. Auksorius, Time-domain full-field optical coherence tomography with a digital defocus correction, Optics Letters **49**(10), 2605–2608 (2024), https://doi.org/10.1364/OL.520911.

[156] I. Yamaguchi, T. Zhang, Phase-shifting digital holography, Opt. Lett. **22**(16), 1268–1270 (1997), https://doi.org/10.1364/OL.22.001268.

[157] V. Barolle, J. Scholler, P. Mecê, J.-M. Chassot, K. Groux, M. Fink, A. C. Boccara, A. Aubry, Manifestation of aberrations in full-field optical coherence tomography, Opt. Express **29**(14), 22044–22065 (2021), https://doi.org/10.1364/OE.419963.

[158] L. Thrane, H. T. Yura, P. E. Andersen, Analysis of optical coherence tomography systems based on the extended Huygens–Fresnel principle, J. Opt. Soc. Am. A **17**(3), 484–490 (2000), https://doi.org/10.1364/JOSAA.17.000484.

[159] G. R. Untracht, M. Chen, P. Wijesinghe, J. Mas, H. T. Yura, D. Marti, P. E. Andersen, K. Dholakia, Spatially offset optical coherence tomography: Leveraging multiple scattering for high-contrast imaging at depth in turbid media, Science Advances **9**(27), eadh5435 (2023), https://doi.org/10.1126/sciadv.adh5435.

[160] Y. Huang, M. Badar, A. Nitkowski, A. Weinroth, N. Tansu, C. Zhou, Wide-field high-speed space-division multiplexing optical coherence tomography using an integrated photonic device, Biomed. Opt. Express **8**(8), 3856–3867 (2017), https://doi.org/10.1364/BOE.8.003856.

[161] Y. Luo, L. J. Arauz, J. E. Castillo, J. K. Barton, R. K. Kostuk, Parallel optical coherence tomography system, Appl. Opt. **46**(34), 8291–8297 (2007), https://doi.org/10.1364/AO.46.008291.

[162] T. Tanaami, S. Otsuki, N. Tomosada, Y. Kosugi, M. Shimizu, H. Ishida, High-speed 1-frame/ms scanning confocal microscope with a microlens and nipkow disks, Appl. Opt. **41**(22), 4704–4708 (2002), https://doi.org/10.1364/AO.41.004704.

[163] Y.-T. Hsiao, T.-Y. Wu, B.-K. Wu, S.-W. Chu, C.-L. Hsieh, Spinning disk interferometric scattering confocal microscopy captures millisecond timescale dynamics of living cells, Opt. Express **30**(25), 45233–45245 (2022), https://doi.org/10.1364/OE.471935.

[164] F. P. Martial, N. A. Hartell, Programmable illumination and high-speed, multi-wavelength, confocal microscopy using a digital micromirror, PLOS ONE **7**, 1–9 (2012), https://doi.org/10.1371/journal.pone.0043942.

[165] M. Liang, R. L. Stehr, A. W. Krause, Confocal pattern period in multiple-aperture confocal imaging systems with coherent illumination, Opt. Lett. **22**(11), 751–753 (1997), https://doi.org/10.1364/OL.22.000751.

[166] Q. S. Hanley, P. J. Verveer, M. J. Gemkow, D. J. Arndt-Jovin, T. M. Jovin, An optical sectioning programmable array microscope implemented with a digital micromirror device, Journal of Microscopy **196**(3), 317–331 (1999), https://doi.org/10.1046/j.1365-2818.1999.00602.x.

[167] Ansys Optics, How to model dmd (mems) in opticstudio, accessed: 2026-10-22 (2025), https://optics.ansys.com/hc/en-us/articles/43071071511187-How-to-model-DMD-MEMS-in-OpticStudio.

[168] SPIE, Digital light processing for high-brightness high-resolution applications (1997).

[169] S. M. Popoff, L. Malosse, R. Gutiérrez-Cuevas, Y. Bromberg, J. Commre, M. Glanc, R. Galicher, M. W. Matthès, A practical guide to digital micromirror devices (dmds) for wavefront shaping (2025), https://arxiv.org/abs/2311.17496.

[170] L. Krafft, P. Senée, E. Gofas, O. Thouvenin, M. Atlan, M. Paques, S. Meimon, P. Mecê, Multimodal high-resolution retinal imaging using a camera-based dmd-integrated adaptive optics flood-illumination ophthalmoscope, Opt. Lett. **48**, 236 (2023), https://doi.org/10.1364/OL.495515.

[171] L. Krafft, et al., Adaptive optics rolling slit ophthalmoscope: Combining cellular-resolution, high-speed and large field-of-view in a multimodal retinal imager, bioRxiv 2024–12, preprint, posted December 23, 2024 (2024), https://doi.org/10.1101/2024.12.23.630080.

[172] B. Hellman, C. Luo, G. Chen, J. Rodriguez, C. Perkins, J.-H. Park, Y. Takashima, Single-chip holographic beam steering for lidar by a digital micromirror device with angular and spatial hybrid multiplexing, Opt. Express **28**(15), 21993–22011 (2020), https://doi.org/10.1364/OE.394114.

[173] D. Lee, D.-G. Gweon, H. Yoo, Multipoint scanning dual-detection confocal microscopy for fast 3d volumetric measurement, Journal of Microscopy **270**(2), 200–209 (2018), https://doi.org/10.1111/jmi.12674.

[174] S. Li, R. Liang, Dmd-based three-dimensional chromatic confocal microscopy, Appl. Opt. **59**(14), 4349–4356 (2020), https://doi.org/10.1364/AO.386863.

[175] D. Rutkauskas, K. Adomavičius, E. Auksorius, Time-domain full-field confocal optical coherence tomography with digital scanning, Photonics **12**(4) (2025), https://doi.org/10.3390/photonics12040304.

[176] D. Rutkauskas, E. Auksorius, Programmable high-speed confocal reflectance microscopy enabled by a digital micromirror device, Opt. Lett. **49**(3), 686–689 (2024), https://doi.org/10.1364/OL.511601.

[177] E. Auksorius, D. Rutkauskas, K. Adomavičius, Fast and programmable reflectance confocal microscopy with digital micromirror device, https://worldwide.espacenet.com/publicationDetails/biblio?FT=D&date=20251231&DB=&locale=&CC=EP&NR=4550021C0&KC=C0&ND=2.

CURRICULUM VITAE

Name: Karolis

Surname: Adomavičius

Education:

2020 – 2026	Center for Physical Sciences and Technology, Lithuania, doctoral studies in physics
2019 – 2020	Vrije University Amsterdam, M.S. internship in Physics of Living Systems
2016 – 2018	Vilnius University, Lithuania M.S. in Laser Physics and Optical Technologies
2012 – 2016	Vilnius University, Lithuania B.S. in Applied Physics

Work experience:

2025-09 – present	Vilnius University Faculty of Medicine *Lecturer.*
2020-08 – present	Center for Physical Sciences and Technology (FTMC), *Junior researcher.*
2019-02 – 2020-04	Vrije University, *Research Assistant.*
2018-09 – 2019-01	Center For Physical Sciences and Technology (FTMC), *Engineer.*
2017-03 – 2018-08	Altechna, *Junior Metrologist.*
2014-07 – 2018-07	Vilnius University Department of Quantum Physics and Laser Research Center (LTTC), *Laboratory Assistant.*

NOTES

Vilnius University Press
Saulėtekio al. 9, LT-10222 Vilnius
e-mail: info@leidykla.vu.lt,
www.leidykla.vu.lt
Print run copies 27